Modeling of aerodynamic rotor interaction for multi-rotor wind turbines

Department of Wind Energy Master Report

Mads Christian Baungaard

DTU Wind Energy-M-0271

July 2019

DTU Wind Energy
Department of Wind Energy

Author: Mads Christian Baungaard

Title: Modeling of aerodynamic rotor interaction for multi-rotor wind turbines

DTU Wind Energy-M-0271
July 2019

Project period:
January – July 2019

ECTS: 35

Education: Master of Science

Supervisors:

Paul van der Laan
DTU Wind Energy

Mikkel Kiilerich Østerlund
Vestas Wind System A/S

Remarks:
This report is submitted as partial fulfillment of the requirements for graduation in the above education at the Technical University of Denmark.

DTU Wind Energy is a department of the Technical University of Denmark with a unique integration of research, education, innovation and public/private sector consulting in the field of wind energy. Our activities develop new opportunities and technology for the global and Danish exploitation of wind energy. Research focuses on key technical-scientific fields, which are central for the development, innovation and use of wind energy and provides the basis for advanced education at the education.

We have more than 240 staff members of which approximately 60 are PhD students. Research is conducted within nine research programmes organized into three main topics: Wind energy systems, Wind turbine technology and Basics for wind energy.

Technical University of Denmark
Department of Wind Energy
Frederiksborgvej 399
2800 Kgs. Lyngby
Denmark
www.vindenergi.dtu.dk

Abstract

Wind energy has become an important and competitive resource of electricity in the modern world, and the size of wind turbines have been growing continuously over the last decades. Several challenges however come with the increasing size of the turbines, for example transport of the enormous structures, structural properties of the blades and diminishing ratios of sweeped rotor area to rotor mass. The multi-rotor turbine concept could potentially solve many of these problems and a multi-rotor turbine with four rotors from Vestas, 4R-V29, was installed at the Risø campus of DTU in 2016 to investigate this potential further in collaboration with DTU Wind Energy.

A multi-rotor wind turbine design introduces additional parameters, which can be varied in many ways, and computational fluid dynamics (CFD) offers a relatively quick and cheap way to study some of these configurations. The simulation tool used in this thesis was EllipSys3D, where the flow was specifically modelled with the Reynolds-Averaged Navier-Stokes- and k-ε-f_P-equations assuming a neutral atmospheric boundary layer and using an actuator disk method based on airfoil data to model the rotor forces. The lower left rotor of the 4R-V29 wind turbine was first investigated as a single-rotor wind turbine with different orientations. The power production as function of yaw was found to scale as $P \sim \cos^{2.2}(\gamma)$ with resulting increases of wake recovery. Studies with two aligned single-rotor turbines however showed that yawing the upstream turbine could not improve the combined power production, which was also found to be the case for two aligned multi-rotor turbines. The pitch and rpm settings of the individual rotors used for these studies were supplied by Vestas, but was found to be sub-optimal as the power production could be improved by 1.8-3.8% with the use of an optimizer coupled to EllipSys3D. As an intermediate step in between the single- and four-rotor turbine, a double-rotor turbine was considered to quantify the rotor interaction as function of tip clearance and the rotor interaction was seen to increase the combined power production compared to two freestanding single-rotor turbines with 0.0-1.9% for the optimal tip clearances of $s_h/D \approx 0.01 - 0.15$ depending on the orientation of the rotors and the ambient turbulence intensity. Finally, it was investigated if counter-rotating rotors could improve the wake recovery due to the rotation of the wakes, but no improvements were found for any of the 15 other combinations of clockwise (CW) and counter-clockwise (CCW) rotating rotors compared to the original 4R-V29 with CW rotating rotors only.

Acknowledgements

I began my master studies at DTU Wind Energy in September 2017 with only little knowledge of wind turbines, but have over the past 2 years learned much from world-leading professors within the field wind energy through various courses and projects. Among these, I would like to thank Martin O. L. Hansen, Jens Nørkær Sørensen, Clara Marika Velte and Henrik Bredmose, with whom I have had many interesting lectures and discussions. I remember especially the offshore wind energy course in Autumn 2018 with Henrik Bredmose as being particularly joyful and inspiring. I would also like to thank all of my fellow wind energy students from all around the world for making my time at DTU enjoyable, both inside and outside of the classrooms.

In September 2018 I attended an open house event hosted by DTU Wind Energy at the Risø campus of DTU, and here I saw the Vestas 4R-V29 multi-rotor turbine for the first time. Søren Oemann Lind guided a tour to the multi-rotor turbine at the event and put me in contact with Erik Carl Lehnskov Miranda from Vestas, who gave me the possibility to write this thesis and facilitated the contact to my two supervisors. I am grateful to both of them for thus being the entrance to this project. Next, I would like to thank my two supervisors, without whom this project would have been impossible: Mikkel Kiilerich Østerlund, who functioned as my link to Vestas during the past 6 months and provided valuable insights from an industrial point of view despite the distance between Risø and the Vestas department in Aarhus. Paul van der Laan, has been the main supervisor of this project and I can not thank him enough for our weekly meetings and discussions, and for introducing me to all of the computational tools needed for this project. The project has been a very practical introduction to state-of-the-art CFD wind turbine research and I could not have thought of anyone better to guide me into this world.

Finally, I would like to thank my dormitory roommates, friends and family for always supporting me and for letting me enjoy life outside of the university.

Contents

Nomenclature

Latin Symbols

P	Power	[W]
C_P	Power coefficient	[-]
T	Thrust	[N]
C_T	Thrust coefficient	[-]
τ	Torque	[N m]
x,y,z	Main coordinate system defined in Figure 2.1	[m]
U,V,W	Time averaged velocity in the main system	[m/s]
P	Time averaged pressure	[Pa]
k	Turbulent kinetic energy	[m^2/s^2]
x_R,y_R,z_R	AD coordinate system defined by the yawing and tilting of the main system	[m]
z_H	Reference height (not necessarily hub height)	[m]
$U_{H,\infty}$	Freestream velocity at reference height	[m/s]
$I_{H,\infty}$	Freestream TI at reference height	[%]
D	Rotor diameter	[m]
R	Rotor radius	[m]

Greek Symbols

γ	Yaw angle	[deg]
ψ	Tilt angle	[deg]
φ	Azimuthal angle	[deg]
ϕ	Inflow angle	[deg]
θ	Blade pitch angle	[deg]
β	Blade twist angle	[deg]
α	Angle of Attack	[deg]
Ω	Rotational speed	[rpm]
λ	Tip speed ratio	[-]
ρ	Density	[kg/m^3]
μ	Dynamic viscosity	[kg/(m s)]
ν	Kinematic viscosity	[m^2/s]
ε	Dissipation	[m^2/s^3]

Mathematical notation

$\{1, 2, \ldots, 10\}$	Collection of values (1 to 10 in steps of 1 in this example).
$\langle \quad \rangle_{AD}$	Disk average.
$\mathbf{f}$	Vector.
$\underline{\underline{a}}$	Matrix.
$\overline{u} = \frac{1}{T}\int_0^T u(t)dt$	Time average.

Abbreviations

OEM	Original Equipment Manufacturer
O&M	Operation and Maintenance
LCoE	Levelized cost of energy
CFD	Computational Fluid Dynamics
ABL	Atmospheric Boundary Layer
AD	Actuator Disk
AL	Actuator Line
AS	Actuator Surface
cD	Cells pr. diameter in the wake region
DNS	Direct Numerical Simulation
RANS	Reynolds-Averaged Navier-Stokes
LES	Large Eddy Simulation
SC	Shape cell
DC	Domain cell
rpm	rpm is used synonymous with rotational speed, even though it really is the unit of rotational speed.
CW	Clockwise
CCW	Counter-Clockwise
VSPR	Variable Speed Pitch Regulated
BC	Boundary Condition
TI	Ambient Turbulent Intensity

Chapter 1

Introduction

1.1 History of wind energy

Nuclear fusion of hydrogen atoms into helium atoms fuels the energy production of the sun, and some of this energy will eventually be radiated towards the earth as electromagnetic waves. Approximately 30% of the energy impacting the earth will be directly reflected, while the rest will go into heating of the earth, which then again will emit electromagnetic waves (although with much longer wavelength, since the earth is much cooler compared to the sun). The heating at the equator is larger than at the poles and this is ultimately the driver of the *wind* on the earth [1].

Humans have extracted energy from the wind for thousands of years for different purposes and the propulsion of ships has probably been the most important application until the steam and combustion engines were invented. The first historical record of what today is known as a wind turbine dates back to Hero, who was a mathematician and engineer living in Alexandria, Egypt from around 10 AD - 70 AD, where he supposedly constructed a windmill to provide air to an organ [2]. The windmill later found other important usages, e.g. grinding grain, irrigation and preventing floods in low lands [3]. It was however first in the end of the 19th century that the windmills began to produce electricity and these machines became known as *wind turbines*. The Danish physicist, inventor and teacher, Poul la Cour, was one of first in the world to built a wind turbine and he had a key role in the initial wind turbine development, since he constructed more than 100 turbines (from 20-35 kW) between 1891 to 1918 [2] and at the same time functioned as a teacher of wind energy at Askov højskole. That Denmark today is one of the world leaders in wind energy (at least pr. capita) can very likely be attributed to the him.

Figure 1.1: Gedsermøllen built in 1956-57 [4].

One of la Cour's students was Johannes Juul, who would go on to built the 200 kW Gedsermøllen in 1956, which at the time was the most powerful turbine in the world and ran until 1967 with almost no maintenance, thus demonstrating durability not seen in other turbines at the time. It was a three-bladed upwind turbine with an asynchronous generator, which was stall-regulated and had emergency tip brakes (invented by Johannes Juul), and this design, known as the "danish concept", was the primary design of most wind turbines up until the 1990's [4]. From there on the variable-speed pitch regulated (VSPR) machine became the standard, which it still is today, where both synchronous and asynchronous generators are used.

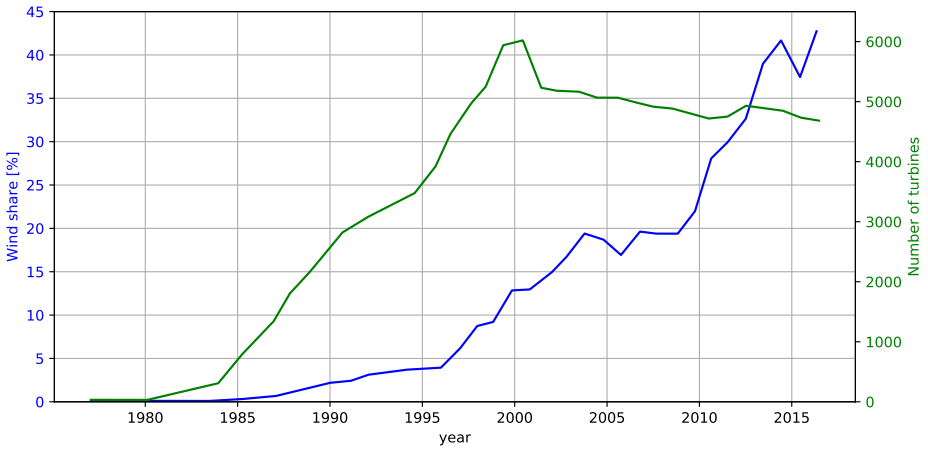

Figure 1.2: Wind energy electricity share and number of turbines in Denmark. Source: Danmarks Vindmlleforening[1].

The contribution of wind energy in the total electricity production was negligible for the most part of the 20th centery for even progressive countries with good wind conditions like Denmark, c.f. Figure 1.2. It was instead dominated by coal, gas and oil, but with the 1st and 2nd oil crisis in respectively 1973 and 1979, the governments started funding alternative energy sources through research and favorable tax options. Gedsermøllen was for example refurbished in 1975 with funds from NASA to conduct new measurements of the turbine and Denmark had in general a very good political backing, which gave the Danish OEM's a headstart that they leveraged to become the world market leaders up through the 80's and 90's. Vestas merged with NEG Micon (which itself was a merger of Nordtank and Micon in 1997) in 2004 to become the absolute world leader, but has in recent years been in tough competition with among others Siemens Gamesa RE (which acquired the danish OEM Bonus in 2004), General Electric RE, Goldwind, Enercon, etc.

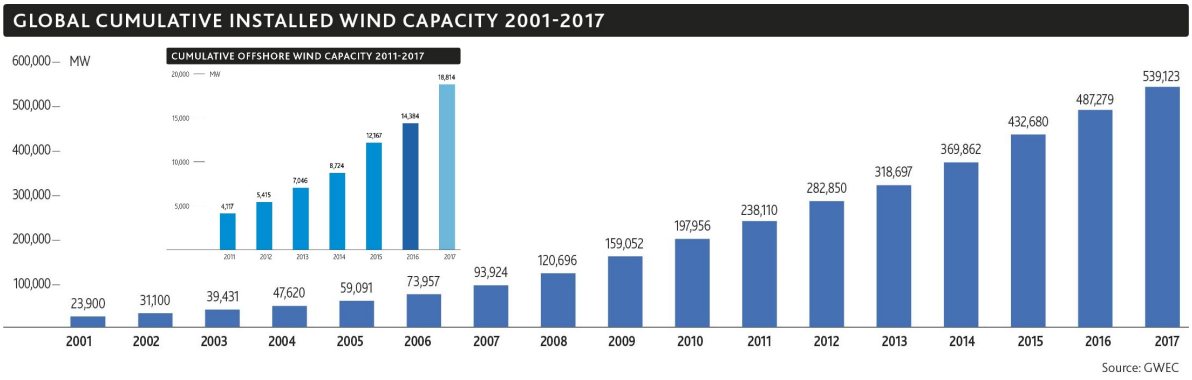

Figure 1.3: Global cumulative wind capacity. Source: GWEC[2]

[1] https://www.dkvind.dk/viden/antal-og-kapacitet-status-ultimo-2017/ (accessed 2019-03-04)
[2] https://gwec.net/global-figures/graphs/ (accessed 2019-03-04)

In 1991 the first offshore wind farm was installed in Vindeby, Denmark with a capacity of 4.95 MW (powered by 11 Bonus 450 kW turbines) and today it is not unusual to have wind farms on the order of 500-1000 MW, which would be impossible to construct onshore in densely populated areas for an array of reasons. It is however still a small market compared to the onshore turbines, c.f. Figure 1.3, since the LCoE is still higher compared to onshore turbines, even though the wind resources at sea are obviously better. The public acceptance aspect and the scale of the offshore wind farms are nevertheless not to be underestimated, and the worlds first zero subsidy offshore wind farm is right now on its way[3]. As can be seen in Figure 1.4, the offshore turbines are pushing the turbine size both in terms of rated power and blade length, and the question is how much larger they will get? The former CTO of Bonus and Siemens, Henrik Stiesdal, gave his guess in a series of 5 letters to Ingeniøren[4] in 2017 based on price levels and scaling laws of the different components: For onshore he predicted 2-4 MW and for offshore 10-20 MW. Some of these scaling laws will be presented in the next section and be applied to explain the advantages of multi-rotor turbines. Stiesdal's onshore guess has already been surpassed with 4+ MW onshore turbines in the pipeline of several OEM's, while commercial 10+ MW offshore turbines are soon to break into the market.

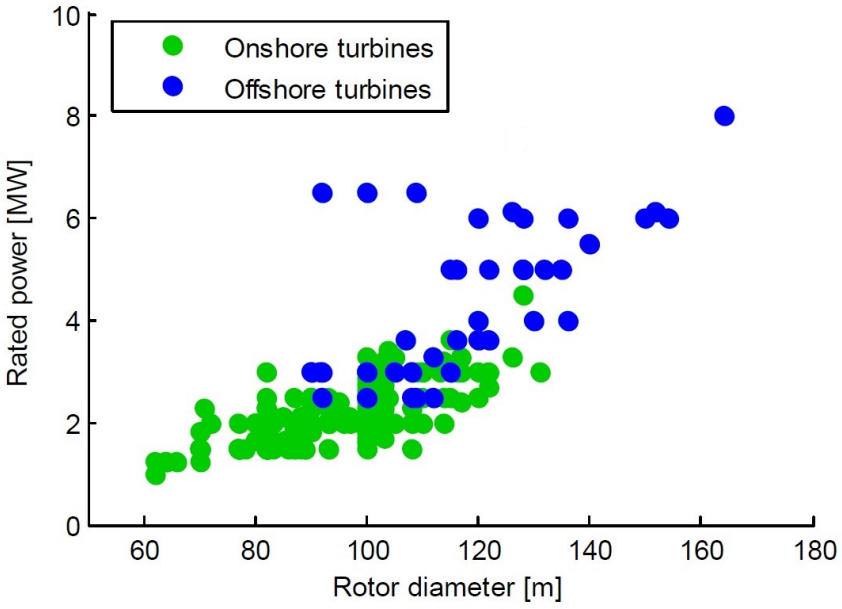

Figure 1.4: Turbine sizes as of Autumn 2018.[5]

[3]https://windeurope.org/newsroom/press-releases/worlds-first-offshore-wind-farm-without-subsidies-to-be-built-in-the-netherlands/

[4]https://ing.dk/blog/bliver-vindmoellerne-ved-med-at-vokse-del-192076

[5]DTU LAC course notes from autumn 2018.

1.2 Multi-rotor turbines

Vestas had a prototype multi-rotor turbine, 4R-V29, installed at Risø in April 2016 (see Figure 1.5). The turbine was operated and tested in collaboration with DTU Wind Energy until its decommission in December 2018, and this thesis is a continuation of this collaboration aiming to investigate the multi-rotor turbine further using CFD. The aesthetics of multi-rotor turbines are debatable, but they hold several advantages compared to single-rotor turbines, e.g. mass production, logistics and material savings. The latter can be explained with the "square-cube scaling law", which will be discussed in the following section.

Figure 1.5: Picture of the Vestas 4R-V29 situated at Risø.

1.2.1 Scaling laws

Scaling laws are seen in all of technology and nature, and one of them is the "square-cube" law, which was first described in 1638 by Galilei[4]:

Area scales with length squared ($A \sim L^2$), while volume scales with length cubed ($V \sim L^3$)

L and the proportionality constants depends on the object, e.g. for a sphere $A = 4\pi R^2$ and $V = \frac{4}{3}\pi R^3$, but the proportionality constants are less important, when ratios are considered. Doubling the radius of a wind turbine rotor, gives a four times larger rotor area (and thus four times as much available wind energy), but the rotor mass is eight times larger (since the mass is proportional to volume). The underlying assumption of scaling is similarity, i.e. geometric similarity, same technology used to design the structure, same tip speed ratio, same Reynolds number (this has a negligible effect, when comparing big turbines [5]), etc. An example of a fair scaling could be the Siemens 3 MW and 6 MW turbines, since they were built using almost the same technology[4]:

Model	Diameter [m]	Area [m^2]	Rotor+Nacelle mass [ton]
Siemens 3 MW	108	9160.8	133
Siemens 6 MW	154	18626.5	350

Table 1.1: Scaling of Siemens turbines.

$$M(D) = \alpha D^{\beta} \tag{1.1}$$

$$\beta = \log\left(\frac{M_6}{M_3}\right) / \log\left(\frac{D_6}{D_3}\right) \approx 2.7 \tag{1.2}$$

This simple example gives a "square-2.7 law", which is generally seen in practice for the combined rotor and nacelle mass, while a "square-2.6 law" is seen for the blades alone. Practical limitations on the components might explain the discrepancy from the theoretical square-cube law, e.g. a lower limit of how small a component can be made. Anyhow, it is clear that the upscaling will be unfavorable with respect to the energy extracted pr. combined rotor and nacelle mass, so why are larger and larger turbines then produced? The answer is to be found in how the price of the different wind turbine components scale and how the *Balance of Plant* scales (BoP includes installation, O&M, service, financing and other "non-turbine" related expenses). It is favorable to have larger wind turbines from a BoP point of view, especially offshore, but an important aspect in this economic discussion is also the industrialization or standardization of the wind turbines: Far more onshore turbines are still produced, c.f Figure 1.3, typically in the range of 2-4MW, and it is well-known that mass-production is one of the most important economic drivers. Larger and larger turbines are however still being developed, even though this development is very costly, and there might also be some "the-bigger-the-better"-mentality and marketing/brand values contributing to this.

The multi-rotor turbine uses the best of both worlds: It uses more, but smaller rotors, to beat the square-cube law and leverage mass-production, and can at the same time offer a high power capacity to beat BoP. A rough estimation of the saved combined rotor and nacelle mass can be made from eq. 1.1 assuming that $A_{single} = A_{multi}$, so that $D^2_{single} = ND^2$, where N is number of rotors, each with diameter D, on the multi-rotor turbine.

$$\frac{M_{multi}}{M_{single}} = \frac{N \cancel{\propto} D^{\beta}}{\cancel{\propto} D^{\beta}_{single}} = N^{-\beta/2+1} \tag{1.3}$$

For $\beta = 2.7$ and $N = 4$, this evaluates to $\frac{M_{multi}}{M_{single}} \approx 0.62$ and 38 % of the mass is thus saved. This looks very promising, but it has to be noted that the extra support structures needed for the multi-rotor turbine was not included and that other complexities also arise. The number of parts, control systems and so on increase, but as discussed earlier this might be beneficial for mass production, while more challenging for the installation and maintenance. On the other hand, the reliability of power production will be enhanced, since in the case a rotor failure, the $N - 1$ other rotors can still produce power. Another advantage is transportation, since it is easier to transport smaller turbines, although there are more of them.

1.2.2 Historical multi-rotor turbines

Two Dutch mills near Saltbæk Vig, Denmark, were modified with two rotors each between 1900 and 1910, thus creating two of the first multi-rotor windmills in the world (the historical records from this time are sparse, so it is possible, that even earlier multi-rotor windmills might have existed). None of them however produced electricity, but instead drove pumps for controlling the water level at the creek.

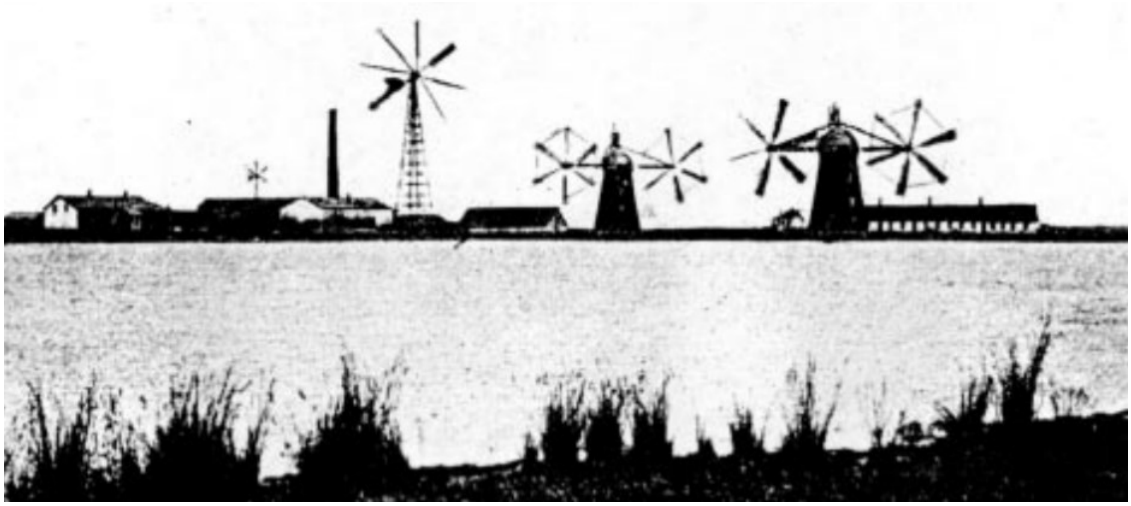

Figure 1.6: Multi-rotor windmills at Saltbæk Vig, Denmark. Source: Danmarks Vindkrafthistoriske Samling[6].

The idea of a multi-rotor wind turbine for producing electricity was first conceived around 1930 by the German engineer Hermann Honnef, who envisioned a 500 m tall lattice tower (he also proposed a "smaller" 250 m tower) equipped with 3 or 5 rotors of each 160 m diameter. The upper part of the tower could tilt to protect the turbine in case of extreme wind conditions.

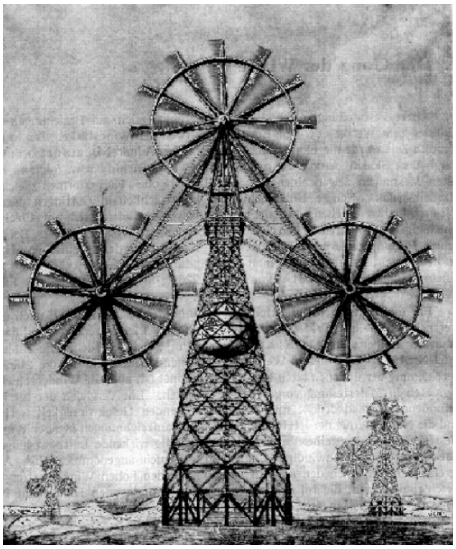

(a) Wind farm of multi-rotor turbines. Illustration from "Windkraftwerke" (1932).

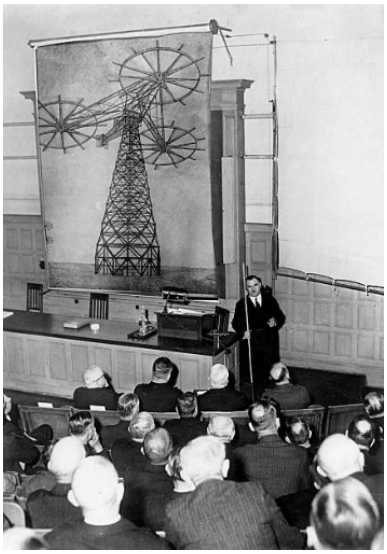

(b) Presentation to german government representatives in 1932.[7]

Figure 1.7: Honnef's multi-rotor turbine with 3 rotors. In (a) upright position and (b) tilted position.

These gigantic turbines were never realized, but a small prototype with a similar design as the 1932 turbine from Figure 1.7 was produced and is displayed in Figure 1.8a with Honnef in the foreground. It has not been possible to find further information about this prototype, so it can only be presumed that this prototype was constructed some time between 1932 and 1939, possibly to gather fundings for a full-scale turbine.

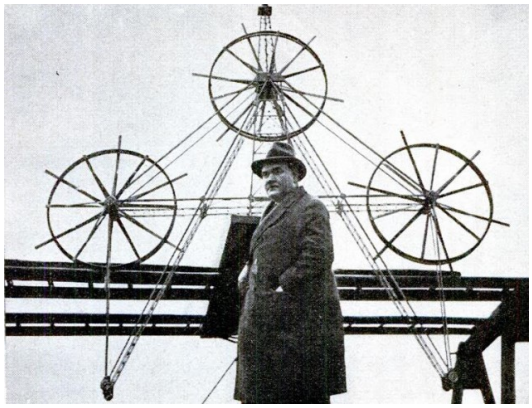

(a) From the August 1939 edition of the Popular Science magazine.

(b) Picture from Mathiasberg test site some time between 1941-1945.[8]

Figure 1.8: Honnef's multi-rotor turbine prototypes.

[6] http://www.vindhistorie.dk/userfiles/downloads/faktablade/Faktablad_2a.pdf (accessed 2019-03-08).

[7] https://www.gettyimages.dk/detail/news-photo/german-inventor-and-wind-energy-pioneer-hermann-honnef-with-news-photo/167442741 (accessed 2019-03-08)

Some funding was eventually obtained, and another multi-rotor turbine prototype with 2 rotors was built in 1941, 15 km northwest of Berlin in Mathiasberg, Germany. Conventional wind turbines were also tested at 3 other test stands, but the whole test facility was demolished in 1945, when the Soviets invaded Germany. Very little information about the turbine was hence preserved, but the multi-rotor turbine supposedly used a small 500 W generator for each of the rotors, which each had a diameter of 10 m (the few available sources[8] [9] say "up to 10 m", so smaller rotors might have been equipped during the tests).

New ideas and proposals of multi-rotor turbines were brought forth by Percy Thomas in 1945 and William Heronemus in 1972, see for example [6], but systematic wind tunnel testing of multi-rotor tubines was first conducted in 1984 by Smulders et. al in the Netherlands [7]. They used a small double-rotor turbine, where each rotor had 2 blades and a diameter of 20 cm, and the support structure could be configured to experiment with different distances between the rotors. All experiments were conducted with an inflow velocity of 4.8 m/s (no turbulence intensity level is mentioned [7]) to avoid Reynolds number effects and the performance was compared through a calculated power coefficient. They also had an anti-symmetrical rotor, which could be used instead of the right rotor to experiment with counter-rotating configurations. Three main results of the experiments were:

1. The average power of a rotor pair is slightly higher than that of a single rotor (a few procent). This was both observed for co- and counter-rotating pairs.
2. The effect is however negligible for $s_h/D \geq 0.4$, where s_h is the horizontal tip clearance.
3. When the twin rotor is yawed, there is self-aligning moment, which tends to force the turbine back to zero yaw.

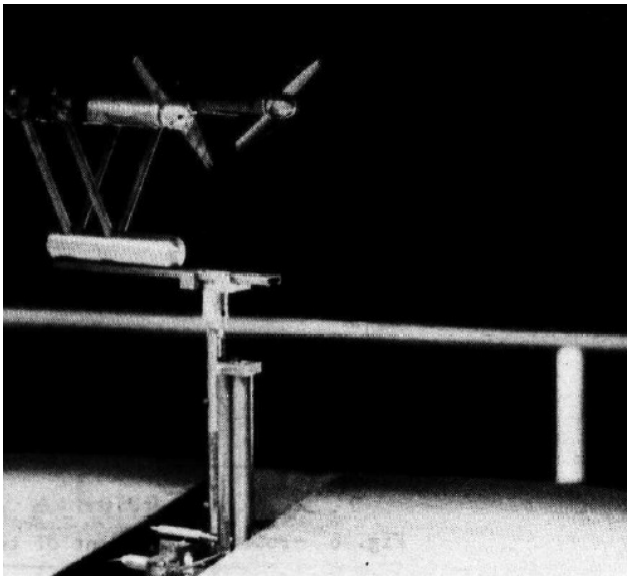

Figure 1.9: Experimental setup of Smulders et. al in 1984 [7].

In the introduction of [7] it is mentioned that at least 8 "twin turbines" (2 x 10.6 m diamter) were operated in Holland in 1984, but it has not been possible to find any other mentioning of these, except the following quote from a small advertising brochure of the Dutch wind turbine manufacturer Lagerwey[10]:

> *The multi-wind turbine is the solution for attaining a high level of wind power on a small site. Since 1982 Lagerwey has been making the twin turbine, two single rotors on one mast [...]*

[8] http://www.boetzow.de/index.php/boetzower-geschichte-n/mathiasberg/31-windkraft-versuchsfeld-1941-45 (accessed 2019-03-08)

[9] http://www.buch-der-synergie.de/c_neu_html/c_08_04_windenergie_d_bis_1993.htm (accessed 2019-03-08)

[10] http://www.windsofchange.dk/WOC-eurturb.php (accessed 19-03-11)

Lagerwey had indeed developed a 15kW single-rotor wind turbine with a diameter of 10.6 m in the early 80's, so the 8 twin turbines have most certainly been made out of two of these turbines, hence reaching a total rated power of 30kW. Lagerwey was also known for using two blades, so this might have been the reason why Smulders et. al used rotors with two blades in their experiments.

Also in 1984 in the Netherlands, the company Karl van der Linden constructed a multi-rotor turbine with two rotors at Hillegom near Amsterdam. Each rotor had three Aerostar 7.5 m blades and a 55kW generator, giving the multi-roter turbine a total rated power of 110 kW, thus becoming the largest multi-rotor turbine ever built at the time. The main business of the company was however antenna masts, and the wind adventure was not pursued further. The company was deconstructed in 1992[11].

Figure 1.10: Karl van der Linden's "Twinmaster" in 1984.[12]

The record only lasted for two years, when Lagerwey constructed a six-rotor turbine with a total rated power of 450kW at Maasvlakte situated west of Rotterdam, Holland. It was based on their succcesful 2-bladed 75kW turbine with a rotor diameter of 15 m, and the support structures were simple, straight cantilevered beams from the main tower. The turbine encountered serious problems in the first time of its lifetime with two blades breaking off in September 1986 and again in October 1987, where one of the support arms also broke off. These problems could be traced back to the vibrations of the turbine, which occurred with many different frequencies due to the complex structure. It was hence decided to remove the two lower rotors after the October 1987 accident and it hereafter operated rather well for at least 15 years [8]. The calculation of natural frequencies for wind turbines can nowadays be obtained from for example the HAWCStab2 software. The modal analysis is however more complicated for multi-rotor turbines and is right now being researched in a Ph.D.-project at Aarhus University in collabration with Vestas[13]. The Lagerwey turbine only had one yawing motor at the bottom of the main tower, while the 4R-V29 can yaw the upper and lower support structures independently.

[11] http://www.buch-der-synergie.de/c_neu_html/c_08_06_08_holland_2.htm (accesed 2019-03-11)
[12] http://www.windsofchange.dk/WOC-eurturb.php (accesed 2019-03-11)
[13] http://eng.au.dk/en/education/phd/phd-projects/mechanical-engineering/ (accessed 2019-03-11)

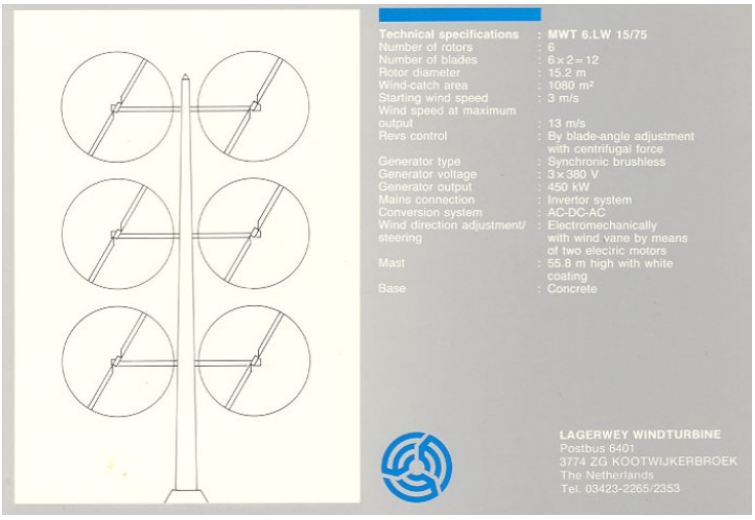

(a) Technical specifications.

(b) Before downgrade to four rotors.

Figure 1.11: Lagerwey multi-rotor turbine from 1986[10]. The two lower rotors were removed after the October 1987 accident.

In 1995 Peter Jamieson, a Garrad Hassan wind engineer, was contacted by the UK Department of Industry to conduct studies regarding potential cost improvements in wind energy, and the output of this request was a report, which suggested multi-rotor turbines as a possible solution due to the scaling properties described in the previous section [5]. He has since then been one of the most firm advocates for multi-rotor turbines with several publications on the subject, e.g. [5]. Marcia Heronemus, daughter of William Heronemus, has carried on the multi-rotor turbine legacy from her father and in 2007 she commissioned the Southwest Research Insitute to conduct wind tunnel tests of a seven-rotor turbine. Each rotor had a rated power of 400W and a diameter of 1.1 m, and the six outer rotors could be moved radially outwards, to obtain different tip clearances between $0.02D$ to $0.16D$. Probably due to the project being private, results were first published three years after the tests and only very briefly in a one page article [9], which concluded that "no significant adverse effects due to rotor interaction" were found.

Figure 1.12: Multi-rotor turbine prototype with seven rotors being tested in the Langley Full Scale Tunnel, Virginia, USA in 2007 [5].

The financial crisis in 2008 also hit the automotive industry including its suppliers like the large German company Brose, which had and has a multi-billion revenue and customers like Audi, BMW, Daimler and VW. Maybe as a consequence of this, they looked into other business opportunities like for example the wind turbine business, and they set up a collaboration with the TU Berlin to investigate a modular multi-rotor wind turbine concept, which was given the name "MOWIAN" (from Modular Windenergieanlagen). Garrad Hassan had merged with the classification and consultancy company Germanischer Lloyd in 2009, and their test facilities in the city of Kaiser-Wilhelm-Koog, Germany, was used to test the MOWIAN concept. A twin turbine test was first conducted in September 2011, and one year later the MOWIAN turbine was tested, which had 24 rotors, each with a diameter of 1.3 m and 500 W rated power[14]. No articles about the test results were published, but in 2016 a spin-off company named MOWEA was founded by two of the involved engineers from TU Berlin. MOWEA produces small turbines similar to the ones used for the MOWIAN turbine and the turbines can be combined together in modules[15]. Brose is not involved in this company[16].

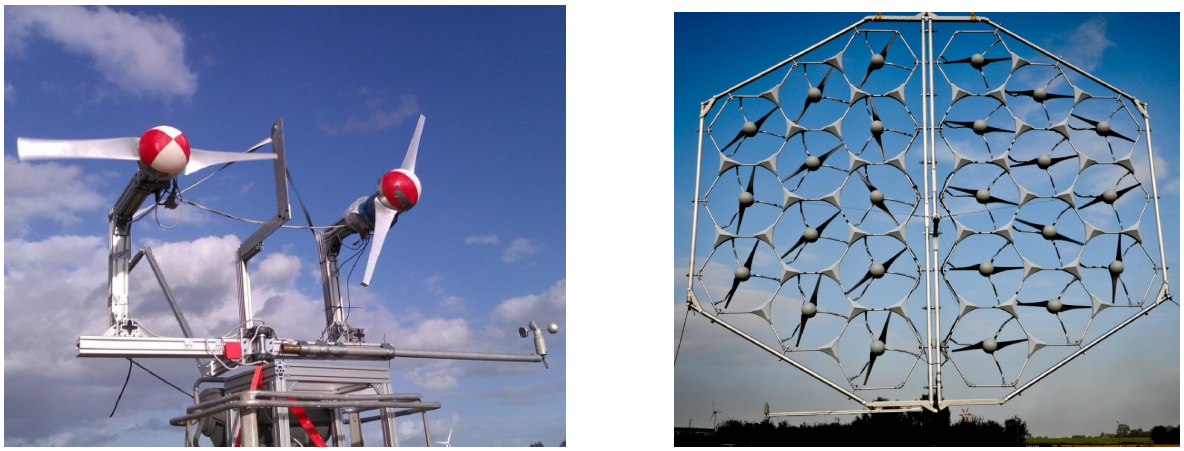

(a) Twin turbine test from September 2011.

(b) Test of MOWIAN in September 2012.

Figure 1.13: Test of the MOWIAN multi-rotor turbine in Kaiser-Wilhelm-Koog. Source: MOWIAN presentation[14].

Diffuser augumented multi-rotor turbines has recently been investigated at the Kyushu University, Fukuoka, Japan with both wind tunnel experiments, CFD and actual field tests [10], [11], [12].

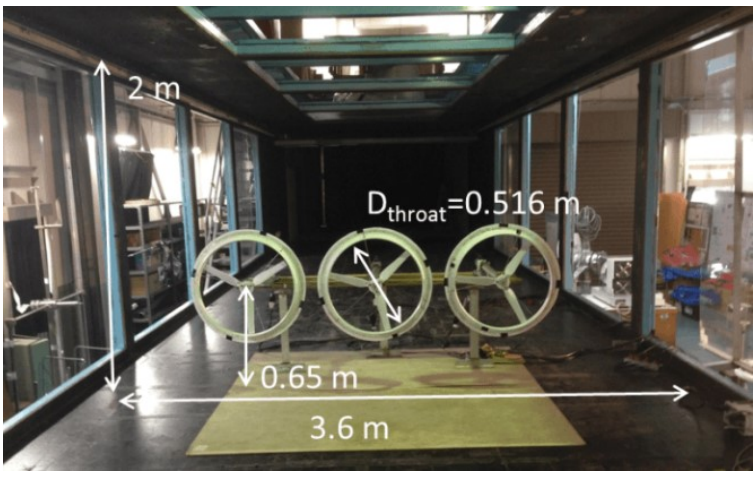

Figure 1.14: Wind tunnel test at Kyushu University, Japan.

[14]http://archiv.windenergietage.de/WT21_15_F5_1020_Mowian.pdf (accessed 2019-3-13)
[15]https://www.mowea.world/ (accessed 2019-03-13)
[16]Personal communication with Dr.-Ing. Till Naumann, CEO of MOWEA.

Several configurations with respect to diffuser type, tip clearance, orientation (not yaw and tilt, but angle between them, c.f. Figure 3.17 in [10]) and number of rotors (2, 3 and 5) have been tested in wind tunnels and with CFD, and results indicated an optimum tip clearance of $s/D = 0.1 - 0.2$ with a resulting power gain as also observed in the Smulders experiments. Prototypes were also constructed on the campus, c.f. Figure 1.15, where the first turbine was put up in December 2014 and had 3 rotors, each with 1 kW rated power and 1.5 m diameter. The rotors was setup as a 60° configuration with $s/D = 0.2$, whereas the larger prototype from March 2016 was setup as a 90° configuration with $s/D = 0.15$ (this is the distance between bottom rotor and top rotor). The prototype from March 2016 had larger rotors with 3 kW rated power and 2.8 m diameter. The concepts are owned by Riamwind Co. Ltd.[17]

(a) 3 kW turbine from December 2014.

(b) 9 kW turbine from March 2016.

Figure 1.15: Turbines at Kyushu University. Source: [10] [11].

This concludes the historical review of the co-planar multi-rotor turbines (co-axial multi-rotor turbines will be discussed briefly in Section 3.3) constructed over the past 100 years, and brings us back to the present and to the Vestas 4R-V29, which was introduced in the beginning of this section. At a total rated power of 900 kW, it is by far the most powerful multi-rotor wind turbine in the history and the test results of the 4R-V29 will decide, whether it will hold this position or a new generation of MW-multi-rotor turbines will emerge.

1.2.3 CFD calculations of multi-rotor turbines

In addition to theoretical and experimental studies, CFD has emerged as an equal discipline in the modern days of fluid mechanics, where the governing equations (discussed in the next section) are discretized and solved on a personal computer or cluster of CPU's. A CFD analysis can provide a quick and cheap way to try out new ideas, compared to setting up a full-scale experiment, and the flow field surrounding the turbine can easily be visualized. This is the purpose of this thesis, where different configurations of the 4R-V29 are tested using the RANS-AD method with k-ε-f_P turbulence modelling (the method is described in Chapter 2) to the evaluate power production and wake characteristics. A summary of multi-rotor turbine CFD publications is given in Table 1.2 and the small number of publications suggests that much is still to be learned.

[17] http://www.riamwind.co.jp/ (accessed 2019-03-13)

Multi-rotor CFD litterature			
Author, year	Title	Method/Properties	Results
Chasapgiannis et. al [13] - 2014	Analysis of the aerodynamic performance of the multi-rotor concept	RANS-AD k-ω with a variant of method III and Vortex simulations of a seven-rotor turbine. $s/D = 0.05$, $\lambda = 9$ and $I_{H,\infty} = 0$.	A power gain of $\tilde{3}\%$ compared to seven single rotors, but also increase of loading amplitude between 0.3-2.13%.
Ghaisas et. al [14] - 2018	Large-eddy simulation study of multi-rotor wind turbines	LES of a four-rotor turbine and an equivalent single-rotor turbine. Different tip clearances, s_h and s_v, are investigated. A setup of 5 aligned turbines are simulated lastly. AD with $C_T = 0.75$ and log-law ($u_* = 0.45$ m/s) are used for all simulations.	The velocity deficit variation is found to match well with the Gaussian model, while the Jensen model matches the disk-averaged deficit well. The difference between the four-rotor cases with different tip clearances is small compared to the difference between any four-rotor case and the single-rotor case.
van der Laan et. al [15] - 2019	Power curve and wake analyses of the Vestas multi-rotor demonstrator	Lidar data is used for both determining the 4R-V29's power curve and comparaing its wake with 4 different CFD models: Fuga, EllipSys3D RANS-AD, MIRAS-FLEX5 and EllipSys3D LES-AL-FLEX5.	A weighthed average based on observations between $V_{cut-in} = 5$ m/s and $V_{rated} = 11$ m/s gives $\Delta C_p = 1.8 \pm 0.2\%$. Using a Weibull distribution, this translates to $\Delta\text{AEP} = 1.5 \pm 0.2\%$. The 4 CFD models show some of the same trends, but does not compare too well to the experimental measurements, which suggest that the actual reference speed and shear was different than the simulated. A simplified RANS-AD simulation of 4R-V29 shows enhanced wake recovery similar to [14].
van der Laan and Akbar [16] - 2019	Improved energy production of multi-rotor wind farms	RANS-AD k-ε-f_P with AD method II and LES of a 4x4 rectangular wind farm with multi-rotor wind turbines and equivalent single-rotor turbines, respectively. Inter spacings of $D_{eq} = \{3, 4, 5\}$ and tip clearances $s_h/D = s_v/D = \{0.05, 0.1, 1\}$ were simulated.	An AEP improvement of 0.3-1.7% was found for the multi-rotor turbine wind farm, which is much less than found in [14]. This difference is caused by the tip clearances, which effected the wake recovery significantly. For $s_h/D = s_v/D = 0.1$, the power production was only improved in the second row of turbines, whereas for $s_h/D = s_v/D = 1$ the power production was improved in all downstream rows.

Table 1.2: Overview of multi-rotor turbine CFD simulations.

1.3 Governing equations

The motion of fluids is governed by the Navier-Stokes equations, which are based on mass conservation, Newtons 2nd law and energy conservation. These three principles give 5 equations (as derived in e.g. [17] or [18]), but with 7 flow field variables (u, v, w, ρ, p, e and T):

$$\frac{D\rho}{Dt} + \rho\frac{\partial u_i}{\partial x_i} = 0 \tag{1.4}$$

$$\rho\frac{Du_j}{Dt} = -\frac{\partial \tilde{p}}{\partial x_j} + \frac{\partial \tau_{ij}}{\partial x_i} + \rho\tilde{f}_j + \rho g_j \tag{1.5}$$

$$\rho\frac{D}{Dt}\left(e + \frac{1}{2}u_i^2\right) = \rho\dot{q} + \frac{\partial}{\partial x_i}\left(k\frac{\partial T}{\partial x_i}\right) - \frac{\partial(\tilde{p}u_i)}{\partial x_i} + \frac{\partial}{\partial x_i}(u_j\tau_{ij}) + \rho\tilde{f}_i u_i \tag{1.6}$$

To close the system, the thermal and caloric equations of state can be included:

$$\tilde{p} = \rho RT \tag{1.7}$$

$$e = c_v T \tag{1.8}$$

The system of equations can be simplified considerably by a few assumptions:

Constant density

If $\rho =$ constant (which is a subset of *incompressible flows*), it is clear that eq. 1.4 reduces to:

$$\nabla \cdot \mathbf{u} = 0 \tag{1.9}$$

The question is now whether this assumption is valid or reasonable for the air flow around a wind turbine? It can be shown that the difference between the local static density and the total density is less than 5 percent for $Ma < 0.32$ for air, which also fits with the classical "$Ma < 0.3$-rule of thumb", [19]. The wind speeds are definitely below this threshold, and the relative speed of the blade tip is typically also designed to operate below this threshold due to noise regulation and rain erosion. Thus, the constant density assumption seems reasonable. However, this argument doesn't take into consideration, that temperature and pressure vary with height and the domain height used in this thesis is $L_z = 50 \cdot D \approx 1.5$ km. Taking the "U.S. standard atmosphere"[18] as an example, $\rho(\{0, 1000, 2000\}\text{ m}) = \{1.225, 1.112, 1.007\}\text{ kg/m}^3$. The density will however be nearly constant over a wind turbine and a log-law inflow profile will be imposed to somehow model the atmospheric boundary layer (cf. Section 1.5). In conclusion: Although $\rho = constant$ might not be totally accurate, the equations are simplified significantly, which makes the trade-off between physical behaviour and simplicity of the equations worth it.

Treatment of Body Forces

$\tilde{f}_j$ is the external body force pr. unit mass in the j'th direction, but since the density is assumed to be constant, an external body force pr. unit volume might equally well be defined:

$$f_j = \rho\tilde{f}_j \tag{1.10}$$

For a static fluid, $\mathbf{u} = \vec{0}$, with no body forces except gravity, eq. 1.5 yields the hydrostatic balance:

$$0 = -\frac{\partial p_s}{\partial x_j} + \rho_s g_j \tag{1.11}$$

where p_s is the hydrostatic pressure and ρ_s is the hydrostatic density. For constant density flows, $\rho = \rho_s$ and subtracting eq. 1.11 from eq. 1.5 eliminates the gravity term and replaces the absolute pressure, $\tilde{p}$, with the gauge pressure $p \equiv \tilde{p} - p_s$.

[18] https://www.engineeringtoolbox.com/standard-atmosphere-d_604.html

Newtonian Fluid

The stress tensor, τ_{ij}, can be related to the velocity gradient tensor, $\frac{\partial u_i}{\partial x_j}$, or more precisely the symmetric part of this tensor, $S_{ij} = \frac{1}{2}\left(\frac{\partial u_i}{\partial x_j} + \frac{\partial u_j}{\partial x_i}\right)$, which embodies the deformation of a fluid element (the antisymmetric part embodies the rotation of a fluid element). This relationship is called *the constitutive equation* and Newton suggested a linear relationship between these:

$$\tau_{ij} = 2\mu S_{ij} + \lambda S_{mm}\delta_{ij} \tag{1.12}$$

A formal proof of the form of eq. 1.12 can be found in [17]. The second term in eq. 1.12 is zero for constant density flows, since $S_{mm} = \frac{\partial u_m}{\partial x_m} = \nabla \cdot \mathbf{u} = 0$. A fluid that follows this linear relationship is called a *Newtonian fluid* (e.g. water, air, gasoline), while a fluid that instead follows some non-linear relationship is called a *Non-Newtonian fluid* (e.g. ketchup, paint, corn starch). Thus, the use of eq. 1.12 is reasonable, since the fluid to be modelled is air.

Constant Viscosity

The proportionality constant, μ, in eq. 1.12 is called the *dynamic viscosity* and physically describes the "stickyness" of the fluid. The viscosity is dependent on temperature and usually decreases with T for liquids, while it increase with T for gases. For air at atmospheric pressure, $\mu(\{-20, 0, 20\}\ ^\circ C) = \{1.63, 1.73, 1.83\}10^{-5}$ kg/(ms). The assumption of constant viscosity is thus equivalent to assuming constant temperature, which might be debatable with a domain height of $50D$. However, in later sections, the turbulence will be modelled through an additional viscosity constant, $\mu_T(\mathbf{x}, t)$, which is typically much larger than μ, so this might diminish the importance of having a varying μ. For this reason, the dynamic viscosity will be treated as constant.

Inertial Frame of Reference

The Navier-Stokes equations are derived in an inertial system, but since the wind turbine is placed on the rotating earth, there should actually be 4 extra terms in eq. 1.5 to account for the non-inertial effects, [17]. All of these 4 terms will however be ignored, because both the rotational and linear acceleration of the earth are fairly constant, and because the maximum length of the domain is $116D \approx 3.4$ km (for length scales < 10 km, omitting the non-inertial terms is reasonable, [20]).

Summary

With the above assumptions, eq. 1.4-1.8 reduce to 4 equations with 4 flow fields (u, v, w and p):

$$\frac{\partial u_i}{\partial x_i} = 0 \tag{1.13}$$

$$\begin{aligned}\rho\frac{Du_j}{Dt} &= -\frac{\partial p}{\partial x_j} + \frac{\partial 2\mu S_{ij}}{\partial x_i} + f_j \\ &= -\frac{\partial p}{\partial x_j} + \mu\frac{\partial u_j}{\partial x_i \partial x_i} + f_j\end{aligned} \tag{1.14}$$

The last equality follows from insertion of the symmetric part of the velocity gradient tensor, and using eq. 1.13. This form of the equations are known as the "constant-density, constant-viscosity equations on *differential and non-conservation form*".

1.4 Wind turbine wakes

Wind turbines installed closely together will from certain wind directions influence each other through their wakes, and this can decrease the annual energy production with 10-20%. The lifetime of the wind turbines will also be decreased, because turbulence is enhanced in the wakes, which will inflict more fatigue damage to the turbines in the wake [21]. A typical wake development is shown in Figure 1.16, where a double bell velocity profile develops into a Gaussian shaped profile. The wake will be axissymmetric in the z-direction for uniform inflow, but slightly non-axissymmetric in the z-direction for sheared inflow, e.g. a neutral atmospheric boundary layer as shown in Figure 1.16 (to be discussed in the next section). The wake will also be slightly asymmetric in the y-direction, if tangential forces are modelled as well.

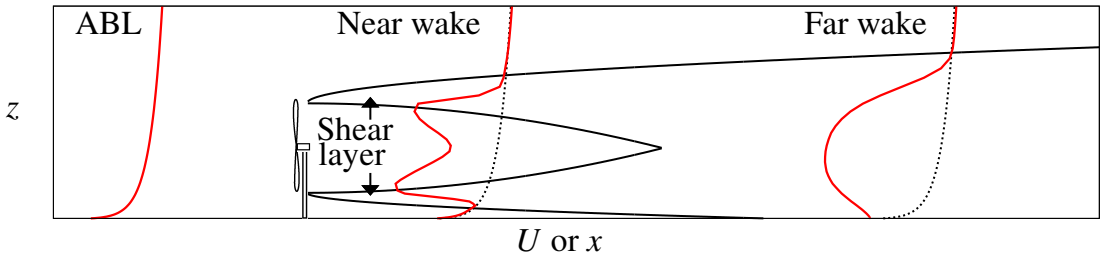

Figure 1.16: Qualitative velocity profile development upstream and downstream of a wind turbine [22].

The double bell profile is produced in the near wake, because of the typical thrust distribution on the rotor (c.f. Figure 2.14). Turbulence will then mix the velocity profile, which can also be viewed mathematically as momentum diffusion in eq. 1.14, and the near wake ends at the point, where the Gaussian shape is obtained. This point is however not very well defined for sheared inflow and furthermore it depends on the ambient turbulence intensity, thrust distribution, ground terrain and atmospheric stability and research regarding the nature of the near wake is still ongoing. In analytical models the far wake is often assumed to be axis-symmetric, which paves the way for very simple wake models, like the Jensen model from 1983 [23]:

$$\frac{U(x,y,z)}{U_\infty} = 1 - 2a\left(\frac{R}{\alpha(x-x_t)+R}\right)^2 = 1-(1-\sqrt{1-C_T})\left(\frac{1}{2\alpha(x-x_t)/D+1}\right)^2 \tag{1.15}$$

for $x > x_t$ and $(y-y_t)^2+(y-y_t)^2 \leq (R+\alpha(x-x_t))^2$, where (x_t, y_t, z_t) is the position of the rotor center in a coordinate system where the x-axis is normal to the rotor and points downstream. This model in combination with a wake superposition model (either linear or quadratic) is used extensively to evaluate the wake losses in wind farms and works surprisingly well [24]. It is interesting that the the normalized velocity U/U_∞ in a normalized coordinate system $(x/D, y/D, z/D)$ only depends on C_T and α. A large C_T will make U/U_∞ go slower towards 1, i.e. a slower *wake recovery*, while a large α will make U/U_∞ go faster towards 1, i.e. a faster *wake recovery*. The parameter α widens the wake in the Jensen wake model and can in this sense be interpreted as a turbulence intensity parameter (a linear relationship is indeed fitted in [25]). The thrust coefficient, C_T, and total ambient turbulence intensity, I_∞, are indeed the most important parameters for wakes, which is why cases with low/high C_T and I_∞ are often used for validation of new wake and turbulence models [21], [26], [27]. The ambient turbulence intensity is sometimes calculated as $I_{u,\infty} = \sigma_u/U$, but this is only the *streamwise ambient turbulence intensity*. The *total ambient turbulence intensity* is instead defined as:

$$I_\infty = \frac{\sqrt{\frac{1}{3}(\sigma_u^2+\sigma_v^2+\sigma_w^2)}}{\sqrt{U^2+V^2+W^2}} = \frac{\sqrt{\frac{2}{3}k}}{|\mathbf{U}|} \tag{1.16}$$

where $\sigma_u = \mathrm{std}(u) = \sqrt{\overline{(u')^2}}$, $U = \mathrm{mean}(u) = \overline{u}$ and $k = \frac{1}{2}(\sigma_u^2+\sigma_v^2+\sigma_w^2)$ is the *turbulent kinetic energy*.

1.5 Atmospheric boundary layer

A log-law type of inflow profile is shown in Figure 1.16 and an analytical formula for a *neutral* ABL, which will be used in this thesis, can be derived with a simple dimensional analysis [1]:

$$U(z) = \frac{u_*}{\kappa} \log\left(\frac{z + z_0}{z_0}\right) \tag{1.17}$$

where $u_* = \sqrt{\tau/\rho}$, τ is the surface shear stress, $\kappa = 0.4$ is von Karmans constant and z_0 is the roughness length, which depends on the ground terrain. The numerator in the log-function is described as in eq. 1.17 in some CFD litterature, e.g. [28], [15], while it is replaced with z other litterature, e.g. [1], so that $U(z = z_0) = 0$ instead of $U(z = 0) = 0$. Eq. 1.17 is only valid for a neutral ABL, which means that the turbulence is mainly driven by wind shear and not by temperature differences. *Unstable* and *stable* ABL's can however be created when the temperature difference between the earth and atmosphere is large enough. The *stability* will also determine the height of the ABL, which usually ranges between $100 - 1000$ m. Analytical formulas for stable and unstable profile can be obtained either by using a modified power law [1] or by extending eq. 1.17 using the Monin-Obukhov similarity theory [29].

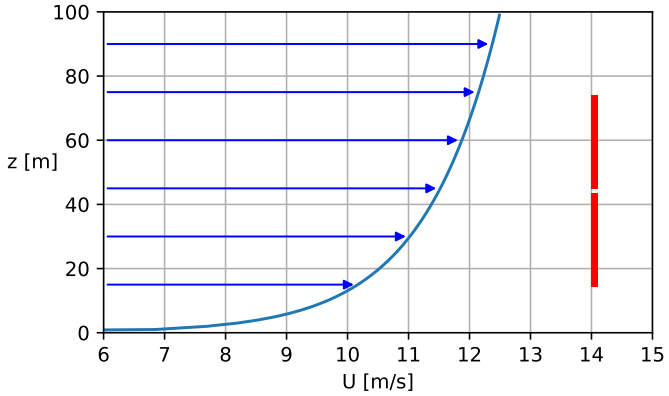

Figure 1.17: Neutral ABL with $z_H = 44.29$ m, $U_{H,\infty} = 11.5$ m/s, $I_{H,\infty} = 8.4\%$ and $C_\mu = 0.03$. Red rectangles = 4R-V29 turbine.

Eq. 1.17 will be imposed as the inlet profile, but it is important that the profile is in equilibrium with the ground shear stress and turbulence model. If not, the velocity profile will depend on the streamwise position and different results for the power and wake of a wind turbine will be obtained depending on its placement in the domain, e.g. a turbine at $x = 0D$ or $x = 5D$ will produce different results, even though the terrain is totally homogeneous (i.e. there are no hills or change in land cover). The neutral log-law will be in equilibrium with the $k - \varepsilon$ turbulence model, if [28]:

$$k = \frac{u_*^2}{\sqrt{C_\mu}} \tag{1.18}$$

$$\varepsilon = \frac{u_*^3}{\kappa(z + z_0)} \tag{1.19}$$

$$\sqrt{C_\mu}\sigma_\varepsilon(C_{\varepsilon,1} - C_{\varepsilon,2}) + \kappa^2 = 0 \tag{1.20}$$

The values of the turbulent constants σ_ε, $C_{\varepsilon,1}$ and $C_{\varepsilon,1}$ are described in Section 2.3. For steady, constant-density 2-dimensional flow with horizontal homogeneity (i.e. $\frac{\partial}{\partial x} = 0$), it can be showed by insertion of eq. 1.17-1.20 into eq. 1.13, 1.14, 2.41 and 2.42, that $\frac{Dk}{Dt} = \frac{D\varepsilon}{Dt} = \frac{Du}{Dt} = \frac{Dw}{Dt} = 0$, i.e. equilibrium.

To adjust the profile to a desired reference velocity, $U_{H,\infty}$, and turbulence intensity, $I_{H,\infty}$, at $z = z_H$, eq. 1.18 is inserted into eq. 1.16, which can be simplified further by insertion of eq. 1.17:

$$I_{H,\infty} = \frac{\sqrt{\frac{2}{3}u_*^2/\sqrt{C_\mu}}}{U_{H,\infty}} = \frac{\kappa\sqrt{\frac{2}{3}}}{\sqrt[4]{C_\mu}\log\left(\frac{z_H+z_0}{z_0}\right)} \tag{1.21}$$

$|\mathbf{U}(z_H)| = U_{H,\infty}$, since $V = W = 0$ is used at the inlet in this thesis. Either u_* (or z_0 through eq. 1.17) or C_μ could be adjusted to fulfill this equation, but u_* is used and $C_\mu = 0.03$ is kept constant (this is the physically most sound option, because a larger C_μ normally enhances mixing, c.f. eq. 2.43, but it acts opposite in eq. 1.21):

$$u_* = I_{H,\infty}U_{H,\infty}\sqrt{\frac{3}{2}}\sqrt[4]{C_\mu} \tag{1.22}$$

Solving for z_0 in eq. 1.17 and inserting u_* into this expression yields the value of z_0:

$$z_0 = \frac{z_H}{\exp\left(\kappa\frac{U_{H,\infty}}{u_*}\right) - 1} = \frac{z_H}{\exp\left(\frac{\kappa}{I_{H,\infty}\sqrt{\frac{3}{2}}\sqrt[4]{C_\mu}}\right) - 1} \tag{1.23}$$

An inflow profile is thus defined, where $U(z_H) = U_{H,\infty}$ and $I_\infty(z_H) = I_{H,\infty}$. The $k(z)$ and $\varepsilon(z)$ profiles are given by respectively eq. 1.18 and eq. 1.19.

Chapter 2

Computational methods

This chapter presents the computational methods, which are used to model the multi-rotor turbine and the surrounding flow. A lot of CFD codes for simulating wind turbines are based on modelling the turbine as a permeable AD, AL or AS, on which body forces are applied to the computational domain. This reduces the computational cost considerably compared to a full-rotor simulation, where the blade boundary layer would have to be resolved. As described in [30], the "permeable body force CFD methods" can be broken down into 3 steps:

1. Calculation of forces on the AL, AD or AS
2. Redistribution of these forces into the computational domain
3. Application of the forces in the flow solver

These steps will be described in the following three sections with the emphasis on the AD, because it is the method used in this thesis.

Litterature overview

The CFD tool used in this thesis is EllipSys3D[19], which was developed by **Søresenen** [20] and **Michelsen** [31] in the early 1990's, at Risø and DTU, and it has continuously been updated through the years and is still in use today. PyEllipSys[20], developed at the Risø campus of DTU in 2018, is a Python interface to EllipSys3D and this has been used to execute all simulations.

Different AD models can be used in EllipSys3D and three of these are described by **van der Laan et. al** in [27], which also discusses their use for a double wind turbine wake (not a twin multi-rotor, but two wind turbines situated in a row). It is possible to simulate a wind farm with these methods, e.g. [21].

The transfer of forces from the AD to the computational domain is described by **Réthoré et. al** in [30] and has later been improved by **Troldborg et. al** [32].

It is also possible to switch between different turbulence models in EllipSys3D, and the model used in this thesis is the k-ε-f_P model developed by **van der Laan** [26]. It is a modification of the classical k-ε model, where the eddy viscosity is multiplied by a f_P-factor depending on the local shear. It has later been realized that this modification is actually a correction to the turbulent length scale in the wake [33].

A summary of some of the important publications regarding the computational methods is given in Table 2.1.

[19] http://www.the-numerical-wind-tunnel.dtu.dk/EllipSys
[20] https://ellipsys.pages.windenergy.dtu.dk/pyellipsys/

AD, Turbulence and CFD			
Author, year	Title	Method/Properties	Results
van der Laan et. al [27] - 2015	The k-ε-f_p model applied to double wind turbine wakes using different actuator disk force methods	The forces on the AD are computed using constant forcing (method 0), AD induction (method I), AD variable scaling (method II) and AD airfoil (method III). The applied force distributions are axis-symmetric for method 0-II and non-axis-symmetric for method III. The k-ε and k-ε-f_p are also compared with LES results.	The purpose of method I-II is to be able to determine $U_{H,\infty}$, when in the lee of an upstream turbine. Method I overpredicts power, while method II produces the correct results, but require a calibration step. Method III outputs power and thrust directly, but overpredicts them severely for $V > V_{rated}$, since it cannot model blade deflections. For $V < V_{rated}$ power is still overpredicted, but the thrust is correct. The k-ε model is seen to underpredict the velocity deficit compared to the k-ε-f_p model and LES. This is a consequence of the too large ν_T and hence too large mixing of the k-ε model.
Réthoré et al. [30] - 2014	Verification and validation of an actuator disk model	RANS-AD, RANS-full rotor computation and Conway analytical model. AD method 0 + normalized loading, AD method III and AD-convolution are used with k-ω turbulence.	The Actuator Shape (AS) model is presented, which describes how to destribute the forces from the AS to the computational domain. For the special case of an AD, it is found to be 1st order accurate and demonstrate overall good agreement with full-rotor computations and the analytical Conway model.
Troldborg et al. [32] - 2015	A consistent method for finite volume discretization of body forces on collocated grids applied to flow through an actuator disk	EllipSys3D RANS-AD-Laminar is used and a mixed-order analysis with analytical thrust loading model is conducted.	The pressure jump and AS methods are improved by including a "center of gravity" for the body forces coming from the different shape cells. The new solver can thus "feel" where the disk is located within the cell. The new algorithm is 2nd order and eliminates the numerical wiggles at all azimuthal directions.
van der Laan et. al [26] - 2015	An improved k-ε model applied to a wind turbine wake in atmospheric turbulence	RANS, LES and measurements from Wieringermeer, Nibe and Risø. AD method 0 + normalized force distribution.	The novel k-ε-f_P model is calibrated using measurements and LES results, and is seen to outperform k-ε in low $I_{H,\infty}$ or high C_T conditions. The reason being, that the k-ε generally mixes too much, which has the most effect in low $I_{H,\infty}$ or large velocity deficit (aka. large C_T) cases.

Table 2.1: Overview of main litterature for actuator disk models, turbulence model and CFD methods.

2.1 Forces on the AD

2.1.1 Definition of the main system and AD system

The AD is placed in the most dense part of the computational domain, which is also called the "wake domain". It is always a balance of the grid size and the computational cost, and since the wind turbine and its wake is studied, most of the cells are located there. To avoid blockage effects and to have a developed inflow, it is however important to have a quite large domain, which is obtained by stretching the grid outside the wake domain. The coordinate system shown in Figure 2.1 is used throughout this thesis and will at times be referred to as the *main system*. x denotes the streamwise direction, y the lateral direction (from right to left seen from an upstream point of view) and z the vertical direction (with $z = 0$ at the ground).

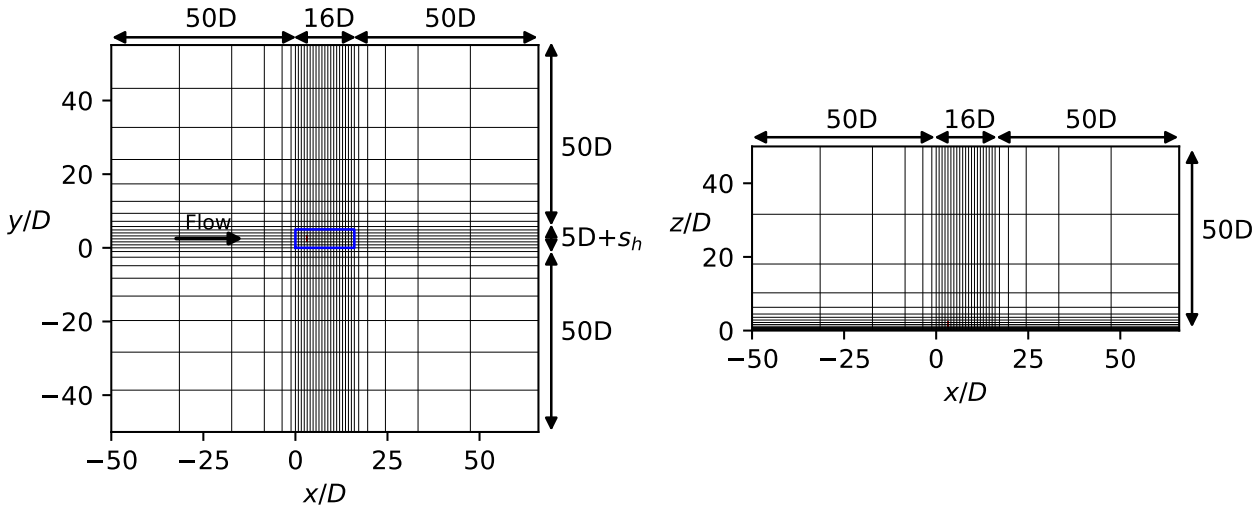

Figure 2.1: Top and side view of computational domain with 5 cells pr. D in the wake domain (only every 4th grid point is shown). The blue rectangle encloses the wake domain.

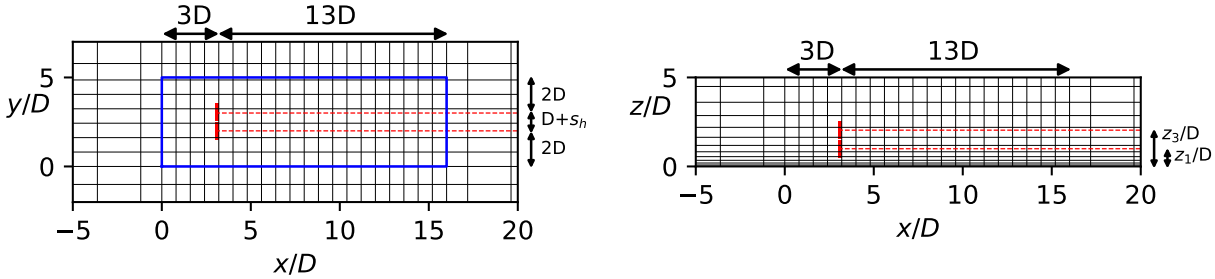

Figure 2.2: Top and side view of the wake domain with 5 cells pr. D (only every 4th grid point is shown). Red line = turbines. Dotted red line = turbine axis.

Three different computational grids will be used in this thesis, which all have the dimension of $L_x/D = 116$, $L_y/D = 105 + s_h/D$ and $L_z/D = 50$, where s_h is the horizontal tip clearance. They also share the same wake domain with $l_x/D = 16$ and $l_y/D = 5 + s_h/D$, where the cells are uniformly spaced with 5, 10 or 20 cells pr. diameter in the x- and y-direction, while the cells are stretched in the z-direction.

Cells pr. D	N_x	N_y	N_z	Total Number of Cells
5	128	96	64	$\approx 0.79 \cdot 10^6$
10	224	128	96	$\approx 2.8 \cdot 10^6$
20	384	192	128	$\approx 9.4 \cdot 10^6$

Table 2.2: N_i = cells in i'th direction. The majority of the cells are located in the wake domain.

Continuing to the AD, this will have its own independent coordinate system known as the *polar grid* defined by (x_R,y_R,z_R), cf. Figure 2.3. The polar grid defines a number of polygons, aka. *shape cells* in [30], and a sample point is defined in the center of each of these. The sample points contain information about $f_{x_R}(y_R, z_R)$, $f_\varphi(y_R, z_R)$, $v_{x_R}(y_R, z_R)$ and $v_\varphi(y_R, z_R)$ and could equally well be described in a polar coordinate system (r,φ). A simple rectangle summation scheme can be used to estimate the thrust, torque and power:

$$T = \int_0^R \int_0^{2\pi} f_{x_R}(r,\varphi) r d\varphi dr \approx \sum_{l=1}^{N_{SC}} f_{x_R}(cc_l) A_l \tag{2.1}$$

$$\tau = \int_0^R \int_0^{2\pi} r f_\varphi(r,\varphi) r d\varphi dr \approx \sum_{l=1}^{N_{SC}} r_l f_\varphi(cc_l) A_l \tag{2.2}$$

$$P = \tau\Omega \tag{2.3}$$

where N_{SC} is the number of shape cells, cc_l is the cell center and A_l is the area of the l'th shape cell. The normal and tangential blade loading can also be estimated:

$$q_N^{AD}(r) \approx \frac{\langle f_{x_R}(r,\varphi)\rangle_\varphi \cdot 2\pi r \cancel{dr}}{B\cancel{dr}} \approx \frac{\sum_{m=i}^{N_{azi}} f_{x_R}(r,\varphi_m)\cdot 2\pi r}{N_{azi}B} \tag{2.4}$$

$$q_T^{AD}(r) \approx \frac{\langle f_\varphi(r,\varphi)\rangle_\varphi \cdot 2\pi r \cancel{dr}}{B\cancel{dr}} \approx \frac{\sum_{m=1}^{N_{azi}} f_\varphi(r,\varphi_m)\cdot 2\pi r}{N_{azi}B} \tag{2.5}$$

Eq. 2.1-2.5 can be used to go from $\{f_{x_R}(r,\varphi), f_\varphi(r,\varphi)\} \rightarrow \{T, \tau, P, q_N^{AD}(r), q_T^{AD}(r)\}$, but can also be used in the opposite direction. E.g. if $T = const$, $\tau = const$, $f_\varphi(r,\varphi) = const$ and $f_{x_R}(r,\varphi) = const$, then eq. 2.1-2.2 can be integrated to give $f_{x_R}(r,\varphi) = \frac{T}{\pi R^2}$ and $f_\varphi(r,\varphi) = \frac{3\tau}{2\pi R^3}$. This is a very simple example, but the same technique can be used for non-uniform thrust distributions as well.

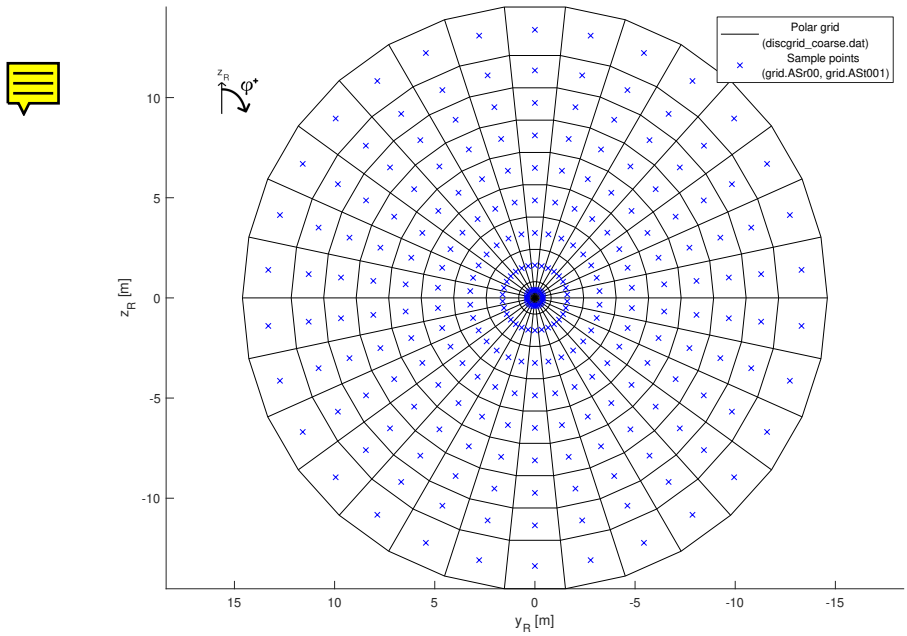

Figure 2.3: Polar grid (black) with sample points (blue) seen from an upstream position.

AD grid	N_φ	N_r	N_{AD}
Coarse	30	9	270
Fine	180	94	16,920

Table 2.3: The original AD grids used for the V29 turbine (a grid study is conducted in Subsection 2.4.3). $N_{\{\varphi,r\}}$ = Number of {azimuthal,radial} sample points. N_{AD} = Number of shape cells.

The AD's will also be tilted and yawed in the following chapters and the (x_R,y_R,z_R)-system will thus be rotated from the (x,y,z)-system. This rotation is defined in PyEllipSys by the two *orientation vectors* $\mathbf{o}_1$ and $\mathbf{o}_2$ (which gives $\mathbf{o}_3 = -\mathbf{o}_1 \times \mathbf{o}_2$, because the orientation coordinate-system is left-handed), which is illustrated in Figure 2.4 for the special cases of yaw and tilt only.

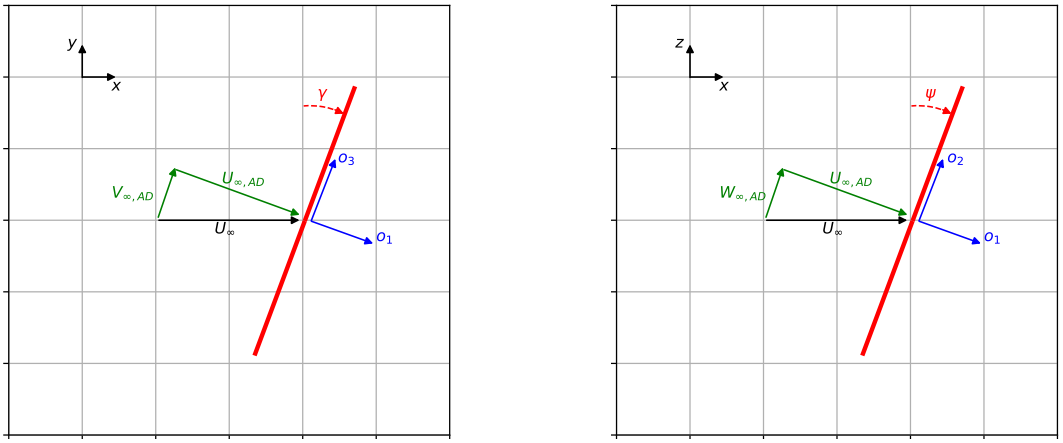

(a) Yaw only. Top view.

(b) Tilt only. Side view.

Figure 2.4: Special cases of the orientation vectors.

"Only yaw - 2D in x-y"

$$\mathbf{o}_1 = \begin{bmatrix} \cos(\gamma) \\ -\sin(\gamma) \\ 0 \end{bmatrix}$$

$$\mathbf{o}_2 = \begin{bmatrix} 0 \\ 0 \\ 1 \end{bmatrix}$$

"Only tilt - 2D in x-z"

$$\mathbf{o}_1 = \begin{bmatrix} \cos(\psi) \\ 0 \\ -\sin(\psi) \end{bmatrix}$$

$$\mathbf{o}_2 = \begin{bmatrix} \sin(\psi) \\ 0 \\ \cos(\psi) \end{bmatrix}$$

Before moving on to the general case, it is worth noticing the positive direction of γ and ψ indicated in Figure 2.4. The convention for the positive direction of the yaw angle, γ, is especially important, since it differs a lot in the literature, cf. Table. 2.4.

Author	Convention used
This thesis	CW
van der Laan et. al - [15]	CW
Smulders et. al - [7]	CW
DTU Aeroelasticity course	CCW
Wind Energy Handbook - [34]	CCW
Bastankhah et. al - [35]	CW
Schottler et. al - [36]	CW
Howland et. al - [37]	CCW
Hansen - [3]	CCW

Table 2.4: Top view convention of yaw angle, γ.

"General case: Yaw and tilt - 3D"

A vector can be transformed from the main system to the yawed and tilted AD system with two rotation matrices, see chapter 9 in [3]. This is done by first rotating from system A to system B, and then from system B to system C, cf. Figure 2.5.

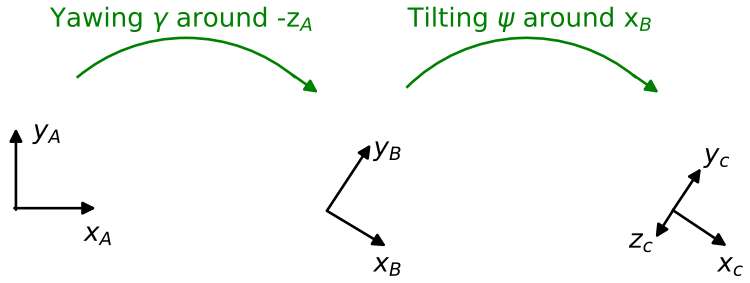

Figure 2.5: Sequence of yawing and tilting.

$$\mathbf{x}_B = \underbrace{\begin{bmatrix} \cos(\gamma) & -\sin(\gamma) & 0 \\ \sin(\gamma) & \cos(\gamma) & 0 \\ 0 & 0 & 1 \end{bmatrix}}_{\underline{\underline{a_{AB}}}} \cdot \underbrace{\begin{bmatrix} x_A \\ y_A \\ z_A \end{bmatrix}}_{\mathbf{x}_A} \tag{2.6}$$

$$\mathbf{x}_C = \underbrace{\begin{bmatrix} \cos(\psi) & 0 & -\sin(\psi) \\ 0 & 1 & 0 \\ \sin(\psi) & 0 & \cos(\psi) \end{bmatrix}}_{\underline{\underline{a_{BC}}}} \cdot \underbrace{\begin{bmatrix} x_B \\ y_B \\ z_B \end{bmatrix}}_{\mathbf{x}_B} \tag{2.7}$$

$\underline{\underline{a_{AB}}}$ rotates a vector from system A to system B, and $\underline{\underline{a_{BC}}}$ from system B to C. Combining these, one can rotate a vector from A to C directly:

$$\mathbf{x}_C = \underline{\underline{a_{BC}}} \cdot \underline{\underline{a_{AB}}} \cdot \mathbf{x}_A \tag{2.8}$$

Rotational matrices have the neat property, that they are *orthogonal*, i.e. $\underline{\underline{a_{AB}}}^{-1} = \underline{\underline{a_{AB}}}^{T}$. Thus, it is also easy to go from system C to system A:

$$\mathbf{x}_A = \underline{\underline{a_{AB}}}^{T} \cdot \underline{\underline{a_{BC}}}^{T} \cdot \mathbf{x}_C \tag{2.9}$$

System A is in our context the main system and system C is the AD system. Since $\mathbf{o}_{1,AD} = (1, 0, 0)$ and $\mathbf{o}_{2,AD} = (0, 0, 1)$, the orientation vectors can in a general case be calculated as:

$$\mathbf{o}_1 = \underline{\underline{a_{AB}}}^{T} \cdot \underline{\underline{a_{BC}}}^{T} \cdot \mathbf{o}_{1,AD} \tag{2.10}$$

$$\mathbf{o}_2 = \underline{\underline{a_{AB}}}^{T} \cdot \underline{\underline{a_{BC}}}^{T} \cdot \mathbf{o}_{2,AD} \tag{2.11}$$

This method can also be used to extract the velocity component normal to the AD for any yaw and tilt:

$$U_{H,\infty,AD} = (\underline{\underline{a_{BC}}} \cdot \underline{\underline{a_{AB}}} \cdot \mathbf{U}_{H,\infty}) \cdot \mathbf{o}_{1,AD} \tag{2.12}$$

2.1.2 Method III: AD Airfoil

The following method describes how to obtain $f_{x_R}(r,\varphi)$ and $f_\varphi(r,\varphi)$ at each sample point on the AD during a CFD simulation. It is the main method used in this thesis, and is also labelled as "method III" in [27]. Three other models can be found in Appendix A.

The AD airfoil method uses airfoil data at discrete radial points to determine the forces on the blade elements, very similar to BEM codes [3]. There is no structural model included, i.e. it models a stiff blade, which limits its applicability to $V \leq V_{rated}$, [27]. It also means that the blade forces can be calculated in the x_R-φ plane in the AD system:

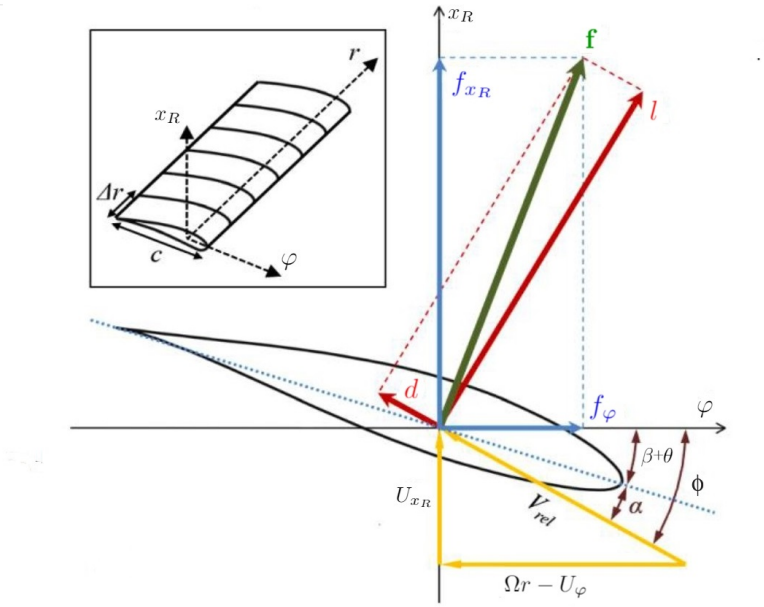

Figure 2.6: Calculation of blade element forces [38].

$$f_{x_R}(r,\varphi) = \mathbf{f}(r,\varphi)\cdot\mathbf{e}_{x_R} \tag{2.13}$$

$$f_\varphi(r,\varphi) = \mathbf{f}(r,\varphi)\cdot\mathbf{e}_\varphi \tag{2.14}$$

$$\mathbf{f}(r,\varphi) = \frac{1}{2}\rho U_{rel}^2(r,\varphi)\frac{Bc}{2\pi r}(c_l\mathbf{e}_l + c_d\mathbf{e}_d)F \tag{2.15}$$

$$U_{rel}(r,\varphi) = \sqrt{U_{x_R}^2 + (\Omega r - U_\varphi)^2} \tag{2.16}$$

$$\phi = \tan^{-1}\left(\frac{U_{x_R}}{\Omega r - U_\varphi}\right) \tag{2.17}$$

$$\alpha = \phi - (\beta + \theta) \tag{2.18}$$

$$F = \frac{2}{\pi}\cos^{-1}\left(\exp\left(-g\frac{B(R-r)}{2r\sin(\phi)}\right)\right) \tag{2.19}$$

$$g = \exp(-c_1(B\lambda - c_2)) + c_3 \tag{2.20}$$

$$c_1 = 0.125, \quad c_2 = 29 \quad c_3 = 0.1 \tag{2.21}$$

$$\lambda = \frac{\Omega R}{U_{\infty,tip}} \tag{2.22}$$

It is assumed that setpoints for θ and Ω are known, as well as blade geometry, i.e. $\beta(r)$, $c(r)$ and airfoil-type(r), and airfoil data, i.e. $c_l(\alpha, Re)$ and $c_d(\alpha, Re)$ for each airfoil type. Usually, only $c_l(\alpha)$ and $c_d(\alpha)$ are used, which have been calculated for a characteristic Re.

Turbine with known inflow properties:

- Step 1: Since $\mathbf{U}_{H,\infty}$ is known, calculate $U_{H,\infty,AD}$ with eq. 2.12. This is the undisturbed freestream velocity at hub height in the x_R-direction of the AD-system.
- Step 2: Look up θ and Ω in the setpoint table, using $U_{H,\infty,AD}$.
- Step 3: Set $U_{\infty,tip} = U_{H,\infty,AD}$ and calculate λ.
- Step 4: For each sample point, look up β, c and the airfoil type. Then sample $U_x(cc_i)$ and $U_\phi(cc_i)$ from the flow field to calculate α and use this to look up c_l and c_d. Finally, use eq. 2.13-2.22 to calculate $f_{x_R}(cc_i)$ and $f_\varphi(cc_i)$.

Method III performs reasonable well for $V \leq V_{rated}$, even when compared to an aeroelastic tool like HAWCStab2 [39] with blade deflections included. It is however found to overpredict the power production with 10-20% and it is suggested in [27], that since the velocity gradients are large at the AD, the extraction point of U_{x_R} and U_φ could be the explanation for this. HAWCStab2 simulations can also be performed with stiff blades, but method III was not compared to such simulations in [27].

Turbine operating in the wake of another:

For a wind turbine operating in the wake of another, there is no clear definition of $\mathbf{U}_{H,\infty}$. It depends on the operating state of the upstream turbine, the atmospheric conditions and the inter wind turbine distance. Thus, step 1-2 need to be modified somehow to estimate θ, Ω and λ. This can be done with either method II, method III-calibration or with a wind turbine controller, c.f. Appendix A.

2.2 Redistribution of forces

The redistribution of forces from the AD to the computational domain is perhaps the most overlooked of the three steps discussed in the beginning of this chapter. It is nevertheless important, because a poorly implemented redistribution algorithm will need a more refined domain to obtain grid independence and thus be more costly in terms of computation-time.

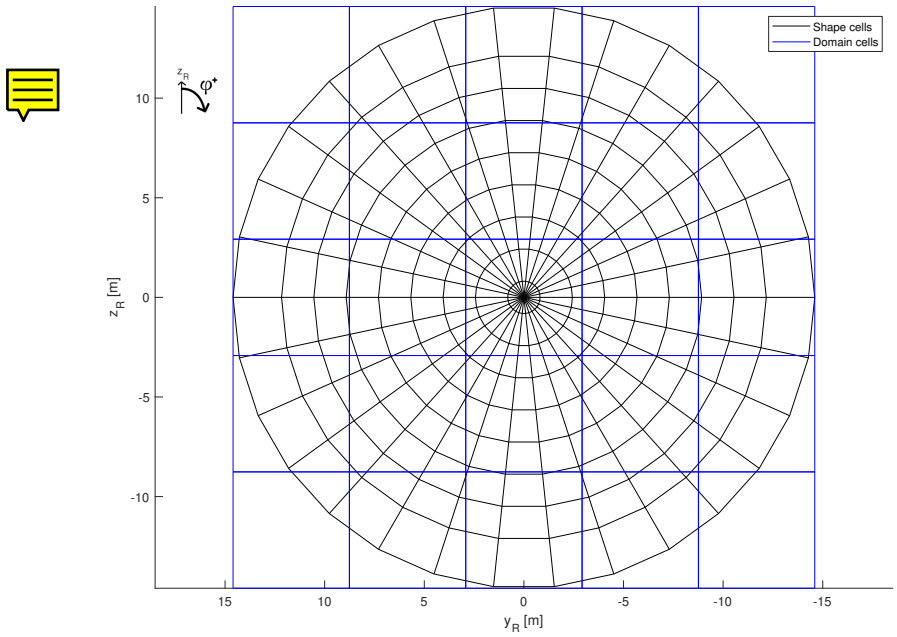

Figure 2.7: Example of an AD aligned with a cartesian domain grid with 5 cells pr. D.

It is clear from Figure 2.7, that transferring forces from a polar to a cartesian grid is a non-trivial task, especially when the polar grid can be yawed and tilted. There is only one force attached to each shape cell (SC), so when a SC is overlapping several domain cells (DC), how is the force then redistributed? Three examples of ways to redistribute forces are:

1. Use the SC cell center, cc^{SC}, to determine, which DC it belongs to:

$$\mathbf{F}_{i,l}^{DC} = \begin{cases} \mathbf{F}_l^{SC} & \text{if } cc_l^{SC} \in V_i^{DC} \\ 0 & \text{else} \end{cases} \tag{2.23}$$

   where V_i^{DC} is the volume of the i'th DC, $\mathbf{F}_l^{SC} = \mathbf{f}(cc_l)A_l$, A_l is the area of the l'th shape cell and $\mathbf{F}_{i,l}^{DC}$ is the force contribution from the l'th SC to the i'th DC.

2. Use shape/domain cell overlap to determine, which domain cell it belongs to:

$$\mathbf{F}_{i,l}^{DC} = \begin{cases} \mathbf{F}_l^{SC} & \text{if } \frac{A_{i,l}}{A_l} = \max_l \frac{A_{i,l}}{A_l} \\ 0 & \text{else} \end{cases} \tag{2.24}$$

   where $A_{i,l}$ is the overlap area of the l'th SC with the i'th DC, c.f. Figure 2.8. $A_{i,l}$ is called the *intersectional area* or an *intersectional polygon*. The collection of all the intersectional polygons is called the *intersectional grid*.

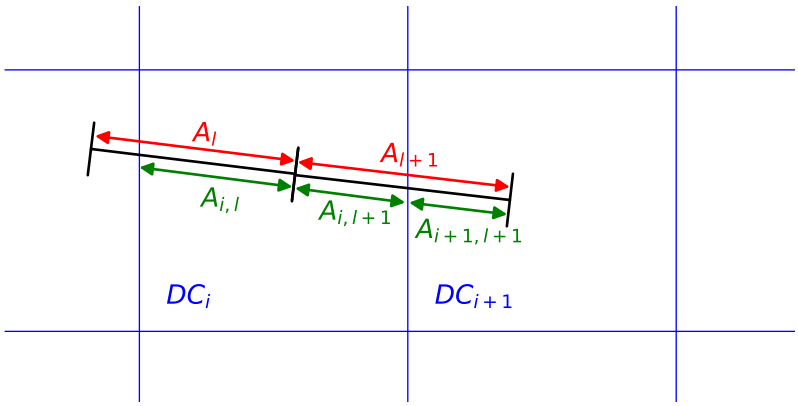

Figure 2.8: Definition of intersectional area, $A_{i,l}$, for a 2D case. Blue = DC. Black = SC.

3. Distribute force from shape cell to several domain cells using the intersectional area as weight.

$$\mathbf{F}_{i,l}^{DC} = \frac{A_{i,l}}{A_l}\mathbf{F}_l^{SC} \tag{2.25}$$

The final force on domain cell i is calculated the same way with all 3 methods:

$$\mathbf{F}_i^{DC} = \sum_{l=1}^{N_{SC}} \mathbf{F}_{i,l}^{DC} \tag{2.26}$$

A fourth method could be to use some kind of smearing function, e.g. a Gaussian kernel [40], but the disadvantage of this method is that it requires a smearing parameter, which then has to be tuned. The algorithm used in EllipSys3D is based on method 3, which was originally described in [30] and is called "the actuator shape model", because it actually generalizes to an arbitrary surface (the 2D polar disk is just a special case). The AS method is able to simulate wind turbine flows with reasonable accuracy down to 10 or even 5 cells pr. D, as will be shown in the grid study in Section 2.4. This is in contrast to some other codes, which would perhaps need 30 or 40 cells pr. D to obtain reliable results. The algorithm was further improved in [32] with a "center-of-gravity" correction, which is further elaborated on in Appendix B.

2.3 The Flow Solver

The ratio of the smallest to the largest length scales in turbulent flows scales as $\eta/L \sim Re^{-3/4}$. For the air flow around a wind turbine $Re = O(10^6)$, so if the Navier-Stokes equations, eq. 1.13-1.14, are to be solved directly (called *DNS*), the grid would have to be discretized very finely and this method is simply not feasible for most applications. The *RANS equations* are instead solved in this thesis. A method with fidelity in between DNS and RANS is *LES*, which however is approximately $O(10^3)$ more computationally expensive than RANS [26] and is hence not feasible for the many parametric studies, which will be conducted in this thesis.

2.3.1 RANS equations

RANS is an acronym for *Reynolds-Averaged Navier-Stokes* and the idea is that often only the mean properties of the flow are desired. Thus, the flow field is *Reynolds Decomposed* into a mean and a fluctuating part:

$$u = U + u' \tag{2.27}$$
$$v = V + v' \tag{2.28}$$
$$w = W + w' \tag{2.29}$$
$$p = P + p' \tag{2.30}$$
$$\tag{2.31}$$

The fluctuations are here meant as fluctuations in time, so that the time average of the different components, denoted by an overbar, are:

$$\bar{u} = U, \quad \bar{U} = U, \quad \bar{u'} = 0 \tag{2.32}$$
$$\bar{v} = V, \quad \bar{V} = V, \quad \bar{v'} = 0 \tag{2.33}$$
$$\bar{w} = W, \quad \bar{W} = W, \quad \bar{w'} = 0 \tag{2.34}$$
$$\bar{p} = P, \quad \bar{P} = P, \quad \bar{p'} = 0 \tag{2.35}$$
$$\tag{2.36}$$

Inserting eq. 2.27-2.30 into eq. 1.13-1.14, taking the time average of the equations and dividing by ρ gives:

$$\frac{\partial U_j}{\partial x_j} = 0 \tag{2.37}$$

$$\frac{\partial U_i}{\partial t} + U_j \frac{\partial U_i}{\partial x_j} = -\frac{1}{\rho}\frac{\partial P}{\partial x_i} + \frac{\partial}{\partial x_j}\left(\nu\left(\frac{\partial U_i}{\partial x_j} + \frac{\partial U_j}{\partial x_i}\right) - \overline{u_i' u_j'}\right) + \frac{1}{\rho}\overline{f_i} \tag{2.38}$$

These equations look almost similar to the original Navier-Stokes equations, but the *Reynolds stress tensor*, $\overline{u_i' u_j'}$, has unfortunately introduced 6 additional flow variables. One could try to develop a conservation equation for $\overline{u_i' u_j'}$, but this equation would contain the 3rd order tensor, $\overline{u_i' u_j' u_k'}$, which would then need to modelled. This is called the *closure problem* and to break this deadlock some turbulence modelling based on experiments, intuition, experience, etc. is needed.

2.3.2 k-ε-f_P turbulence

A popular method for modelling $\overline{u_i' u_j'}$ is the Boussinesq hypothesis, introduced already in 1877 [17], which also introduces the concept of *turbulent eddy viscosity*, ν_T:

$$\overline{u_i' u_j'} = \frac{2}{3}k\delta_{ij} - \nu_T\left(\frac{\partial U_i}{\partial x_j} + \frac{\partial U_j}{\partial x_i}\right) \tag{2.39}$$

Insertion of eq. 2.39 into eq. 2.38 and using eq. 2.37 yields:

$$\frac{\partial U_i}{\partial t} + U_j \frac{\partial U_i}{\partial x_j} = -\frac{1}{\rho}\frac{\partial P}{\partial x_i} + \frac{\partial}{\partial x_j}\left((\nu + \nu_T)\frac{\partial U_i}{\partial x_j} - \frac{2}{3}k\delta_{ij}\right) + \frac{1}{\rho}\overline{f_i} \tag{2.40}$$

The six unknowns of $\overline{u_i' u_j'}$ has thus been eliminated, but the two variables $k = 1/2\overline{u_i'^2}$ (called the *turbulent kinetic energy*) and ν_T have instead been introduced. In the k-ε-f_P turbulence model, introduced in [26] and based on the classical k-ε model, the system is closed by the following 2 equations:

$$\frac{Dk}{Dt} = \underbrace{\nabla \cdot \left(\left(\nu + \frac{\nu_T}{\sigma_k}\right)\nabla k\right)}_{Diffusion} + \underbrace{\mathcal{P}}_{Production} - \underbrace{\varepsilon}_{Dissipation} \tag{2.41}$$

$$\frac{D\varepsilon}{Dt} = \nabla \cdot \left(\left(\nu + \frac{\nu_T}{\sigma_\varepsilon}\right)\nabla \varepsilon\right) + (C_{\varepsilon,1}\mathcal{P} - C_{\varepsilon,2}\varepsilon)\frac{\varepsilon}{k} \tag{2.42}$$

Eq. 2.41-2.42 are transport equations, and it is clear that ν_T plays the role as a variable diffusion coefficient, where a large ν_T will make k diffuse more easily. This can also be interpreted as that a larger ν_T enhances the mixing of U_i, which would also be apparent if eq. 2.39 was inserted into eq. 2.38. The standard k-ε model is known to overpredict the velocities in the wake and to diffuse the wake too much, and this problem is addressed in the modified k-ε-f_P model, where an additional f_P factor is introduced in the definition of ν_T [26]:

$$\nu_T = C_\mu f_P \frac{k^2}{\varepsilon} \tag{2.43}$$

$$f_P = \frac{2f_0}{1 + \sqrt{1 + 4f_0(f_0 - 1)(\frac{\sigma}{\tilde{\sigma}})^2}}, \quad f_0 = \frac{C_R}{C_R - 1} \tag{2.44}$$

$$\sigma \equiv \frac{k}{\varepsilon}\sqrt{\left(\frac{\partial U_i}{\partial x_j}\right)^2} \tag{2.45}$$

The *local shear parameter*, σ, is a scalar field, because the mean velocity gradient tensor is doubly contracted, and it describes somehow the amount of shear at each point in space. $\tilde{\sigma}$ is the local shear parameter for a log-law solution, and when $\sigma = \tilde{\sigma}$ it can be shown from eq. 2.44 that $f_P = 1$. In the wake, where there exists large velocity gradients, generally $\sigma > \tilde{\sigma}$, so that $f_P < 1$. Thus, ν_T will be smaller in the wake with the k-ε-f_P model compared to the k-ε model, and there will be less mixing of velocity. This leads to more reliable predictions of the velocity deficit, especially for low turbulent intensity or high thrust coefficient cases, [26]. The usual constants used in the k-ε-f_P model are summarized in Table 2.5.

C_R	C_μ	$C_{\varepsilon,1}$	$C_{\varepsilon,2}$	σ_k	σ_ε	κ
4.5	0.03	1.21	1.92	1.00	1.30	0.40

Table 2.5: Constants of the k-ε-f_P turbulence model.

The production of k can be derived to be [17]:

$$\mathcal{P} = -\overline{u_i' u_j'}\frac{\partial U_i}{\partial x_j} \tag{2.46}$$

where the Reynolds stress tensor again can be modelled using eq. 2.39 and the system of equations are now complete with 6 equations (eq. 2.37-2.38 and 2.41-2.42) and 6 flow fields (U, V, W, P, k, ε).

2.3.3 Discretization and solution of the equations

To solve the continuous RANS equations on a computer, the equations need to be discretized and this is done in EllipSys3D with the *finite-volume method*, where the computational grid shown in Figure 2.1 divides the domain into non-overlapping cells. Each cell contains information about the flow variables at the center of the cell, which is known as a *collocated arrangement* (other codes have velocities stored at one point and pressure at another point) and Appendix B explains how these values are solved for.

2.4 Grid study and validation cases

EllipSys3D is executed on the DTU HPC cluster Jess through PyEllipSys and to validate the installation and settings, a few test cases were considered. These tests have also functioned as grid studies to find the balance between accuracy and computational cost. A FAQ of common problems encountered in PyEllipSys and on clusters in general can be found in Appendix D, and may be a help to new users of PyEllipSys.

A setup completely identical to the near wake case of [15] (which is referred to as the "demonstrator article") is used for the test cases in Subsection 2.4.1-2.4.4, while a single-rotor turbine with $U_{H,\infty} = 7$ m/s is used in the rest of the cases.

2.4.1 Computational grid: Velocity profiles

The velocity profiles at three heights and three downstream positions are shown in Figure 2.9, which is constructed similarly as Figure 13 in [15] and the results from this article is also included in the figure. Three computational grids with respectively 5, 10 and 20 cells pr. D in the wake domain have been tested, c.f. Table 2.2, and all of these simulations have been done with the finely resolved AD polar grid, c.f. Table 2.3.

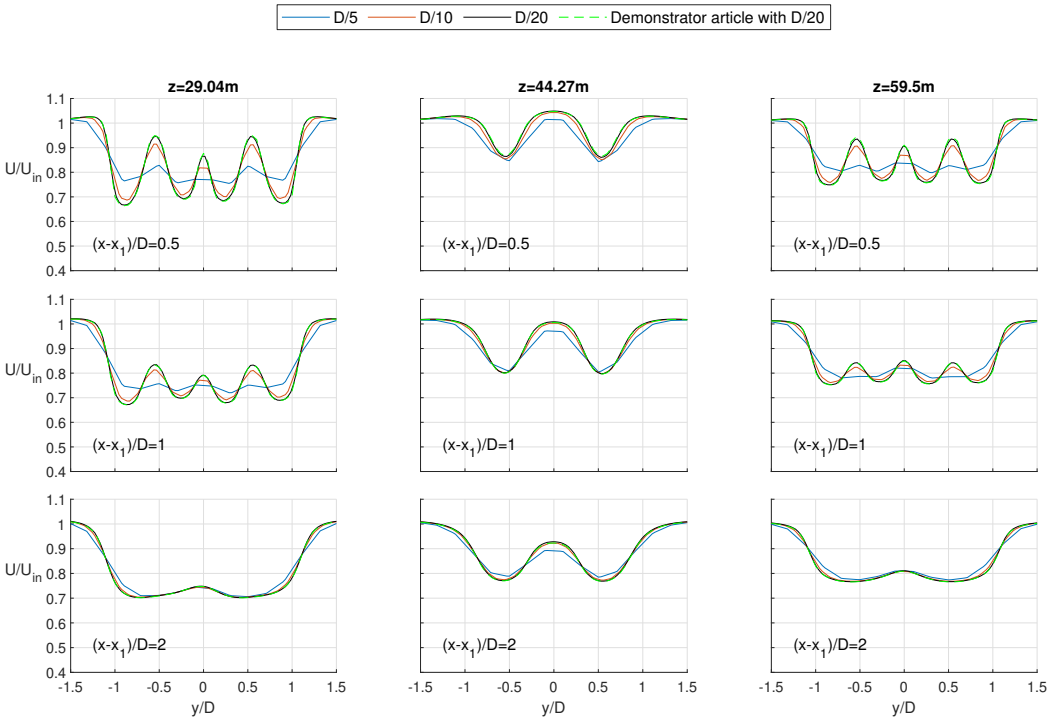

Figure 2.9: Velocity profiles in the near wake with 5, 10 and 20 cells pr. D compared with [15].

The D/20 solution almost matches the results from [15] perfectly, while the D/5 solution is alright for $(x - x_1)/D \geq 2$, but not for the near wake, where the wake is diffused too much.

2.4.2 Computational and AD grid: Power

The power production of the 4R-V29 is also effected by the computational and polar grid resolution as seen in Figure 2.10. The power during the simulation is shown in the left subplots, which gives confidence that the simulation has indeed converged. The converged power is shown in the right subplots, which show that the coarse AD grid generally overestimates the power by $\sim 5\%$. The power obtained with the fine AD grid and D/20 in the wake region is very close to the value from [15] marked with the red x in Figure 2.10.

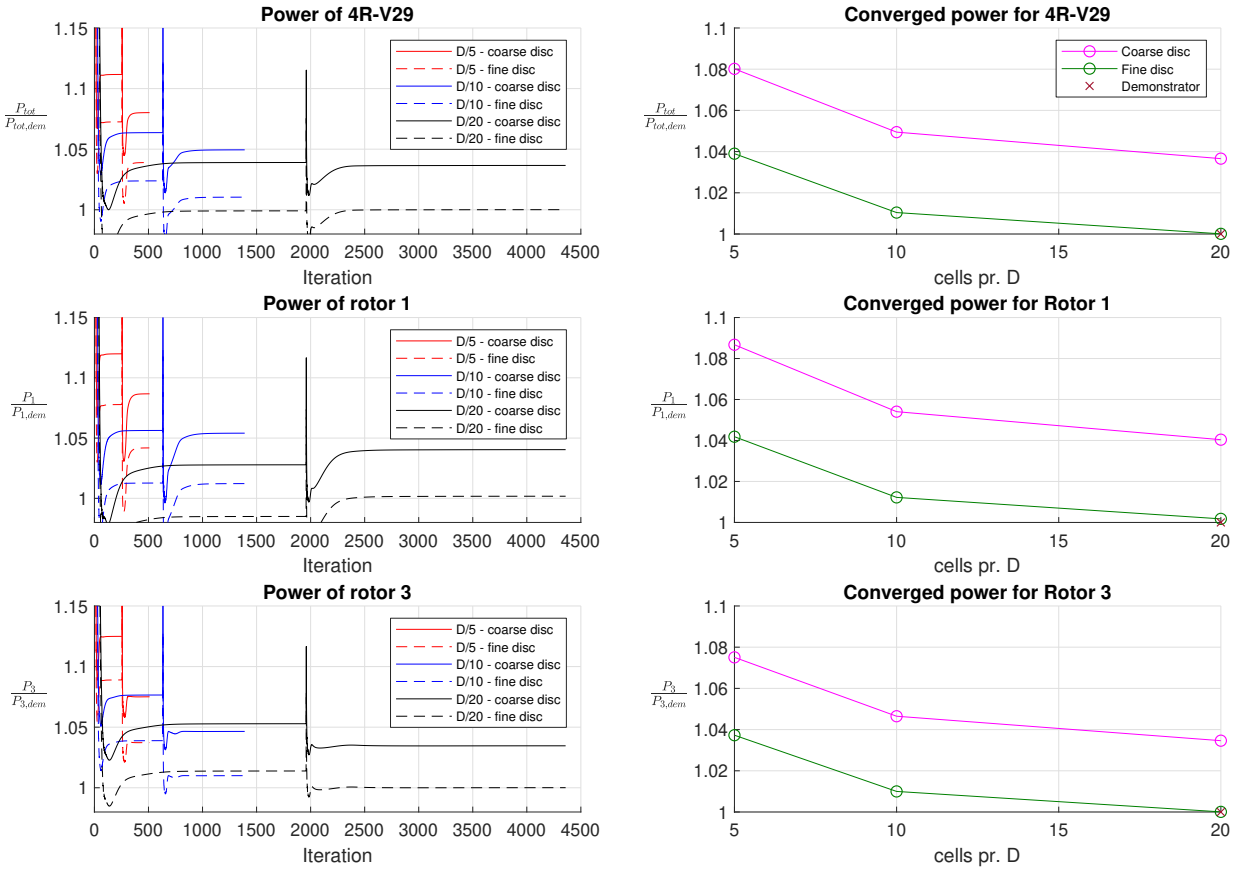

Figure 2.10: Power convergence with 5, 10 and 20 cells pr. D and different AD resolutions.

2.4.3 AD grid

Halfway through the project, it became clear that considerable computational time and memory could be saved by creating an AD grid with a resolution in between the coarse and fine grids from Table 2.3 with almost no trade-off in accuracy. The combinations shown in Table 2.6 were tested with regards to power production and wake recovery $5D$ downstream of the turbine, i.e. at $(x - x_1)/D = 5$. The relative power and wake recovery are also plotted in Figure 2.11 and 2.12. The jumps in Figure 2.11-2.12 are seen because the combinations of Table 2.6 are not listed in order of the total number of points and because the thrust distribution is not properly distributed with only $N_r = 16$. For small N_φ, the disk is also under-resolved and hence not perfectly circular, which could also explain the jumps.

N_φ	N_r	N_{AD}
32	16	512
32	32	1024
32	64	2048
64	16	1024
64	32	2048
64	64	4096
128	16	2048
128	32	4096
128	64	8192

Table 2.6: AD grids with resolution in between the coarse and fine grids from Table 2.3.

The $(N_\varphi = 64, N_r = 64)$ AD grid has a relative difference in power and wake recovery of less than 0.1% compared to the fine AD grid, cf. Figure 2.11 and 2.12, and will instead be used in this thesis.

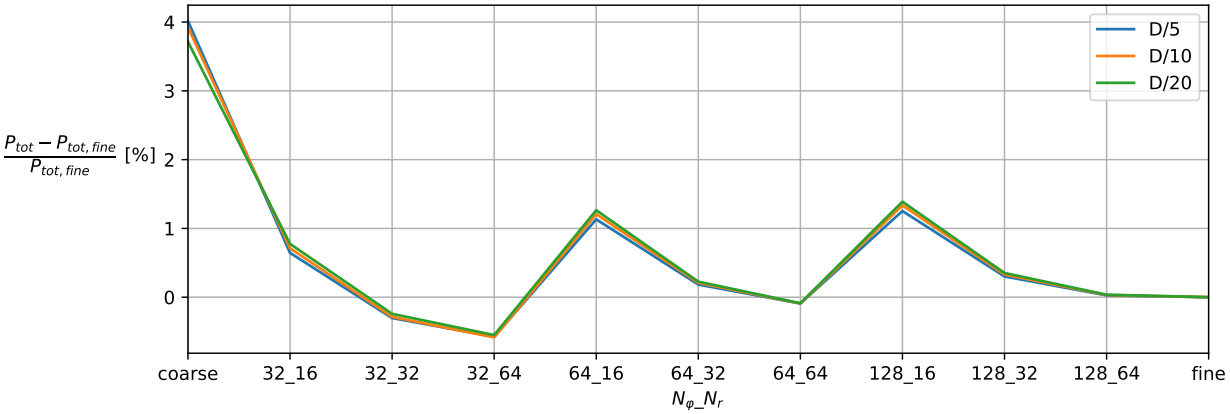

Figure 2.11: AD convergence with relative power. $P_{tot,fine}(\{D/5, D/10, D/20\}) = \{1022.5, 994.4, 984.3\}$ kW.

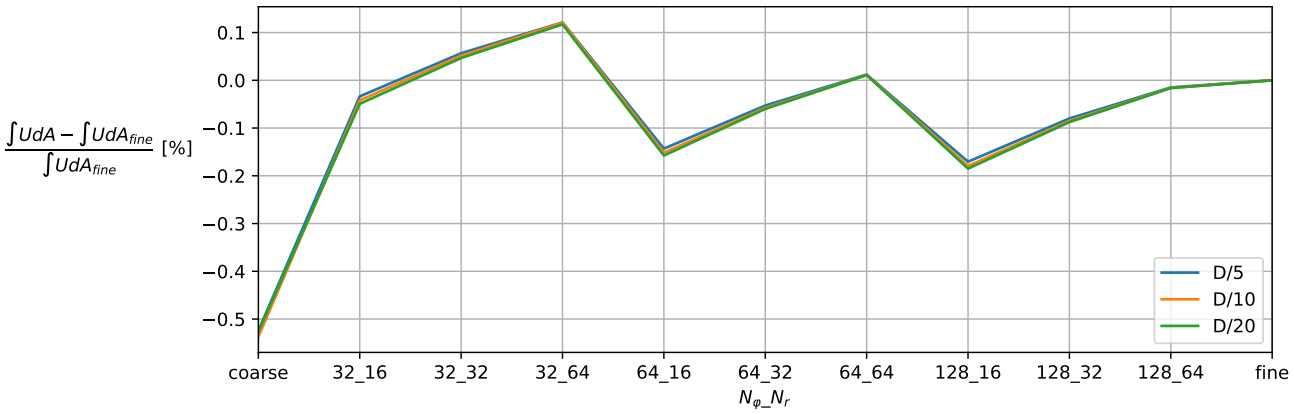

Figure 2.12: AD convergence with relative wake recovery at $(x-x_1)/D = 5$. $\int UdA_{fine}(\{D/5, D/10, D/20\}) = \{0.816, 0.817, 0.817\}$.

2.4.4 AD distribution

EllipSys3D can also output f_{x_R}, f_φ, U_{x_R} and U_φ in all of the shape cell centers of the AD marked with blue crosses in Figure 2.3. The normal force on shape cell i is then $F_{x_R,i} = f_{x_R,i} A_i$, where A_i is the area of the i'th shape cell, and the thrust can be found by summing up $F_{x_R,i}$ as described in eq. 2.1. As a reminder for Figure 2.13: $\varphi = 0°$, when the blade points vertical upwards and φ is positive CW seen from an upstream point of view, c.f. Figure 2.3.

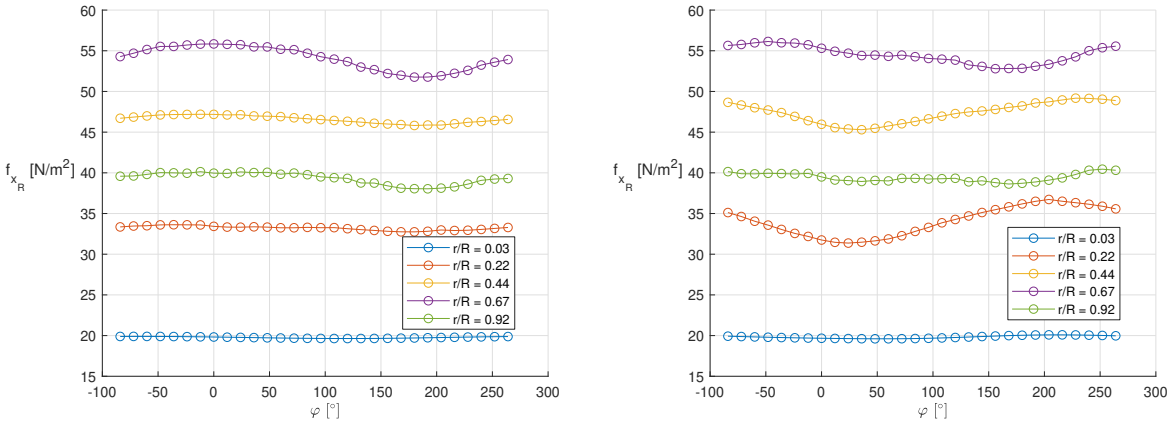

(a) Yaw $\gamma = 0°$.

(b) Yaw $\gamma = 3°$.

Figure 2.13: Normal force pr. area, $f_{x_R}(r, \varphi)$, of rotor 1.

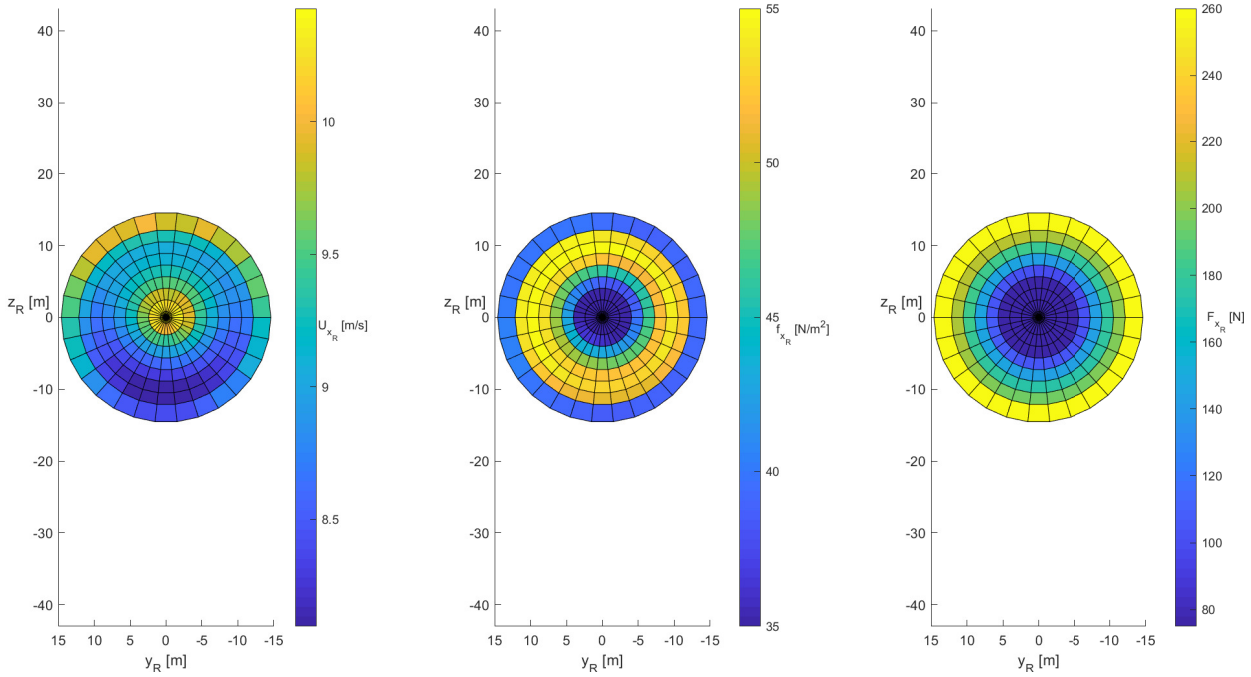

Figure 2.14: Normal velocity, normal force pr. area and normal force on rotor 1, which has a yaw of $\gamma = 3°$.

The highest velocities in Figure 2.14 are at the top of the rotor (at $\varphi = 0°$) as expected because of the wind shear. The normal force distributions however look quite azimuthal symmetric, but they are in fact not as

documented by Figure 2.13. The normal force pr. area generally increases with r except at $r = 13.38$ m, which is close to $R = D/2 = 14.6$ m, where the tip loss kicks in. For the $\gamma = 0°$ case, the loading is generally largest at $\varphi = 0°$, where the velocities are largest and lowest at $\varphi = 180°$, where the velocities are lowest. For the $\gamma = 3°$ case, the opposite behaviour is however seen at $r = \{0.41, 3.24, 6.49\}$ m , but this can be explained with a short analysis: For a yawed rotor, there is another in-plane velocity in form of $V_{\infty,AD}$, c.f. Figure 2.4, which for positive yaw will add on to the rotational speed at $\varphi = 0°$ and subtract at $\varphi = 180°$. The "effective rotational speed" will therefore be different, i.e. $V_{rot,eff}(r, \varphi = 0°) \geq V_{rot}(r, \varphi) \geq V_{rot,eff}(r, \varphi = 180°)$. The shear effect is small at small r, i.e. $U_{x_R} \approx constant$, which means that the angle angle of attack, α, is important there:

$$\text{At } \varphi = 0° \text{ and } \gamma > 0° : V_{rot,eff}(r, \varphi = 0°) \geq V_{rot}(r, \varphi) \Rightarrow \alpha_{eff} \leq \alpha \Rightarrow \text{ Smaller forces} \tag{2.47}$$

$$\text{At } \varphi = 180° \text{ and } \gamma > 0° : V_{rot,eff}(r, \varphi = 180°) \leq V_{rot}(r, \varphi) \Rightarrow \alpha_{eff} \geq \alpha \Rightarrow \text{ Larger forces} \tag{2.48}$$

The effect is less important at larger radius $r = \{9.73, 13.38\}$ m, where $V_{\infty,AD} << V_{rot}$, i.e. $V_{rot,eff} \approx V_{rot}$ and the shear effect will thus dominate.

2.4.5 Tip-loss

The TSR, λ in eq. 2.22, is in EllipSys3D calculated from the disk's rotational speed and the freestream velocity at hub height. There are however two hub heights for the 4R-V29 and the freestream velocity is different at these because of shear. Furthermore, the freestream velocity normal to the disk will change when the disk is yawed and tilted, c.f. Figure 2.4a-2.4b. To account for these two effects a modification was made to EllipSys3D, so that each rotor has a "tip speed correction velocity", $U_{\infty,tip}$, as well (can be controlled with `adcontrol.set_adfreestream()` in PyEllipSys). Two special cases can be identified with eq.2.19-2.22:

$$U_{\infty,tip} \to 0 \Rightarrow \lambda \to \infty \Rightarrow g = c_3 \approx 0 \Rightarrow F \approx 0 \Rightarrow \text{ big tip loss} \tag{2.49}$$

$$U_{\infty,tip} \to \infty \Rightarrow \lambda \to 0 \Rightarrow g = \exp(c_1 c_2) + c_3 \approx 37.6 \Rightarrow F \approx 1 \Rightarrow \text{ no tip loss} \tag{2.50}$$

This is in contrast to the usual perception that $\lambda \to \infty \Rightarrow$ no tip loss (as seen in BEM codes), but one has to remember that this is Navier-Stokes AD and *not* BEM. Keeping all other parameters constant, $U_{\infty,tip}$ was varied from 4 m/s to 25 m/s, and the power and normalized averaged disk velocity are shown in Figure 2.15.

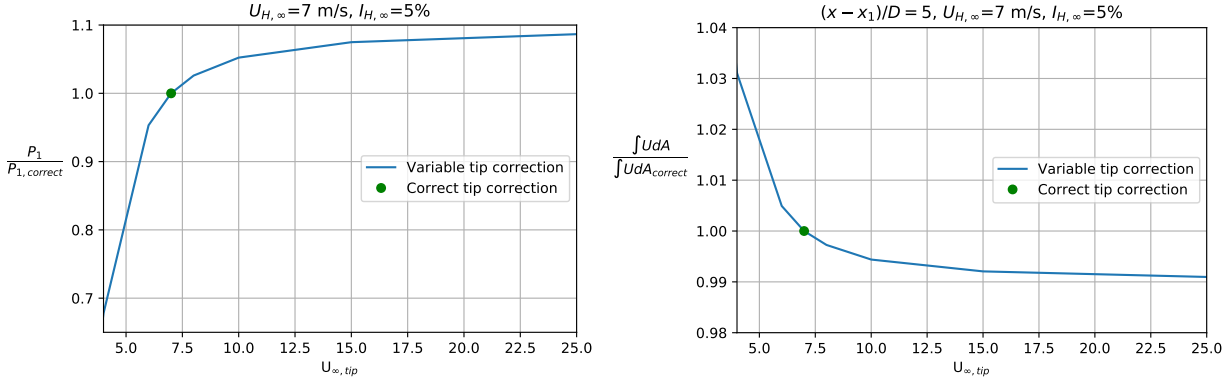

(a) Power.

(b) Wake recovery $5D$ downstream of the turbine.

Figure 2.15: Validation of tip loss correction model and implementation of $U_{\infty,tip}$. The $D/5$ grid was used with the fine AD grid. The power and wake recovery of rotor 1 were used as metrics, where $P_{1,correct} = 72.6$ kW and $\frac{\int UdA_{correct}}{\int U_0 dA} = 0.731$.

Figure 2.15 confirms that a low $U_{\infty,tip}$ gives a big tip loss and hence a low power as argued in eq. 2.49. It is seen that $\frac{\partial P}{\partial U_{\infty,tip}}$ is largest at low $U_{\infty,tip}$, which makes it especially important to use the correct $U_{\infty,tip}$ below rated wind speed and in yawed/tilted configurations.

2.4.6 Residuals

The convergence criterion on the residuals is an input to EllipSys3D and it effects both the computational time and accuracy for a given simulation. Rotor 1 has been used to study the effect of 4 different convergence criteria of the residuals: res $= \{10^{-3}, 10^{-4}, 10^{-5}, 10^{-6}\}$.

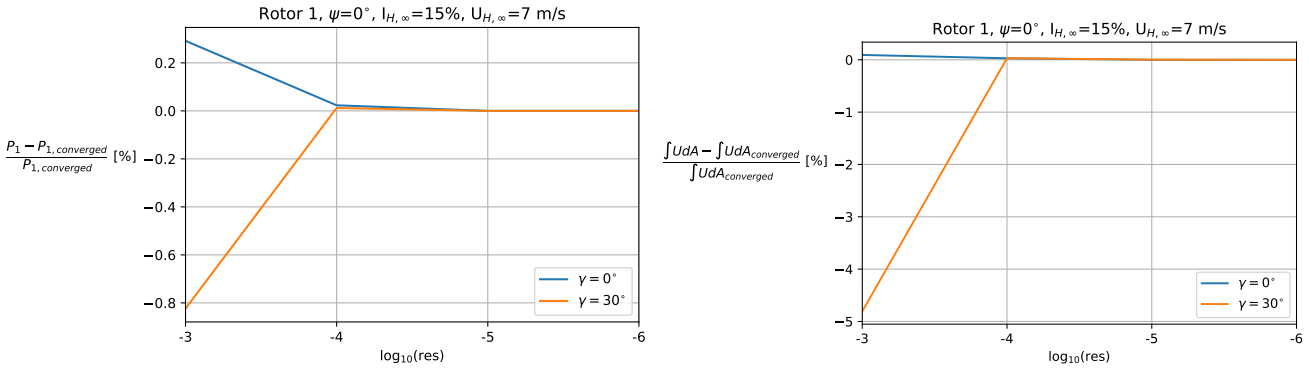

(a) Relative increase of rotor 1 power production.

(b) Relative increase of wake recovery.

Figure 2.16: Study of residuals.

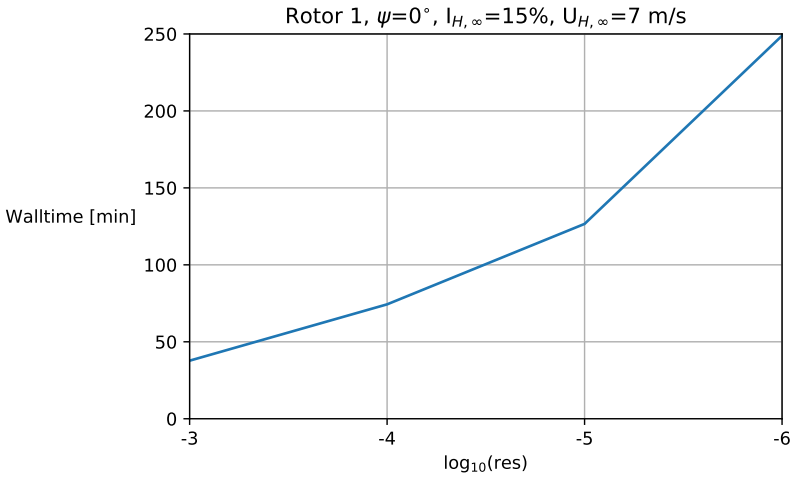

Figure 2.17: Walltime. All simulations done on 48 CPUs.

The increase of rotor 1's power production is $< 1\%$ for all the convergence criteria, while the wake recovery is more critical. A conservative criterion of res $= 10^{-5}$ will be used throughout this thesis.

2.4.7 Inflow profile

U, V, W, P, k and ε are extracted on the line $\mathbf{x}/D = (-42, 2.5, \{0, 0.1, 0.2, \ldots, 8\})$ to validate that the inflow profile in EllipSys3D is equal to theoretical profiles discussed in Section 1.5, i.e. eq. 1.17-1.19. All of the variables follow the expected analytical formulas except k, which deviates slightly near the ground. This is a known error of eddy viscosity models [22], but the error is small enough to be neglected.

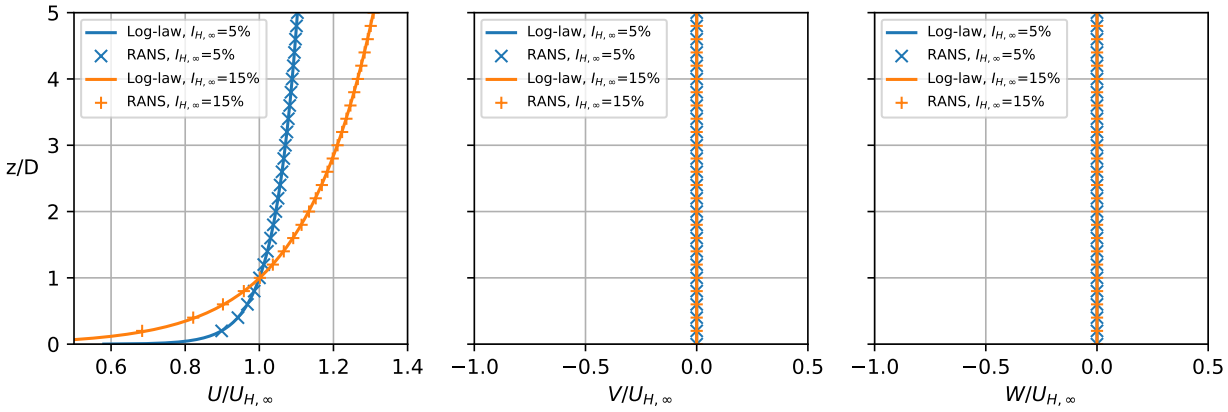

Figure 2.18: U-, V- and W-inflow profiles. $U_{H,\infty} = 7$ m/s.

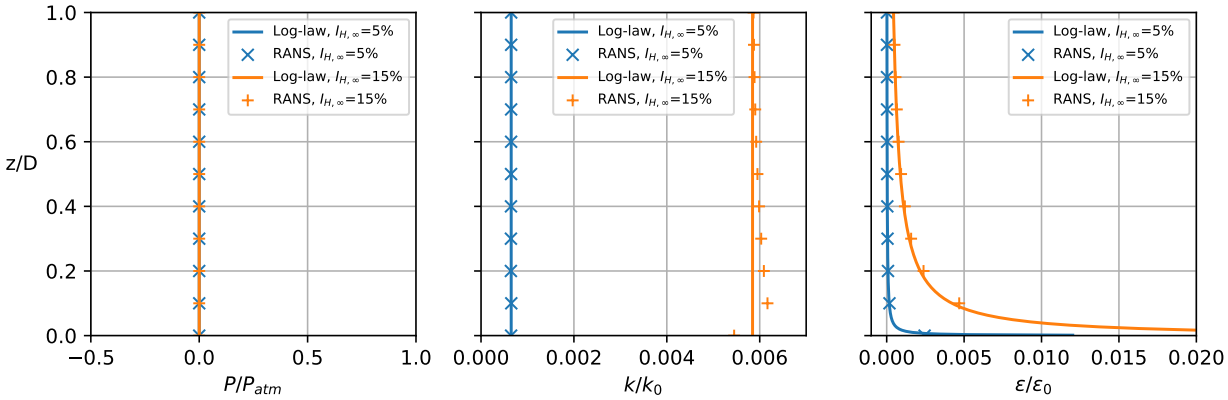

Figure 2.19: P-, k- and ε-inflow profiles. $P_{atm} = 1$ bar, $k_0 = \frac{U_{H,\infty}^2}{\sqrt{C_\mu}}$ and $\varepsilon_0 = \frac{U_{H,\infty}^3}{\kappa z_H}$.

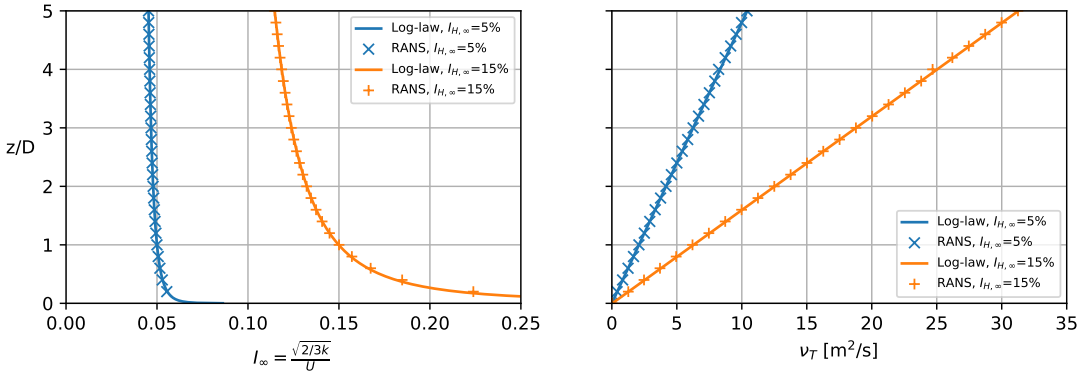

Figure 2.20: I_∞- and μ_T-inflow profiles. Eq. 2.43 with $f_P = 1$ is used for the theoretical profile in the right plot, because the flow at the extracted positions follows the log-law.

2.4.8 Method III-calibration

Method III-calibration (cf. Appendix A) is used in Section 3.5 and 4.7 for a "wind farm" of two aligned turbines. To validate this AD model, rotor 1 with $U_{H,\infty} = 7$ m/s and $I_{H,\infty} = 5\%$ is simulated with both method III-calibration and method III for a non-tilted and non-yawed rotor, i.e. $\psi = 0°$ and $\gamma = 0°$. The results are shown in Figure 2.21.

As mentioned in the ADres.dat question in Appendix D, method III-calibration has been updated to include λ in the control-file, because the old method overestimated $U_{\infty,tip}$ (method I was used to obtain this), which also meant an overestimation of the power. Although the overestimation of the power was only 0.27% for this case, it might be a significant difference, when searching for small differences in performance. The updated method III-calibration has a relative difference of less than 0.01% in all of the variables listed in Table 2.7.

	Method III-calibration (old)	Method III-calibration (updated)
θ	0.00%	0.00%
Ω	-0.02%	0.00%
$U_{\infty,tip}$	1.30%	0.00%
T	0.11%	0.00%
P	0.27%	0.00%

Table 2.7: Relative increase in percent, i.e. $\frac{(\text{method II} - \text{method III})}{\text{method III}} \cdot 100$, for $\psi = 0°$ and $\gamma = 0°$.

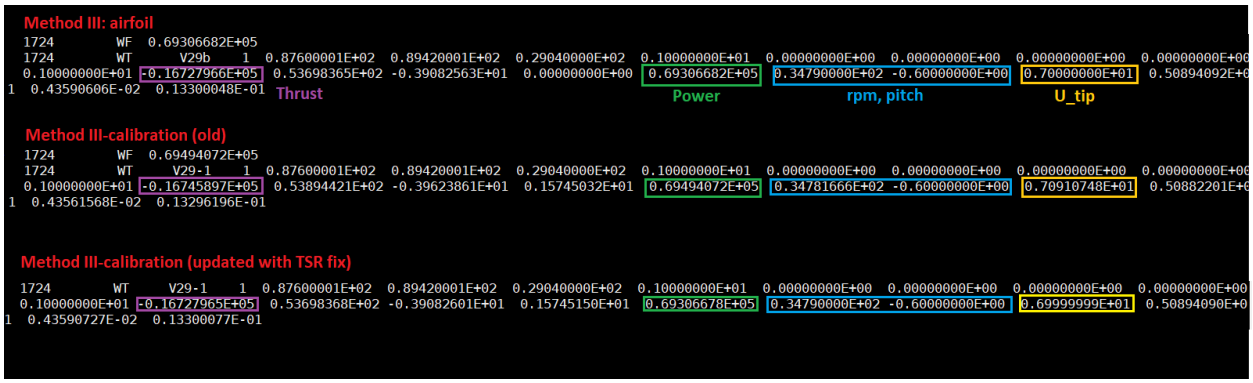

Figure 2.21: Raw results of the simulations with $\psi = 0°$ and $\gamma = 0°$.

The updated method III-calibration is also tested for a non-tilted, but yawed rotor and the results in Table 2.8 show that the method overpredicts the power and thrust for $\gamma > 0°$. The calibration was made with a non-tilted and non-yawed rotor, which explains the discrepancy and it is thus necessary to re-do the calibration step of method III-calibration everytime the orientation of the rotor is changed. This is not very practical, when studying several different tilt and yaw settings, so method III should be preferred for such studies.

	$\gamma = 0°$	$\gamma = 10°$	$\gamma = 20°$	$\gamma = 30°$
θ	0.00%	0.00%	0.00%	0.00%
Ω	0.00%	0.47%	2.42%	5.36%
$U_{\infty,tip}$	0.00%	0.46%	2.38%	5.27%
T	0.00%	0.38%	2.07%	5.02%
P	0.00%	0.10%	0.75%	2.42%

Table 2.8: Relative increase in percent, i.e. $\frac{(\text{method III-calibration} - \text{method III})}{\text{method III}} \cdot 100$, for $\psi = 0°$ and variable γ.

2.4.9 Distance from turbine to wake domain

In the simulations of two aligned V29 turbines in Section 3.5 and two aligned 4R-V29 turbines in Section 4.7, turbine 2 is situated only $3D$ upstream of the wake domain boundary when $(x_2 - x_1)/D = 10$ (since $x_1/D = 3$ and $l_x/D = 16$, c.f. Figure 3.28), and to determine if this could bias the results, the length of the wake domain, l_x, is varied, while holding $x_1/D = 3$ and $x_2/D = 13$ fixed. The power of respectively turbine 1 and 2 are used as metrics in Figure 2.22 to quantify the effect of the wake domain length and the test has been made with both the D/5 and D/10 computational grid.

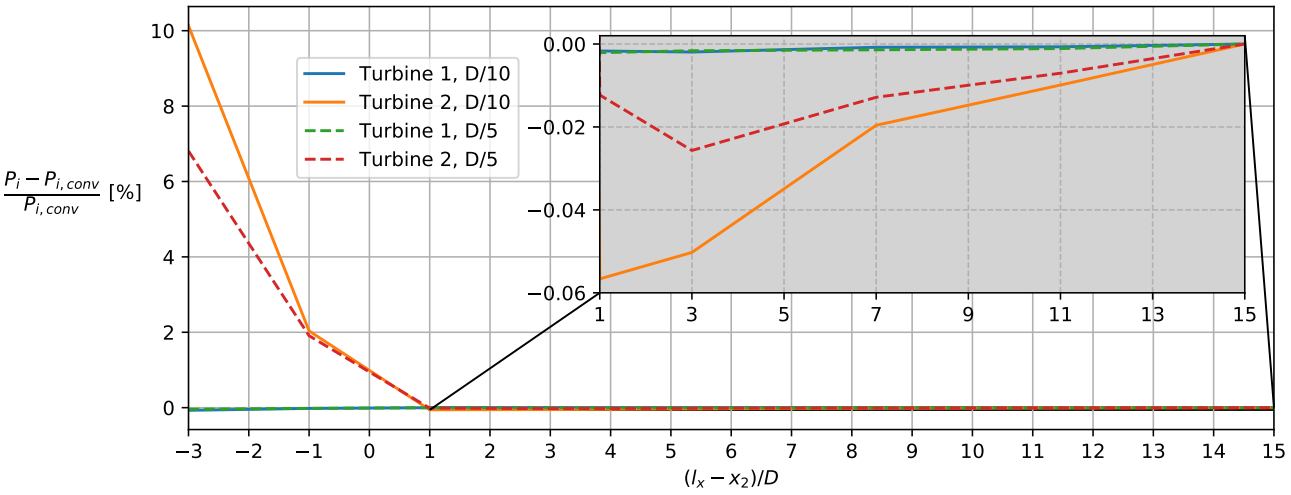

Figure 2.22: Effect of the distance between turbine 2 and wake domain border, when $x_1/D = 3$ and $x_2/D = 13$.

Almost no difference in power, i.e. a power decrease of $< 0.06\%$, is seen when there is $1D$ or more between turbine 2 and the wake domain end, while a large difference is seen when turbine 2 is outside the wake domain. The first observation may perhaps seem surprising, since almost all of the wake of turbine 2 is outside the wake domain, when for example $(l_x - x_2)/D = 1$, which one could imagine should influence the power production of turbine 2 significantly. However, the inflow of turbine 2 is highly turbulent due to the wake of turbine 1, which could explain why turbine 2 can be placed so close to the border of the wake domain.

Based on this grid study, $l_x/D = 16$ will be used in Section 3.5 and 4.7, where the maximum x-position of turbine 2 will be $x_2/D = 13$, hence the minimum distance between turbine 2 and the border of the wake domain will be $(l_x - x_2)/D = 3$.

Chapter 3

Single-rotor turbine studies

It is necessary to study a single rotor first in order to understand how the individual rotors of the multi-rotor behave and to quantify the effect of rotor interactions. The 4R-V29 multi-rotor turbine consists of four V29 turbines, which are named rotor 1, 2, 3 and 4 and this chapter will focus on rotor 1 (cf. Figure 3.1). The structure of this chapter is:

- **Section 3.1:** Presents the V29 turbine and the computational setup used in the following sections.
- **Section 3.2:** Power production, wake recovery and wake deflection are investigated for different yaw and tilt combinations.
- **Section 3.3:** Results of a counter-clockwise rotating turbine are shown.
- **Section 3.4:** The pitch and rpm settings are optimized.
- **Section 3.5:** A turbine is added downstream and two methods are used to simulate the two aligned turbines.

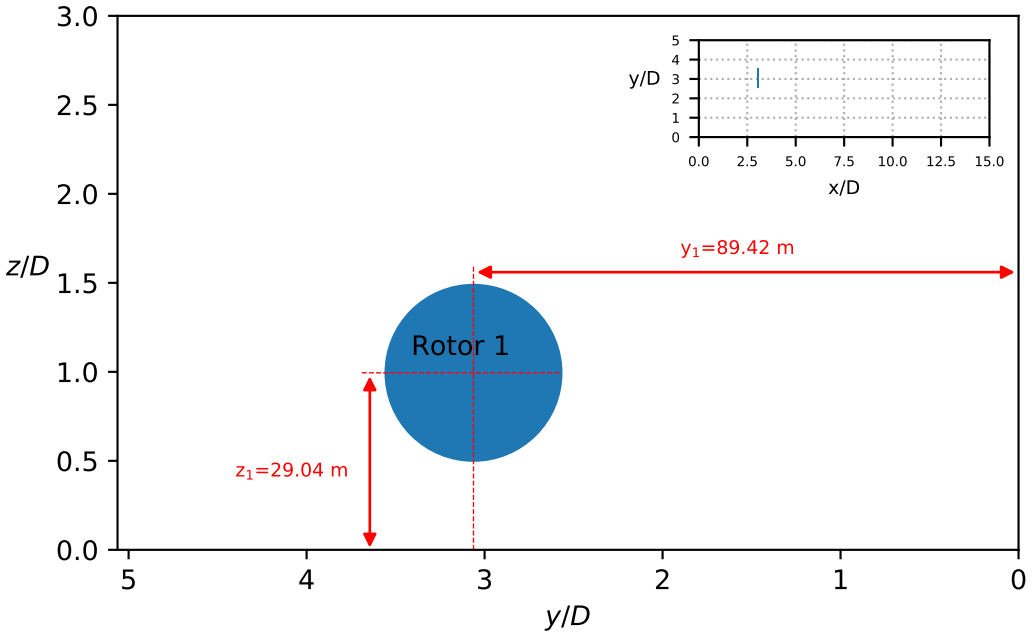

Figure 3.1: Upstream view of rotor 1. Inlet: Top view of the position of rotor 1 .

3.1 The V29 turbine

The Vestas V29-225 kW wind turbine was developed in the mid-90's as an upgrade of the V27-225 kW turbine, which is still in operation today at the Risø campus of DTU, c.f. Figure 3.2. Basic info of the V29 rotor is described in Table 3.1 [41].

Figure 3.2: Risø test site in June 2019.

Diameter	29.2 m
Rotor mass (incl. hub, bladebearing and blades)	5000 kg
$U_{cut,in}$	4 m/s
U_{rated}	14 m/s
$U_{cut,out}$	25 m/s
Ω_{max}	41.3 rpm

Table 3.1: V29 properties.

Vestas has supplied the pitch-rpm settings and power-thrust curves shown in Figure 3.3 and 3.4, which has been calculated with a software similar to HAWCStab2 [39]. Such an aeroelastic tool assumes uniform inflow and uses the BEM method with a structural model, which means that an EllipSys3D simulation will not give the same thrust and power, even though the same pitch and rpm are used. For this reason a pitch-rpm optimization is conducted in Section 3.4, but until then the settings of Figure 3.3 are used. It should be noted that the settings in Figure 3.3 were tuned specifically for the 4R-V29 turbine (for example with regards to noise) and a conventional single-rotor V29 turbine does hence not use these exact settings.

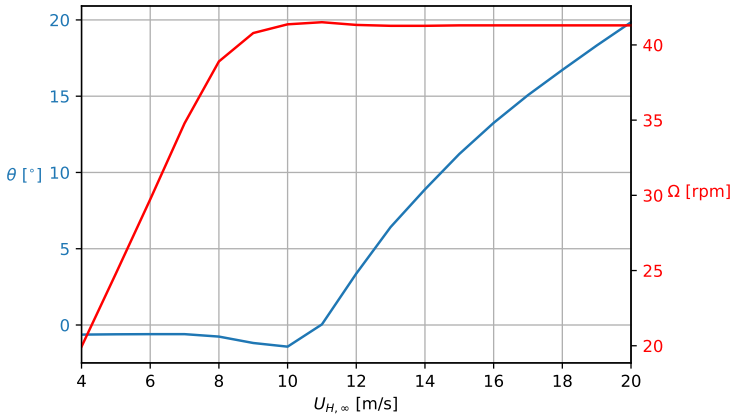

Figure 3.3: Pitch and rpm settings of the V29 turbine tuned specifically for the 4R-V29 turbine.

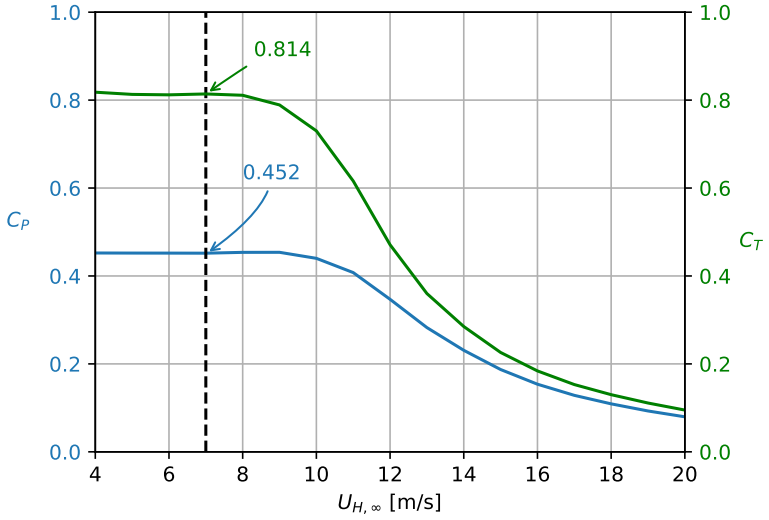

Figure 3.4: Power and thrust coefficients of the V29 calculated with an aeroelastic tool. The values at $U_{H,\infty} = 7$ m/s are annotated.

To limit the extent of the studies, it has been chosen to focus on $U_{H,\infty} = U(z_1) = 7$ m/s, which is representative of the below rated region, where $C_T \approx const.$ Above rated wind speed C_T is decreasing and there is plenty of energy available, so it would not make sense to investigate wake effects and power production in this region. Low (5 %) and high (15 %) ambient turbulence intensities are tested for all simulations.

z_H	$z_1 = 29.04$ m
$U_{H,\infty}$	7 m/s
$I_{H,\infty}$	{5, 15} %
Computational grid	D/20
AD grid	$N_\varphi = 64$, $N_r = 64$

Table 3.2: Computational input parameters

The parameters in Table 3.2 are used in this chapter unless otherwise stated. A neutral ABL with $I_{H,\infty}$ and $U_{H,\infty}$ is set as described in Section 1.5 and the methods described in Chapter 2 are implemented in EllipSys3D, which is executed from the PyEllipSys interface.

3.2 Yaw and tilt

Each of the rotors of the 4R-V29 are permanently yawed slightly outwards (called toe-out, which will be discussed more thoroughly in Chapter 4) and it is possible to actively yaw the support arms. For this reason the effect of yaw and tilt are first investigated here for a single rotor.

3.2.1 Brief literature summary

Wind turbines in yaw has become a hot research topic in recent years with the prospect of improving the wind farm production through "wake steering". Large eddy simulations of a yawed turbine were made in 2009 by **Jiminez et. al** [42] and a simple analytical model was developed based on a top hat wake profile ($\alpha = dy_c/dx$ of [42] is integrated with $y_c(x = 0) = 0$):

$$\frac{y_c(x)}{D} = \cos^2(\gamma)\sin(\gamma)\frac{C_T}{2\beta}\left(1 - \frac{1}{\beta x/D + 1}\right) \tag{3.1}$$

where β is an expansion factor similar to α in the Jensen model, c.f. eq.1.15. The thrust coefficient is here calculated from the normal force and velocity on the disk:

$$C_T = \frac{F_N}{0.5\rho A U_N^2} \tag{3.2}$$

Wake steering studies are typically conducted with $\gamma = 0° - 30°$ and **Howland et. al** [37] compared different CFD codes with wind tunnel test for $\gamma = 30°$. A "center-of-gravity" method was deployed to estimate the wake center and the results showed $y_c(x/D = 5)/D \approx 0.4$ and $y_c(x/D = 10)/D \approx 0.55$. This is slightly less than the results of Jiminez et al., but they also used a "95%-midpoint"-rule to estimate the wake deflection. Quite elaborate analytical formulas for velocity deficit and deflection of a yawed wake was developed by **Bastankhah et. al** [35] and among these was also a formula for the asymptoptic wake deflection, which was found to depend highly on C_T and $I_{H,\infty}$. Larger C_T or smaller $I_{H,\infty}$ leads to a larger asymptotic wake deflection, which also makes sense from physical point of view.
Burton et. al [34] derived that $P \sim \cos^3(\gamma)$ from simple momentum considerations, but $P \sim \cos^2(\gamma)$ is also sometimes used in the industry, e.g. by ROMOWind [43].

3.2.2 Only yaw

Following the research community, rotor 1 is yawed from $\gamma = 0°$ to $\gamma = 30°$ and with no tilt, i.e. $\psi = 0°$. The wake recovery is measured with a non-yawed and non-tilted disk average of U normalized by a far upstream disk average (situated at $x/D = -42$ corresponding to 45 rotor diameters upstream, since the turbine is situated at $x = x_1 = 3D$, cf. Figure 3.5):

$$\frac{\int U dA}{\int U_0 dA} = \frac{\int_r \int_\varphi U(x, r, \varphi) r d\varphi dr}{\int_r \int_\varphi U(x/D = -42, r, \varphi) r d\varphi dr} \tag{3.3}$$

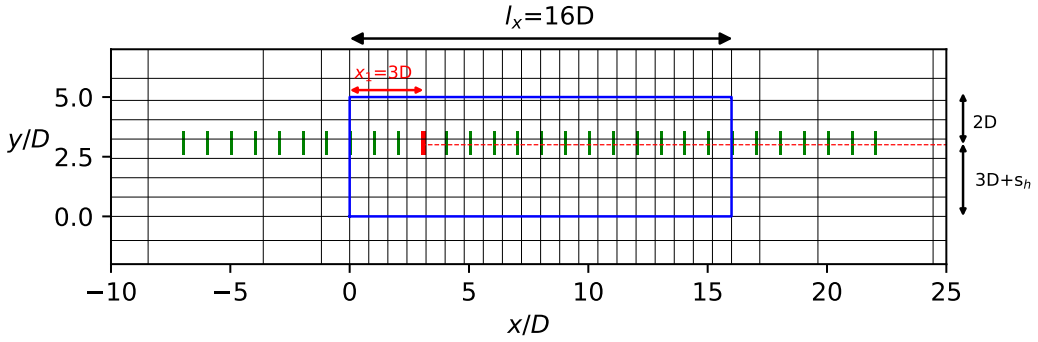

Figure 3.5: Red rectangle = rotor 1. Dotted red line = axis of rotor 1. Blue rectangle = Wake region. Green rectangles = probe disks.

The "probe disks" used for these disk averages are of the same size as the actual rotor and is located at the same y- and z-coordinates, but translated in the x-direction, see Figure 3.5. The disk averages of the probe disks hence provide an estimate for the incoming velocity of a potential downstream turbine.

The disk averaged velocity is close to 1 upstream of the turbine, then decreases fast over the turbine and finally recovers again towards 1. The high TI case recovers faster, which is caused by the enhanced mixing in the wake. Larger yaw also causes a faster recovery, because the wake is deflected and because the loading on the disk is reduced, since fewer air particles will impinge a yawed disk pr. time unit (the same reason, why less power is produced by a yawed turbine).

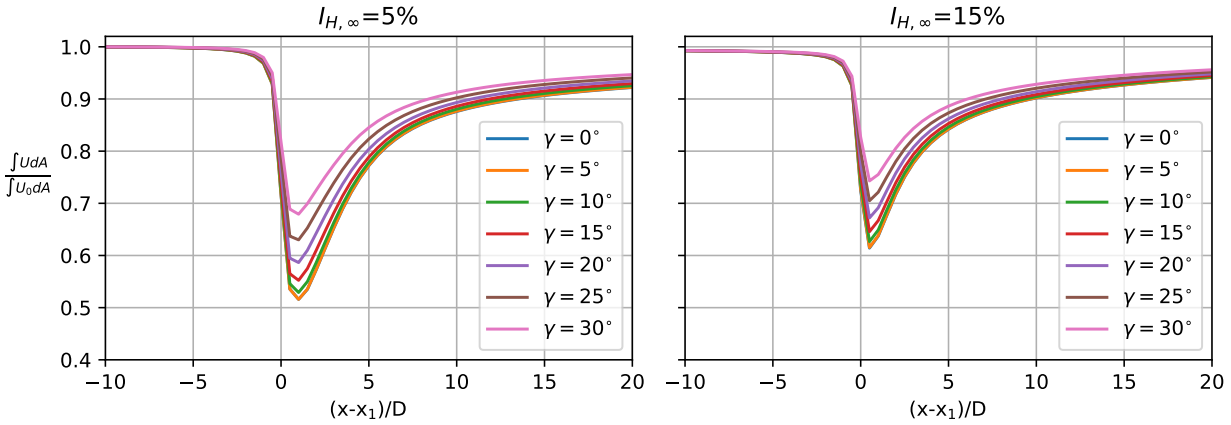

Figure 3.6: Wake recovery for yaw only, i.e. $\psi = 0°$.

The power production is a direct output of EllipSys3D and the theoretical cubed cosine relation is plotted in the left plot of Figure 3.7 for comparison:

$$P_{an}(\gamma) = P(\gamma = 0°) \cdot \cos^3(\gamma) \tag{3.4}$$

The relation however underpredicts the power and a $\cos^{2.2}(\gamma)$-relation fits the RANS results better as can be seen in the right plot of Figure 3.7. The cubed cosine relation is obtained from a simple momentum analysis with several assumptions, c.f. [34], which is probably the reason for its discrepancy with the RANS results.

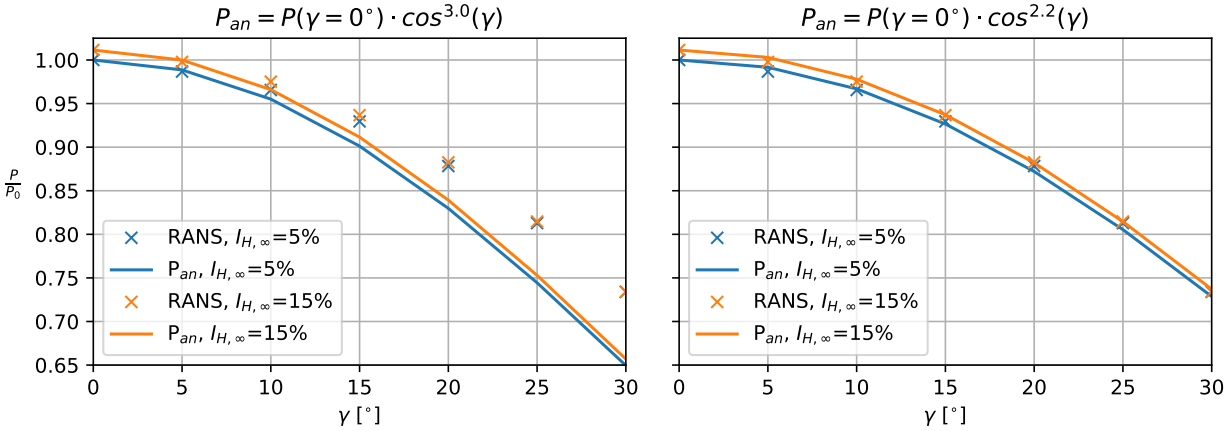

Figure 3.7: Power production for yaw only, i.e. $\psi = 0°$. $P_0 = P(\gamma = 0°, I_{H,\infty} = 5\%) = 68.4$ kW.

The high TI case is seen to produce slightly more power even though $U_{H,\infty} = 7$ m/s is used for both and this was at first believed to be due to the larger shear associated with high TI inflow profiles. This is however not

the case, as can be proved with a disk integral of the cube of $U(z; U_{H,\infty}, I_{H,\infty})$ from eq. 1.17:

$$P_{av}(U_{H,\infty}, I_{H,\infty}) = \int_{z_H-R}^{z_H+R} \int_{-\sqrt{R^2-(z-z_H)^2}}^{\sqrt{R^2-(z-z_H)^2}} U(z)^3 dy dz = 2 \int_{z_H-R}^{z_H+R} U(z)^3 \sqrt{R^2-(z-z_H)^2} dz \tag{3.5}$$

The integral is non-trivial to solve analytically (also in polar coordinates), but can easily be solved numerically with for example Python's scipy.quad scheme, which gives:

$$\frac{P_{av}(U_{H,\infty} = 7 \text{ m/s}, I_{H,\infty} = 0.15)}{P_{av}(U_{H,\infty} = 7 \text{ m/s}, I_{H,\infty} = 0.05)} \approx 0.994 \tag{3.6}$$

This ratio can be validated numerically by extracting the velocities from the EllipSys3D simulations at a probe disk at $x/D = -42$ and calculating the ratio as:

$$\frac{P_{av,num}(U_{H,\infty} = 7 \text{ m/s}, I_{H,\infty} = 0.15)}{P_{av,num}(U_{H,\infty} = 7 \text{ m/s}, I_{H,\infty} = 0.05)} \approx \frac{\sum_{i=1}^{N_r} \sum_{i=1}^{N_\varphi} U_{i,j}(x = -42D, I_{H,\infty} = 0.15)^3}{\sum_{i=1}^{N_r} \sum_{i=1}^{N_\varphi} U_{i,j}(x = -42D, I_{H,\infty} = 0.05)^3} \approx 0.996 \tag{3.7}$$

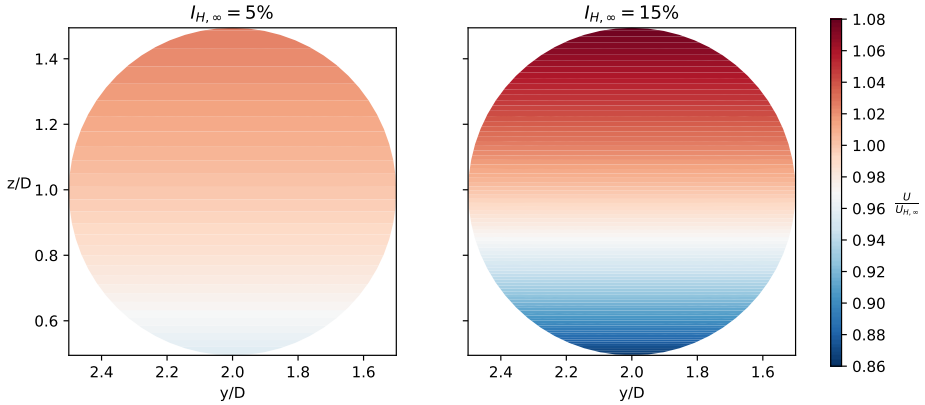

Figure 3.8: U-distribution on a disk far upstream at $x/D = -42$.

The explanation could instead be that the pitch-rpm setting from the aeroelastic code is favorable for the high TI setting in this case, but this argument is also proven to be wrong in the pitch-rpm study of Section 3.4, where this difference will be discussed further.
Another thing to notice, is that the power obtained for both the low and high TI cases is approximately 5% larger than the annotated in Figure 3.4, but this is expected, because method III generally overpredicts power and thrust below rated wind speed compared to conventional aeroelastic codes like HAWCStab2 [27].

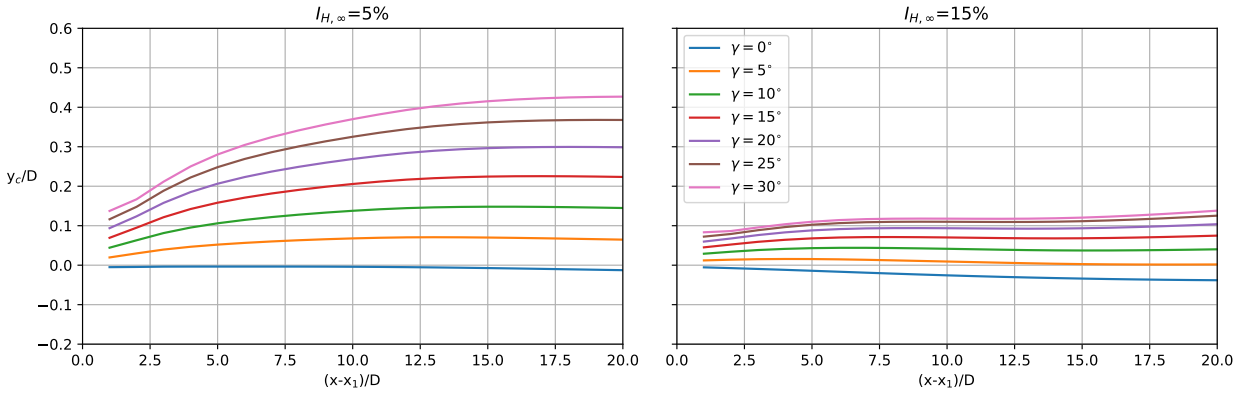

Figure 3.9: Wake center deflection at $z = z_1$ for yaw only, i.e. $\psi = 0°$.

The wake deflection is shown in Figure 3.9 and is calculated using a "center-of-gravity" method similar to the one of Howland et al. [37], but in this thesis the inflow is not uniform, so a 1D line version of the method is used instead. The wake deflection is thus only calculated at hub height:

$$y_c(x) = \frac{\int_{y_1-2D}^{y_1+2D}(U_{H,\infty} - U(x, y, z = z_1))y dy}{\int_{y_1-2D}^{y_1+2D}(U_{H,\infty} - U(x, y, z = z_1))dy} - y_1 \tag{3.8}$$

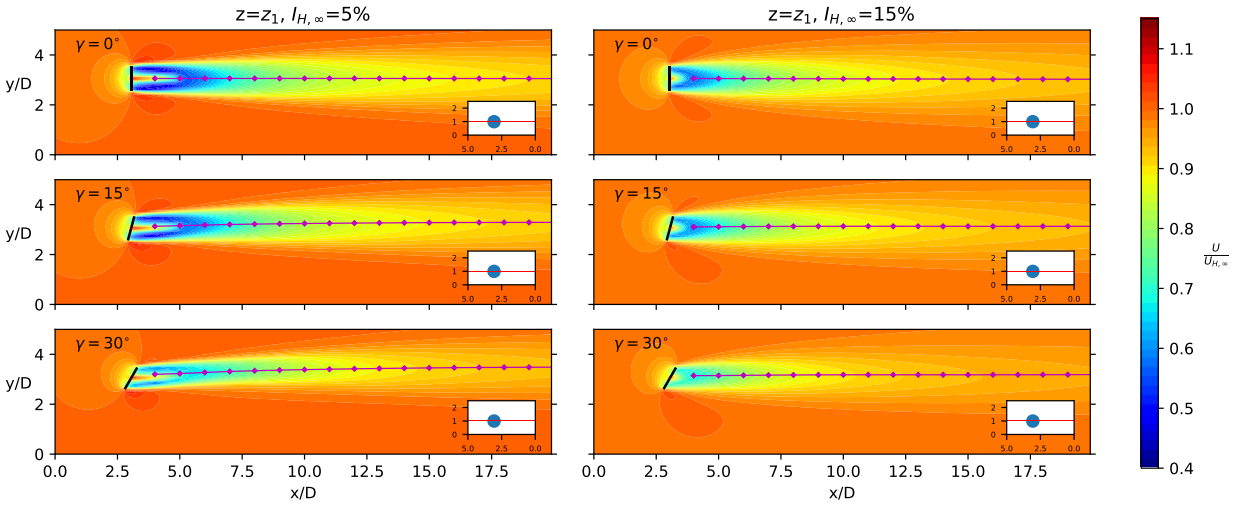

Figure 3.10: Countour plot of U at $z = z_1$ with overlayed $y_c + y_1$ for yaw only, i.e. $\psi = 0°$.

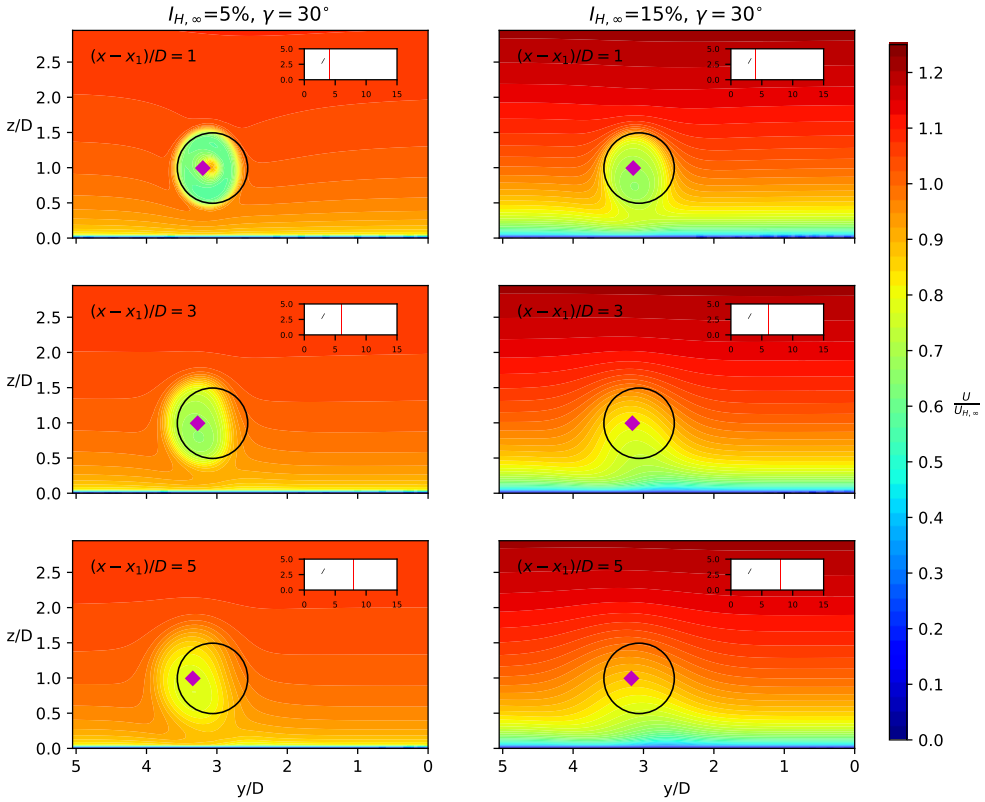

Figure 3.11: Countour plot of U with overlayed $(z_1, y_c + y_1)$ for yaw only, i.e. $\psi = 0°$. Black circle is the non-yawed AD. Inlets show top view, where the red line marks the position of the extracted y-z plane.

Notice in Figure 3.9, that y_c is not calculated at $(x - x_1)/D = 0$, since there is only wake for $y < y_1$ at this position. It should also be stressed that the wake center is only calculated at $z = z_1$, which might bias y_c and eq. 3.8 hence only gives a first rough estimate of the wake center. The wake is clearly deflected in the low TI case with an asymptotic value of $y_c(\gamma = 30°, x/D = 20)/D \approx 0.4$, which is slightly lower than the results of e.g. Howland et. al [37], but the method and disk settings are also different. The wake is on the other hand not deflected much for the high TI case and converges already at $(x - x_1)/D \approx 5$, which is expected for high TI flows as discussed in the brief litterature summary. For both cases there seems to be an initial displacement of wake, when the turbine is operating in yaw, which is likely caused by the 1D line method, since the line is not orthogonal to the wake close to the turbine. Another small contributing effect could be that the flow upstream "feels" a lateral force in the y-direction (similar to that the axial velocity is reduced upstream of a turbine), i.e. the flow equations are elliptic.

3.2.3 Yaw and tilt parametric study

There is usually a restriction on the tilt of a rotor due to tower clearance issues, but for the 4R-V29 there is instead a restriction on the yaw, because the support arm is horizontally connected to the rotor. The tilt can therefore both be negative and positive, and the effect of these tilts are shown in Figure 3.12 and 3.13 for different yaw angles. The tilt angles $\psi = \{-10, -8, \ldots, 10\}°$ are chosen, since in reality $|\psi| > 10°$ would be less feasible in terms of the cost of the other components of the turbine, e.g. the bearings and gearbox design. The power is as expected maximum at $\gamma = 0°$ and $\psi = 0°$, i.e. with the disk orthogonal to the flow, for both low and high TI. The wake recovery is however faster for negative tilt angles than for positive tilt angles (c.f. Figure 2.4b for the definition of positive tilt).

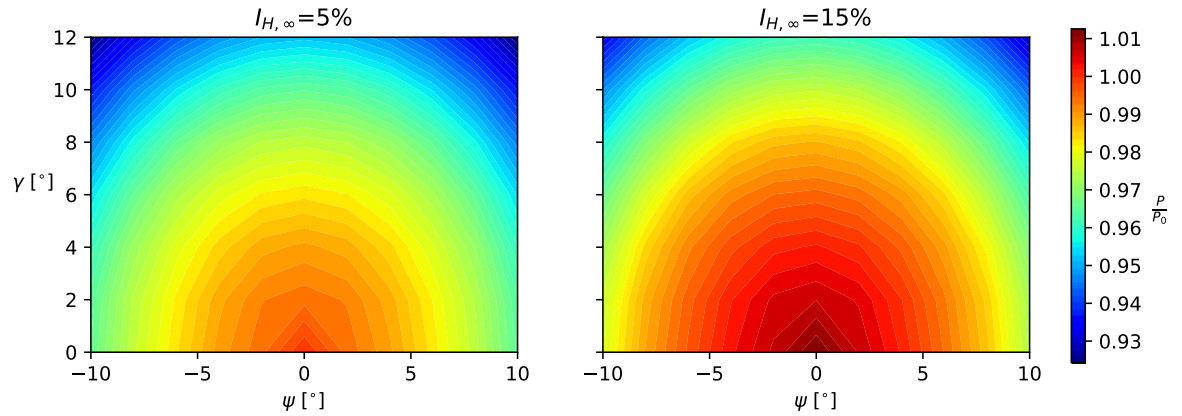

Figure 3.12: Countour plot of power production. $P_0 = P(\gamma = \psi = 0°, I_{H,\infty} = 5\%) = 68.4$ kW.

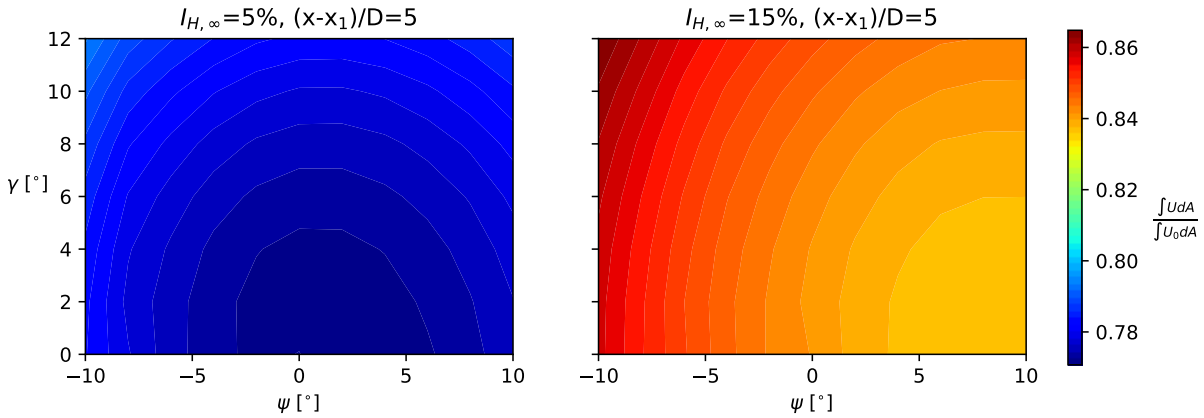

Figure 3.13: Contour plot of wake recovery.

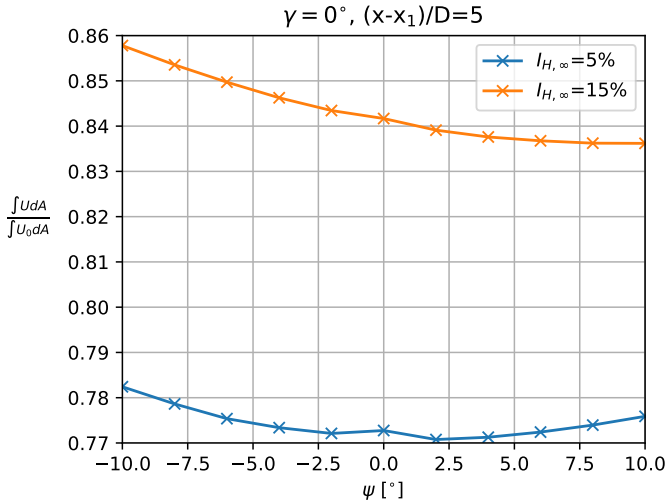

Figure 3.14: Wake recovery at $\gamma = 0°$.

The results of Figure 3.13 at $\gamma = 0°$ are reprinted in Figure 3.14, which show that the "asymmetric" tilt effect or bias of the wake recovery is most pronounced for the high TI case and is on the order of 2%. Table 3.3 assures that the difference between the thrust of the $\psi = -10°$ and $\psi = 10°$ cases is less than 0.1%, which is unlikely to cause the much larger difference of the wake recovery. Hence, the asymmetry effect must come from the wake deflection and it can be concluded that downward wake deflection (caused by $\psi = -10°$) is stronger than upward deflection (caused by $\psi = 10°$). The inflow is sheared, which could explain why the upwards wake deflection is weaker, cf. Figure 3.15.

	$\psi = -10°$	$\psi = 0°$	$\psi = 10°$
T_x [kN]	16.10	16.65	16.11
T_y [kN]	2.80	0.00	-2.80
T [kN]	16.34	16.65	16.35
P [kW]	66.07	68.40	66.02

Table 3.3: Disk results of the cases with $\gamma = 0°$ and $\psi = \{-10, 0, -10\}°$.

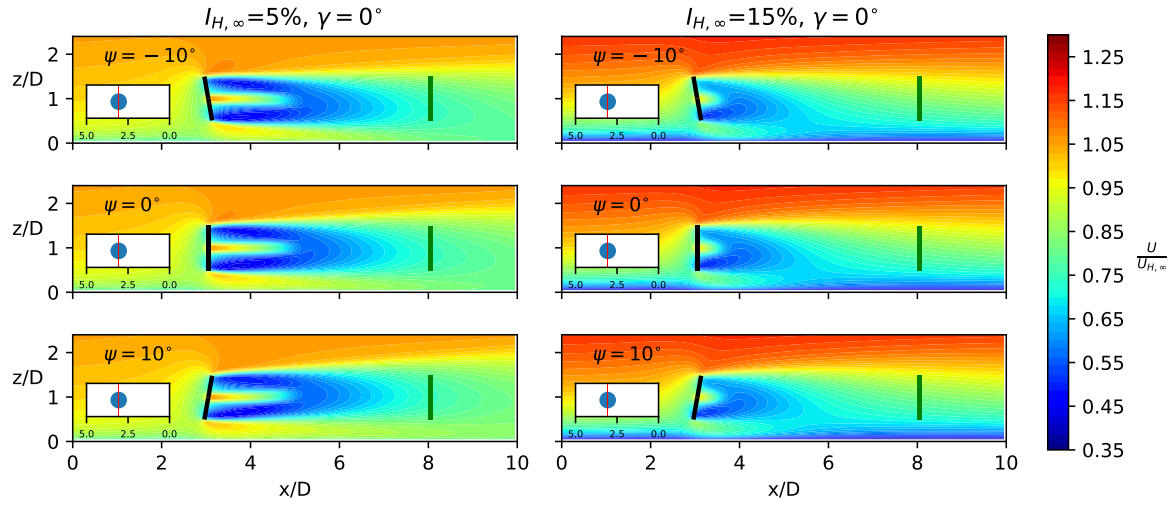

Figure 3.15: Side view of the U-field. The green disk shows where the wake recovery, as shown in Figure 3.14, is measured.

3.3 Counter-rotating

Windmills traditionally rotated counter-clockwise (CCW) as seen from an upstream position and the early wind turbines continued this convention. In 1977 **Erik Grove-Nielsen** went into the wind turbine blade business and to separate himself on the market, he decided to produce blades for clockwise (CW) operation. Among his customers were Vestas, Nordtank, Bonus and Enercon, and these companies would eventually dominate the wind turbine market, which explains why almost all large turbines today rotate CW. For some time in the 80's, it was however common to see both CCW and CW turbines in the landscape, which some people disliked the aesthetics of, and at some point it became a standard requirement in the permissions for new turbines, that they should rotate CW.[21]
This chapter is a precursor to Section 4.5, where the rotors of the 4R-V29 will be operated in different combinations of CW and CCW.

3.3.1 Brief literature summary

The studies of **Smulders et. al** [7] of their small twin multi-rotor turbine also included a small study of counter-rotating rotors, where the left rotor would turn CW and the right rotor CCW. They observed the same effects as for the co-rotating case, when testing different γ and λ, but didn't quantify the C_P or wake characteristics further. Besides this study, it seems that no further investigations have been made with regards to the interaction of counter-rotating co-planar multi-rotor turbines, which motivates the study of this section and Section 4.5.

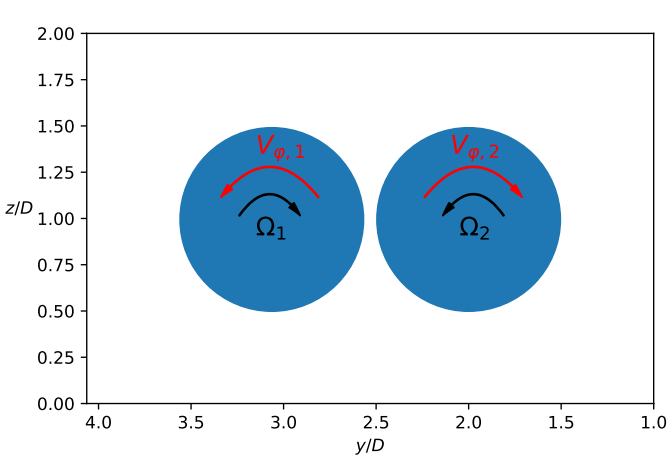

(a) Co-planar, counter-rotating.

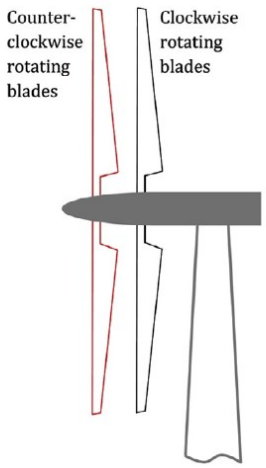

(b) Co-axial, counter-rotating [44].

Figure 3.16: Two types of multi-rotor twin turbines.

Counter-rotating co-axial wind turbines or contra-rotating wind turbines (CRWT) have however been studied by several researchers and a comprehensive review is given by **Vasel-Be-Hagh et. al** [44]. As explained by **Yuan et. al** [45], the tangential force of the first rotor will induce an azimuthal velocity in the opposite direction (the effect is called "pre-rotation" and is a direct consequence of Newtons 3rd law), which means that a co-rotating rotor situated in the wake will experience a smaller effective angle of attack. However, if the second rotor is counter-rotating the effective angle of attack will be larger and a larger lift force will be produced and hence also a larger power production. In the CRWT experiments of **Yuan et. al** [45] an increased power production is achieved with 17% for $(x_2 - x_1)/D = 0.7$, 3.7% for $(x_2 - x_1)/D = 4.8$ and <1.0% for $(x_2 - x_1)/D = 6$. A noticeable power increase is thus also observed for typical inter wind turbine spacings in a wind farm and this is confirmed with LES by **Vasel-Be-Hagh et. al** [44] of the Lillegrund wind farm with alternating CW and CCW turbines, which resulted in an increase of the mean power production of 1.4% compared to a CW-only wind farm.

[21] https://ing.dk/artikel/ugens-ekspertsporgsmal-hvorfor-drejer-vindmoller-altid-med-uret-108378

3.3.2 CCW-rotating V29

The rotational direction of an AD can be set in PyEllipSys with the `set_ad_rot_dir()`-method and the purpose of this section is to ensure that the behaviour of the CCW-rotating V29 and its wake is as expected. For $\gamma = 0°$ and $\psi = 0°$ the power production and U should stay constant for CW and CCW, while V and W should be mirrored. Rotor 1 is again the test subject with $U_{H,\infty} = 7$ m/s and settings as described in Table 3.1-3.2. Only $I_{H,\infty} = 5\%$ is used in this section.

P_{CCW}/P_{CW}	T_{CCW}/T_{CW}
1.00000263	1.00000120

Table 3.4: Power and thrust for the V29 turbine in CW- and CCW-operation with all other settings equal.

The power and thrust are as expected almost identical with a relative difference of less than 0.0003%, which is related to the chosen convergence criteria. Figure 3.17-3.23 show contour plots of U, V, W and V_φ, and the following is observed:

- **U-field:** Figure 3.17 shows two almost identical plots as expected. This is also apparent in Figure 3.18, where a small downward wake deflection can be noticed. This occurs because the top part of the wake recovers faster than the bottom, since it is surrounded by flow with higher velocity.
- **V-field:** V is mainly induced at the top and bottom of the rotor, so only the effect of flow expansion at hub height is seen in Figure 3.19. In the vertical plots in Figure 3.20 the distribution of V is approximately mirrored around $z = z_1$, when comparing the CW and CCW disks. The V-deficit (blue shaded areas) or speed-up (red shaded areas) at the three different downstream position $(x - x_1)/D = \{1, 3, 5\}$ appears to rotate in the same direction as the disk, which seems to contradict that the wake should rotate in the opposite direction (Newtons 3rd law). The explanation is that V is transformed into W and vice versa in the rotational motion of the wake, which solves the contradiction and illuminates the interesting fact that the single velocity components appear to rotate with the disk.
- **W-field:** W is mainly induced at the left and right side of the rotor and is hence clearly visible at hub height in Figure 3.21, where the distribution of W is approximately mirrored around $y = y_1$, when comparing the CW and CCW disks. The W-deficit (blue shaded areas) and speed-up (red shaded areas) decreases downstream and rotates with the disk, which is due to the same transformation of W to V as also explained previously.
- **V_φ-field:** An azimuthal velocity composed of V and W can be defined with the origin at the center of the disk and with CW defined as the positive direction (indicated with φ^+ in Figure 3.23) and $\varphi = 0°$ at the top of the rotor, c.f. Figure 2.7:

$$\varphi(y, z) = \text{atan2}\left(\frac{y_1 - y}{z - z_1}\right) \tag{3.9}$$

$$V_\varphi(y, z) = -V\cos(\varphi(y, z)) - W\sin(\varphi(y, z)) \tag{3.10}$$

  Figure 3.23 clearly visualizes the rotation of the wake, which is in the opposite direction of the disk's rotation as expected from Newtons 3rd law. The wake rotation decreases fast downstream with approximately $V_\varphi((x - x_1)/D = \{1, 3, 5\}) \approx \{0.7, 0.2, 0.1\}$ m/s, while the radial position of the maximum V_φ increases downstream, which is probably caused by the flow expansion.

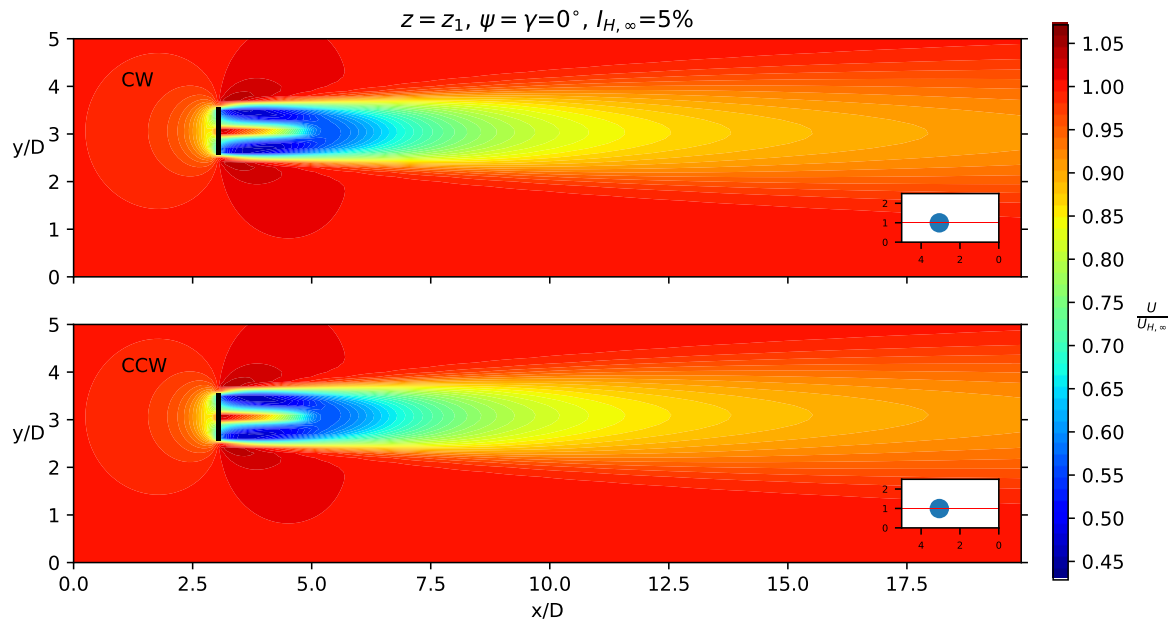

Figure 3.17: Top-view of U at $z = z_1$.

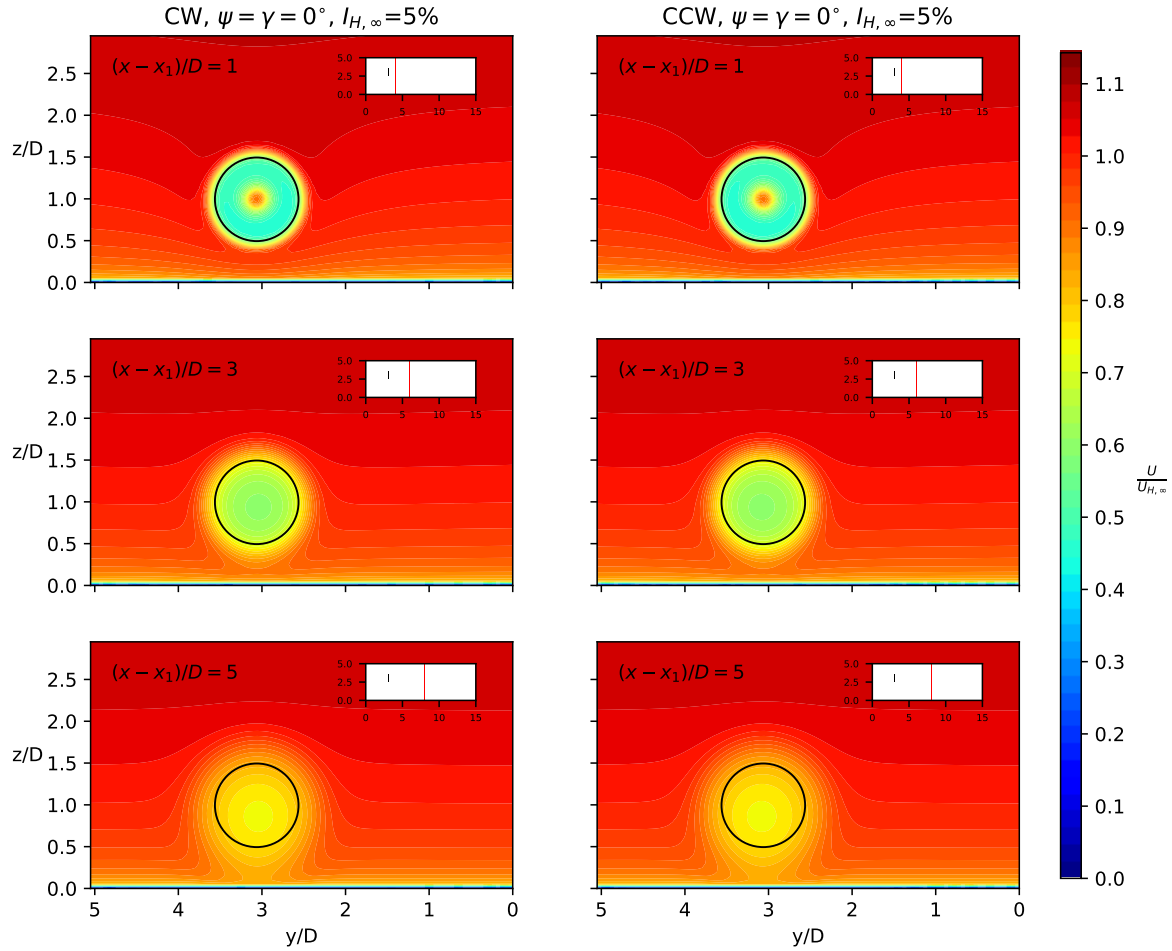

Figure 3.18: Upstream-view of U at $(x - x_1)/D = \{1, 3, 5\}$.

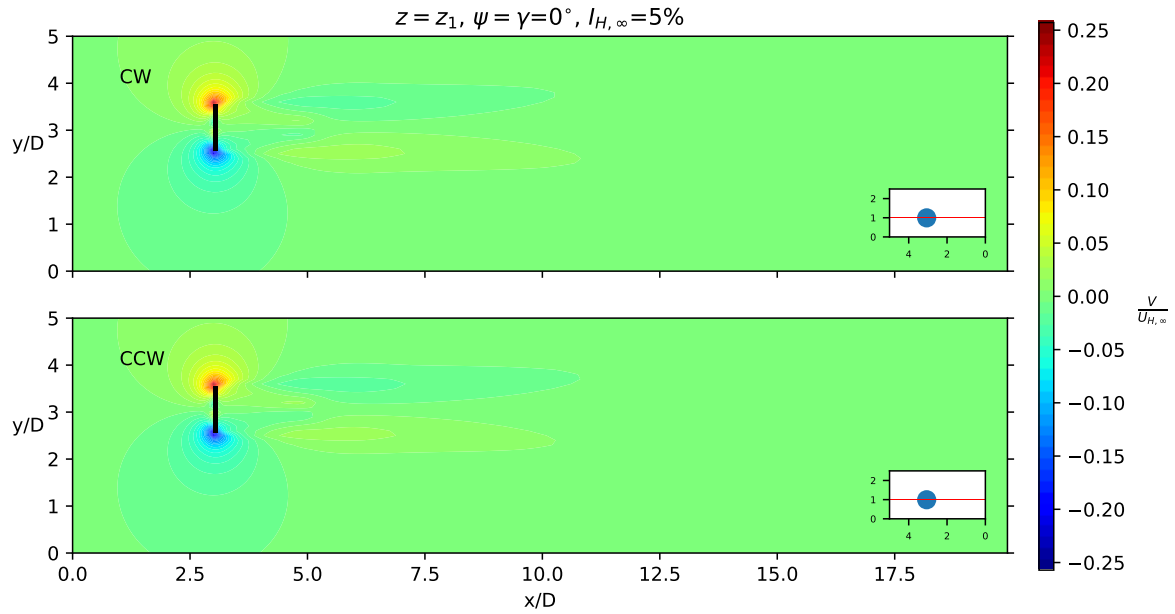

Figure 3.19: Top-view of V at $z = z_1$.

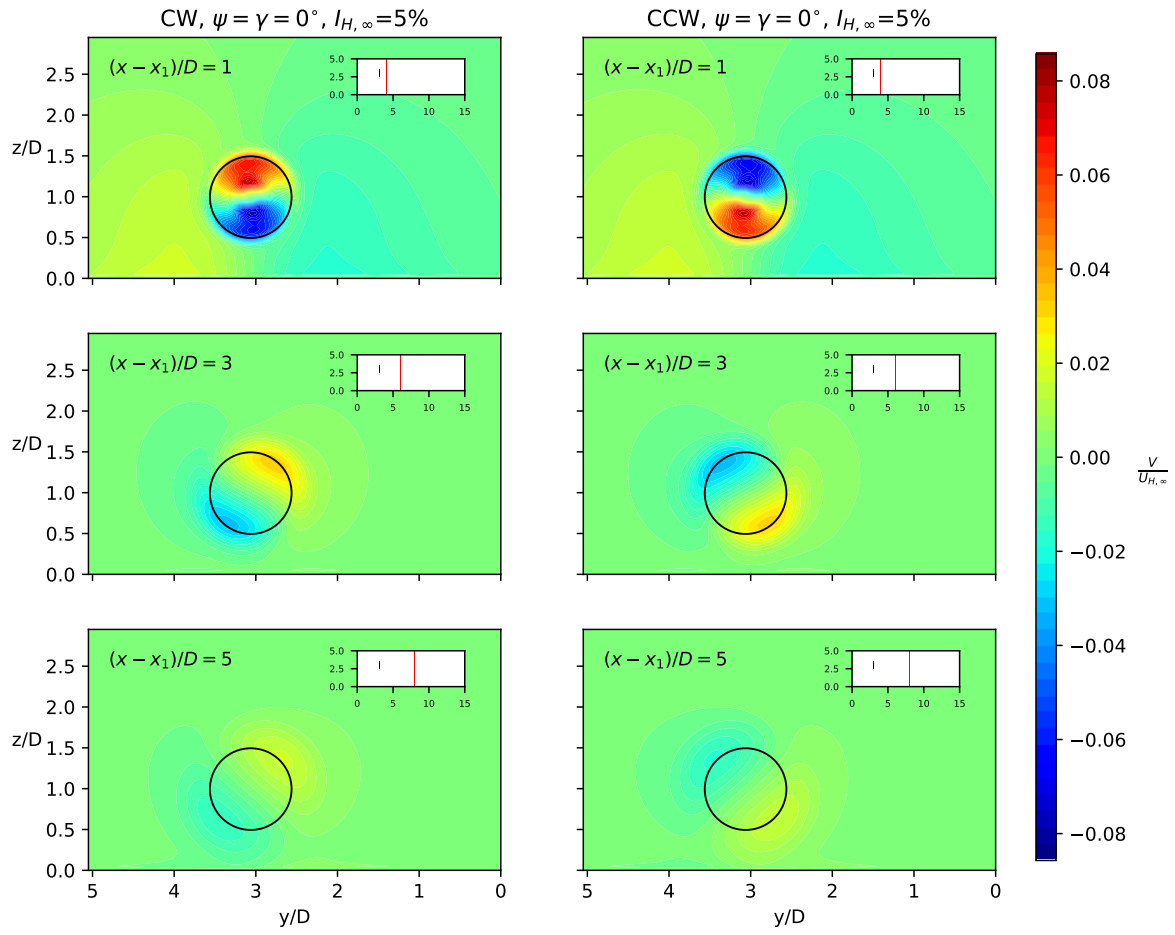

Figure 3.20: Upstream-view of V at $(x - x_1)/D = \{1, 3, 5\}$.

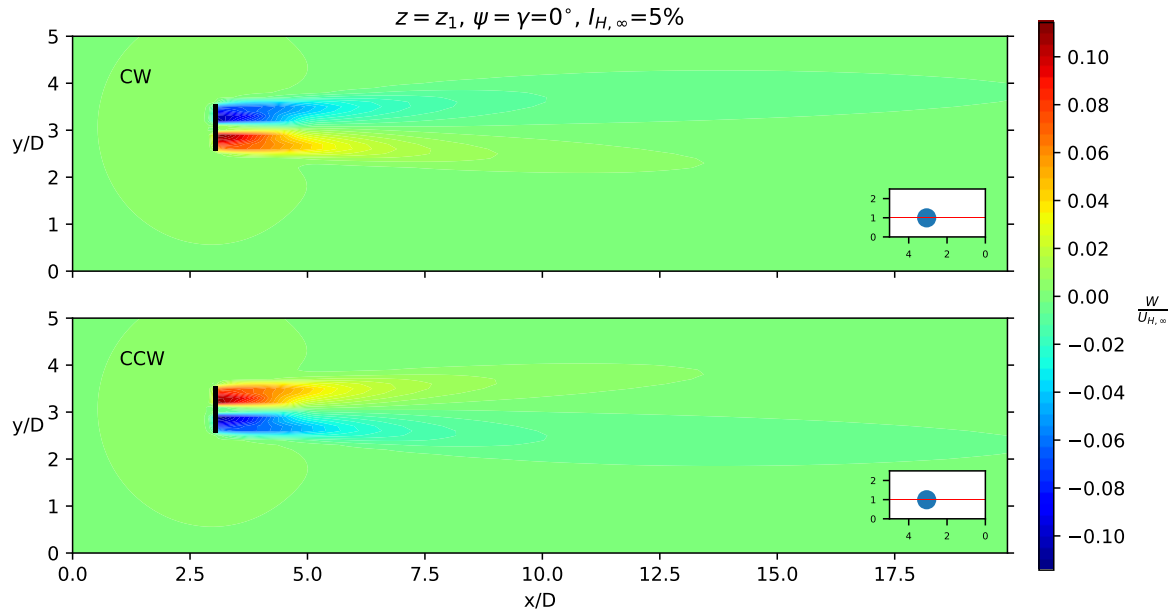

Figure 3.21: Top-view of W at $z = z_1$.

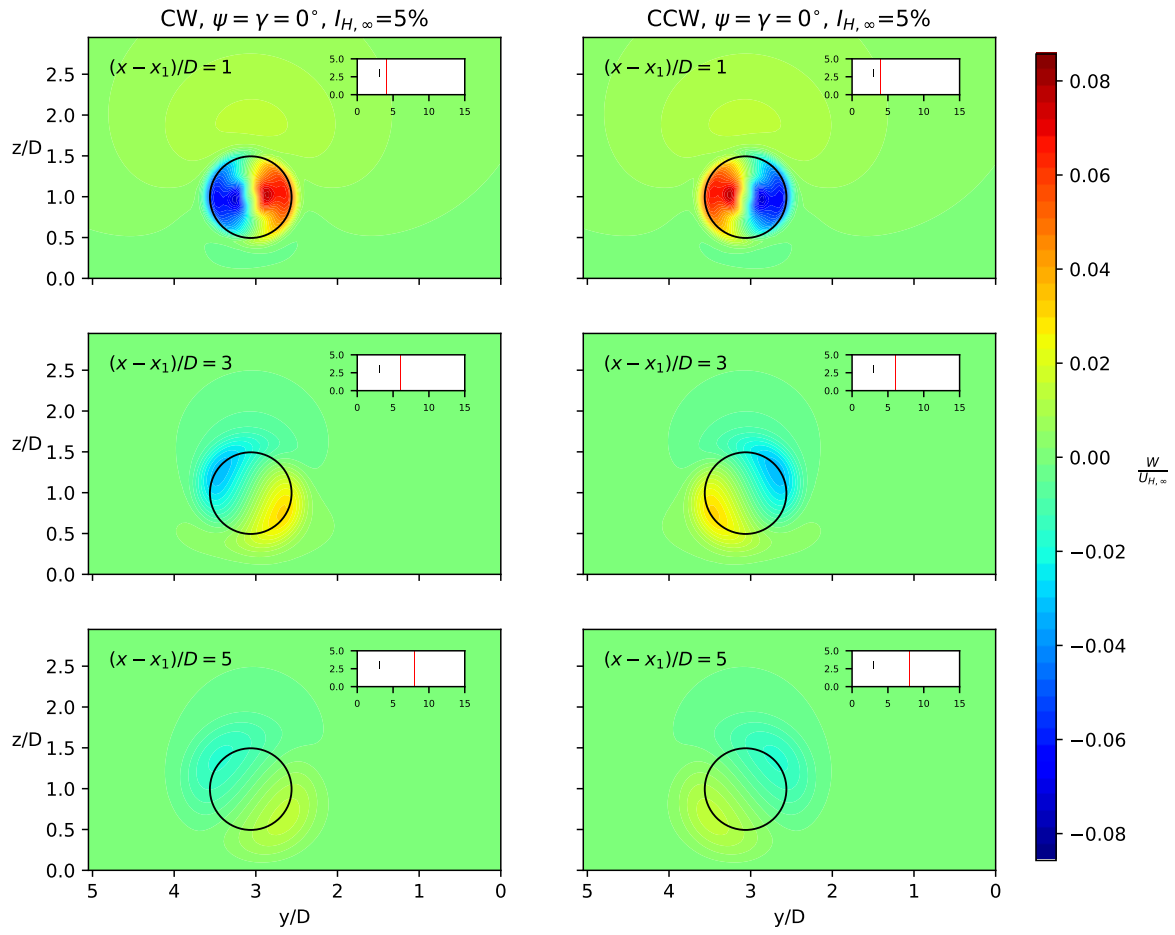

Figure 3.22: Upstream-view of W at $(x - x_1)/D = \{1, 3, 5\}$.

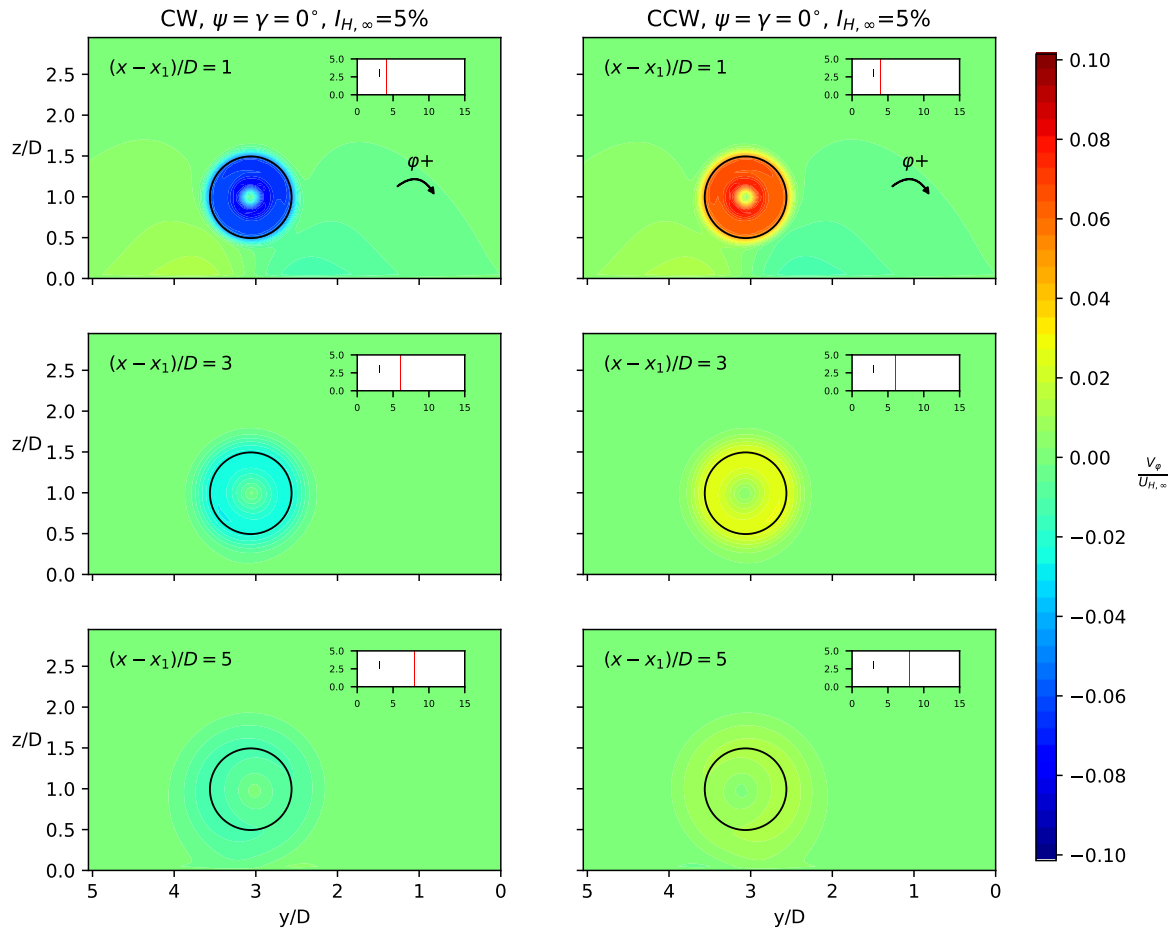

Figure 3.23: Upstream view of V_φ at $(x - x_1)/D = \{1, 3, 5\}$. Positive direction is indicated with the curved arrow, c.f. Figure 2.3.

3.4 Pitch-rpm optimization

A modern Variable Speed Pitch Regulated (VSPR) wind turbine is operated differently depending on the available wind and for a moderate wind speed of $U_{H,\infty} = 7$ m/s the turbine would operate in a "optimal C_P tracking mode". Using the Buckingham-Pi theorem on C_P:

$$C_P = \frac{P(\rho, \mu, U_{H,\infty}, R, \Omega, \theta_p)}{\frac{1}{2}\rho U_{H,\infty}^3 \pi R^2} = f(Re, \lambda, \theta_p) \approx f(\lambda, \theta_p) \tag{3.11}$$

Uniform inflow (corresponding to $I_{H,\infty} \to 0$ in a log-law inflow profile), zero tilt/yaw and Reynolds number independence is assumed in this derivation, which shows that λ and θ_p are the main parameters to be controlled. In reality these are adjusted dynamically in an advanced control system based on the torque and rotational speed of the rotor, but in the simulations of this thesis they are adjusted as described in Section 2.1.2 using the values of Figure 3.3. As discussed in Section 3.1 these values might not be the optimal settings in a sheared inflow and Python's COBYLA optimizer[22] has been coupled to EllipSys3D through PyEllipSys to investigate this. The cost function to be minimized by the optimizer is $J(\theta, \Omega) = -P(\theta, \Omega)$ subject to the constraints $0 \leq \Omega \leq \Omega_{max}$ and $P \leq P_{rated}$.

The optimal pitch and rpm settings could be found using a 2D parametric study, but as the design variable space increases, the number of evalutions needed increases exponentially, e.g. if 5 settings of each design variable are tested, then $N_{eval} = 5^{N_{design}}$. An optimizer will on the other hand use an advanced algorithm to approach the optimum in a more efficient way. The size of the optimization problem and the desired accuracy thus determines whether a parametric study or an optimizer is the most feasible option. In this section both methodologies are used as a way of validating the implementation of the COBYLA optimizer in PyEllipSys.

3.4.1 Pitch only

Rotor 1 with $\gamma = \psi = 0°$, $U_{H,\infty} = 7$ m/s and $I_{H,\infty} = 5\%$ is tested at the D/10 grid. $\Omega(U_{H,\infty}) = 34.79$ rpm is fixed according to Figure 3.3 to limit the problem to a "pitch only" 1D problem.

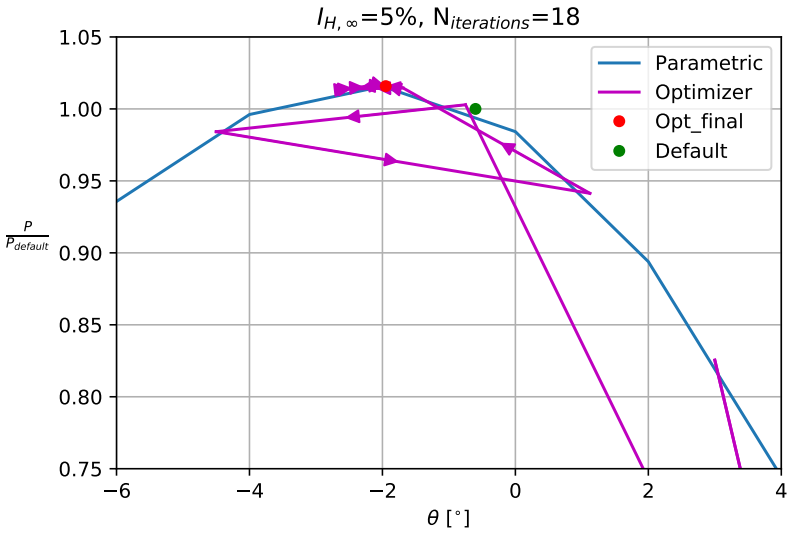

Figure 3.24: $\Omega(U_{H,\infty}) = 34.79$ rpm fixed. Comparison of 1D parametric study and optimizer. Magenta arrows indicates the "direction" of the optimizer. $P_{default} = 69.3$ kW.

Figure 3.24 shows that the COBYLA optimizer indeed reaches the maximum of the parabola-like 1D parametric curve. More importantly, the study reveal that default value of $\theta(U_{H,\infty}) = -0.6°$, indicated with

[22]The COYBYLA optimizer is a derivative-free optimization algorithm, but it is out of scope of this thesis to describe the inner mechanics of the algorithm further. Tol=5e-3 and normalized variables, e.g. P/P_{rated}, Ω/Ω_{max}, θ/θ_{max}, etc. are used. https://docs.scipy.org/doc/scipy/reference/optimize.minimize-cobyla.html

the green dot in Figure 3.24, is not the optimum in an EllipSys3D simulation. It can however not be ruled out that this might have been a deliberate choice, because there sometimes is a "buffer" on the angle-of-attack (and hence the pitch) to avoid premature stall for large gusts and due to future leading edge corrosion [46]. The pitch and rpm settings of Figure 3.3 are also tuned for noise, which could also explain why these settings are sub-optimal.
The power increase from 69.31kW (default pitch, green dot in Figure 3.24) to 70.41kW (optimized pitch, red dot in Figure 3.24) expressed in percentage is 1.59%, but both powers are considerably higher than the 63.6 kW noted in Figure 3.4 due to the D/10 grid used and the optimistic bias of AD method III (c.f. Subsection 2.1.2).

3.4.2 Pitch and rpm combined

The full 2D problem of optimal pitch and rpm is now considered and both $I_{H,\infty} = 5\%$ and $I_{H,\infty} = 15\%$ are tested.

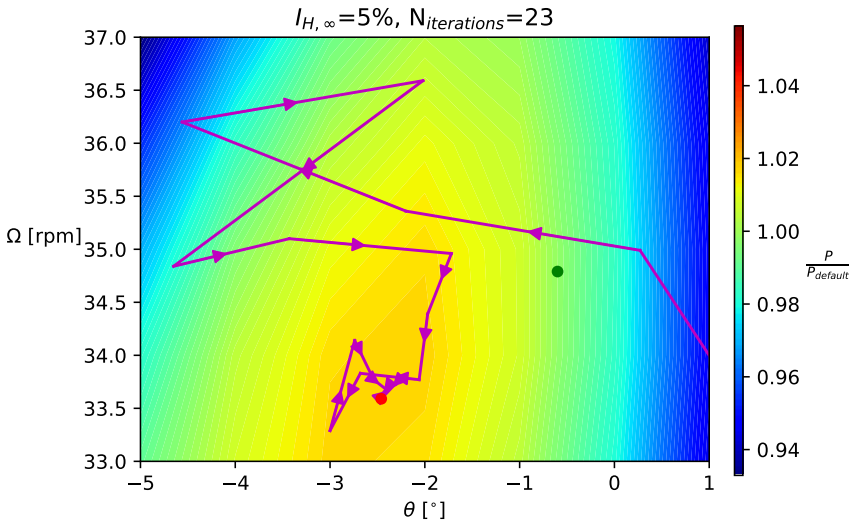

Figure 3.25: Low TI. Comparison of 2D parametric study and optimizer. Magenta arrows indicates the "direction" of the optimizer. Red dot = $(\theta_{opt}, \Omega_{opt})$. Green dot = $(-0.6°, 34.79$ rpm). $P_{default} = 69.3$ kW.

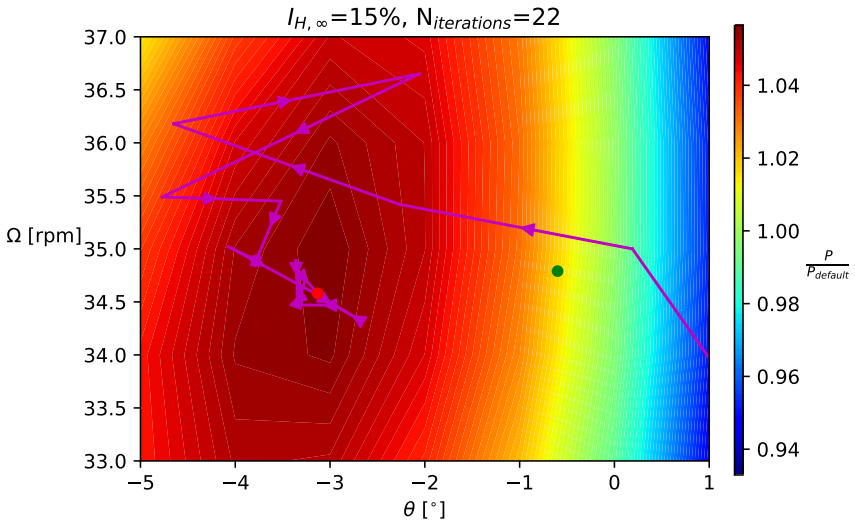

Figure 3.26: High TI. Comparison of 2D parametric study and optimizer. Magenta arrows indicates the "direction" of the optimizer. Red dot = $(\theta_{opt}, \Omega_{opt})$. Green dot = $(-0.6°, 34.79$ rpm). $P_{default} = 69.3$ kW.

The optimizer is seen in Figure 3.25-3.26 to reach the same maximum as the maximum produced by the 2D parametric study. The optimizer uses ($\theta = 0°, \Omega = 30$ rpm) as initial guess in both cases, resulting in respectively 22 and 23 evaluations to reach the final answer. This is to be compared with the 35 evaluations needed for the parametric study ($\theta = \{-5, -4, \ldots, 1\}°$ and $\Omega = \{33, 34, \ldots, 37\}$ rpm), and the optimizer hence obtains the optimal setting faster. Figure 3.27 shows the results of the optimizer applied to $U_{H,\infty} = \{4, 5, \ldots, 10\}$ m/s and $I_{H,\infty} = \{5, 15\}$%.

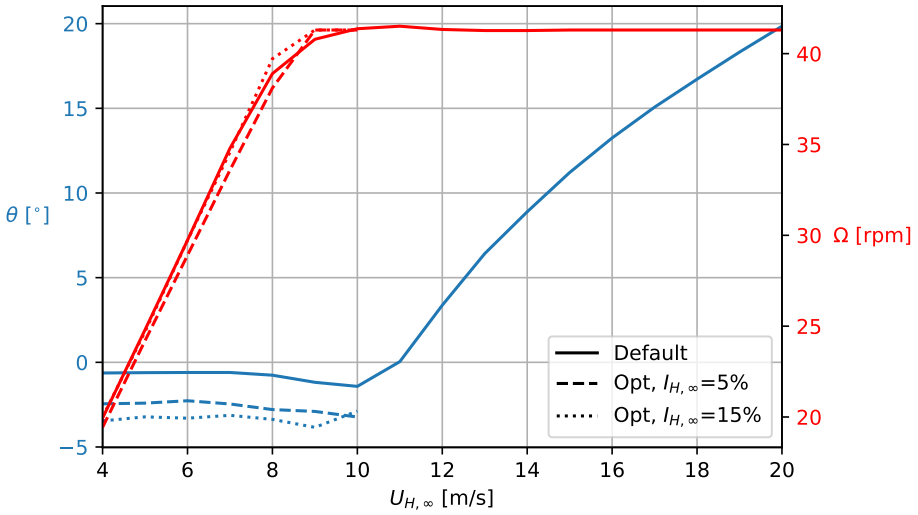

Figure 3.27: EllipSys3D optimized θ and Ω settings for $V < V_{rated}$. The default values from Figure 3.3 are shown with full lines.

	θ [°]	Ω [rpm]	$\frac{P-P_{default}}{P_{default}}$ [%]
Default, $I_{H,\infty} = 5\%$	-0.60	34.79	0.00
Optimizer, $I_{H,\infty} = 5\%$, $\Omega = 34.79$ rpm fixed	-1.95	34.79	1.59
Optimizer, $I_{H,\infty} = 5\%$	-2.46	33.59	1.77
Default, $I_{H,\infty} = 15\%$	-0.60	34.79	1.90
Optimizer, $I_{H,\infty} = 15\%$	-3.13	34.58	5.66

Table 3.5: Default vs. optimizer θ-Ω settings for $U_{H,\infty} = 7$ m/s. $P_{default} = 69.3$ kW.

The optimization results for $U_{H,\infty} = 7$ m/s is shown in Table 3.5 and the inclusion of Ω as design variable only improved the pitch optimized $I_{H,\infty} = 5\%$-case marginally, because the fixed $\Omega = 34.79$ rpm is relatively close to the optimized $\Omega = 33.59$ rpm and because the power gradient is small in this part of the design variable space.

There is a notable amount of extra power production in the $I_{H,\infty} = 15\%$-case compared to the $I_{H,\infty} = 5\%$-case (1.77% and 3.81% for the default and pitch/rpm-optimized values, respectively). It has previously been shown semi-analytical in eq.3.5-3.6 and numerically in eq.3.7 that the $I_{H,\infty} = 5\%$-case holds slightly more available power and it was further hypothesized that the default pitch and rpm setting was simply more beneficial for the $I_{H,\infty} = 15\%$-case. This hypothesis is clearly disproved by this pitch-rpm optimization study and raises the question again. The following 3 points could instead explain the difference:

1. The computational grid is stretched vertically. It is a common fact that an AD in a coarse grid produces more power, c.f. Figure 2.10, and the upper part of an AD will hence produce more power, even for uniform inflow. This effect would be more pronounced with sheared inflow, thus explaining the difference of the $I_{H,\infty} = 15\%$-case (high shear) and $I_{H,\infty} = 5\%$-case (low shear). It is however doubtful, that this effect could account for such large differences, but is listed here, since it cannot be disproved as of now.

2. More energy could be entrained into the induction zone of the $I_{H,\infty} = 15\%$-case or more power is simply produced for high $I_{H,\infty}$, because the wake flow changes, which influences the velocities at the AD and thus the forces and resulting power.

3. Complex aerodynamic effects due to the blade element methodology of AD method III.

Further studies with respectively uniform vertical grid spacing, uniform inflow and shear should be tested independently with different ambient turbulence intensities to confirm/reject these three hypotheses.

3.5 Two aligned V29 turbines

Wake recovery was investigated with normalized averaged disk velocity as the metric in Section 3.2, c.f. eq. 3.3, and the wake deflection of a yawed turbine was calculated from the flow field as well, but these metrics are only of interest in a wind farm scenario. The simplest wind farm is a wind farm with two aligned turbines like the one shown in Figure 3.28, which will be the case of this section.

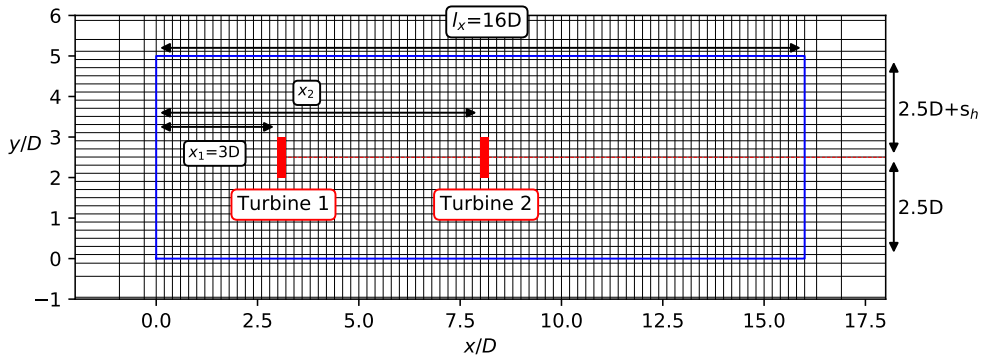

Figure 3.28: Top view of the D/20 grid (every 4th grid point is shown) with a $(x_2 - x_1)/D = 5$ configuration. Blue rectangle encloses wake region. The two turbines are marked with red and their rotor axis is marked with the dotted red line.

3.5.1 Method III-calibration

It was described in Subsection 2.1.2 that method III cannot be used on a turbine in the lee of another (turbine 2 in Figure 3.28), because $U_{H,\infty}$ is not defined for this turbine and it is hence unclear what Ω, θ and λ should be set to. An extension of this method (aka. method III-calibration) is therefore applied and more details about this method and its calibration step can be found in Appendix A. The calibration results for the low and high turbulent cases are shown in Figure 3.29, where the default pitch and rpm values have been used. The difference between the low and high TI cases is small, which is usually the case, when the same turbulence model is used, c.f. van der Laan et. al [27].

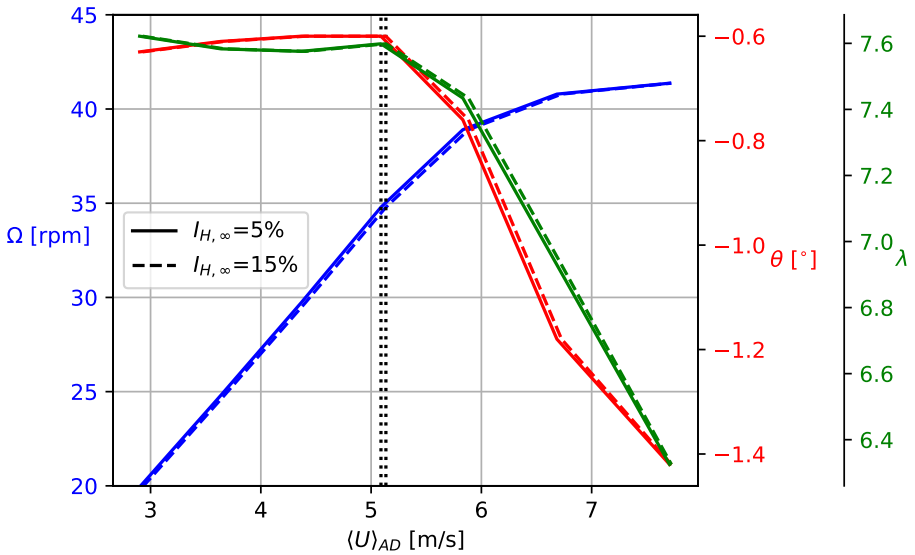

Figure 3.29: Calibration results for method III-calibration. The vertical dotted lines indicate the disk averaged velocity, $\langle U \rangle_{AD}$, for an inflow of $U_{H,\infty} = 7$ m/s and $I_{H,\infty} = \{5, 15\}\%$.

The method has been applied to the usual cases of $U_{H,\infty} = 7$ m/s, $I_{H,\infty} = \{5, 15\}\%$ and $\gamma = \psi = 0°$. Inter spacings of $(x_2 - x_1)/D = \{1, 2, \ldots, 10\}$ have been simulated and the U-field at hub height for $(x_2 - x_1)/D = 5$ is shown in Figure 3.30 as an example of the wake interaction between the turbines.

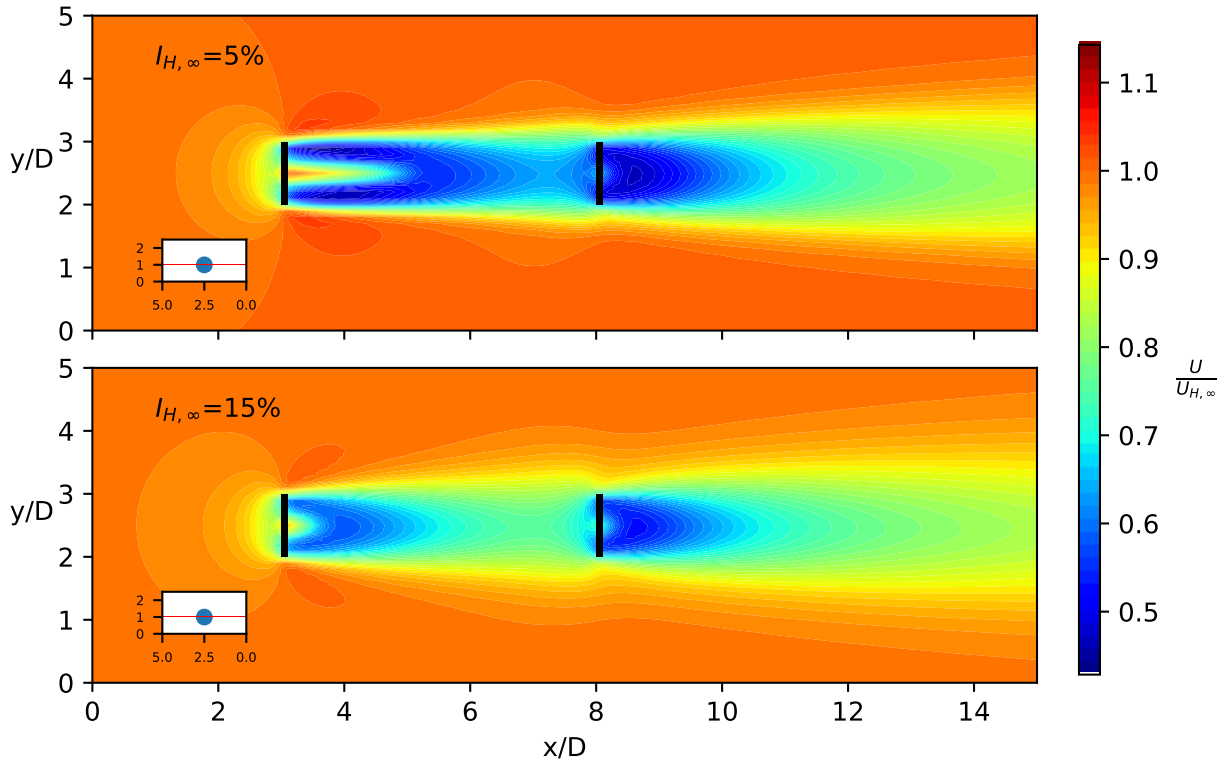

Figure 3.30: Top view of U at $z = z_H$ for the $(x_2 - x_1)/D = 5$ case.

As shown in previous sections, the wake recovers faster for the high TI case, which is also apparent in Figure 3.30 and this translates into a power increase of turbine 2 as seen by the shift of the curves in Figure 3.31. The control parameters for the different configurations are shown in Figure 3.32, which shows that the rotational speed of turbine 2, Ω_2, changes significantly, while Ω_1 and $\theta_{\{1,2\}}$ stay almost constant. This is expected for $U_{H,\infty} = 7$ m/s, which is in the optimal C_P-tracking region, c.f. Figure 3.3 and Figure 3.29.

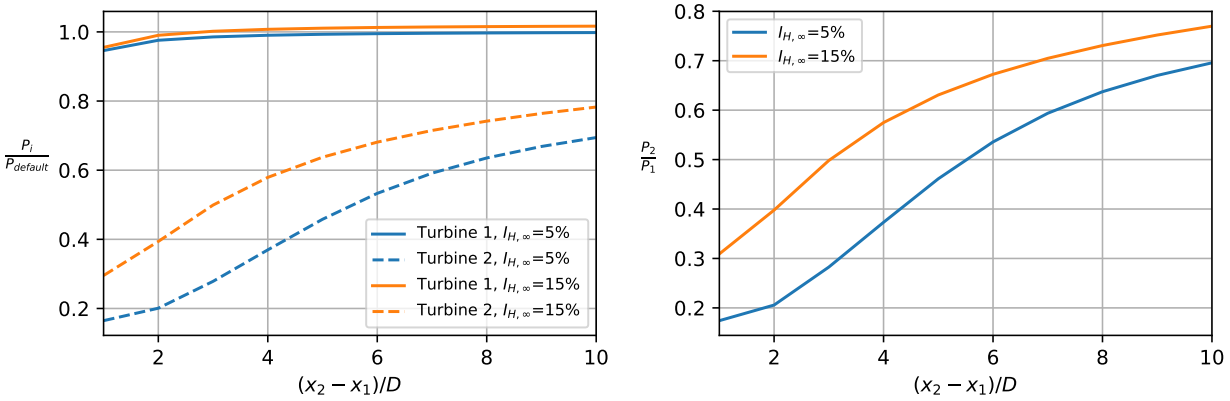

Figure 3.31: Power of the individual rotors (left plot) and relative power (right plot). $P_{default} = 69.3$ kW.

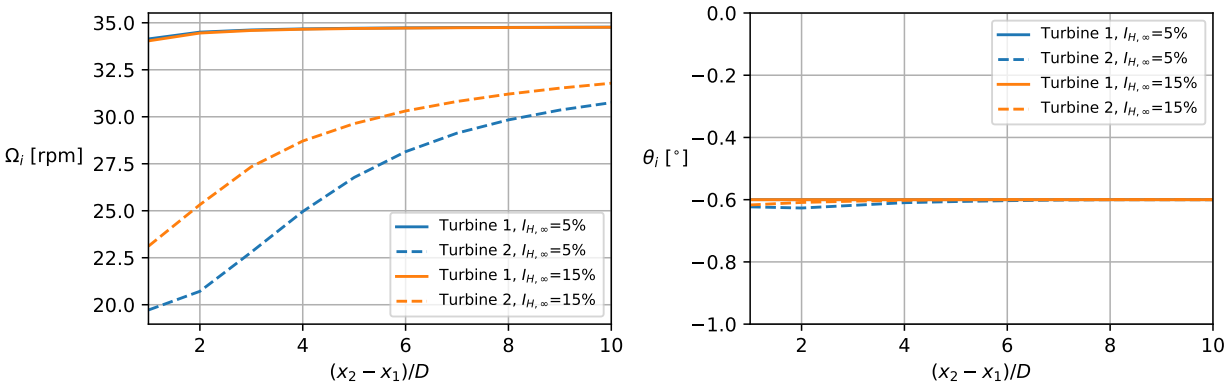

Figure 3.32: Control algorithm for varying inter spacing.

The normalized disk averaged velocity, i.e. $\frac{\int U dA}{\int U_0 dA}$, for a single turbine simulation is shown in Figure 3.6 and this is plotted against P_2 in Figure 3.33, which shows that a positive correlation exists between the two. The energy contained in the flow is related to $\frac{\int U^3 dA}{\int U_0^3 dA}$, which explains the positive curvature seen in Figure 3.33 for both the low and high TI cases.

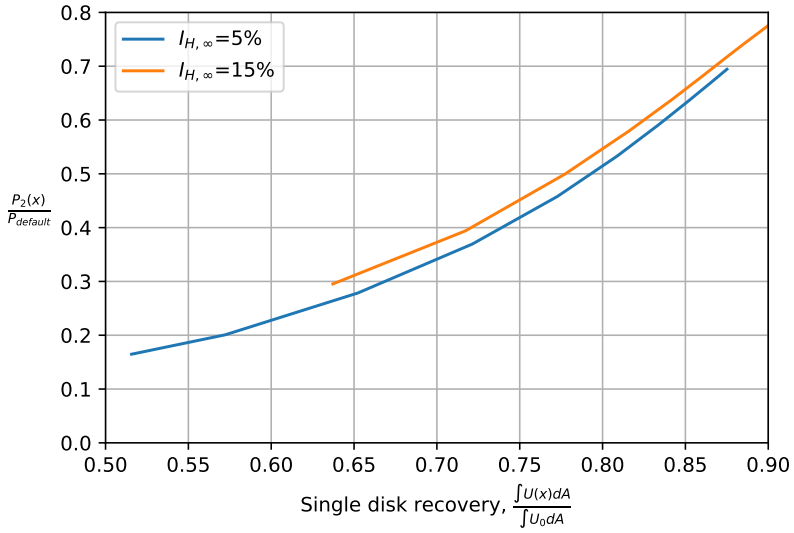

Figure 3.33: Correlation between the single turbine normalized disk averaged velocity results from Figure 3.6 and the power production of turbine 2 in the two turbine case. $P_{default} = 69.3$ kW.

As discussed in Subsection 2.4.8, method III-calibration is not applicable for tilted/yawed rotors, unless a new calibration is made for each yaw and tilt configuration (errors of the power in the order of 2-3% are seen for $\gamma \approx 30°$). This error will be accepted for now and the effect of yawing turbine 1, γ_1, is seen in Figure 3.34-3.35. The high TI case has a significantly larger total power production due to faster recovery (and also a slightly larger turbine 1 power production as discussed in Section 3.4), but it is worth noticing that the difference is smaller at larger γ_1, which is due to the larger wake deflection at lower turbulence intensities, c.f. Section 3.2. Another important point is that the total power production is largest at $\gamma_1 = 0°$, which means that a wake deflection control strategy would be redundant for this configuration at both low and high TI. For other wind farm configurations, wake deflection control might be advantageous and one also has to bear in mind that the RANS simulations in this thesis generally seem predict slightly smaller wake deflections compared to other CFD/analytical models, c.f. Section 3.2.

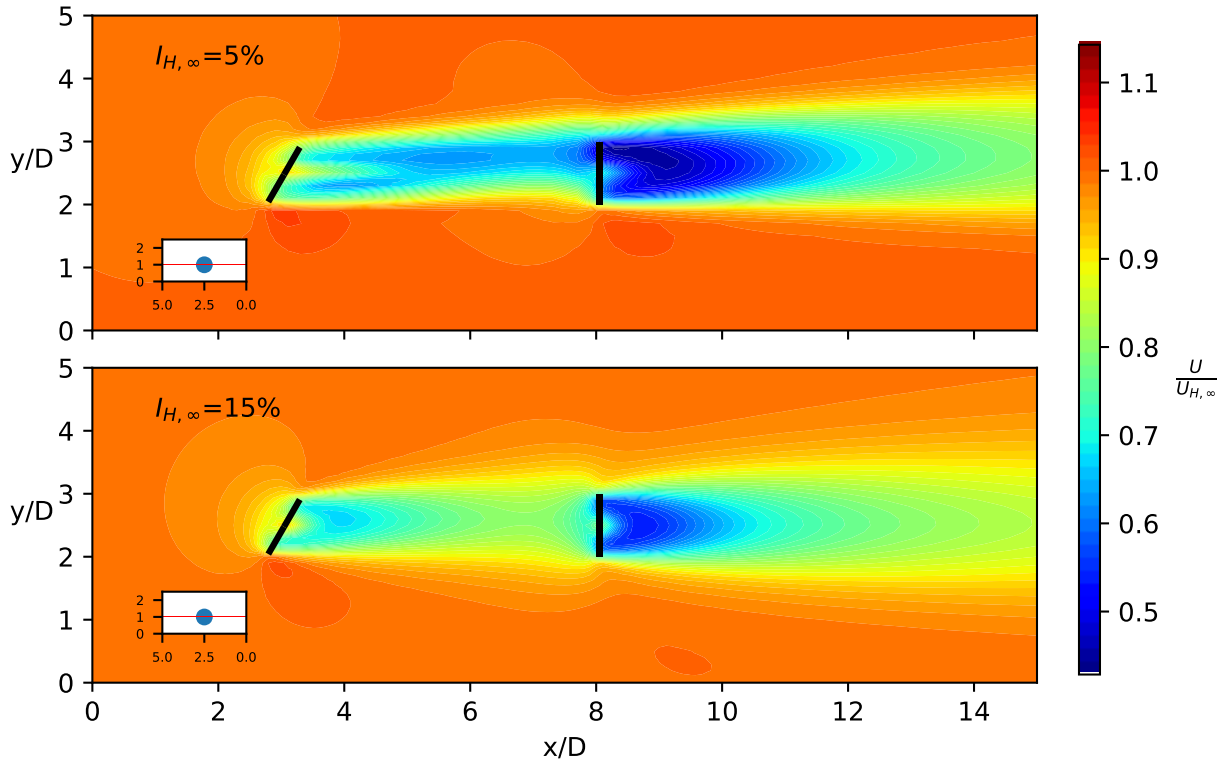

Figure 3.34: Top view of U at $z = z_H$ for the $(x_2 - x_1)/D = 5$ case with $\gamma_1 = 30°$.

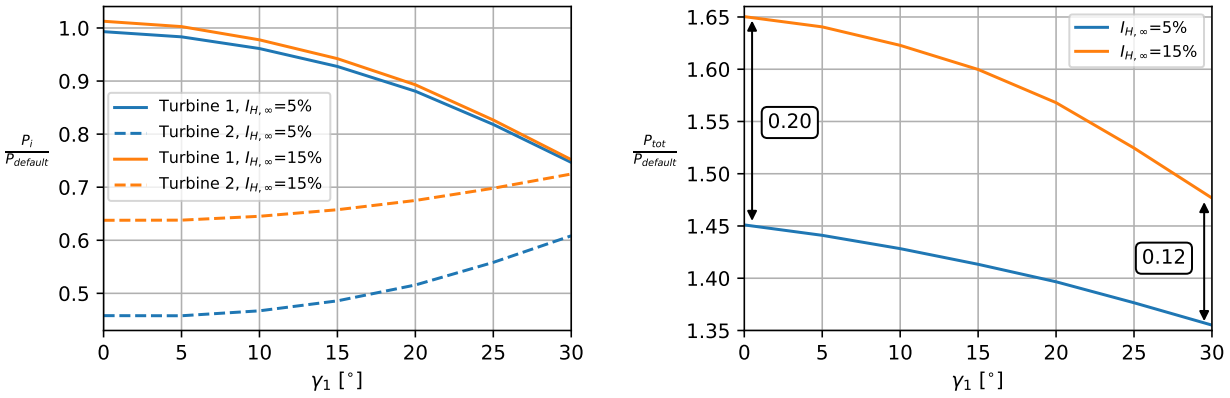

Figure 3.35: Power of individual turbines and total power for varying γ_1. $P_{default} = 69.3$ kW, $(x_2 - x_1)/D = 5$ and $\gamma_2 = 0°$.

3.5.2 Method III-optimizer for turbines with constant TSR and pitch

As explained in the previous section, it is not possible to use method III in a wind farm study, unless some control algorithm is added, e.g. the method III-calibration from the previous subsection or a $\tau - \Omega$ controller, c.f. van der Laan et. al [21]. Figure 3.29 however reveals that for low inflow speed simulations, $U_{H,\infty} \lesssim 7$ m/s, the pitch is nearly constant, $\theta \approx -0.6°$, as well as the tip speed ratio, $\lambda \approx 7.6$. Hence, the only unknown control parameter for turbine 2 is the rotational speed, Ω_2, which can be found in a 1D parametric study or using an optimizer. This method will be referred to as *method III-optimizer* and to check the validity of this approach, the $(x_2 - x_1)/D = 5$ case with $I_{H,\infty} = 5\%$ is tested and compared to the results of method III-calibration. The three test cases of Table 3.6 are tested:

	θ_1 [°]	θ_2 [°]	Ω_1 [rpm]	Ω_2 [rpm]	λ_1	λ_2
Case 1	-0.6	-0.6	34.79	Optimized	7.6	7.6
Case 2	-0.6	-0.6	Optimized	Optimized	$\frac{2\pi\Omega_1 R}{60U_{H,\infty}}$	7.6
Case 3	$\theta_1(\gamma)$	-0.6	$\Omega_1(\gamma)$	Optimized	$\frac{2\pi\Omega_1(\gamma)R}{60U_{H,\infty}\cos(\gamma)}$	7.6

Table 3.6: Test cases for the method III-optimizer studies of the $(x_2 - x_1)/D = 5$ configuration. Inflow upstream of turbine 1: $U_{H,\infty} = 7$ m/s and $I_{H,\infty} = 5\%$.

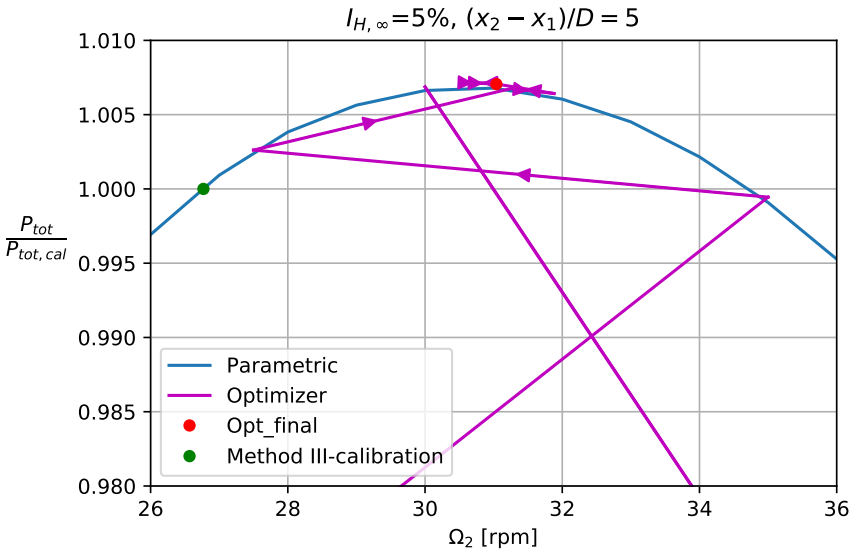

Figure 3.36: Case 1: Optimized turbine 2 control. Green dot $= (\Omega_2, P_{tot})_{method\ III-calibration} =$ (26.8 rpm, 101.6 kW).

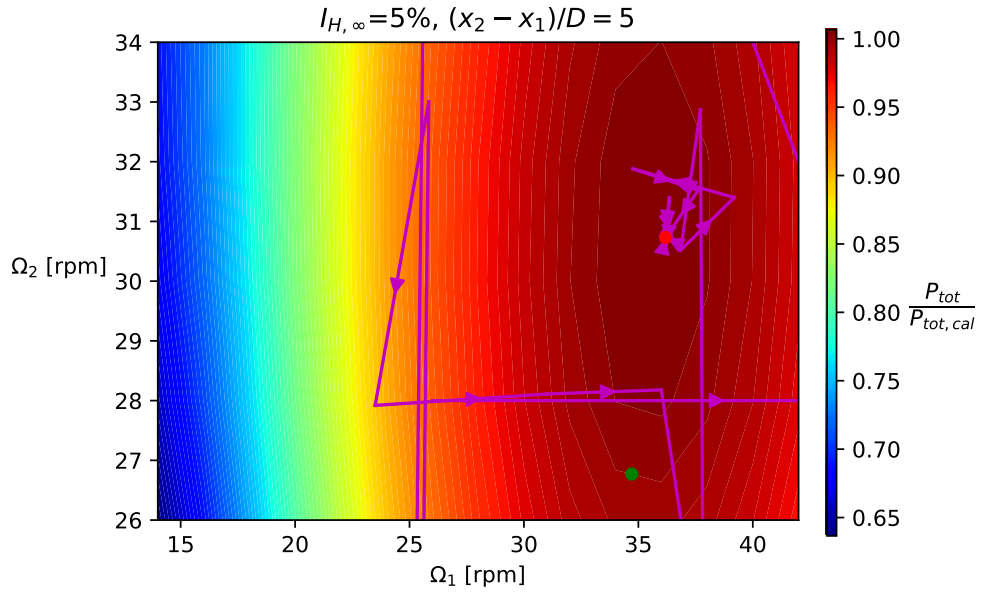

Figure 3.37: Case 2: Optimized turbine 1 and 2 control. Green dot $= (\Omega_1, \Omega_2)_{method\ III-calibration} =$ (34.7 rpm, 26.8 rpm).

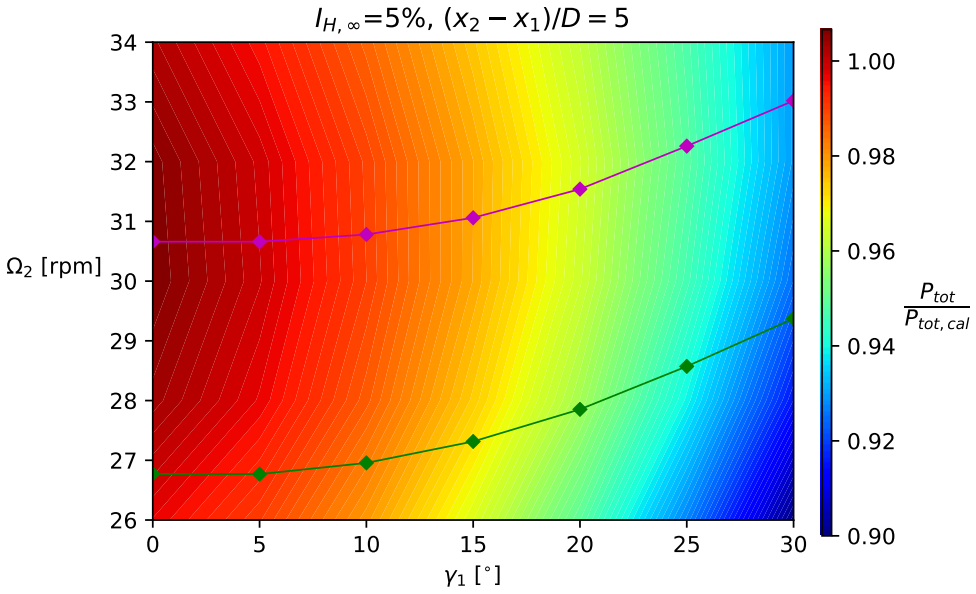

Figure 3.38: Case 3: Optimized turbine 2 control for varying γ_1. Green dots = $(\gamma_1, \Omega_2)_{method\ III-calibration}$. Magenta dots = optimal setting for the given γ_1. $P_{tot,cal}(\gamma = 0°) = 101.6$ kW.

- **Case 1:** The optimizer and 1D parametric study find that $\Omega_2 \approx 31$ rpm is the optimal setting of turbine 2, which is significantly larger than $\Omega_2 \approx 27$ rpm as predicted by the variable scaling control algorithm, although the difference in total power is only $< 1\%$. It was at first believed that this was caused by the calibration being based on the default values for pitch and rpm, but the same trend is seen for a calibration based on optimized pitch and rpm, c.f. Appendix C. It could instead be caused by the fact that the induction zone of a turbine in a wake is different from that of a single freestanding turbine (as used in the calibration procedure for method III-calibration), so that turbines with equal $\langle U \rangle_{AD}$ have different optima. One could also very well argue, that the assumption of constant $\lambda_2 = 7.6$ is questionable, because varying Ω_2 then implies varying inflow speeds. It is nevertheless interesting, that this method can simulate the flow without the need of a calibration step and obtain a result $< 1\%$ from that of method III-calibration.

- **Case 2:** This case shows the same trend as case 1, i.e. the power production increases slightly for larger Ω_2, while the optimal Ω_1 is close to the default value of $\Omega_1 \approx 35$. One could imagine a situation with turbine 1 deregulated (by lowering Ω_1) to increase the production of turbine 2 and hence increase the total production, but Figure 3.37 clearly shows that this is not the case for this particular configuration. The optimal control is instead to let each turbine produce as much as possible, which is also known as "greedy" control. In real wind farms, fatigue, maintenance, etc. will also play into the optimal farm control strategy, and such advanced considerations are interesting, but out of scope for this thesis.

- **Case 3:** Yet again, turbine 2 can advantageously be operated at larger Ω_2. The optimal Ω_2 is seen to increase with increasing γ_1, which is not surprising since turbine 2 experiences larger velocities, when the wake is deflected. Figure 3.39 supports this claim for $\gamma_1 < 25°$, but method III-calibration is supposedly superior at larger yaw angles. This comes from the overprediction of power of method III-calibration at large yaw angles, which was also discussed in the previous subsection and in Subsection 2.4.8. This can also be seen in left plot of Figure 3.40.

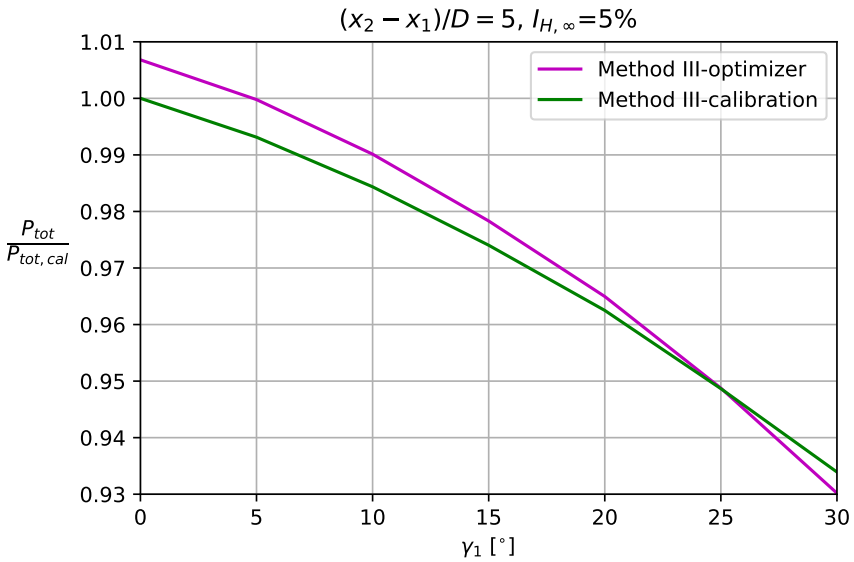

Figure 3.39: Magenta line = power produced by optimal Ω_2-control as documented by the magenta dots in Figure 3.38. Green line = reproduction of results from Figure 3.35. $P_{tot,cal}(\gamma = 0°) = 101.6$ kW.

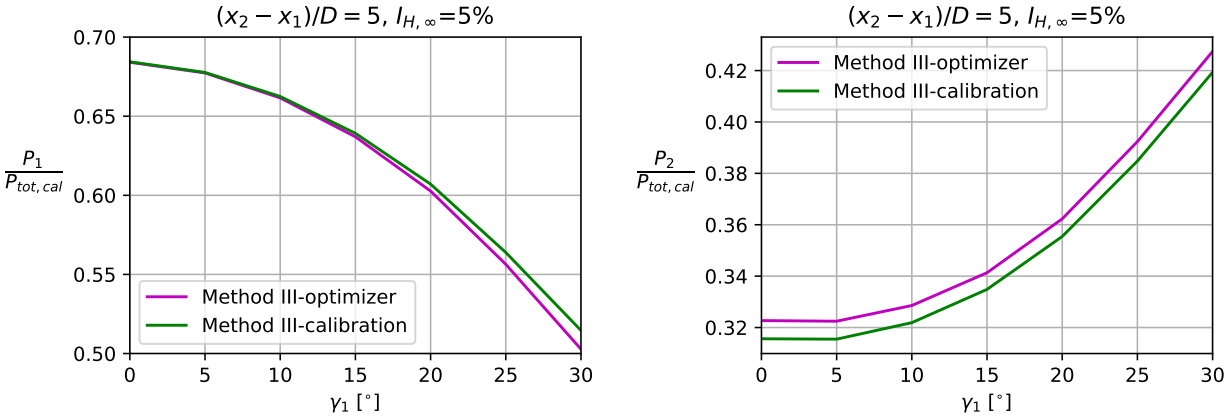

Figure 3.40: Contribution of turbine 1 and 2 to the total power production of Figure 3.39. $P_{tot,cal}(\gamma = 0°) = 101.6$ kW.

Chapter 4

Multi-rotor turbine studies

This chapter first investigates a double-rotor turbine and later the full 4R-V29 multi-rotor turbine. The structure is as follows:

- **Section 4.1:** Presents the 4R-V29 multi-rotor turbine and the computational setup.
- **Section 4.2:** The effect of tip clearance for a double-rotor turbine is investigated.
- **Section 4.3:** The double-rotor turbine is simulated with a range of different tilt and yaw configurations.
- **Section 4.4:** Power production and wake recovery of the 4R-V29 is investigated for different toe-out and tilt-out combinations as well as yaw of the support structures.
- **Section 4.5:** The 16 different combinations of CW- and CCW-rotating disks of the 4R-V29 are investigated.
- **Section 4.6:** The pitch and rpm settings of all four rotors are optimized simultaneously.
- **Section 4.7:** A downstream multi-rotor turbine is added and the total power production is investigated with regards to calibration method, inter spacing and de-regulation of turbine 1.

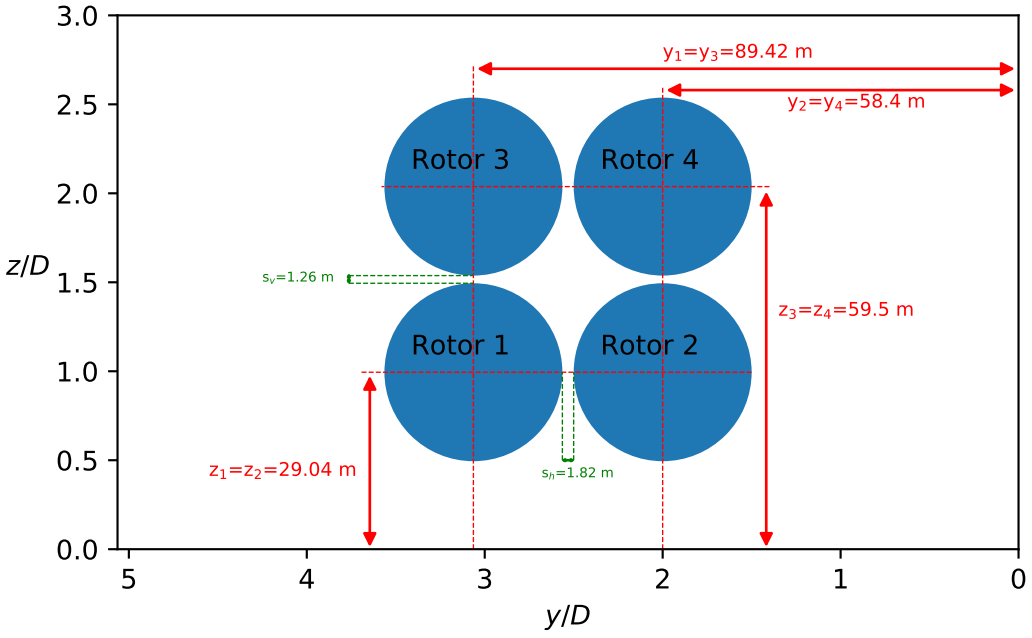

Figure 4.1: Upstream view of the 4R-V29 with $\gamma_{\{1,2,3,4\}} = \psi_{\{1,2,3,4\}} = 0°$. For top and side view, c.f. Figure 2.1-2.2.

4.1 The 4R-V29 turbine

The backsground and motivation of the Vestas 4R-V29 multi-rotor turbine is described in Section 1.2 and this section instead presents the technical definitions and computational setup.

Each of the rotors has the properties described in Table 3.1 and default control settings of Figure 3.3. When rotor 1 and 3 are yawed together, $\gamma_{\{1,3\}}$ and rotor 2 and 4 also yaw together with $\gamma_{\{2,4\}} = -\gamma_{\{1,3\}}$, the turbine is defined to have a positive *toe-out* (i.e. the yaw of rotor 1 determines the positive convention of toe-out). The *tilt-out* is defined simarly, but where the bottom rotors tilt together and top rotors together with $\psi_{\{3,4\}} = -\psi_{\{1,2\}}$ (the tilt of rotor 1 determines the positive convention of tilt-out).

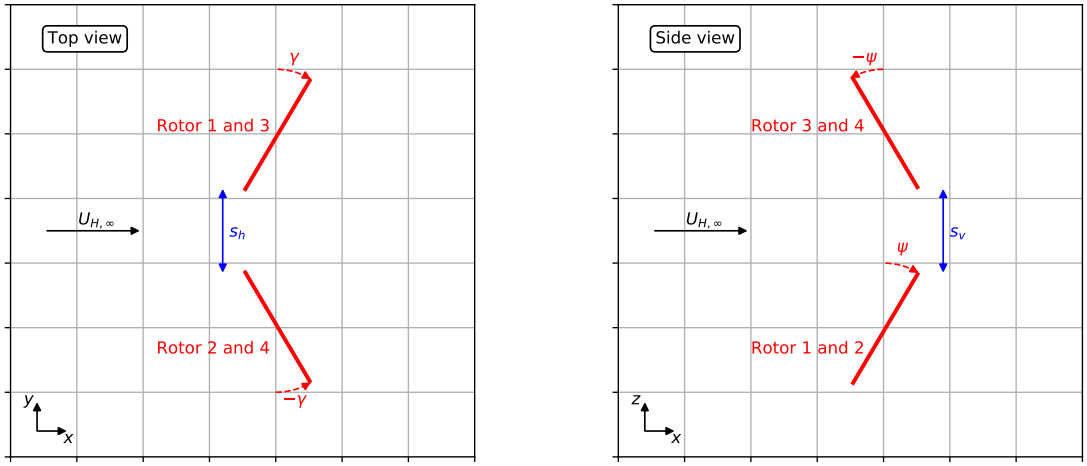

(a) Example of positive toe-out.

(b) Example of positive tilt-out.

Figure 4.2: Definition of tip clearance, and convention of positive toe- and tilt-out.

As can be seen in Figure 4.2, there is a tip clearance between both the horizontal and vertical rotors, which depends on the toe-out and tilt-out, respectively:

$$s_h = y_1 - y_2 - D + 2\left(1 - \cos(\gamma_{\{1,3\}})\right) R \tag{4.1}$$

$$s_v = z_3 - z_1 - D + 2\left(1 - \cos(\psi_{\{1,2\}})\right) R \tag{4.2}$$

The hub height of the 4R-V29 is set to the center of the four disks, which is where $U_{H,\infty}$ and $I_{H,\infty}$ are fixed:

$$z_H = \frac{z_3 + z_1}{2} \tag{4.3}$$

$\gamma_{\{1,2,3,4\}}$	0°
$\psi_{\{1,2,3,4\}}$	0°
s_h	1.82 m
s_v	1.26 m
z_H	$(z_1 + z_3)/2 = 44.27$ m
$U_{H,\infty}$	7 m/s
$I_{H,\infty}$	{5, 15} %
Computational grid	D/20
AD grid	$N_\varphi = 64$, $N_r = 64$

Table 4.1: Default setting of 4R-V29 and computational input parameters.

The parameters of Table 4.1 are used in this chapter unless otherwise is stated. A neutral ABL with $I_{H,\infty}$ and $U_{H,\infty}$ is set as described in Section 1.5 and the methods described in Chapter 2 are implemented in EllipSys3D, which is executed from the PyEllipSys interface.

4.2 2R-V29 tip clearance

The research on wind turbine wakes in wind farms has naturally been mostly focused on the direct "shadowing" effect, i.e. the impingement of the wake onto the next turbine. There exists however also a considerable lateral or side-side interaction between the turbines caused by local blockage effects. This lateral interaction is less intuitive and has less effect compared to the direct shadowing effect in a traditional wind farm, but is very relevant for multi-rotor turbines.

4.2.1 Brief literature summary

The early experiments of **Smulders et. al** [7] (c.f. Figure 1.9) showed a power increase of their twin-rotor compared to the operation of two single turbines, indicating a beneficial lateral rotor interaction.
Lateral rotor interaction and blockage effects has in recent years gained attention in connection with research of tidal wave turbines and **Nishino et. al** [47] transferred some of this knowledge to wind turbines. Using RANS-AD (with an optimal C_T AD method), configurations with respectively 1, 3, 5, 7, 9 and ∞ horizontal rotors were tested in both uniform and sheared inflow resulting in an increase of C_P up to 5% for both cases. A tip clearance of $s_h = 0.5D$ was used for all simulations.
Experimental measurements of a horizontal 3 rotor configuration with $s_h = \{1D, 0.5D\}$ conducted by **McTavish et. al** [48] showed an average power increase of respectively 2-3% and 5-7%. The experimental setup had a global blockage ratio of 5% and only $\mathrm{Re}_{tip} = V_{tip}c_{tip}/\nu = 38,000$, which could be of concern when transferring the results to a real multi-rotor (the V29 turbine with $V_{tip} = R\Omega_{max}$ and $c_{tip} = c(r/R = 0.97) = 0.8$ m has $\mathrm{Re}_{tip} \approx 2.7 \cdot 10^6$), although a vortex method code with $\mathrm{Re}_{tip} \approx 0.38 \cdot 10^6$ approximately confirmed the results.
The effect of blockage on 5 aligned wind turbines with $s_h = 2D$ was studied by **Forsting and Troldborg** [49] using RANS-AD method III (the same as used in this thesis), which concluded that a D/32 grid and global blockage ratio below 0.165% was sufficient to obtain reliable results. A power increase of $\sim 0.5\%$ was observed.
A beneficial rotor interaction of the 4R-V29 multi-rotor turbine has been documented by **van der Laan et. al** [15] and this was mainly achieved by an increased power production of the bottom rotors, rotor 1 and 2. It was believed to be caused by the blockage effect induced by rotor 3 and 4 due to their higher thrust force in a sheared flow.

4.2.2 Horizontal 2R-V29

A double-rotor turbine consisting of rotor 1 and 2 is investigated with $z_H = z_1$. The wake domain is widened from $5D + s_h$ (c.f. Figure 2.2) to $8D$ to allow the test of $s_h = \{0D, \ldots, 4D\}$ using the rule-of-thumb that there should be at least $1D$ between the boundary of the wake domain and the tip of the blade. The $s_h = 4D$ configuration is shown in the right plot of Figure 4.3.

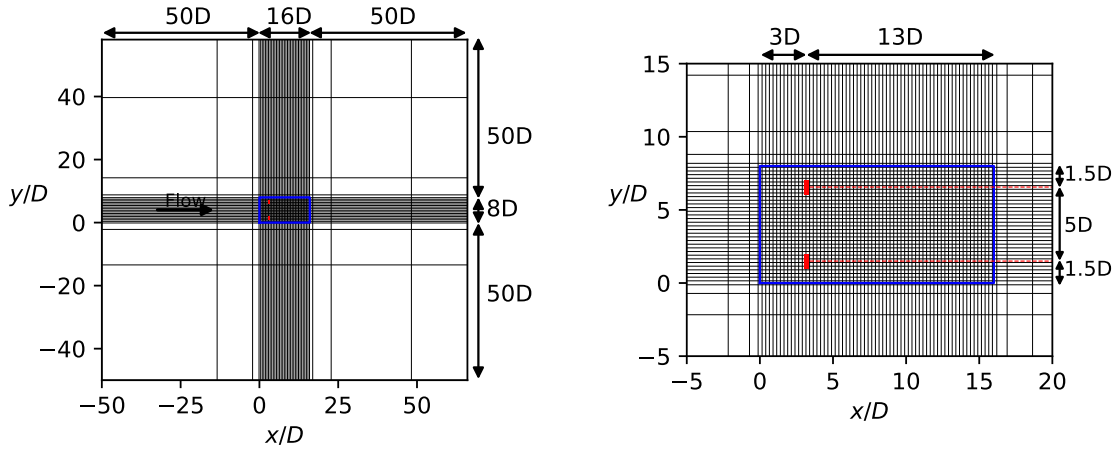

Figure 4.3: Top view of the D/20 grid used for horizontal tip clearance studies (only every 10th grid point is shown in the left plot and only every 5th in the right plot). The blue rectangle encloses the wake domain.

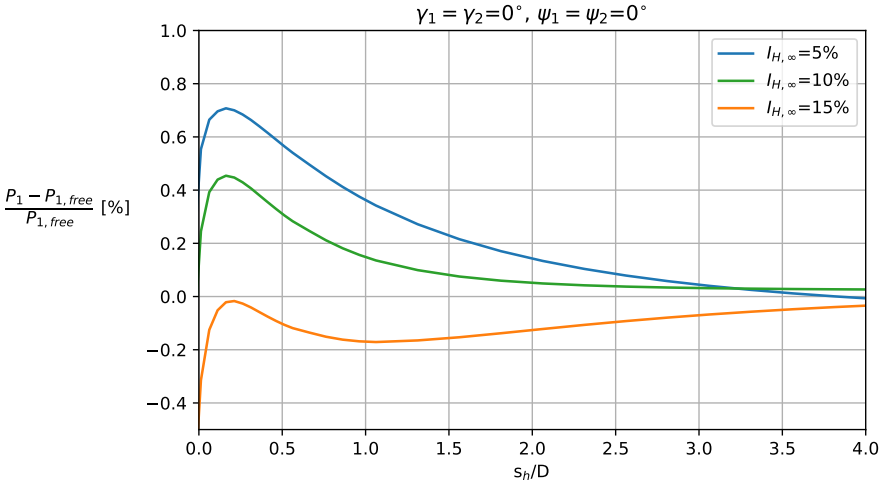

(a) Case 1: Base case.

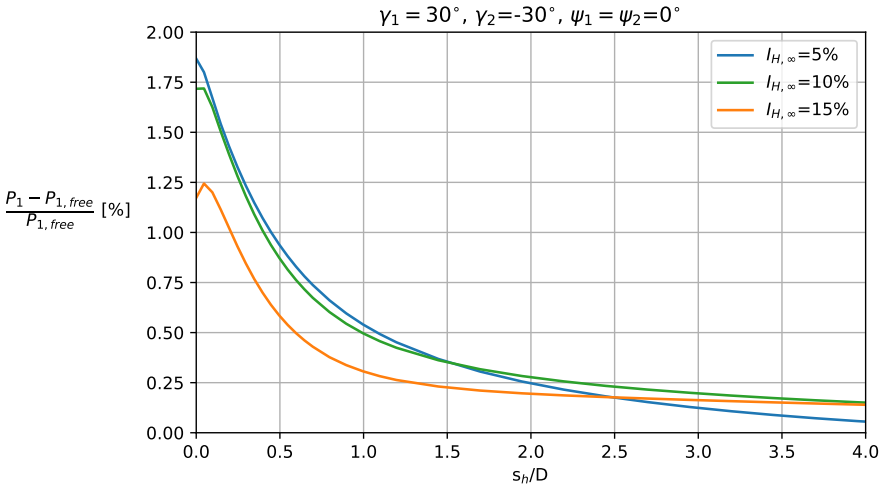

(b) Case 2: Extreme case of toe-out.

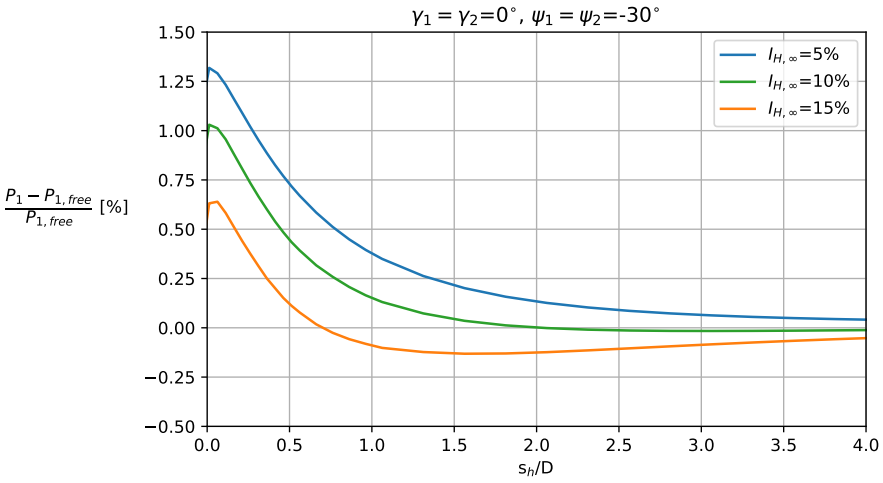

(c) Case 3: Extreme case of tilt-out.

Figure 4.4: Power of rotor 1 of the horizontal 2R-V29 normalized by the single turbine simulations from Section 3.2.

Three configurations are tested using the power of rotor 1, P_1, as the metric of interaction, since the problem is approximately symmetric (i.e. $P_1 \approx P_2$). It was found that the turbulence intensity was an important parameter for the rotor interaction, which is why the cases are also tested at an "intermediate" turbulence intensity level of $I_{H,\infty} = 10\%$ in addition to the usual $I_{H,\infty} = \{5, 15\}\%$. The default pitch and rpm settings of Figure 3.3 have been used.

	$I_{H,\infty} = 5\%$	$I_{H,\infty} = 10\%$	$I_{H,\infty} = 15\%$
Case 1	0.71 %	0.45 %	-0.02 %
Case 2	1.87 %	1.71 %	1.24 %
Case 3	1.32 %	1.03 %	0.64 %

Table 4.2: Relative maximum power increase of rotor 1 in percent, $\frac{(P_{1,max} - P_{1,free})}{P_{1,free}} \cdot 100$.

The optimal tip clearance for case 1 is approximately $s_h = 0.16D$, while it is between $s_h \approx 0.01D$ and $s_h \approx 0.05D$ for case 2 and 3. All the cases (except case 1, $I_{H,\infty} = 15\%$) follow the same trend of maximum power at this optimal s_h followed by a decay, which converges towards the single disk result. Another common trend is that the rotor interaction is weakened for high TI, c.f. Table 4.2. It is however important to note, that high TI inflow also has larger shear, which could also be the cause of the weakened interaction.

4.2.3 Vertical 2R-V29

The same exercise can be done with a double-rotor turbine consisting of vertically aligned rotors, i.e. rotor 1 and rotor 3, where $z_H = z_1$ is used again. The shear however obstructs a "pure" analysis compared to the horizontal double-rotor turbine, because $P_1 \neq P_3$, so this should be kept in mind, when interpreting the results. Rotor 1 is kept at its original position, z_1, while rotor 3 is translated upwards to vary s_v, and the power of rotor 1 is again used as the metric in Figure 4.5. Figure 4.6 shows the power of rotor 3.

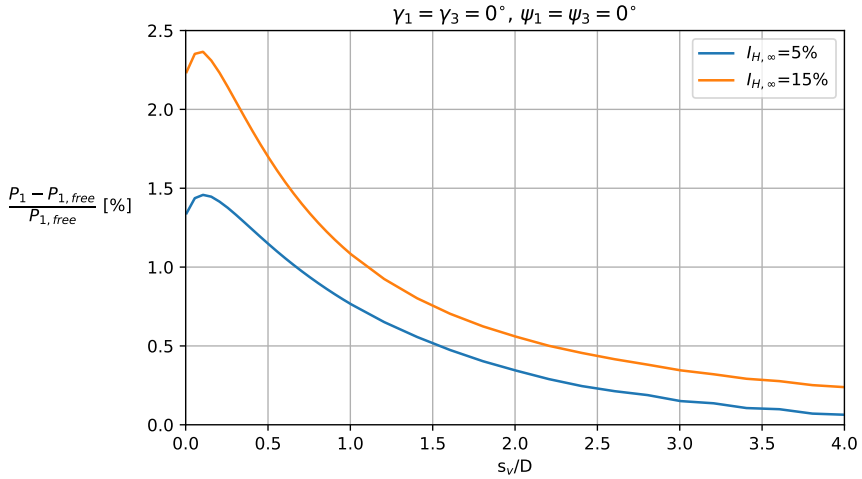

Figure 4.5: Power production of rotor 1 normalized by the single turbine simulations from Section 3.2. s_v is varied by translating rotor 3 vertical upwards.

	$I_{H,\infty}$=5%	$I_{H,\infty}$=15%
$\frac{(P_{1,max} - P_{1,free})}{P_{1,free}}$ [%]	1.46	2.37

Table 4.3: Vertical tip clearance results for $\gamma_1 = \gamma_3 = 0°$ and $\psi_1 = \psi_3 = 0°$.

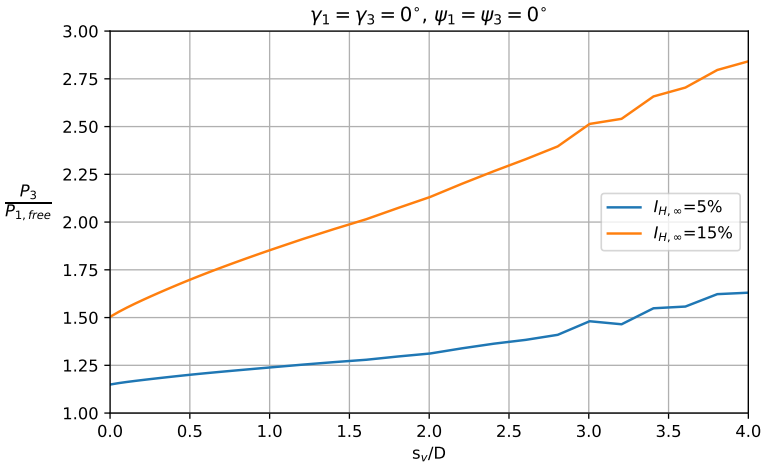

Figure 4.6: Power production of rotor 3 normalized by the single turbine simulations from Section 3.2. s_v is varied by translating rotor 3 vertical upwards.

The power increase of rotor 1 due to vertical rotor interaction is slightly larger than that of horizontal rotor interaction, as can be seen in Table 4.3, while the overall trend resembles the one of the previous section. For rotor 3, the shear effect dominates the rotor interaction heavily and the power is also significantly larger for the high TI, which is caused by the larger shear of associated with high TI inflow, c.f. Figure 2.18. This also explains why the power increase of the high TI case is largest in Figure 4.5, contrary to the trend observed for the horizontal double-rotor turbine.

The conclusion of this subsection must hence be that vertical tip clearance is of less importance compared to the shear and rotor 3 and 4 should be placed at the largest possible z with rotor 1 and 2 approximately $s_v \approx 0.05D$ below for the 4R-V29 turbine.

4.3 2R-V29 tilt and yaw

The horizontal 2R-V29 is investigated with $z_H = z_1$, $U_{H,\infty} = 7$ m/s and $I_{H,\infty} = \{5, 15\}\%$.

4.3.1 Tilt

It has previously been shown that tilt might have a larger potential for deflecting wakes compared to the conventional yaw steering, c.f. Figure 3.12-3.13, and the effect of tilt on the double-rotor turbine is shown in this section. In reality, tilt steering will most likely be unfeasible compared to yaw steering due to the engineering challenges of an active tilt motor and other load related issues. Rotors of conventional turbines do however usually have a small fixed tilt (around $\psi \approx 5 - 6°$ [34]), because of tower clearance issues, so it might not be unthinkable to construct a multi-rotor turbine with tilt angles in this range. As discussed in connection with Figure 3.12-3.13, the rotors can have negative tilt, because the rotors are connected to the main tower by horizontal support structures, which enables the possibility of leveraging the "asymmetric tilt effect", c.f. Figure 3.14, in a multi-rotor wind farm scenario.

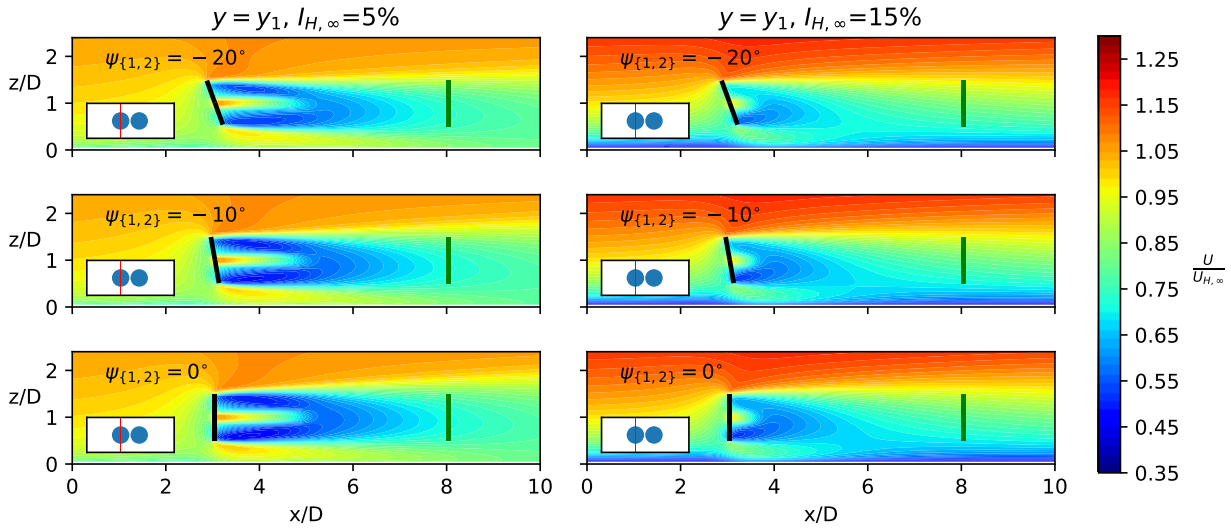

Figure 4.7: Side view of the U. The plane goes through the center of rotor 1 as shown in the inlet. The permeable green disk is shown for reference and does not influence the flow.

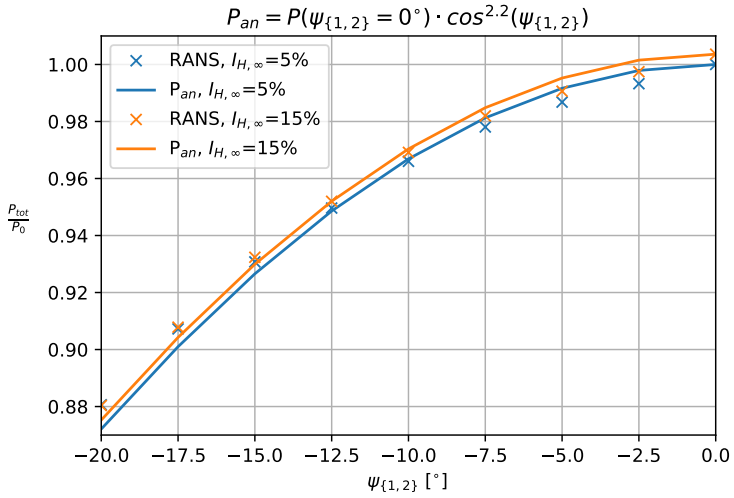

Figure 4.8: Total power and fit of cosine power function. $P_0 = P(\psi_{\{1,2\}} = 0°, I_{H,\infty} = 5\%) = 137.9$ kW.

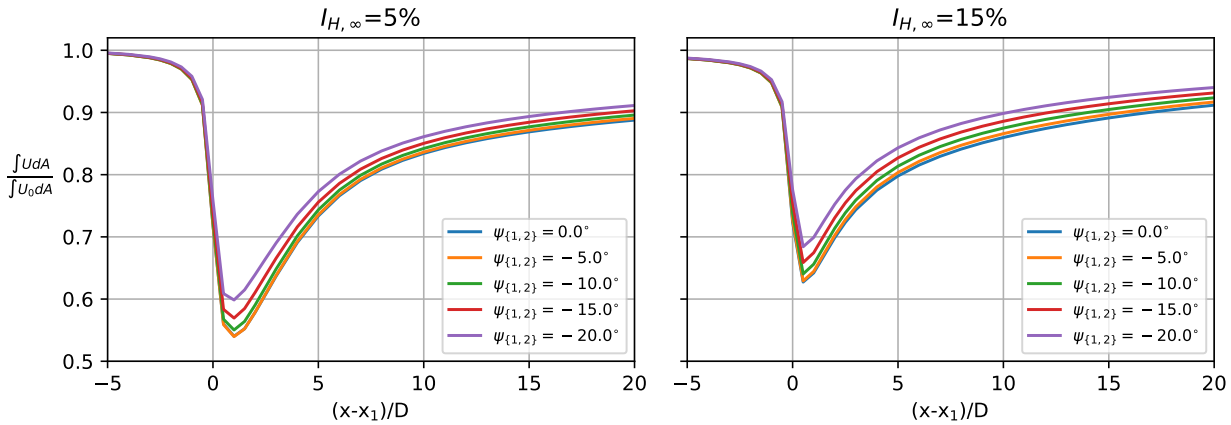

Figure 4.9: Normalized disk averaged velocity for varying $\psi_{\{1,2\}}$ as function of downstream distance.

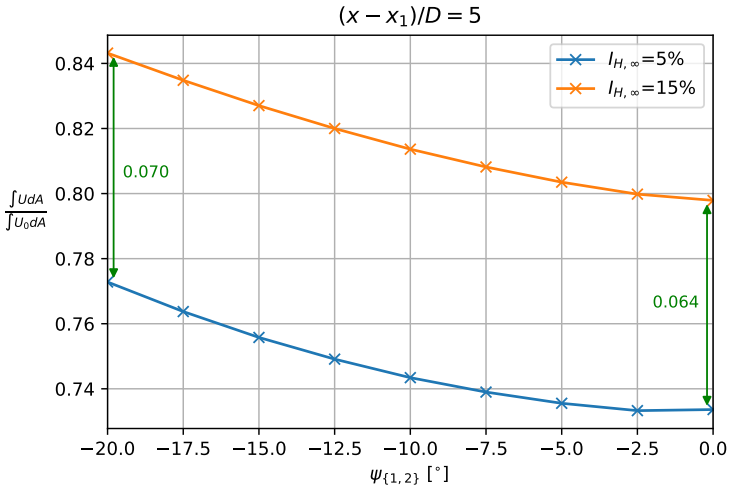

Figure 4.10: Normalized disk averaged velocity for varying $\psi_{\{1,2\}}$ at $(x - x_1)/D = 5$.

The double-rotor turbine with $\gamma_1 = \gamma_2 = 0°$ and $\psi_1 = \psi_2 = \{0, -2.5, -5, \ldots, -20\}$ is investigated for low and high TI. The side view of the U in Figure 4.7 shows the two consequences of negative tilt: The thrust decreases, which weakens the wake, and the wake is deflected downwards, because the thrust vector is rotated. This is quantified by the power decrease and faster wake recovery shown in Figure 4.8-4.10, which generally resembles the results for the single-rotor turbine in Section 3.2. Two differences can however be noticed:

- The $\cos^{2.2}$-relation overpredicts the power slightly around $\psi_{\{1,2\}} \approx -5°$ and underpredicts it at $\psi_{\{1,2\}} \approx -20°$, whereas the $\cos^{2.2}$-relation fitted well at all yaw angles for the single-rotor turbine, c.f. Figure 3.7. This could be because the physical relation for power-tilt and power-yaw are different, but is probably more likely to be caused by the interaction between the rotors, which was discussed in the previous section.

- The wake recovery of the double-rotor turbine appears to be slower compared to the single-rotor result, which can be seen by comparing Figure 4.10 and Figure 3.14. At $\psi = -10°$ the single-rotor turbine has $\frac{\int UdA}{\int U_0 dA} \approx \{0.78, 0.86\}$ for low and high TI, respectively, whereas the double-rotor turbine has $\frac{\int UdA}{\int U_0 dA} \approx \{0.74, 0.81\}$. The merging of the wakes, c.f. Figure 4.7, effectively decreases the surface area of the wakes (the right side of rotor 1 and left side of rotor 2 do not have access to high energy flow) and the fact that the double-rotor turbine extracts twice as much energy, explains the apparent "slower wake recovery" and the comparison using $\frac{\int UdA}{\int U_0 dA}$ as metric is hence not fair.

4.3.2 Yaw of support structure

The rotors have until now been yawed and tilted individually, but the support arms can also be yawed. The bottom rotors yaw collectively together and this yaw is denoted γ_b, c.f. Figure 4.11, while the top rotors yaw together with the angle γ_t (the top rotors will be included in the next section). The individual rotors could on top of this also be yawed and tilted, but this subsection will assume that they are not, i.e. $\gamma_{\{1,2\}} = \psi_{\{1,2\}} = 0°$.

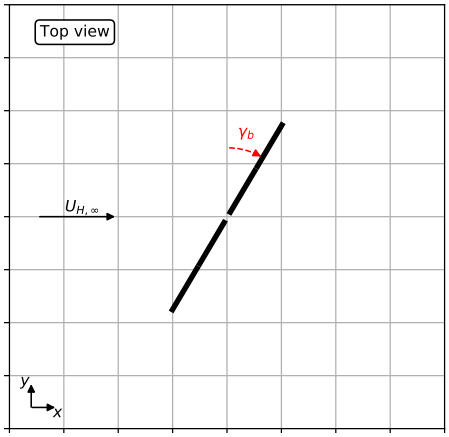

Figure 4.11: Example of positive bottom yaw, $\gamma_b > 0°$.

Figure 4.12 shows the merging of the two wakes and that this merged wake is deflected more for the low turbulence case. The faster wake recovery for the high turbulence case, c.f. Figure 4.14, is thus mainly caused by the reduction of thrust for the yawed turbine. This explains why the wake steering with yaw is more effective for low turbulence cases (as documented in Figure 4.15 by the decrease from 0.064 to 0.051). The reason why tilt steering on the other hand is more effective for the high turbulence case (as documented in Figure 4.10 by the increase from 0.064 to 0.070) is probably due to shear, since the downward deflection of the wakes allows high velocity flow from above to impinge the rotors.
The wake recovery of the yawed double-rotor turbine in Figure 4.15 is seen to be generally lower compared to the wake of the single-rotor turbine, c.f. Figure 3.6, which is again a consequence of the unfair wake recovery comparison as discussed in the previous subsection.

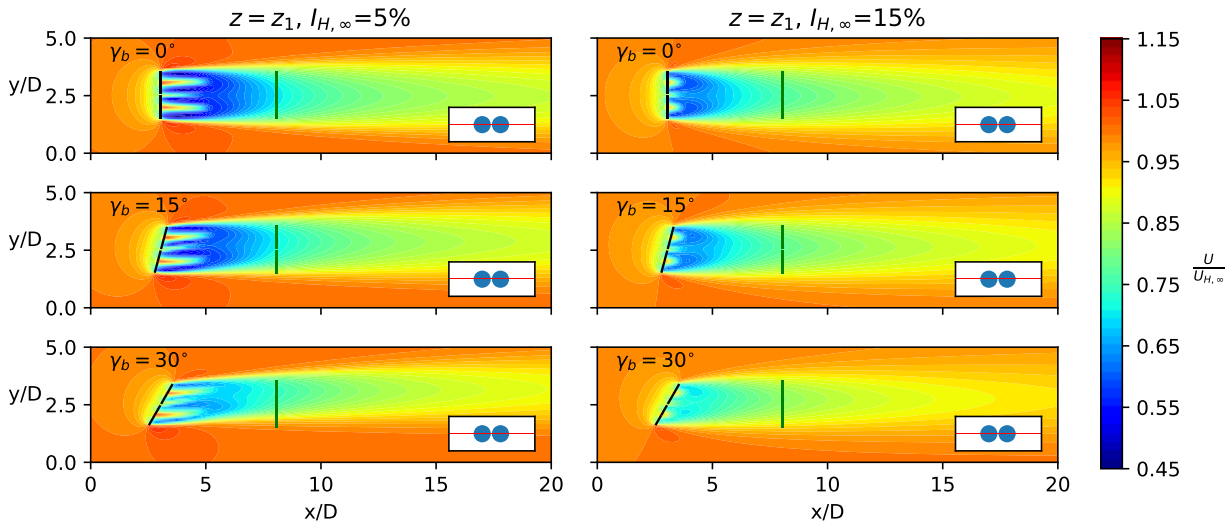

Figure 4.12: Top view of U. The permeable green disks are shown for reference and do not influence the flow.

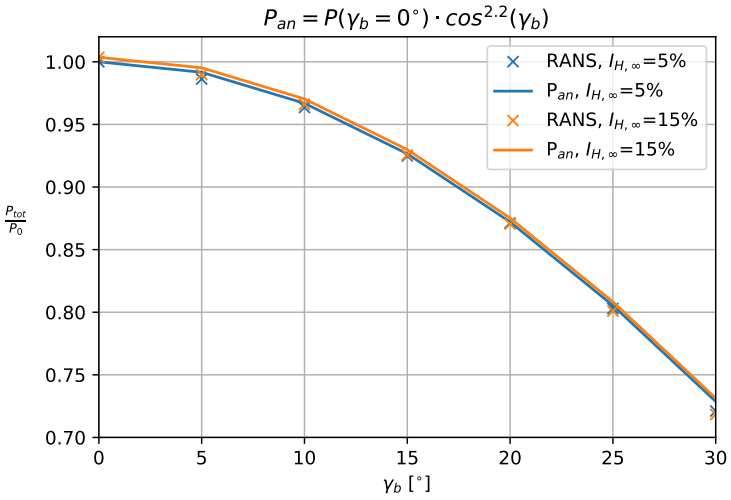

Figure 4.13: Total power and fit of cosine power function. $P_0 = P(\gamma_b = 0°, I_{H,\infty} = 5\%) = 137.9$ kW.

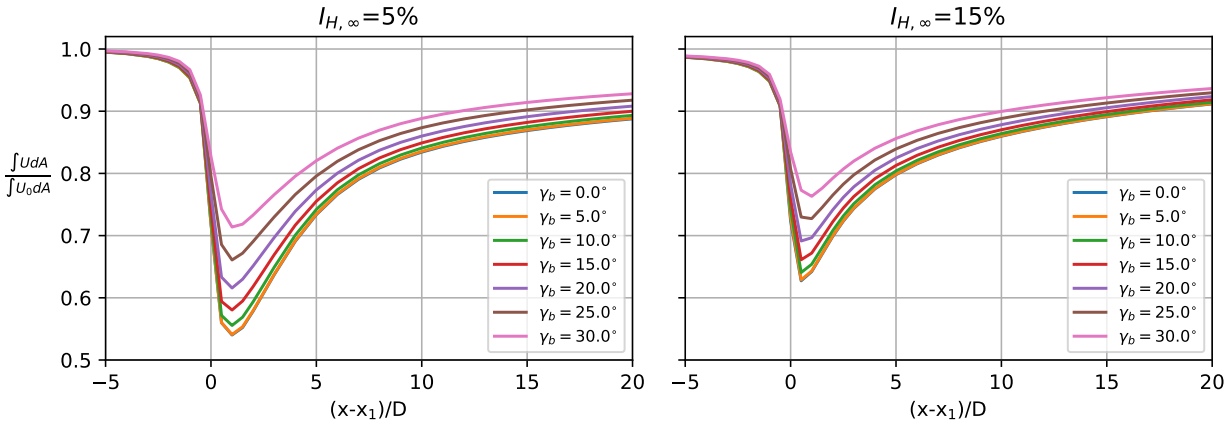

Figure 4.14: Normalized disk averaged velocity for varying γ_b as function of downstream distance.

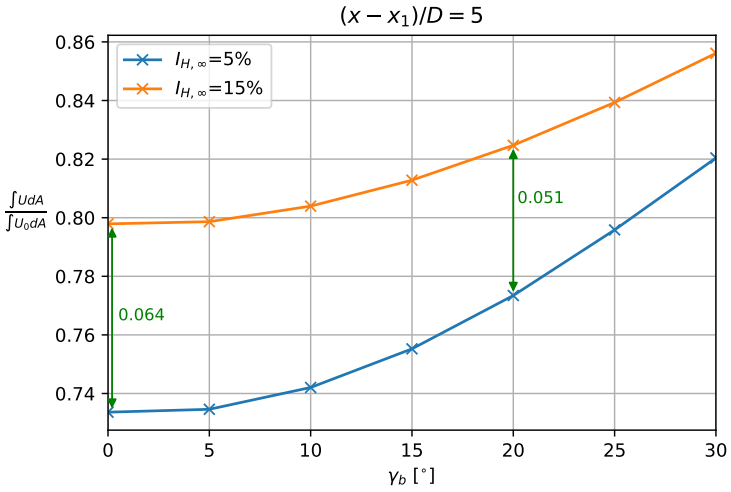

Figure 4.15: Normalized disk averaged velocity for varying γ_b at $(x - x_1)/D = 5$.

4.4 4R-V29 toe-out and tilt-out

The toe-out and tilt-out of the 4R-V29 cannot be changed dynamically via for example a controller, but are fixed in the installation of the turbine, and this section investigates the effect of different combinations of these, which could possibly be beneficial in a wind farm scenario.
The yaw of the bottom and top rotors, γ_b and γ_t, can on the other hand be controlled dynamically and independently. This can be used to set the rotors perpendicular to the main flow direction, but also in a wake steering context, which will be investigated in the last part of this section.

4.4.1 Toe-out and tilt-out

Symmetric toe-out and tilt-out angles, as defined in Figure 4.2, are tested parametrically with the total power and wake recovery at $(x - x_1)/D = 5$ as the metrics similar to the studies of the single-rotor turbine in Section 3.2. Figure 4.16-4.17 show that the power is maximum and the wake recovery is slowest (with a slight advantage for negative tilt angles), when the rotors are perpendicular to the main flow direction. The wake does hence not recover significantly faster for negative tilt angles, which was the case for the single-rotor turbine, c.f. Figure 3.13. This is so, because the wakes of rotor 3 and 4 are deflected upwards for symmetric tilt-out, which can be seen in upper row of Figure 4.18, and downward deflection was shown in Section 3.2 to be advantageous.

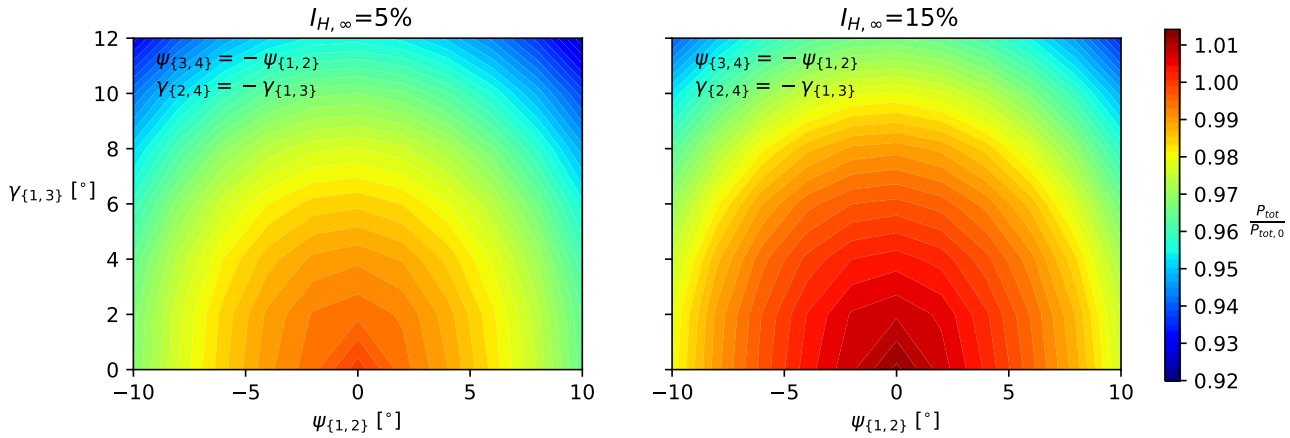

Figure 4.16: Total power production for a range of toe-out and tilt-out angles. $P_{tot,0} = P_{tot}(\gamma_{\{1,2,3,4\}} = \psi_{\{1,2,3,4\}} = 0°, I_{H,\infty} = 5\%) = 277.1$ kW.

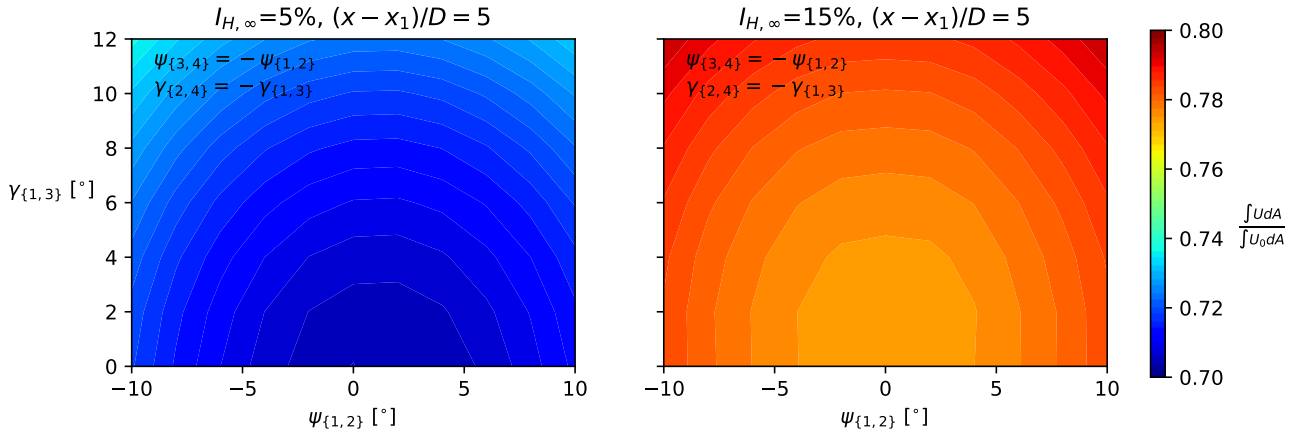

Figure 4.17: Wake recovery for a range of toe-out and tilt-out angles.

Asymmetric tilt-out, c.f. bottom row of Figure 4.18, was simulated to investigate if such a tilt configuration could improve the wake recovery and this is indeed the case as documented by Figure 4.19. This was first believed to be caused solely by the downward deflection of the wakes of rotor 3 and 4, but the power (and thrust) of the two configurations are surprisingly not equal, c.f. Figure 4.20, and this of course also affects the wake recovery. The total power production is broken into the production of respectively the bottom and top rotor pairs in Figure 4.21 and these plots show that the bottom pair produces less power, while the top pair produce more power for the asymmetric configuration. This rotor interaction is not obvious to understand physically, so to simplify the situation, the tilt of the bottom rotor pairs was fixed at $\psi_{\{1,2\}} = -16°$, while the tilt of the top rotors, $\psi_{\{3,4\}}$, was varied and the results are shown in Figure 4.22. The power of the top rotors are seen to be smallest for $\psi_{\{3,4\}} = 16°$, while the power of the bottom rotors are largest for $\psi_{\{3,4\}} = 16°$, but the reward of the bottom rotors are larger than the loss of the top rotors, which is why the symmetric tilt-out outperforms the asymmetric tilt-out with regards to total power production.

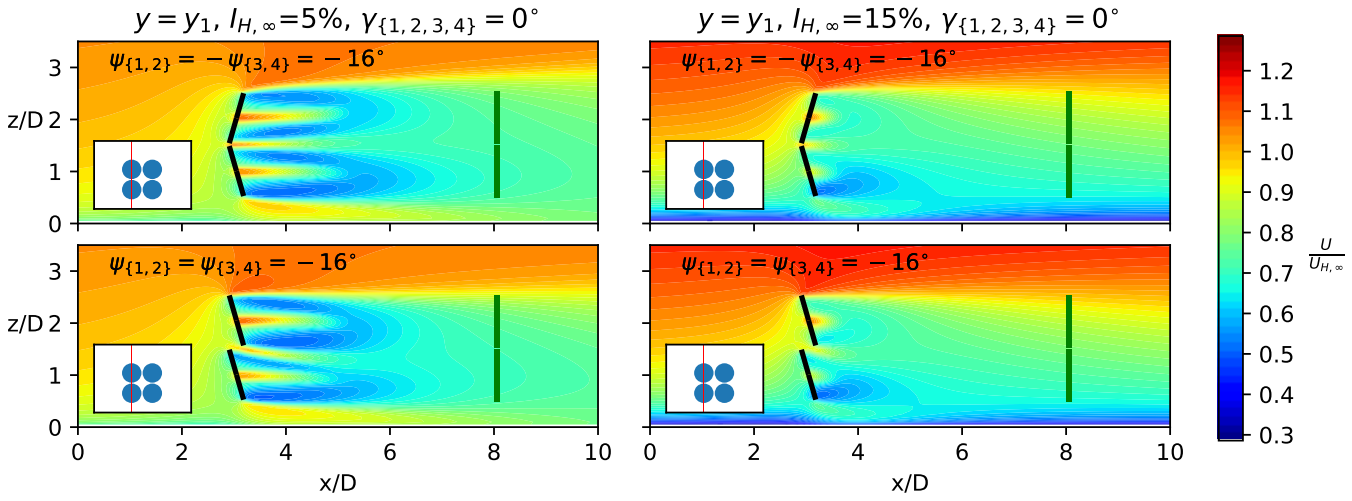

Figure 4.18: Side view of U. $\gamma_{\{1,2,3,4\}} = 0°$.

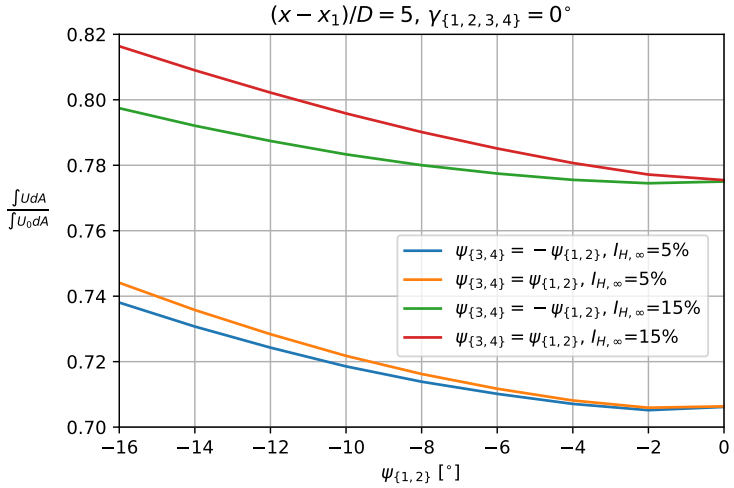

Figure 4.19: Normalized disk averaged velocity at $(x - x_1)/D = 5$ for symmetric and asymmetric tilt-out. $\gamma_{\{1,2,3,4\}} = 0°$.

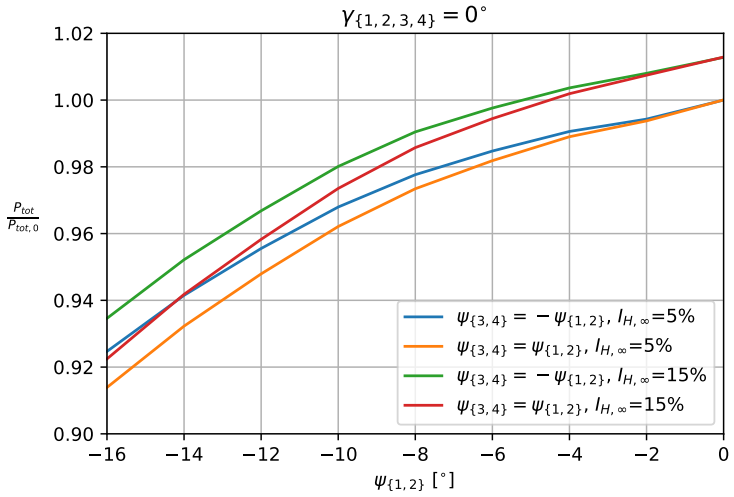

Figure 4.20: Total power production for symmetric and asymmetric tilt-out. $P_{tot,0} = P_{tot}(\gamma_{\{1,2,3,4\}} = \psi_{\{1,2,3,4\}} = 0°, I_{H,\infty} = 5\%) = 277.1$ kW.

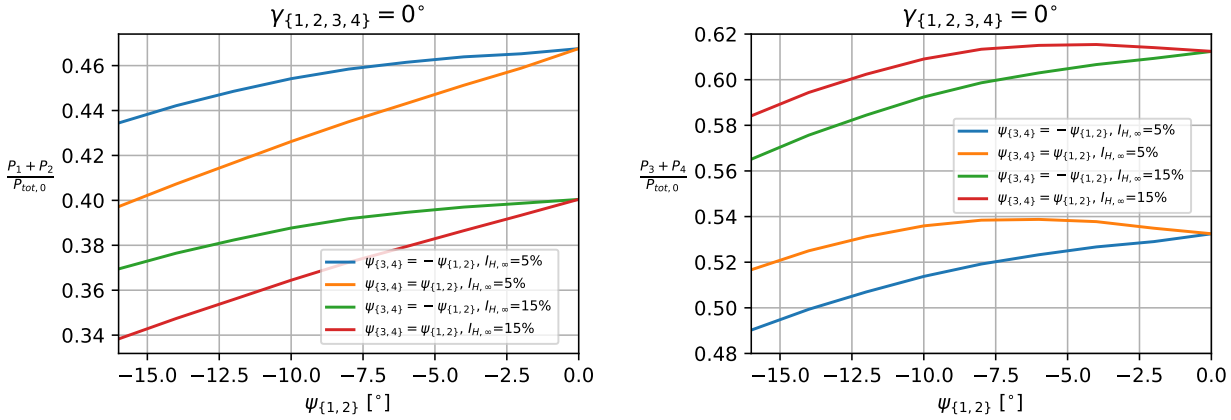

Figure 4.21: Power production of bottom (left plot) and top (right plot) rotor pairs for symmetric and asymmetric tilt-out. $P_{tot,0} = P_{tot}(\gamma_{\{1,2,3,4\}} = \psi_{\{1,2,3,4\}} = 0°, I_{H,\infty} = 5\%) = 277.1$ kW.

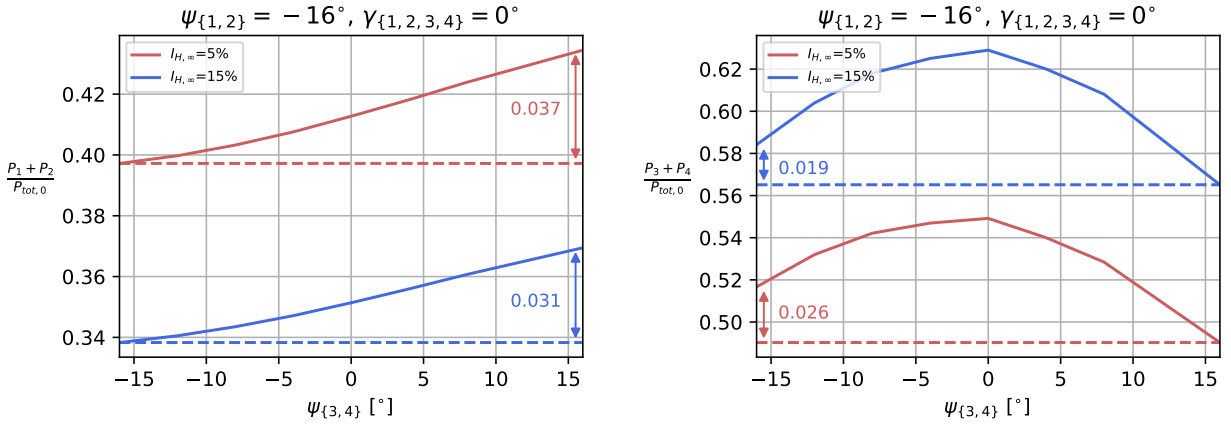

Figure 4.22: Power production of bottom (left plot) and top (right plot) rotor pairs for fixed tilt angle of bottom rotors. $P_{tot,0} = P_{tot}(\gamma_{\{1,2,3,4\}} = \psi_{\{1,2,3,4\}} = 0°, I_{H,\infty} = 5\%) = 277.1$ kW.

4.4.2 Yaw of bottom and top support structures

The bottom and top support structures are yawed together ($\gamma_t = \gamma_b$, i.e. the whole turbine is yawed) and opposite each other ($\gamma_t = -\gamma_b$, i.e. in an "x-wing" configuration) in this subsection. The individual rotors could additionally be yawed and tilted, but they are not, i.e. $\gamma_{\{1,2,3,4\}} = \psi_{\{1,2,3,4\}} = 0°$. Figure 4.23 shows that the power production of a turbine with equal amount of top and bottom yaw is better and the $\cos^{2.2}$-relation also fits well in this case. The diminished power production of the turbine with opposite bottom and top yaw should improve the wake recovery, but this is only found to be true for the high TI case. This might be related to that the wake deflection is stronger for low TI.

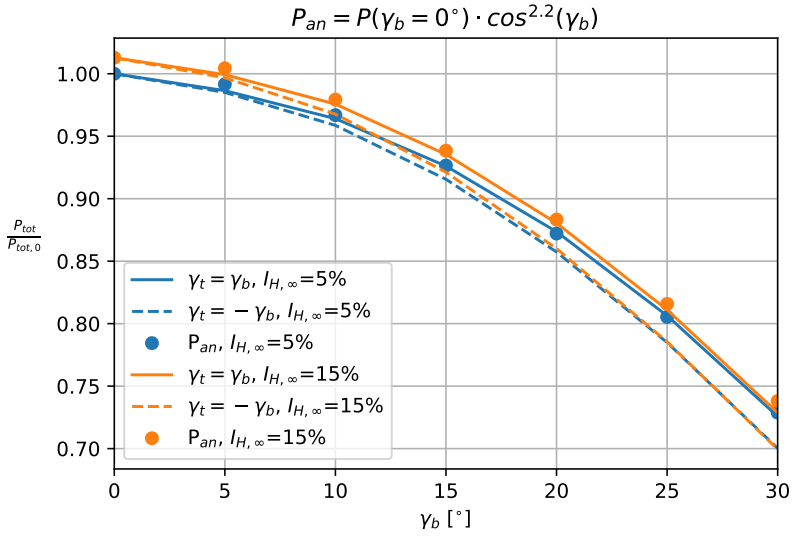

Figure 4.23: Total power production of 4R-V29 for the yawed and x-wing configurations. $P_{tot,0} = P_{tot}(\gamma_{\{1,2,3,4\}} = \psi_{\{1,2,3,4\}} = 0°, I_{H,\infty} = 5\%) = 277.1$ kW.

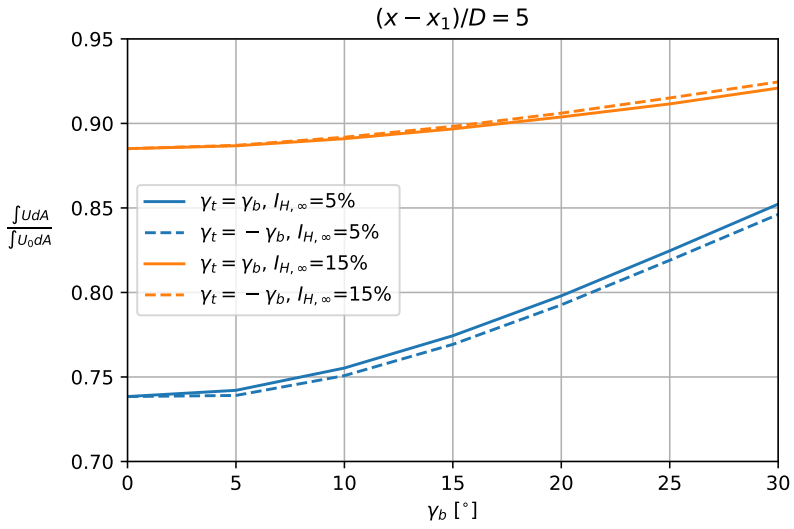

Figure 4.24: Wake recovery of the 4R-V29 turbine for the yawed and x-wing configurations.

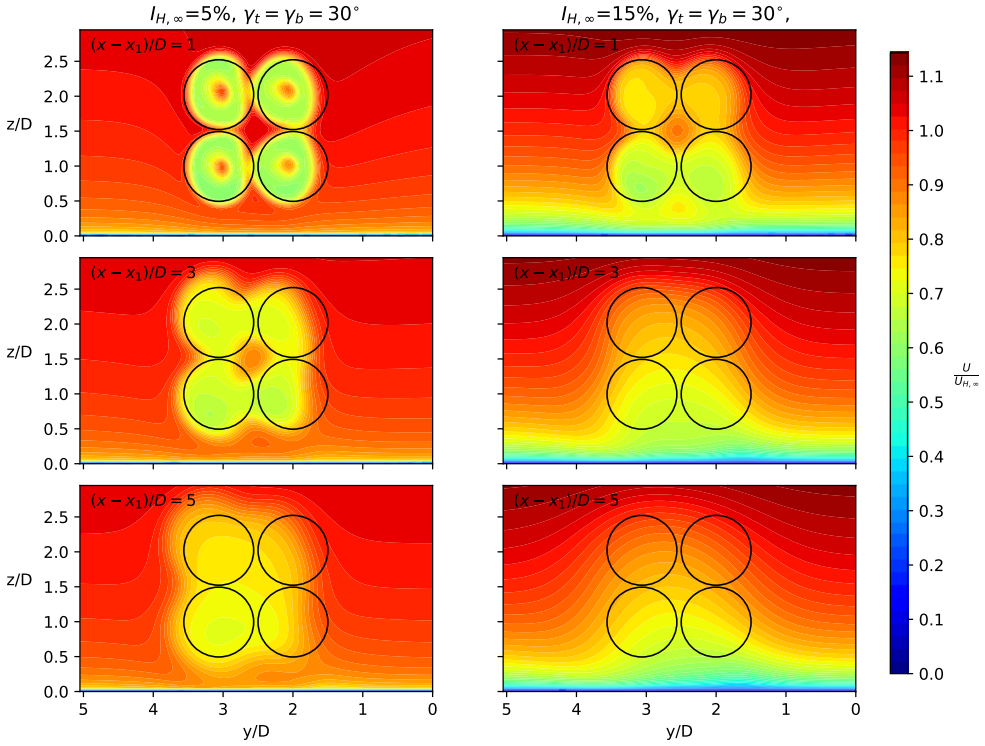

Figure 4.25: Upstream view of U for the yawed 4R-V29 turbine.

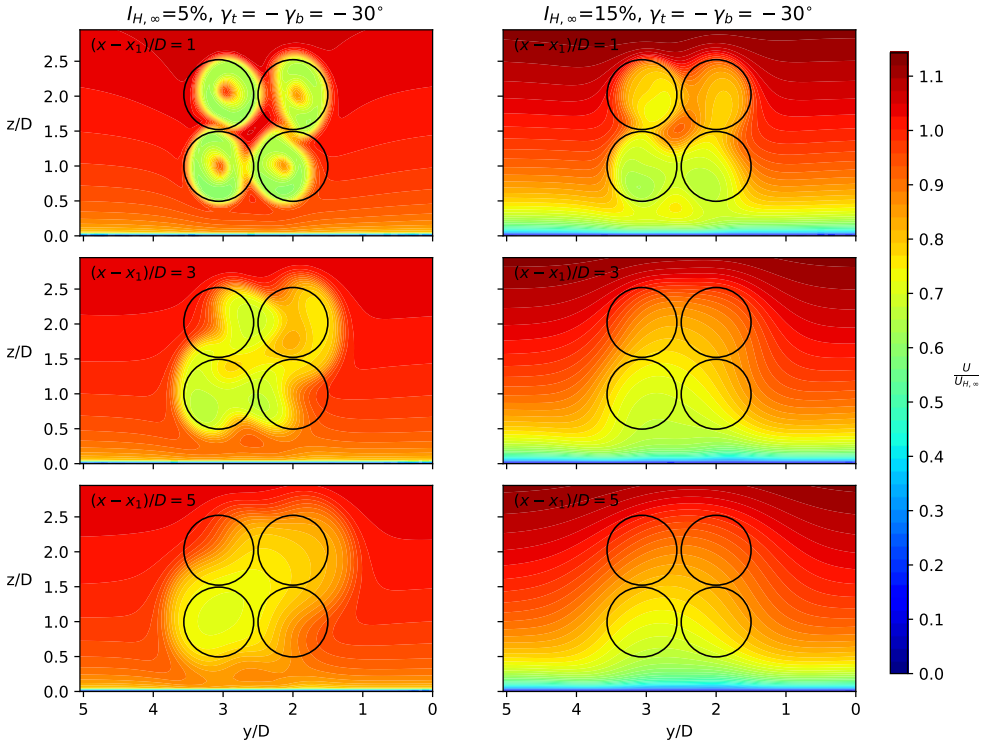

Figure 4.26: Upstream view of U of the 4R-V29 turbine in the x-wing configuration.

4.5 4R-V29 counter-rotating

All simulations have $z_H = \frac{z_1+z_3}{2}$, $U_{H,\infty} =$ 7 m/s, $I_{H,\infty} =$ 5 % and $\gamma_{\{1,2,3,4\}} = \psi_{\{1,2,3,4\}} = \gamma_b = \gamma_t = 0°$.

4.5.1 Combinations

The wake of a counter-clockwise rotating single-rotor turbine was studied in Section 3.3 with the motivation of studying the 4R-V29 with counter-rotating rotors and this is the purpose of this section. There exists 16 different combinations of CW- and CCW-rotating rotors for a multi-rotor turbine with four rotors, c.f. Table 4.4, where Ω_i is the rotational speed of rotor i with the following sign convention:

$$\text{sgn}(\Omega_i) = \begin{cases} 1 & \text{if } \Omega_i > 0, \text{ defined as CW} \\ -1 & \text{if } \Omega_i < 0, \text{ defined as CCW} \end{cases} \tag{4.4}$$

In EllipSys3D $\Omega_i > 0$ for both CW and CCW, and a switch is used to toggle between CW and CCW, c.f. Appendix D.

	Class 0	Class 1				Class 2						Class 3				Class 4
Combination	1	2	3	4	5	6	7	8	9	10	11	12	13	14	15	16
sgn(Ω_1)	1	-1	1	1	1	-1	-1	-1	1	1	1	-1	-1	-1	1	-1
sgn(Ω_2)	1	1	-1	1	1	-1	1	1	-1	-1	1	-1	-1	1	-1	-1
sgn(Ω_3)	1	1	1	-1	1	1	-1	1	-1	1	-1	-1	1	-1	-1	-1
sgn(Ω_4)	1	1	1	1	-1	1	1	-1	1	-1	-1	1	-1	-1	-1	-1

Table 4.4: Combinations of rotating disks. Class j has j number of CCW-rotating rotors.

As explained and shown in Section 3.3, the wakes have an azimuthal velocity component, V_φ, in the opposite direction of Ω_i due to Newtons 3rd law and it could be imagined that two counter-rotating wakes could function as a sink for the highly energized flow above the wakes, c.f. Figure 4.27. In the brief litterature review of Section 3.3, studies of co-axial counter-rotating turbines were described, but litterature about co-planer counter-rotating turbine seems to lack and this section will try to fill out some of this void.

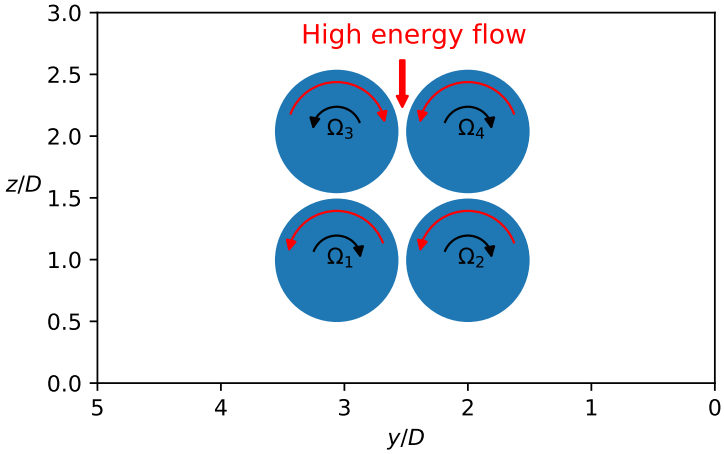

Figure 4.27: Upstream view of multi-rotor turbine with combination 4. The counter-rotating wakes could potentially function as a sink of high energetic flow.

The wake rotation of the 16 different combinations of Table 4.4 are visualized in Figure 4.28, which shows that combination 4, 7, 9 and 12 could have the wake rotation sink effect.

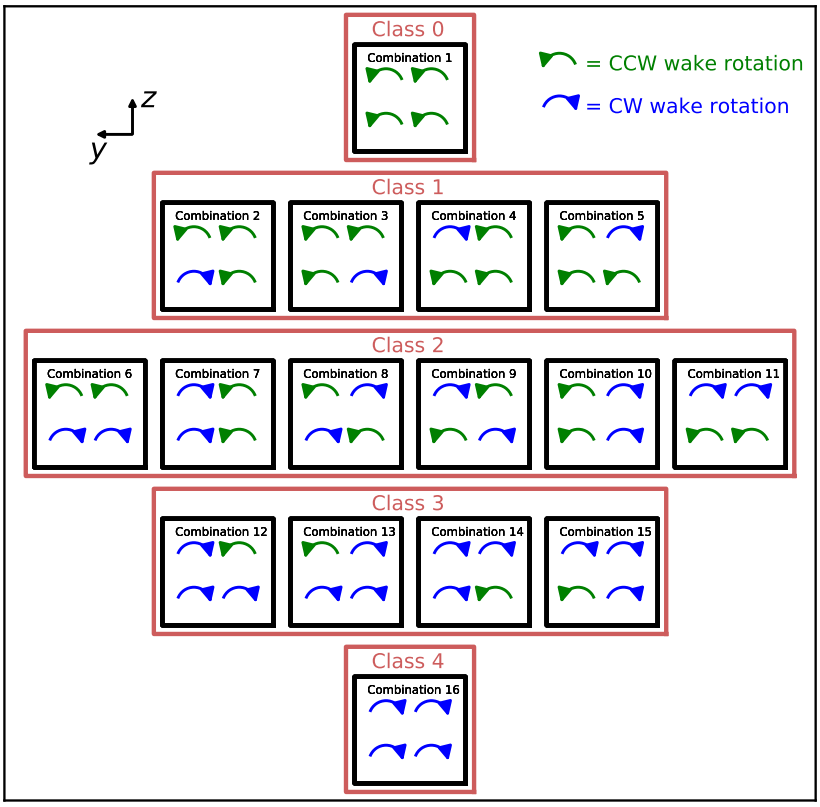

Figure 4.28: Upstream view of the 16 possible combinations of wake rotations.

4.5.2 Power and thrust

The power and thrust was shown to be near identical for a single V29 in CW and CCW operation, c.f. Table 3.4, and Figure 4.29 shows that this is also the case for the 16 combinations of Figure 4.28. It can hence be concluded that interacting counter-rotating disks causes practical no power decrease (and even a slight increase for some configurations). The performance of a turbine with counter-rotating rotors is thus not depreciated, although such a turbine would arguably be more costly, since all rotors today are designed for CW operation.

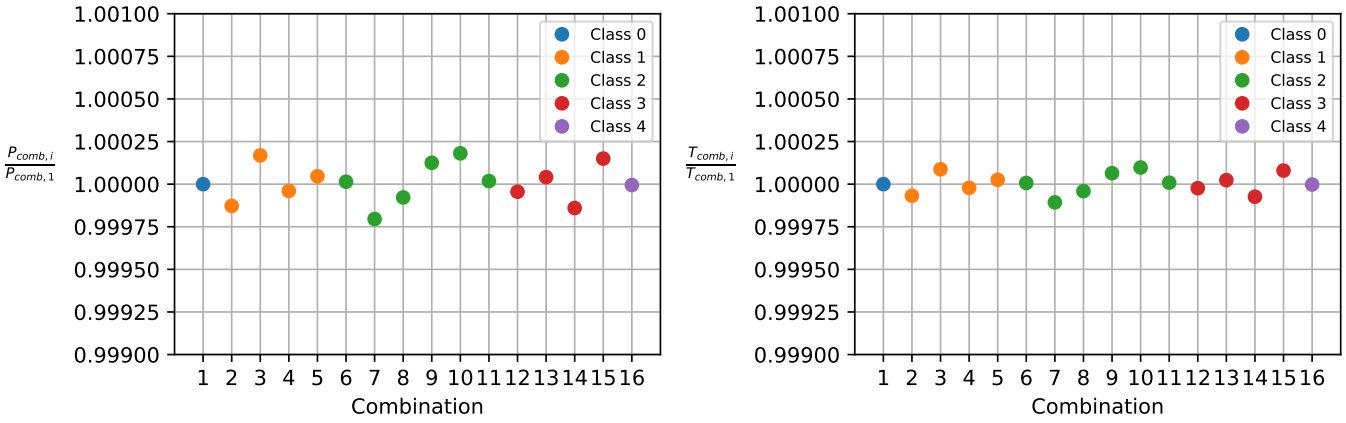

Figure 4.29: Total power and thrust of the 16 different rotational combinations of the 4R-V29 turbine.

4.5.3 Wake

The wake recovery is quantified with the usual normalized disk averaged velocity, $\frac{\int UdA}{U_0 dA}$, at $(x-x_1)/D = \{5, 10\}$ and is calculated for each of the 16 combinations with the results shown in Figure 4.30. The wake recovery deviates less than 0.001 from the base case and is thus very weakly affected by the different combinations, although with a larger variation compared to the thrust and power.

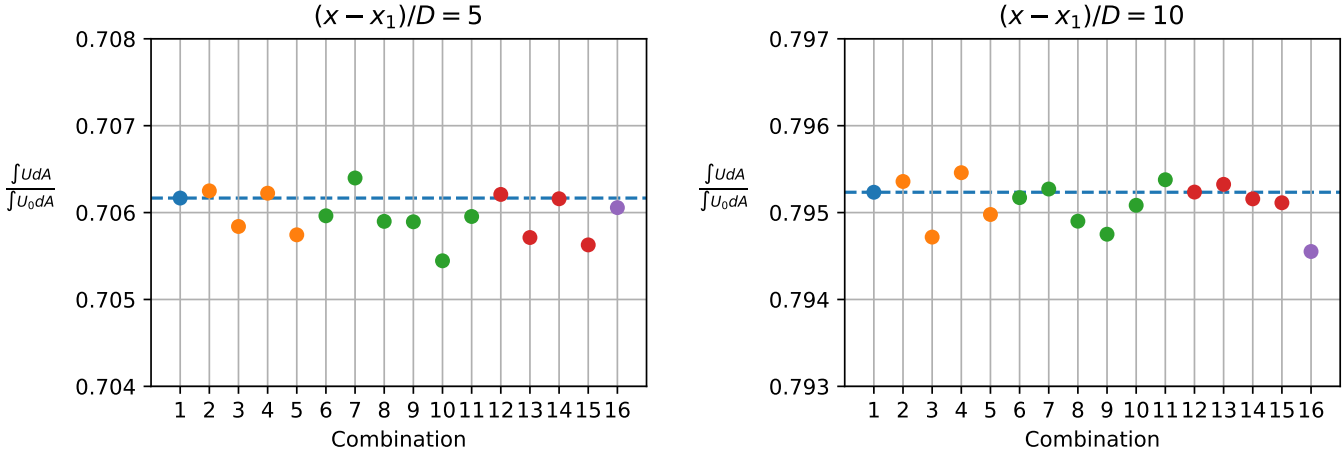

Figure 4.30: Normalized disk averaged velocity of the four rotors at two characteristic downstream distances.

The wake rotation sink would supposedly transfer high energetic flow from above the turbine to the center of the four disks and this effect could hence be underestimated by the usual disk average over the four rotors, so a better metric could be the disk averaged velocity over an equivalent single rotor disk as the one in Figure 4.31. The normalized disk averaged velocity over such an equivalent rotor is shown in Figure 4.32 and the variation is slightly larger than the mutli-rotor disk average of Figure 4.30, but still too small to be considered a real improvement of the wake recovery. In Figure 4.30 and 4.32, combination 4, 7 and 12 consistently have on par or larger wake recovery compared to the default configuration, which shows that the wake rotation sink indeed could have an effect (although very small) on the wake recovery and to investigate this further, but also to understand the reason for the small effect, U, V and W are plotted at $(x-x_1)/D = \{1, 3, 5\}$ in Figure 4.33-4.35 for combination 1 and 4. The azimuthal velocity measured from the center of rotor 3 and 4, respectively, are plotted in Figure 4.36-4.37 to highlight the difference between combination 1 and 4.

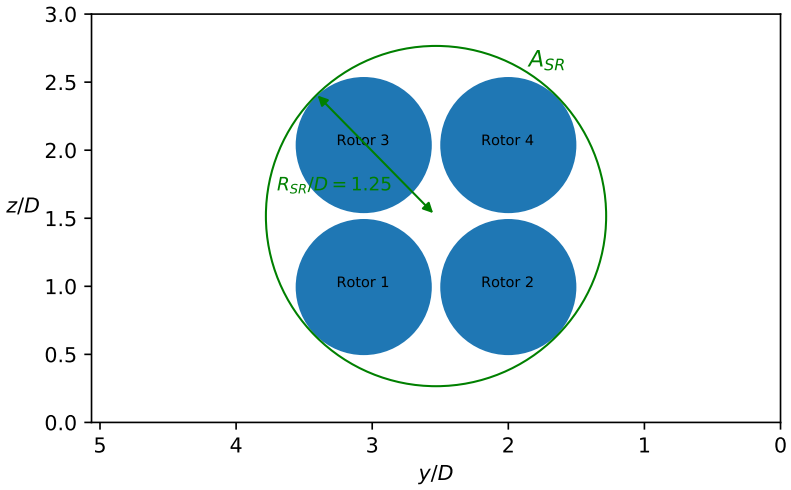

Figure 4.31: Equivalent single rotor disk with with $D_{SR} = 2.5D$.

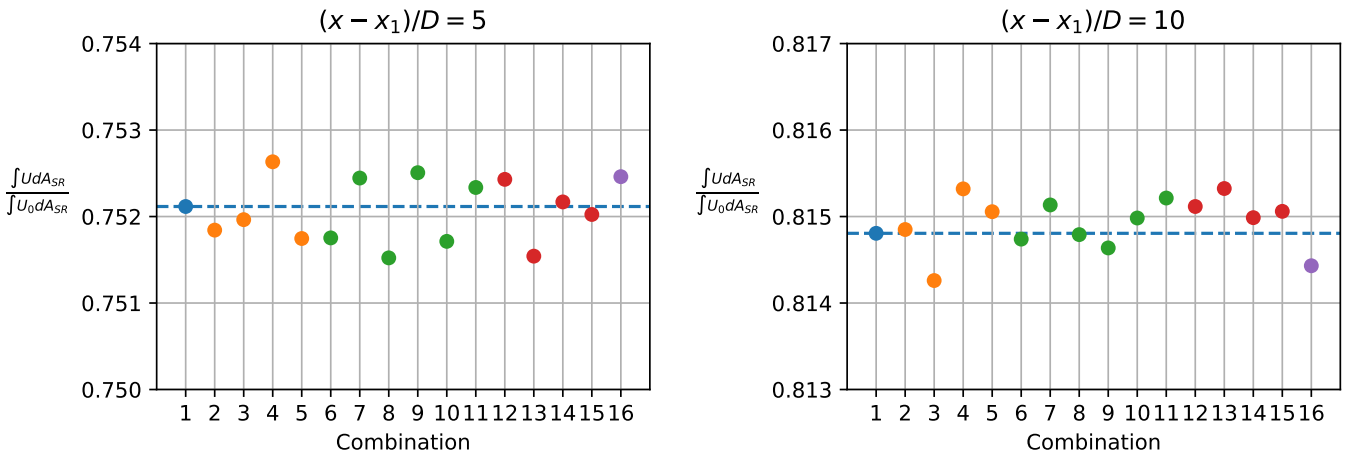

Figure 4.32: Normalized disk averaged velocity of an equivalent single rotor with $D_{SR} = 2.5D$ at two characteristic downstream distances.

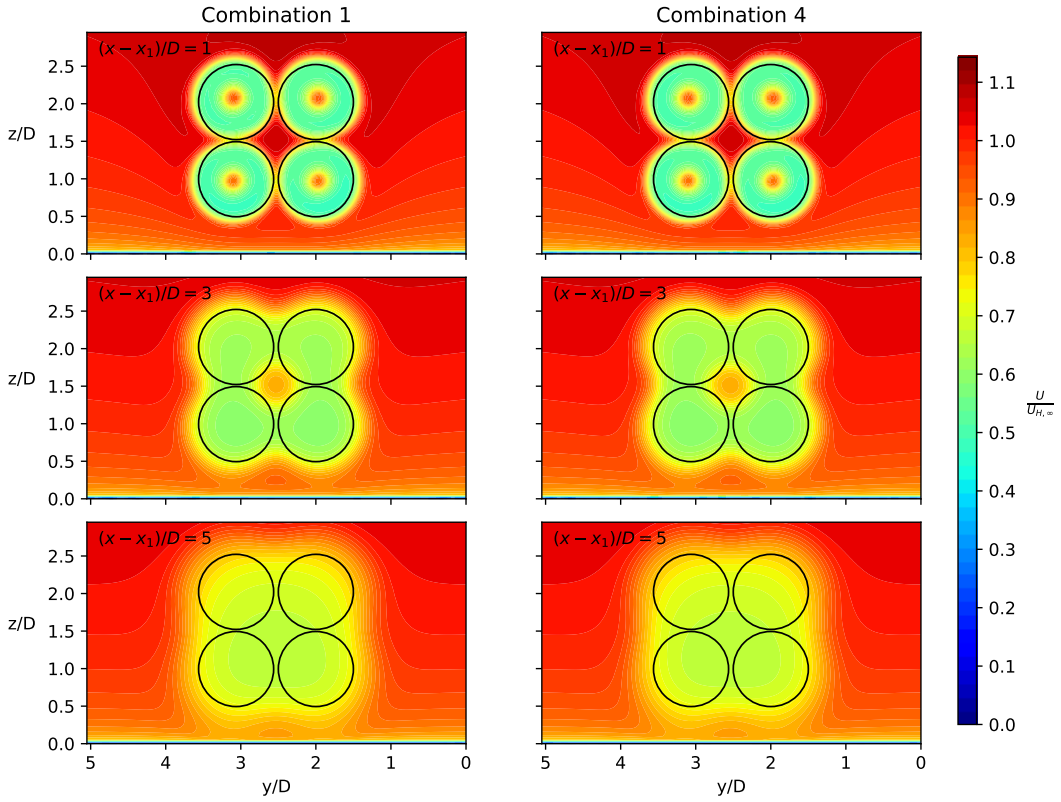

Figure 4.33: Upstream view of U for combination 1 and 4.

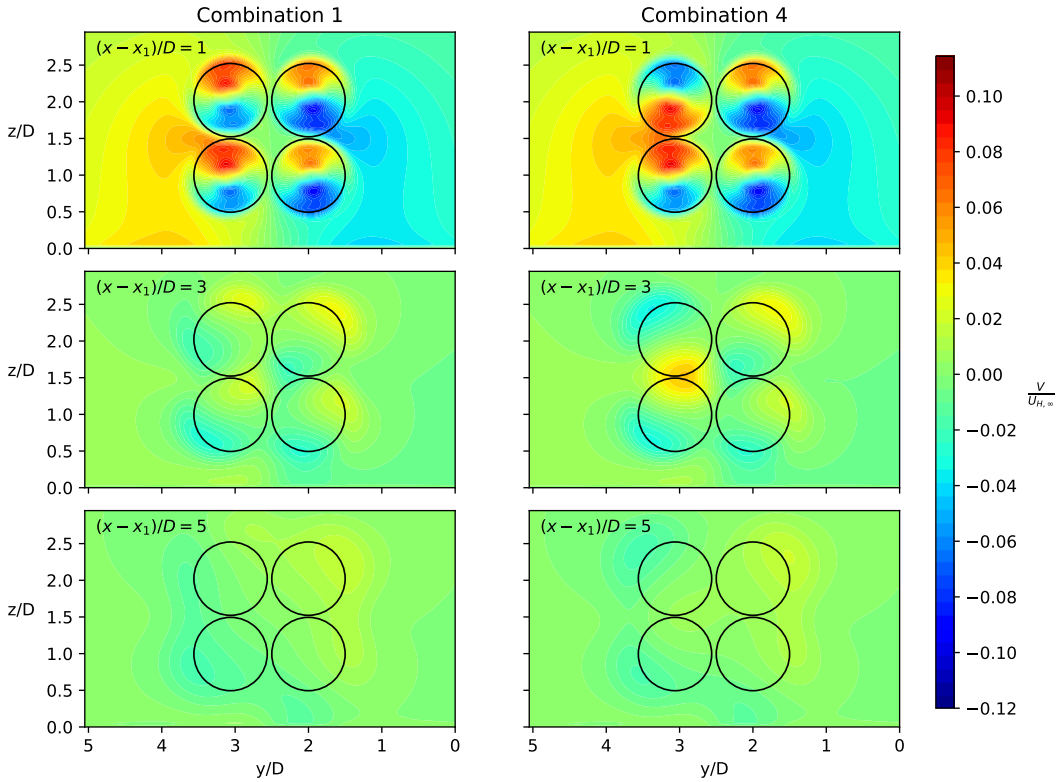

Figure 4.34: Upstream view of V for combination 1 and 4.

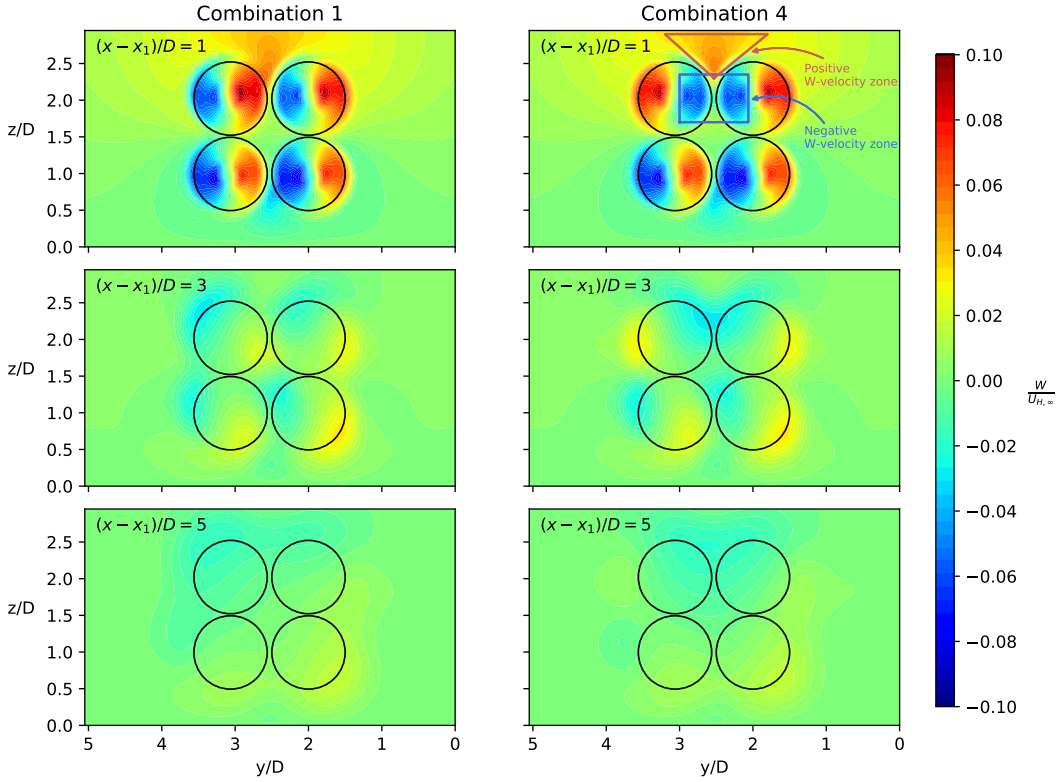

Figure 4.35: Upstream view of W for combination 1 and 4.

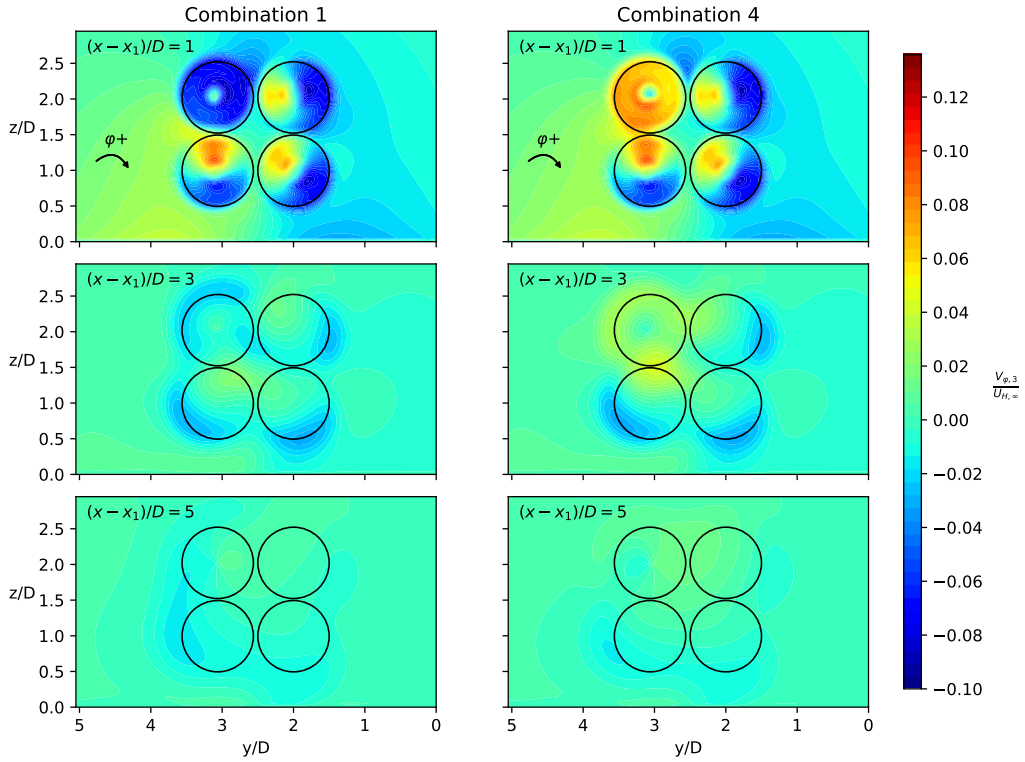

Figure 4.36: Upstream view of $V_{\varphi,3}$ (azimuthal velocity as measured from the center of rotor 3) for combination 1 and 4. The curved arrow indicates positive direction.

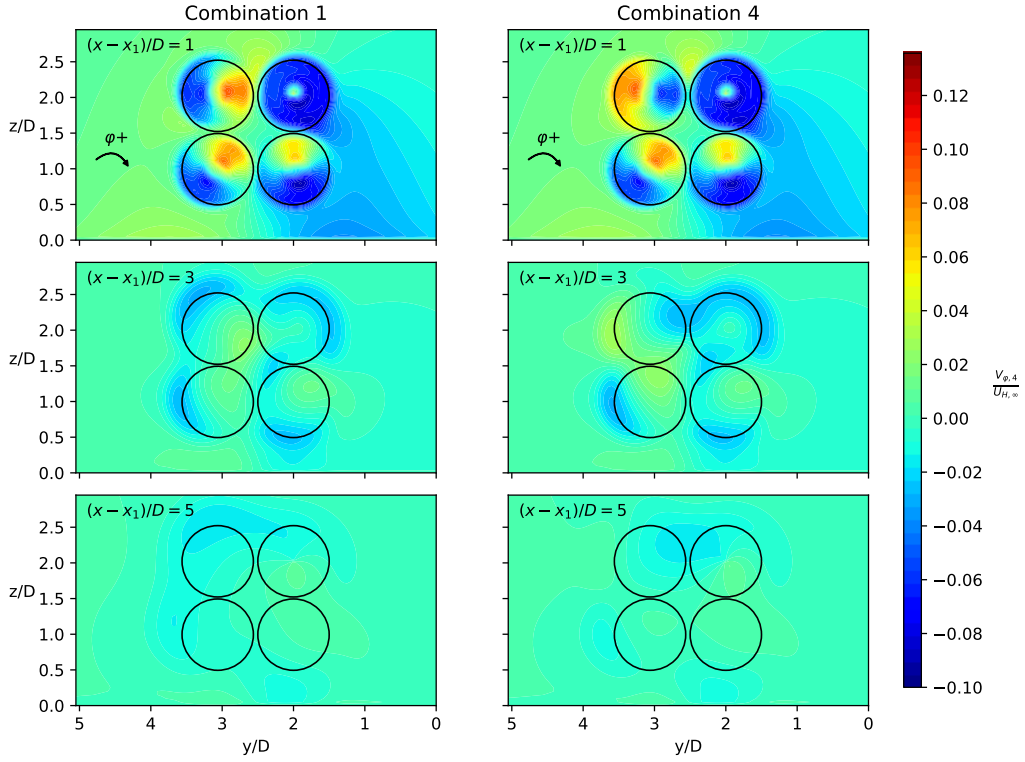

Figure 4.37: Upstream view of $V_{\varphi,4}$ (azimuthal velocity as measured from the center of rotor 4) for combination 1 and 4. The curved arrow indicates positive direction.

The U-field in Figure 4.33 for combination 1 and 4 are almost indistinguishable from each another, which fits well together with the observations of the wake recovery made prior in Figure 4.30-4.32. The wakes are however seen to be counter-rotating, which can be identified from the symmetric inversion of V and W at rotor 3 in Figure 4.34-4.35, but also directly from Figure 4.36-4.37.
The most interesting feature with regards to the wake rotation sink effect is the plot of W, Figure 4.35, which shows that combination 4 indeed has a zone with negative W between top rotors, but that a triangular area of positive W surprisingly exists above this, which ruins the sink effect in the near wake. To understand what causes this, U and W were plotted at a horizontal plane above the turbine in Figure 4.38 including combination 5 as well. The flow in front of the turbine generally has positive W, which is caused by the expansion of the streamtube. The large U in between the rotors (which is there because of the gap between the rotors and the weaker thrust distribution near the tip) then advects this upward moving flow and this explains the triangular area of positive W seen in Figure 4.35. The merging of the negative "W-wakes" in middle plot of Figure 4.38 is hence delayed and far from strong enough to contribute to a faster wake recovery.

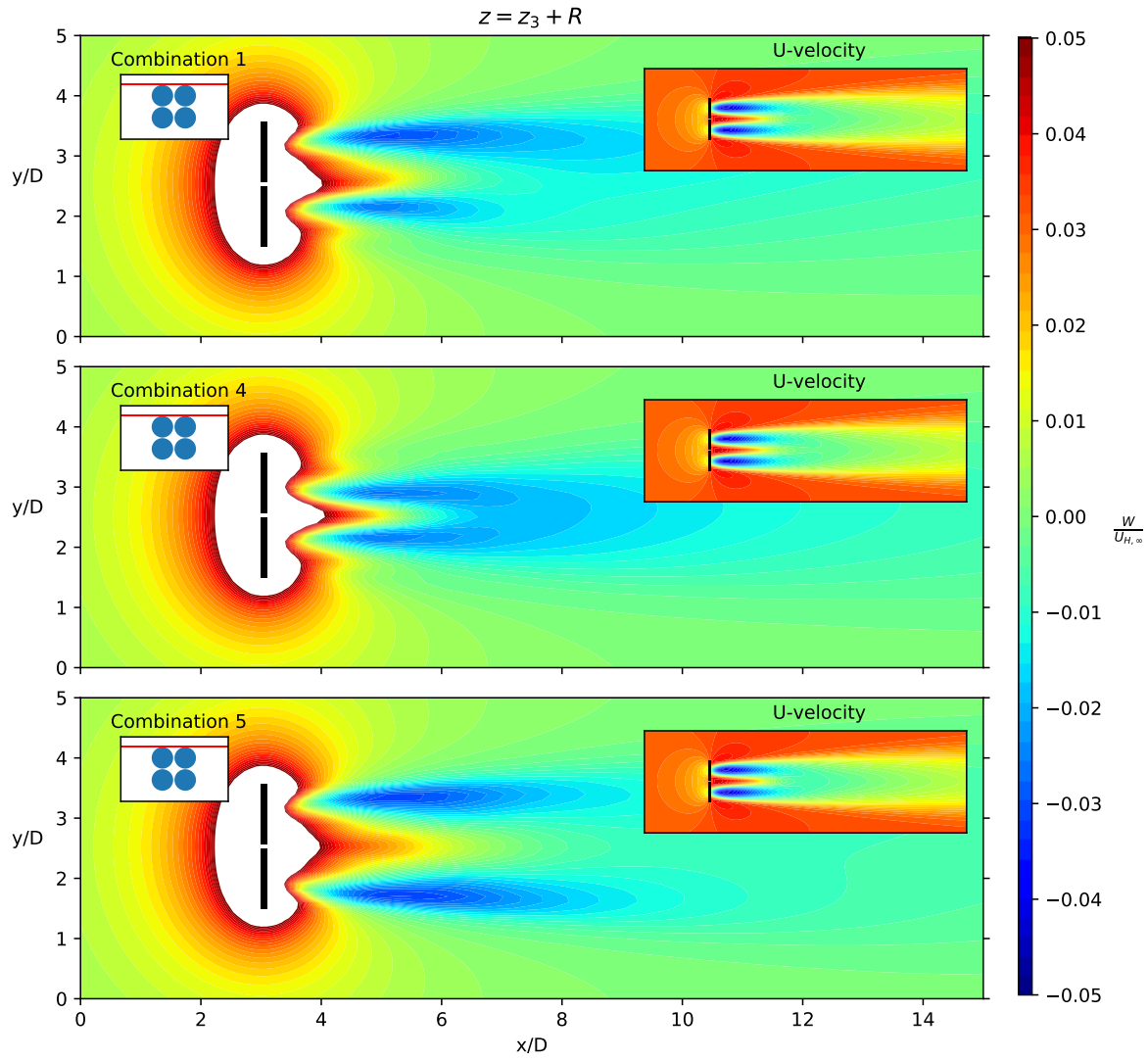

Figure 4.38: Top view of W for combination 1, 4 and 5. Left inlet: The red line shows the position of the extracted plane. Right inlet: Top view of U at the same plane.

The final conclusion must be that the wake rotation sink effect is too small to leverage, but it needs also to be stressed that the simulations were carried out with steady RANS-AD simulations. Simulations with higher fidelity (e.g. URANS-AL or LES-AL) could result in another conclusion.

4.6 4R-V29 optimization

Python's COBYLA optimizer was coupled to EllipSys3D and applied as a pitch-rpm optimizer for a single-rotor turbine in Section 3.4. The optimizer generally showed $\theta_{opt} < \theta_{default}$ and $\Omega_{opt} < \Omega_{default}$ with a resulting power increase of 1.5-4% and the purpose of this section is to obtain similar improvements for the pitch-rpm settings of the four rotors of the 4R-V29. Two strategies can be identified:

- **Individually optimized rotors:** Each rotor is optimized by itself using the same procedure as in Section 3.4 and the obtained pitch-rpm settings are then applied in a multi-rotor simulation. It is important for this approach that the same inflow profile is used for all of the rotors, and since $z_1 = z_2$, $\gamma_1 = \gamma_2 = 0°$ and $\psi_1 = \psi_2 = 0°$ are used, it is only necessary to optimize one of the rotors (the same goes for rotor 3 and 4).

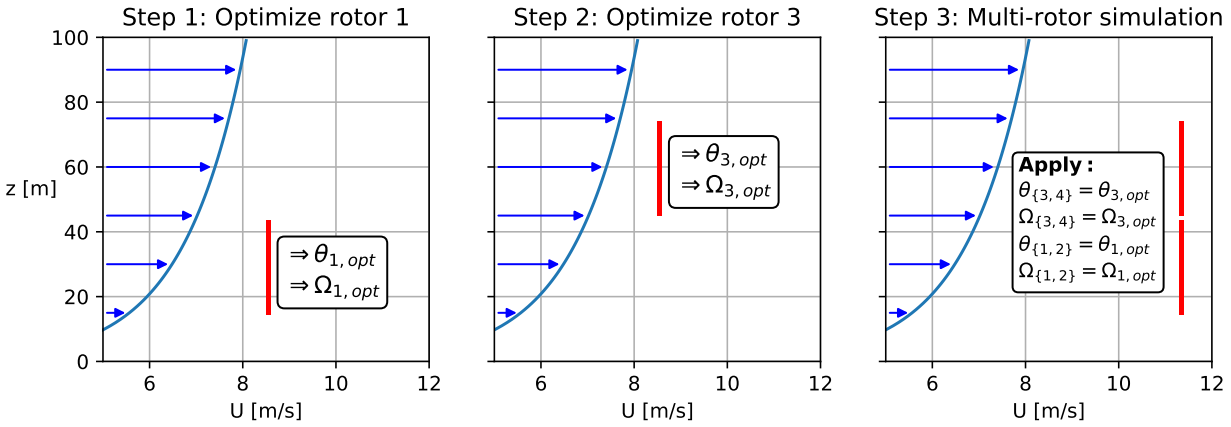

Figure 4.39: Procedure for individually optimized rotor approach.

- **Collectively optimized rotors:** Another approach is to increase the design variable space of the optimizer to $(\theta_1, \Omega_1, \theta_2, \Omega_2, \theta_3, \Omega_3, \theta_4, \Omega_4)$ and directly obtain the optimized solution. If it is assumed that $\theta_2 = \theta_1$, $\Omega_2 = \Omega_1$, $\theta_4 = \theta_3$ and $\Omega_4 = \Omega_3$, the design variable space can be reduced to $(\theta_1, \Omega_1, \theta_3, \Omega_3)$, and this simplification will be used throughout this section.

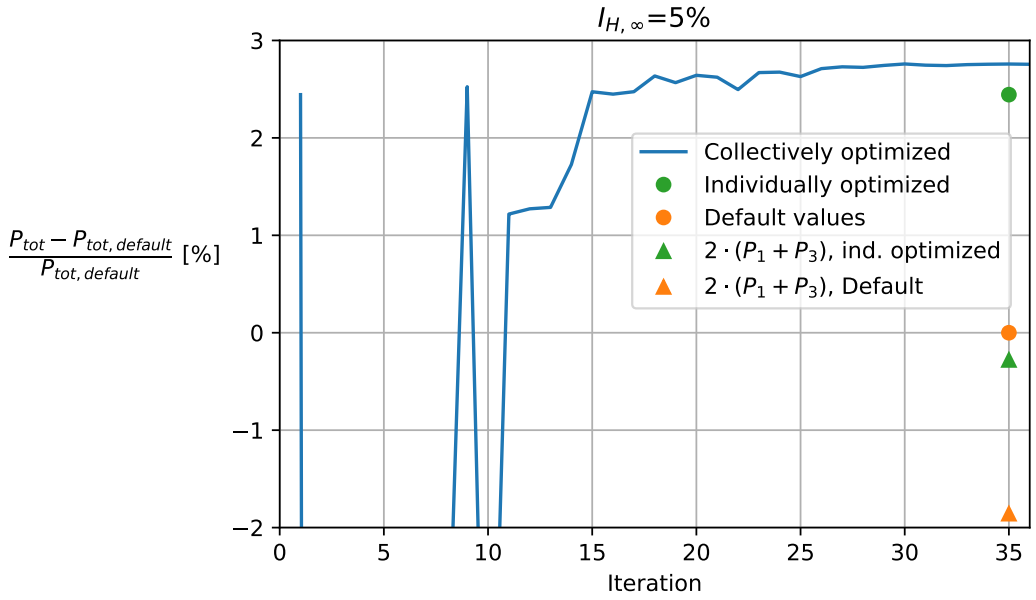

Figure 4.40: Iteration process of the collective optimizer.

Figure 4.40 shows the iterations process of the "collectively optimized rotors"-approach (blue line) as well as the result of the "individually optimized rotors"-approach (green dot) and the result of using the default pitch-rpm settings. The converged results are summarized in Table 4.5 and both approaches yield a power increase compared to the default pitch-rpm setting of approximately 2.5% with slightly more for the collective optimizer. The summed single disk results, $2 \cdot (P_1 + P_3)$, inspired by the test cycle procedure used by van der Laan et. al [15], are also shown as triangles in Figure 4.40, which gives a measure of the rotor interaction. The power increase due to rotor interaction is found to be approximately 2%, while the combined rotor interaction and optimization increase is almost 5%.

Method	$\frac{P_{tot,i}-P_{tot,def}}{P_{tot,def}}$ [%]	$\frac{P_{tot,i}-P_{tot,def,single}}{P_{tot,def,single}}$ [%]
Collectively optimized	2.76	4.70
Individually optimized	2.44	4.38
Default values	0.00	1.89
$2 \cdot (P_1 + P_3)$, Ind. optimized	-	1.61
$2 \cdot (P_1 + P_3)$, Default	-	0.00

Table 4.5: Converged results of the optimizations.

Figure 4.41-4.42 shows the evolution of the pitch and rpm in the collective optimization as well as the individually optimized and default values. The collective optimizer converges to the individually optimized values for $\theta_{\{1,2\}}$ and $\Omega_{\{3,4\}}$, while it differs for $\theta_{\{3,4\}}$ and $\Omega_{\{1,2\}}$, which results in the slight difference between the collectively and individually optimized solutions.

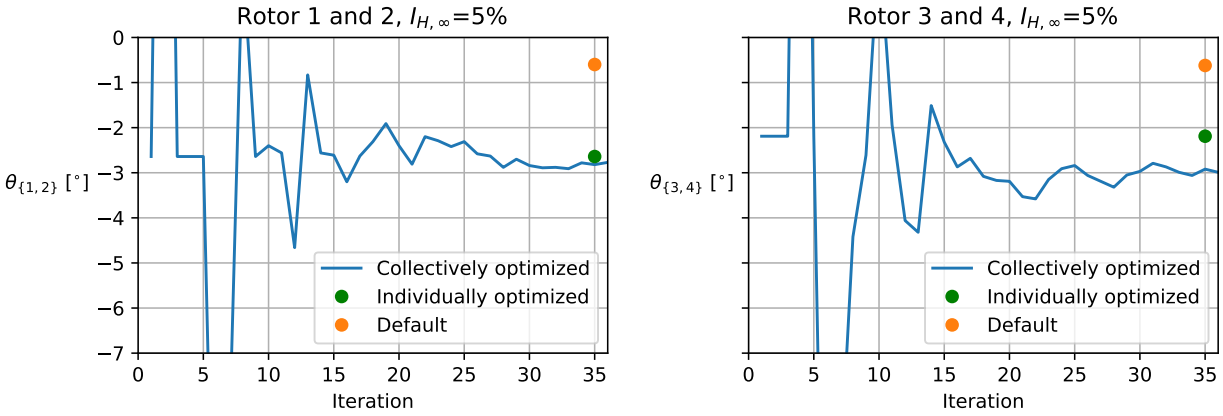

Figure 4.41: Pitch vs. iteration in the collective optimizer.

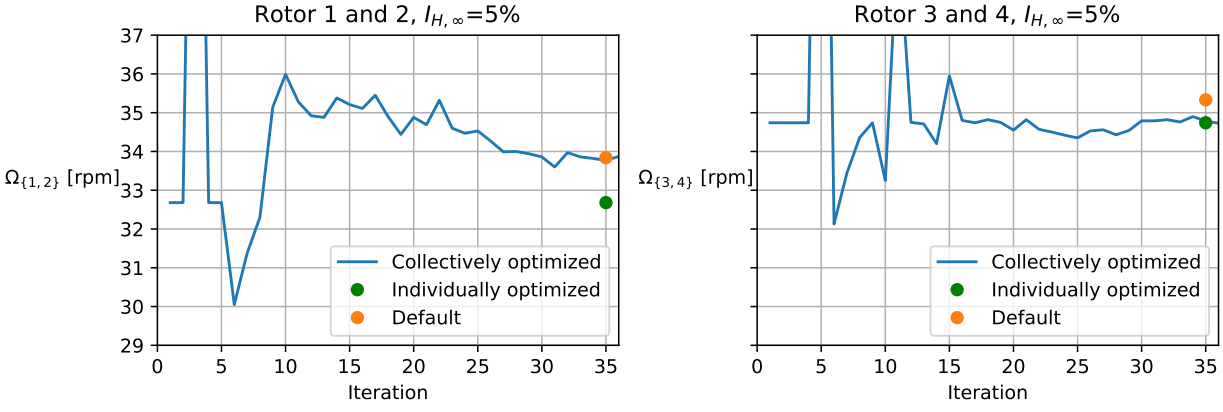

Figure 4.42: Rpm vs. iteration in the collective optimizer.

4.7 Two aligned 4R-V29 turbines

The inflow upstream of turbine 1 is $U_{H,\infty} = 7$ m/s and $I_{H,\infty} = 5\%$ with $z_H = \frac{z_1+z_3}{2}$ and the D/10 grid is used. Both turbines have $\gamma_{\{1,2,3,4\}} = \psi_{\{1,2,3,4\}} = 0°$.

4.7.1 Method III-calibration for multi-rotor turbines

Section 3.5 introduced method III-calibration for the V29 turbine and the same method can be applied to a multi-rotor turbine, where two strategies for the calibration can be identified (somewhat similar to the optimization strategies in the previous section):

- **Individually calibrated rotors:** Rotor 1 is first submerged into the flow and the calibration process described in Section 3.5 and Appendix A is carried out. This process is repeated for rotor 3 (rotor 1 and 2 are assumed to operate equally, and rotor 3 and 4 likewise), which yields the necessary control-files needed for method III-calibration.

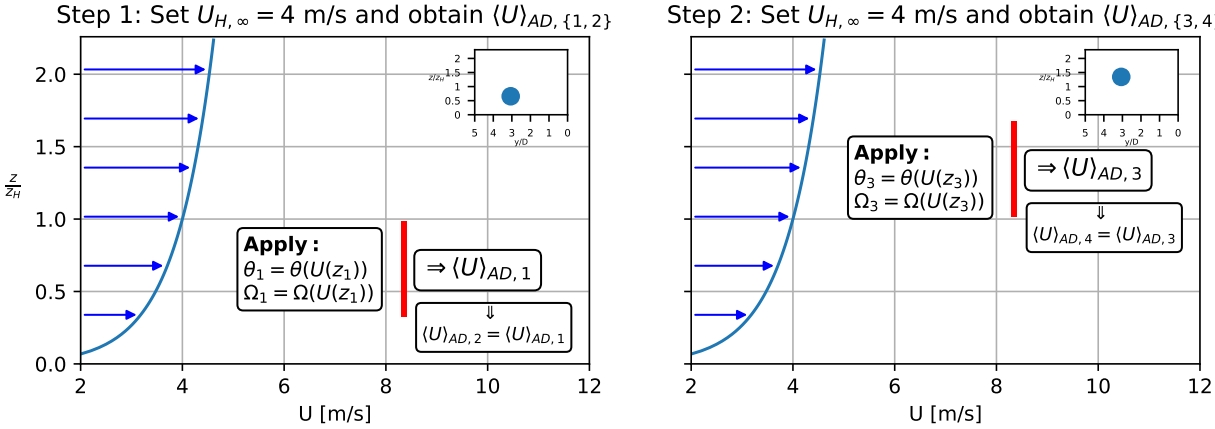

Figure 4.43: Step 3: Repeat step 1 and 2 for $U_{H,\infty} = \{5, 6, \ldots\}$ m/s. Procedure for the individual calibration approach.

- **Collectively calibrated rotors:** All four rotors are submerged into the flow and the calibration of the bottom and top rotors are hence carried out simultaneously to yield the needed control-files.

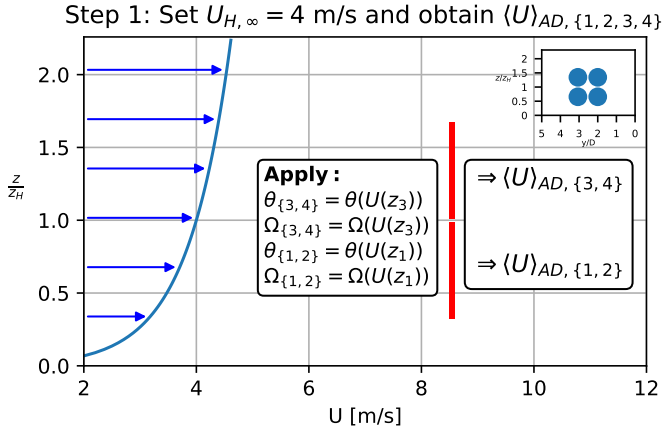

Figure 4.44: Step 2: Repeat step 1 for $U_{H,\infty} = \{5, 6, \ldots\}$ m/s. Procedure for the collective calibration approach.

Both of the calibration strategies can either use the default, individually optimized or collectively optimized θ and Ω values. In Table 4.6 the two calibration methods (both using the collectively optimized θ and Ω

values from the previous section) are compared to method III for the $U_{H,\infty} = 7$ m/s case and it is clear that the collective calibration method performs better. The collective calibration method implicitly has the rotor interaction included, which affects $\langle U \rangle_{AD}$, and this is the reason for its better performance compared to individual calibration method. Although the relative power increase of both methods compared to method III is $< 0.25\%$, it is nevertheless recommended to use the collective calibration method, which also has the advantage that the optimization and calibration can be done in the same step.

	$\theta_{\{1,2\}}$	$\theta_{\{3,4\}}$	$\Omega_{\{1,2\}}$	$\Omega_{\{1,2\}}$	$U_{\infty,tip,\{1,2\}}$	$U_{\infty,tip,\{3,4\}}$	T_{tot}	P_{tot}
Ind. calibrated	0.952%	-0.205%	1.503%	1.008%	1.535%	0.910%	1.441%	0.243%
Col. calibrated	0.001%	-0.001%	-0.002%	-0.002%	-0.002%	-0.002%	-0.006%	-0.006%

Table 4.6: Relative increase in percent, i.e. $\frac{(\text{method III-calibration} - \text{method III})}{\text{method III}} \cdot 100$, for the two multi-rotor calibration methods. The collectively optimized θ and Ω values have been used for both calibrations and $U_{H,\infty} = 7$ m/s was used for this test.

Method III-calibration is now applied to two aligned 4R-V29 turbines with $(x_2 - x_1)/D = \{5, 6, \ldots, 10\}$. For the $(x_2 - x_1)/D = 10$ configuration, the wake domain ends $3D$ downstream of turbine 2, but it was found in Subsection 2.4.9 that this has a negligible effect on the results, hence the usual grid with $l_x/D = 16$ is used. Figure 4.45 shows that turbine 2 only produces approximately 35-55% compared to a freestanding turbine depending on the inter spacing, which was also the range found by van der Laan and Akbar [16]. Turbine 1 is also affected by the downstream turbine, although the corresponding power reduction is minimal compared to turbine 2. Turbine 1 and 2 with both the collectively optimized and default θ-Ω settings have been simulated, and turbine 1 obviously produces more power with the optimized settings, hence leaving less energy for turbine 2. Nevertheless, the optimized turbine 2 manages to outperform the default turbine 2 at the whole range of inter spacings investigated here. The smallest margin is seen at the lowest inter spacing, where the difference in wake recovery is typically also largest, e.g. Figure 3.6. Another contributing factor to the diminishing difference could be that the optimization of θ and Ω was made for a freestanding turbine, c.f. Section 4.6.

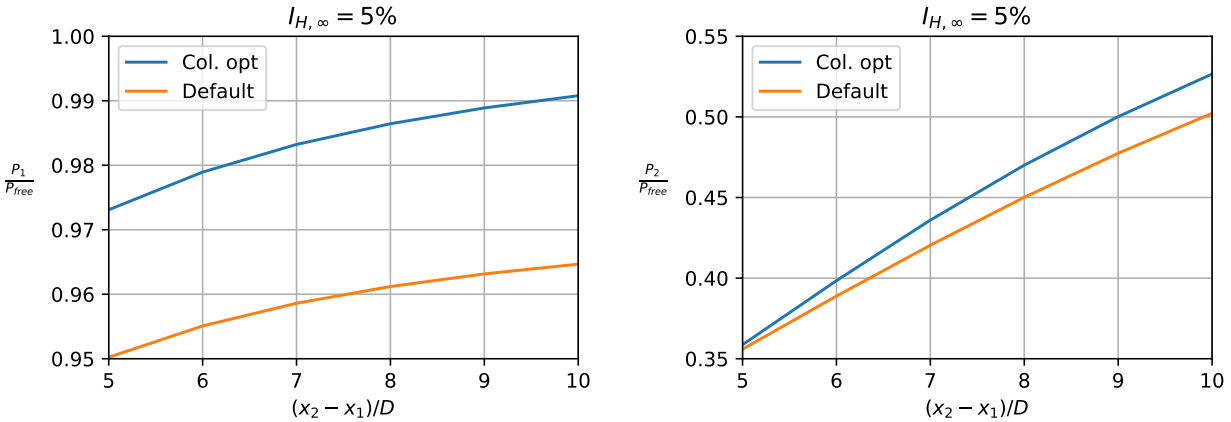

Figure 4.45: Power production of turbine 1 and 2 as function of inter spacing. $P_{free} = 289.0$ kW is the power of a freestanding turbine operating with optimized θ and Ω. Blue line = Optimized θ and Ω are used for turbine 1 and 2. Orange line = Default θ and Ω are used for turbine 1 and 2.

4.7.2 De-regulation of turbine 1

Turbine 1 is now de-regulated by changing the rotational speed of the upper and lower rotors independently to potentially improve the combined power production of turbine 1 and 2, where $(x_2 - x_1)/D = 5$. Turbine 1 uses method III with fixed $\theta_{\{1,2\}} = -2.77°$ and $\theta_{\{3,4\}} = -2.99°$, while turbine 2 uses method III-calibration with the optimized θ and Ω values.
The total power is seen in Figure 4.46 to increase by $(1.3433 - 1.3318)/1.3318 \cdot 100 = 0.87\%$, when comparing the optimized de-regulation setting with the method III-calibration results from the previous subsection. Both the rotational speed of the bottom and top rotors are de-regulated to achieve this, but with more de-regulation of the bottom rotors. This can be seen to be caused mainly by $\left|\frac{\partial P_1}{\partial \theta_{\{1,2\}}}\right| < \left|\frac{\partial P_1}{\partial \theta_{\{3,4\}}}\right|$ around the method III-calibration result in Figure 4.47, since the top rotors have more available wind energy due to shear.

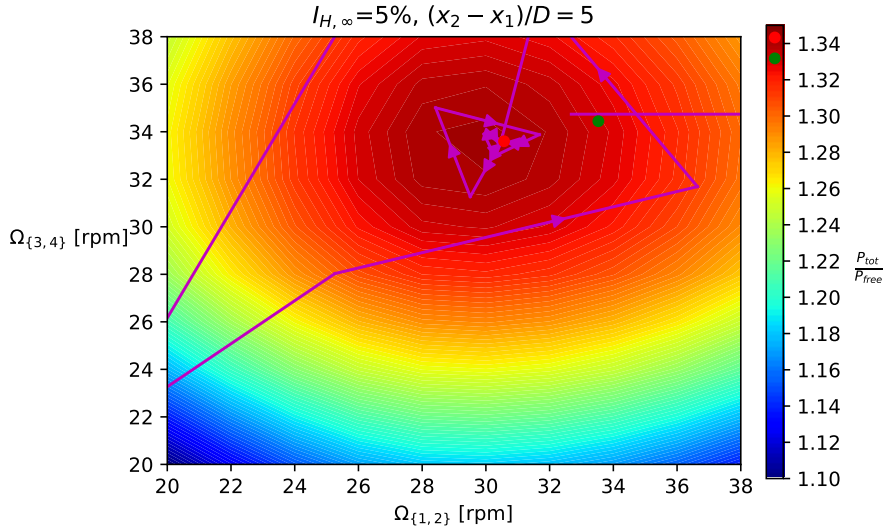

Figure 4.46: Total power production of turbine 1 and 2 in optimization of $\Omega_{\{1,2\}}$ and $\Omega_{\{3,4\}}$. Green dot = $(\Omega_{\{1,2\}}, \Omega_{\{3,4\}})_{methodIII-calibration}$.

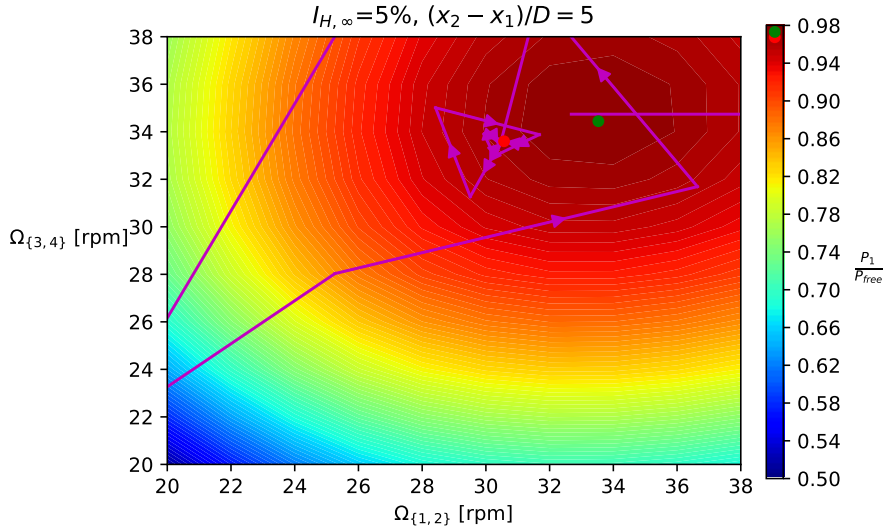

Figure 4.47: Power production of turbine 1 in optimization of $\Omega_{\{1,2\}}$ and $\Omega_{\{3,4\}}$. Green dot = $(\Omega_{\{1,2\}}, \Omega_{\{3,4\}})_{methodIII-calibration}$.

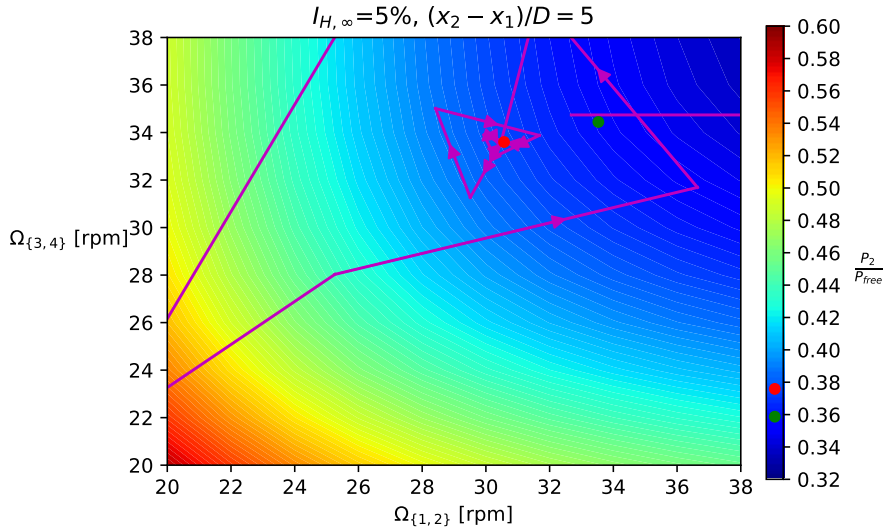

Figure 4.48: Power production of turbine 2 in optimization of $\Omega_{\{1,2\}}$ and $\Omega_{\{3,4\}}$. Green dot = $(\Omega_{\{1,2\}}, \Omega_{\{3,4\}})_{methodIII-calibration}$.

4.7.3 Yaw of turbine 1 support arms

The power production of turbine 1 can also be de-regulated by yawing the whole turbine, which will also deflect the wake. It was found in Subsection 4.4.2, that yawing the top and bottom support structures together, $\gamma_t = \gamma_b$, is better both in terms of power and wake recovery compared to $\gamma_t = -\gamma_b$ at $I_{H,\infty} = 5\%$, which is the TI used in this section.

Turbine 2 will as in the previous two subsections be modelled using method III-calibration with the optimized θ and Ω values in a non-yawed position, i.e. $\gamma_{t,2} = \gamma_{b,2} = 0°$. Turbine 1 will use method III and contrary to the previous section, the default values for θ and Ω are used to make the analysis directly comparable to the studies in Subsection 3.5.1 and 4.4.2. Figure 4.49 shows that the combined power production of turbine 1 and 2 can not be improved by the yawing of turbine 1 at any of the inter spacings investigated here, which was also the conclusion for a single-rotor turbine in Subsection 3.5.1. The power of respectively turbine 1 and 2 are shown in Figure 4.50, while the U-field is shown for the "extreme cases" of $(x_2 - x_1)/D = \{5, 10\}$ and $\gamma_b = \{0, 30\}°$. While these studies may seem pessimistic with regards to the prospects of wake steering, it must be stressed that other studies using other methods have shown more positive results.

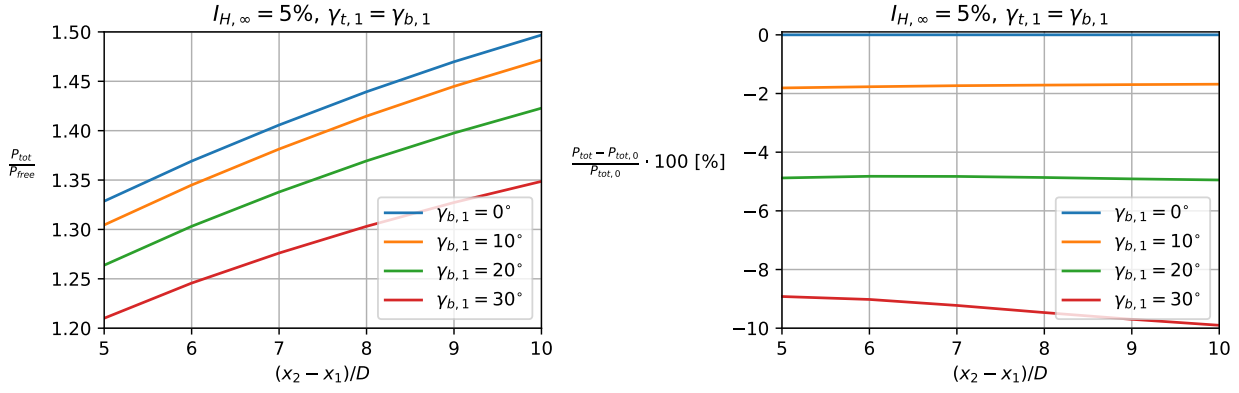

Figure 4.49: Total power production for varying yaw of turbine 1 and inter spacing. $P_{tot,0} = P_{tot}(\gamma_b = 0°)$.

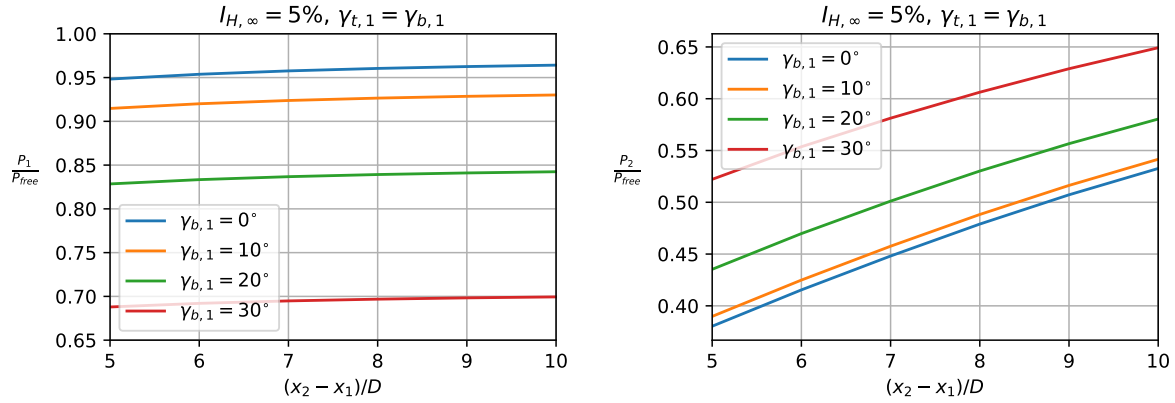

Figure 4.50: Power production of turbine 1 and 2 for varying yaw of turbine 1 and inter spacing.

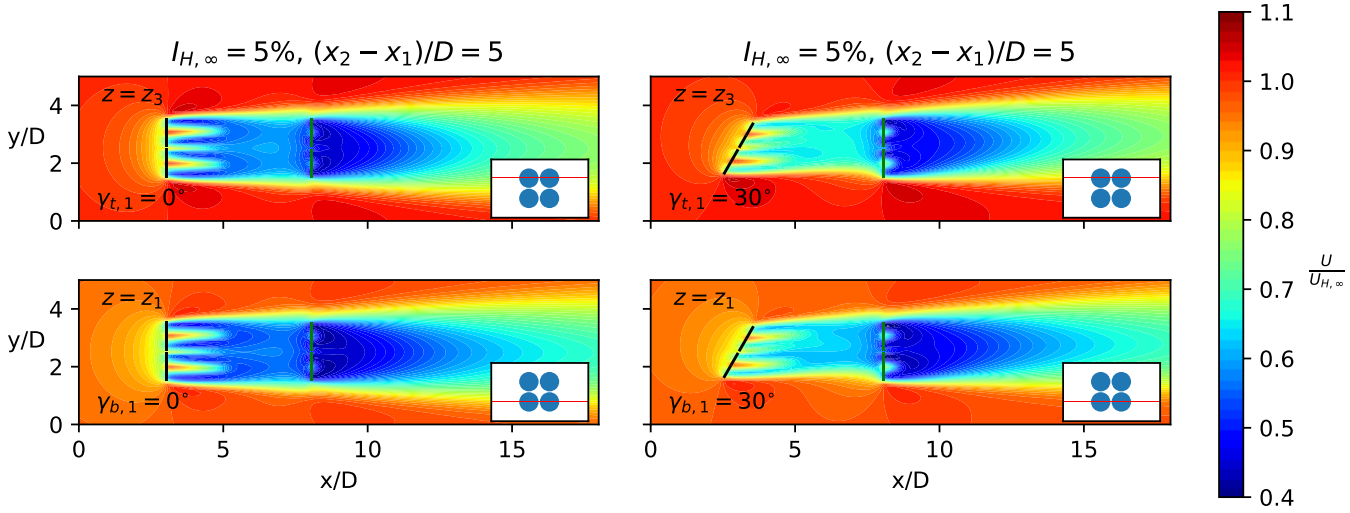

Figure 4.51: Top view of U at $z = \{z_1, z_3\}$, where turbine 2 is $5D$ downstream of turbine 1.

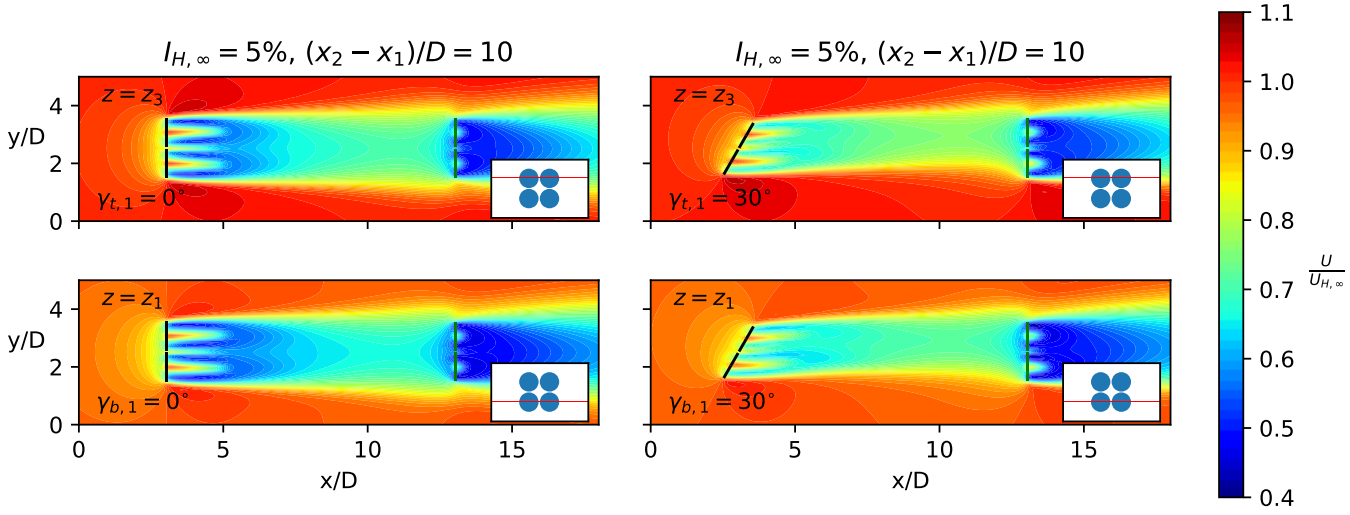

Figure 4.52: Top view of U at $z = \{z_1, z_3\}$, where turbine 2 is $10D$ downstream of turbine 1.

Chapter 5

Conclusion

Multi-rotor wind turbines have in recent years regained interest due to the potential cost savings associated with the square-cube-scaling law, but as the number of rotors increases, the complexity and number of possible configurations also increase manifold. This thesis has thus only investigated a small number of the many possible combinations of the parameters of the multi-rotor turbine and has mainly used the power production and velocity field as the metrics of performance. The flow and turbulence has been modelled with the RANS- and k-ε-f_P-equations, while the AD-airfoil method was used for the turbine, which assumes a stiff rotor. Even though the model is steady state it nevertheless predicts the power and wake characteristics rather well.

The RANS equations can be solved relatively fast on a HPC cluster compared to higher fidelity CFD methods like LES or DNS, and this enables the possibility to conduct parametric studies of the different settings of the multi-rotor turbine. The simulation tool used for this thesis was EllipSys3D, which has been used through the Python interface PyEllipSys, and several validation tests were first considered in Section 2.4 to gain confidence in the computational setup and grid studies were also performed in the same section.

A single-rotor turbine corresponding to the lower left rotor of the 4R-V29 was the first test subject of the analyses, and the effect of yaw and tilt were first considered, which revealed two interesting observations: $P \sim \cos^{2.2}(\gamma)$, which was also found to be true for a yawed multi-rotor turbine, and that the wake recovery is slightly faster for negative tilt compared to positive tilt, although the power production is the same for both. An optimizer was then coupled to EllipSys3D to optimize the pitch and rpm w.r.t. power production, and an improvement of 1.8% and 3.8% were found for low and high TI, respectively, compared to the default settings. In the end of the single-rotor chapter, two force control methodologies for simulating turbines operating in the wake of another were tested, where one required a calibration and the other an optimizer. Two aligned single-rotor turbines were considered for both of these methods and a larger ambient TI was for example seen to increase the power production of the second turbine considerably due to enhanced mixing of the impinging wake from the first turbine. Both methods also showed that the combined power of turbine 1 and 2 with a turbine spacing of $5D$ could not be increased by yawing the first turbine.

A double-rotor turbine was then considered to quantify the effect of rotor interaction between two co-planar disks caused by blockage effects, which can also be seen as the velocity speed-ups next to the rotor in the contour plots of the single-rotor simulations. The maximum power increase compared to a freestanding turbine was found to be 0.7-1.9% for low TI and 0.0-1.2% for high TI depending on the yaw and tilt of the rotors with optimal tip clearance in the order of $s_h/D \approx 0.01 - 0.15$. A vertical double-rotor turbine was also shortly investigated, which showed an opposite trend of larger power increase for high TI, but this type of turbine is only a hypothetical one, because more energy could be extracted with a horizontal type due to shear. The horizontal double-rotor turbine could however be feasible and the tilt of both rotors were varied simultaneously, which almost gave $P \sim \cos^{2.2}(\psi_{\{1,2\}})$.

Finally, the full 4R-V29 turbine was considered, where toe-out and tilt-out were first investigated, which however did not show any surprising results. Two types of tilt-out configurations were then tested: Asymmetric, $\psi_{\{3,4\}} = \psi_{\{1,2\}}$, and symmetric, $\psi_{\{3,4\}} = -\psi_{\{1,2\}}$, where the latter was found to produce more power. Next, the 16 possible combinations of counter-rotating disks were investigated, but the difference in power and wake recovery compared to a conventional turbine with all CW-rotating disks was minimal. The interaction of counter-rotating co-planer disks might well be a time dependent phenomenon, hence transient methods as LES or URANS could reveal other results, and could be of interest for future studies. Similar to the

single-rotor studies, the 4R-V29 was also optimized with regards to pitch and rpm, and power increases of 2.8% and 4.9% were found compared to the default settings for low and high TI, respectively. Only low TI inflow was used for the simulation of two aligned 4R-V29 turbines, where de-regulation of turbine 1 in form of lower rotational speed and yaw of the support structures were tested. The wake steering control was again not able to improve the combined power production for a range of different inter spacings, but the rotational speed control optimization, however showed a small improvement of the total power of 0.9%.

Many interesting future studies of the multi-rotor turbine can be imagined. For example, one could perform a comparision of the multi-rotor wind turbine and an equivalent single-rotor wind turbine based on the AD-airfoil method, instead of the scaled force AD-methods as conducted in [14], [15], [16], which have axis-symmetric force distributions contrary to the AD-airfoil method used in thesis. It might however be challenging to construct such an equivalent single-rotor turbine, since the geometry and airfoils of the blade would have to be scaled properly for a fair comparison. Another interesting subject could be the effect of shutdowns of one or more of the rotors and how this would effect the wake. Finally, the tip clearance has been seen to impact the rotor interaction, but the free space in between the four rotors might also be very relevant for the rotor interaction, and this could be varied by considering a 4R-V29 in different staggered arrangements. As of now, the relevance of these questions will depend on whether the multi-rotor turbines will be able to outperform the single-rotor turbines in terms of LCoE.

Appendix A

AD models

A.1 Method 0: AD Prescribed

Method 0 can only be used for wind turbines, where the undisturbed inflow is known, i.e. turbines not operating in the lee of another turbine. The C_T (or thrust), C_P (or power) and rotational speed curves need also to be known.

- Step 1: Since $\mathbf{U}_\infty(z)$ is known, calculate $U_{\infty,AD}(z = z_H) = U_{H,\infty,AD}$. This is the undisturbed velocity at hub height in the x_R-direction of the AD-system.
- Step 2: Read off C_T, C_P and Ω in a look-up table using $U_{H,\infty,AD}$.
- Step 3: Calculate thrust and torque:

$$T = \frac{1}{2}\rho U_{H,\infty,AD}^2 A C_T \tag{A.1}$$

$$\tau = \frac{P}{\Omega} = \frac{\frac{1}{2}\rho U_{H,\infty,AD}^3 A C_P}{\Omega} \tag{A.2}$$

- Step 4: Calculate normal and tangential force distributions using either uniform or scaled loading:

$$f_{x_R}(r,\varphi) = \begin{cases} \frac{T}{\pi R^2} & \text{uniform thrust distribution} \\ \frac{B q_{x_R}^{AD}(r)}{2\pi r} & \text{scaled thrust distribution} \end{cases} \tag{A.3}$$

$$f_\phi(r,\varphi) = \begin{cases} \frac{3\tau}{2\pi R^3} & \text{uniform tangential force distribution} \\ \frac{B q_\varphi^{AD}(r)}{2\pi r} & \text{scaled tangential force distribution} \end{cases} \tag{A.4}$$

$$q_{x_R}^{AD}(r) = \hat{q}_{x_R}^{AD}(r)\frac{T}{B} \tag{A.5}$$

$$q_\varphi^{AD}(r) = \hat{q}_\varphi^{AD}(r)\frac{\tau}{B} \tag{A.6}$$

  Scaled loading: The normalized blade loadings, $\hat{q}_{x_R}^{AD}(r)$ and $\hat{q}_\varphi^{AD}(r)$, are obtained from higher fidelity CFD models, e.g. full-rotor DES or LES-AL, [26]. Since these normalized blade loadings are given only as a function of r, $f_{x_R}(r,\varphi) = f_{x_R}(r)$ and $f_\varphi(r,\varphi) = f_\varphi(r)$, i.e. they are azimuthal symmetric. No tip correction is needed for this method since this is indirectly included through $\hat{q}_{x_R}^{AD}(r)$ and $\hat{q}_\varphi^{AD}(r)$.

  Uniform loading: The thrust and tangential force distributions for uniform loading are of course also azimuthal symmetric. This method can be applied, if $\hat{q}_{x_R}^{AD}(r)$ and $\hat{q}_\varphi^{AD}(r)$ are unknown and if the main interest is the far wake.

  The thrust and torque are the same for both scaled and uniform loading, but their distributions over the disk differ.

- Step 5: The thrust and tangential force distribution will stay constant during the simulation, hence the name "prescribed".

A.2 Method I: AD Induction

For a wind turbine operating in the wake of another, there is no clear definition of $\mathbf{U}_\infty(z)$. It depends on the operating state of the upstream turbine, the atmospheric conditions and the relative distance. Furthermore, there might be a time dependence, e.g. down-regulation of the upstream turbine. Thus, variable AD methods are needed. The AD induction method is the most simple of these and is based on 1D momentum theory:

- Step 1: In the first iteration, guess $U_{H,\infty,AD}$.
- Step 2-4: Same as step 2-4 in method 0.
- Step 5: Probe $\langle U \rangle_{AD}$, use C_T from step 2 and estimate $U_{H,\infty,AD}$:

$$a_x = 0.5(1 - \sqrt{1 - C_T}) \tag{A.7}$$

$$U_{H,\infty,AD} = \frac{\langle U \rangle_{AD}}{1 - a_x} \tag{A.8}$$

- Step 6: Step 2-5 are repeated in the next iteration.

This method might not be appropriate for yawed and tilted AD's, since it is based on 1D momentum theory. It is also found to generally overpredict power production and be numerically unstable for certain inflow velocity conditions, [27].

A.3 Method II: AD Variable Scaling

The AD variable scaling method was introduced by van der Laan et. al [27] as an alternative to method I and III for especially wind farm calculations. It does not suffer of numerical unstability like method I and neither overpredicts power above rated wind speed like method III does. A calibration is needed, before it can be applied.

For this method $C_T(U_{H,\infty})$, $C_P(U_{H,\infty})$ and $\Omega(U_{H,\infty})$ are assumed to be known.

Calibration step:

- Step 1: Set inlet to $U_{H,\infty} = 4$ m/s.
- Step 2: Same as step 2-4 in method 0.
- Step 3: Probe $\langle U \rangle_{AD}$ and calculate:

$$C_T^* = C_T \left(\frac{U_{H,\infty}}{\langle U \rangle_{AD}} \right)^2 \tag{A.9}$$

$$C_P^* = C_P \left(\frac{U_{H,\infty}}{\langle U \rangle_{AD}} \right)^3 \tag{A.10}$$

$$\Omega^* = \Omega \tag{A.11}$$

- Step 4: Repeat step 1-3 with $U_{H,\infty} = \{5, 6, 7, \ldots, 25\}$ m/s. Construct a table with columns:

$$\text{Control-file: } \begin{bmatrix} | & | & | & | \\ \langle U \rangle_{AD} & C_T^* & C_P^* & \Omega^* \\ | & | & | & | \end{bmatrix} \tag{A.12}$$

Application:

- Step 1: Initialize solution, i.e. assign the value of the 6 flow variables at all cells.
- Step 2: Sample $\langle U \rangle_{AD}$ and obtain C_T^*, C_T^* and Ω^*.
- Step 3: Calculate thrust and torque:

$$T = \frac{1}{2}\rho \langle U \rangle_{AD}^2 A C_T^* \tag{A.13}$$

$$\tau = \frac{P}{\Omega} = \frac{\frac{1}{2}\rho \langle U \rangle_{AD}^3 A C_P^*}{\Omega^*} \tag{A.14}$$

- Step 4: Same as step 4 in method 0.
- Step 5: Step 2-4 are repeated in the next iteration.

A.4 Method III: AD Airfoil

The method is described in Subsection 2.1.2.

A.4.1 Extension: Method III-calibration

Method III can not be used for a turbine in the wake of another, unless the method is extended with pitch- and rpm-control. This is achieved in method III-calibration with a calibration similar to the one in method II.

$\Omega(U_{H,\infty})$ and $\theta(U_{H,\infty})$ are assumed to be known, as well as blade geometry, i.e. $\beta(r)$, $c(r)$ and airfoil-type(r), and airfoil data, i.e $c_l(\alpha, Re)$ and $c_d(\alpha, Re)$. Usually, the airfoil data is given for a specific Re.

Calibration step:

- Step 1: Set inlet to $U_{H,\infty} = 4$ m/s.
- Step 2: Look up or interpolate Ω and θ using $U_{H,\infty}$. Run simulation with method III and these values, c.f. Subsection 2.1.2.
- Step 3: Probe $\langle U \rangle_{AD}$, calculate C_T^*, C_T^* and Ω^* with eq.A.9-A.11, set $\theta^* = \theta$ and calculate λ^*:

$$\lambda^* = \frac{\Omega^* R}{U_{H,\infty}} \tag{A.15}$$

- Step 4: Repeat step 1-3 with $U_{H,\infty} = \{5, 6, 7, \ldots, 25\}$ m/s. Construct a table with columns:

$$\text{Control-file: } \begin{bmatrix} | & | & | & | & | & | \\ \langle U \rangle_{AD} & C_T^* & C_P^* & \Omega^* & \theta^* & \lambda^* \\ | & | & | & | & | & | \end{bmatrix} \tag{A.16}$$

Application:

- Step 1: Initialize solution, i.e. assign the value of the 6 flow variables at all cells.
- Step 2: Sample $\langle U \rangle_{AD}$ and obtain θ^*, Ω^* and λ^*.
- Step 3: Use method III described in Subsection 2.1.2, but with $\theta = \theta^*$, $\Omega = \Omega^*$ and $\lambda = \lambda^*$
- Step 4: Step 2-3 are repeated in the next iteration.

Appendix B

Discretization of RANS equations

B.1 Discretized equations

A set of discrete equations are obtained by integrating the RANS equations from Section 2.3 with respect to time and volume, and discretizing these integrals. This process is quite involved for several reason: The equations of the Section 2.3 first have to be cast into an alternative form called the *conservation form*, which makes sure that the flow variables are conserved for each cell, no matter how small or large the cells are. The idea is to convert the convective terms into a divergence form, and eq. 2.40 for example becomes:

$$\frac{\partial \rho U_i}{\partial t} + \nabla \cdot (\rho U_i \mathbf{u}) = -\nabla P - \rho \frac{2}{3} \nabla k + (\mu + \mu_T) \nabla \cdot (\nabla U_i) + \overline{f_i} \tag{B.1}$$

The mixed Einstein and divergence notation is used on purpose, since it hints to the use of Gauss' theorem, which can be used when eq. B.1 is integrated over the volume of a cell:

$$\rho \int_V \frac{\partial U_i}{\partial t} dV + \rho \int_S (U_i \mathbf{U}) \cdot \mathbf{dA} = \int_V \left(-\nabla P - \rho \frac{2}{3} \nabla k + \overline{f_i} \right) dV + (\mu + \mu_T) \int_V (\nabla U_i) \cdot \mathbf{dA} \tag{B.2}$$

For a cell with volume V and f faces, each with area vector $\mathbf{A}_f$, the momentum equations can be discretized as:

$$\rho \frac{\partial U_i}{\partial t} V + \rho \sum_f (U_{i,f} \mathbf{U}_f) \cdot \mathbf{A}_f = \left(-\nabla P - \rho \frac{2}{3} \nabla k + \overline{f_i} \right) V + (\mu + \mu_T) \sum_f (\nabla U_{i,f}) \cdot \mathbf{A}_f \tag{B.3}$$

The subscript f denotes, that the quantity is evaluated at the face f, and it is thus apparent that the velocity needs to be evaluated at the face. As mentioned in Subsection 2.3, the velocity is stored in the center of the cell in a collocated arrangement, and some sort of interpolation technique is therefore needed. This is usually done with the Rhie-Chow algorithm to avoid "numerical wiggles", which can be caused by an odd-even pressure decoupling (the so called "checkerboard solutions"). The problem however pertains for flows with discrete body forces, like for example AD forces, and the problem is solved with the *pressure jump method* developed in [50] and improved in [32]. The idea is to transform the body force located at the cell center to face pressures, $\hat{p}_f$, which fulfills:

$$f_i V = \sum_f \hat{p}_f A_{i,f} \tag{B.4}$$

The method for calculating $\hat{p}_f$ is what separates [50] and [32], where in the latter a "center-of-gravity"-modification is added: The body force, f_i, is typically composed of forces from several domain cells (cf. Figure 2.8) and the way that $\hat{p}_f$ is distributed should reflect this. This is done by calculating the "center-of-gravity":

$$\mathbf{r}_F = \frac{\sum_{l=1}^{N^{IP}} S_l^{IP} \mathbf{r}_l}{\sum_{l=1}^{N^{IP}} S_l^{IP}} \tag{B.5}$$

where N^{IP} are the number of shape cells within the i'th domain cell, S_l^{IP} is the overlapping area of l'th shape cell and i'th domain cell and $\mathbf{r}_l$ is the center position of the l'th shape cell. From $\mathbf{r}_F$ and the total force on the i'th domain cell, $\hat{p}_f$ can be calculated for the different faces of the i'th domain cell. The way to do this is described in [32] and it is indeed found to eliminate the numerical wiggles for any orientation of the AD.

The above discussion is somewhat simplified, because in reality the RANS equations are first transformed from Cartesian to curvilinear coordinates to allow the grid to adapt to complex boundaries, which add a lot of extra terms. Secondly, the time integration has not been performed and thirdly it has not been mentioned how to calculate the gradients. On top of this, several differencing schemes exists (EllipSys3D uses for example the QUICK scheme) and serious care must be taken so that the resulting algebraic equations are linear, decoupled, conservative, bounded and transportive. A complete description of the procedure used in EllipSys3D is found in [20].

B.2 SIMPLE algorithm

The resulting discretized equations are solved forward in time with the SIMPLE technique, which is a so called *pressure correction technique*. For the case of steady flow, the time step is instead called an *iteration*, and Δt is not a physical time step, but merely a numerical parameter. The general outline of the technique (without turbulence modelling) is:

1. Guess initial pressure and velocity field, $(p*)^n$, $(u*)^n$, $(v*)^n$ and $(w*)^n$.
2. Use initial fields and the momentum equations to calculate $(u*)^{n+1}$, $(w*)^{n+1}$ and $(w*)^{n+1}$.
3. Correct this velocity field with the continuity equation, i.e. create a pressure correction, p', and set $p^{n+1} = (p*)^n + p'$.
4. For the pressure correction to have an effect, set $(p*)^n = p^{n+1}$, return to step 2 and recompute $(u*)^{n+1}$, $(v*)^{n+1}$ and $(w*)^{n+1}$.
5. Step 2-4 are repeated until convergence, and the final velocity field at step n+1 is: $u^{n+1} = (u*)^{n+1}$, $v^{n+1} = (v*)^{n+1}$ and $w^{n+1} = (w*)^{n+1}$. One iteration has now been completed.

The above procedure is superficial and only presented for the case without the k and ε, but nevertheless gives an overall idea of the algorithm, which is more thoroughly described in for example [18].

B.3 Residuals

Many iterations are needed to reach a converged solution, and the amount of iterations depends on the initial conditions, grid size, AD, desired accuracy, etc. *Residuals* are useful for determining when to stop and are defined for each of the flow variables (U, V, W, P, k, ε). Each of the Navier-Stokes equations eventually ends up as a linear, decoupled and algebraic equation [20], which gives the following generic equation for each grid point P (nb = neighbour and S = source terms):

$$A_P \phi_P + \sum A_{nb} \phi_{nb} = S \tag{B.6}$$

There are hence as many equations as there are cells, and these equations can be compressed into a linear system $\underline{\underline{A}}\boldsymbol{\phi} = \boldsymbol{S}$, which is solved iteratively and the residual at step n is:

$$\boldsymbol{\rho}^n \equiv \mathbf{S} - \underline{\underline{A}}\boldsymbol{\phi}^n \tag{B.7}$$

In EllipSys3D, the residuals are reduced to a single scalar for each of the flow variables and normalized by the initial solution. The simulation is stopped, when the convergence criterion is reached for all of the flow variables, i.e. $\rho^n_{\{U,V,W,P,k,\varepsilon\}} < 10^{-5}$ (the justification for choosing this number is shown in Section 2.4.6), which for example can be seen in the example in Figure B.1. The reason for the sudden increase in residuals approximately halfway through the simulation, is because a *grid level technique* is used, where a coarse grid

is first used to obtain a solution. When this solution is obtained (i.e. the residuals are all less than 10^{-5}), the grid is refined and the coarse solution is used as the initial solution.

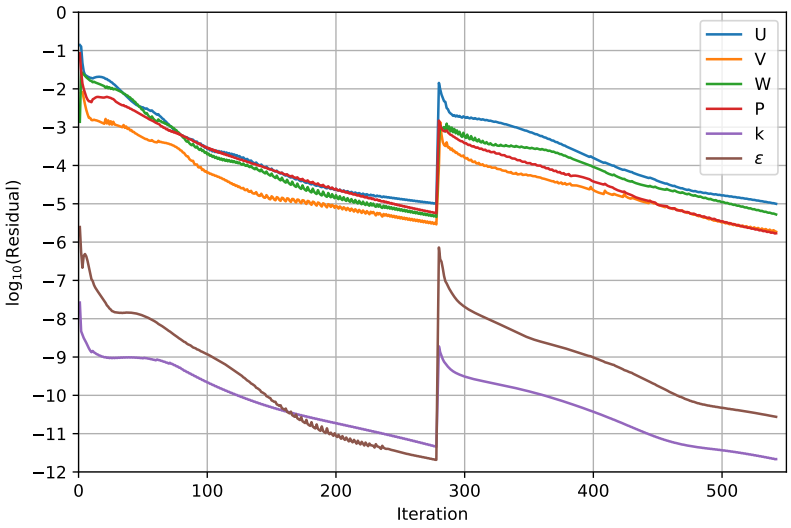

Figure B.1: Example of the residuals in a D/5 simulation.

B.4 Boundary and initial conditions

6 boundary conditions (BC) must be described on each boundary of the computional domain, because the system of equations consists of 6 equations. The flow variables also need to be initialized at all cell centers.

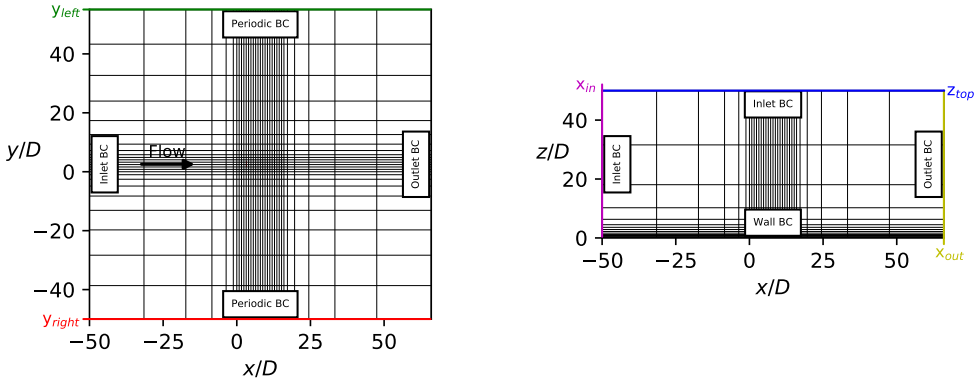

Figure B.2: Boundary conditions.

Inlet:

The boundary conditions for the inlet of the computational domain has already been discussed in Section 1.5, c.f. eq. 1.17-1.19. A constant pressure gradient equal to zero is assumed at the inlet, i.e. $\frac{\partial P(x_{in},y,z)}{\partial x} = 0$. The values of the flow variables are probed near the inlet and compared to the theoretical formulaes in Subsection 2.4.7.

Top:

Eq. 1.17-1.19 are evaluated at $z_{top} = 50D$ and these values are used for all (x, y, z_{top}) points. The top boundary is therefore also in principle an inlet.

Ground:

It is clear that ε becomes very large for $z \to 0$ and the atmospheric k-ε model, c.f. [28], is indeed only valid at high Reynolds numbers, which is not fulfilled at the ground because of the no-slip condition. The boundary at $z = 0$ is instead modelled as a "rough wall", where the flow domain is placed on top of the roughness height. The values of U and ε in the first layer of cells are calculated with analytical formulas [20], [51], while a Neumann condition is imposed on k in the first cell:

$$\frac{\partial k}{\partial z}|_{x,y,z_0<z<(z_0+\Delta z)} = 0 \tag{B.8}$$

where Δz is the height of the first cell.

Sides:

The sides of a domain are normally modelled either as symmetry planes aka. slip walls, where $V = 0$ and $\frac{\partial U}{\partial y} = \frac{\partial W}{\partial y} = \frac{\partial P}{\partial y} = \frac{\partial k}{\partial y} = \frac{\partial \varepsilon}{\partial y} = 0$, or as periodic boundaries, where:

$$U_i(x, y_{left}, z) = U_i(x, y_{right}, z) \tag{B.9}$$
$$P(x, y_{left}, z) = P(x, y_{right}, z) \tag{B.10}$$
$$k(x, y_{left}, z) = k(x, y_{right}, z) \tag{B.11}$$
$$\varepsilon(x, y_{left}, z) = \varepsilon(x, y_{right}, z) \tag{B.12}$$

The periodic boundary condition is usually preferred for flows, which do not have y-symmetry, for example if the inlet has a V-component or if the turbine is yawed.

Outlet:

A fully developed solution is assumed at the outlet, which means that $\frac{\partial}{\partial x}|_{x_{out},y,z} = 0$ (would be a normal derivative in the general case), where $x_{out} = 66D$ in this case, c.f. Figure 2.1. Global mass conservation is not guaranteed with this assumption, so the velocities at the outlet are scaled with the ratio of the inlet mass flux to the outlet mass flux:

$$U_{scaled}(x_{out}, y, z) = \frac{\int_{-50D}^{55D+s_x} \int_0^{50D} \rho U(x_{in}, y, z) dydz}{\int_{-50D}^{55D+s_x} \int_0^{50D} \rho U(x_{out}, y, z) dydz} U(x_{out}, y, z) \tag{B.13}$$

Initial conditions:

The flow variables are initialized in all of the interior grid points with the log-law values also used for the inlet and top, i.e. 1.17-1.19.

Summary

A summary of the BC's and initial conditions are given in Table B.1 and they are specified in EllipSys3D through input files (inlet and initial conditions are set in the usual `input.dat`-file, while wall, periodic and outlet BC's are set in another `input.dat`-file used for the grid generation).

	U	V	W	P	k	ε
Inlet	Eq. 1.17	0	0	$\frac{\partial P}{\partial x} = 0$	Eq. 1.18	Eq. 1.19
Top	Eq. 1.17	0	0	$\frac{\partial P}{\partial x} = 0$	Eq. 1.18	Eq. 1.19
Ground	[51]	0	0	$\frac{\partial P}{\partial x} = 0$	$\frac{\partial k}{\partial z} = 0$	[51]
Sides	Eq. B.9	Eq. B.9	Eq. B.9	Eq. B.10	Eq. B.11	Eq. B.12
Outlet	$\frac{\partial U}{\partial x} = 0$	$\frac{\partial V}{\partial x} = 0$	$\frac{\partial W}{\partial x} = 0$	$\frac{\partial P}{\partial x} = 0$	$\frac{\partial k}{\partial x} = 0$	$\frac{\partial \varepsilon}{\partial x} = 0$
Initial condition	Eq. 1.17	0	0	0	Eq. 1.18	Eq. 1.19

Table B.1: Summary of BC and initial conditions.

Appendix C

Additional results

C.1 Method III-calibration and method III-optimizer with optimized pitch and rpm

The optimized pitch and rpm values of Figure 3.27 is used to make the calibration in Figure C.1 and the test case 1 and 2 of Table 3.6 are conducted with these. The calibration in Figure C.1 appears slightly more "bumpy" compared to Figure 3.29, which comes from the optimization results in Figure 3.27. However, for $I_{H,\infty} = 5\%$ and $\langle U \rangle_{AD} < 4.83$ m/s (corresponding to $U_{H,\infty} = 7$ m/s) the settings are approximately constant $\theta \approx -2.4°$ and $\lambda \approx 7.3$.

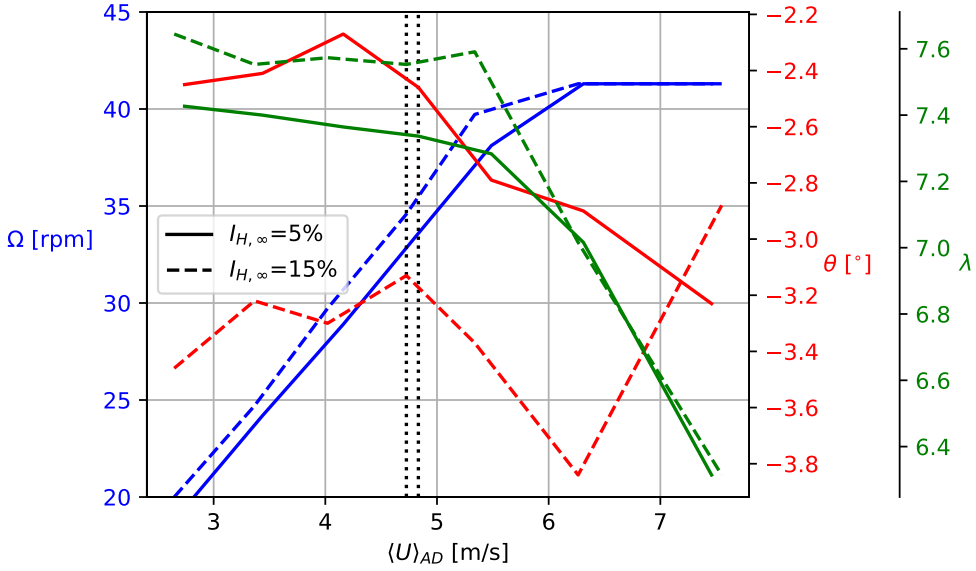

Figure C.1: Calibration from optimized pitch and rpm values. The vertical dotted lines indicate the disk averaged velocity, $\langle U \rangle_{AD}$, for an inflow of $U_{H,\infty} = 7$ m/s and $I_{H,\infty} = \{5, 15\}\%$.

	θ_1 [°]	θ_2 [°]	Ω_1 [rpm]	Ω_2 [rpm]	λ_1	λ_2
Case 1	-2.4	-2.4	33.6	Optimized	7.3	7.3
Case 2	-2.4	-2.4	Optimized	Optimized	$\frac{2\pi\Omega_1 R}{60 U_{H,\infty}}$	7.3

Table C.1: Method III-optimizer studies of the $(x_2 - x_1)/D = 5$ configuration, but now with an optimized calibration. Inflow upstream of turbine 1: $U_{H,\infty} = 7$ m/s and $I_{H,\infty} = 5\%$.

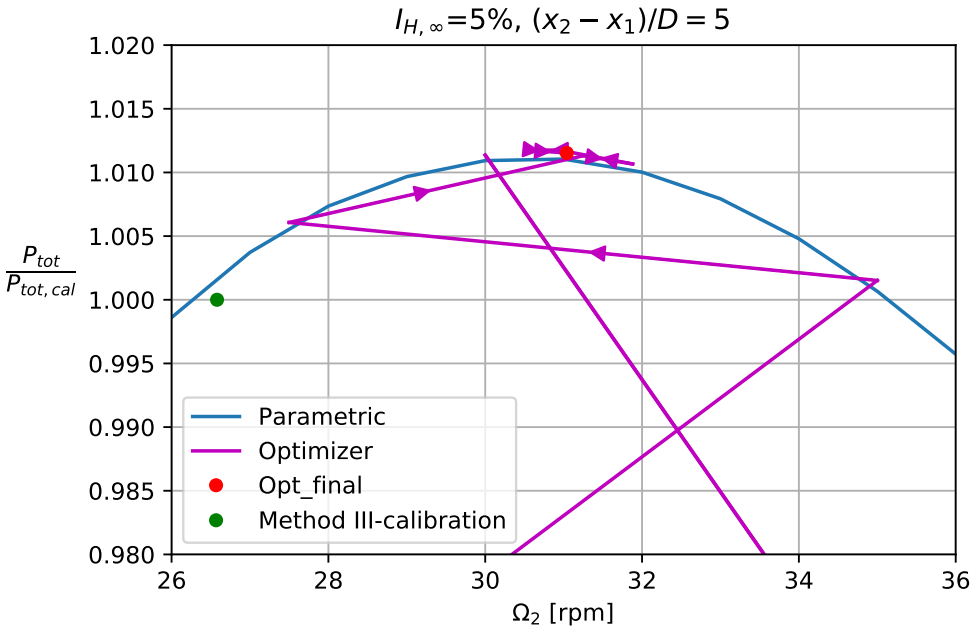

Figure C.2: Case 1 updated with optimized calibration.

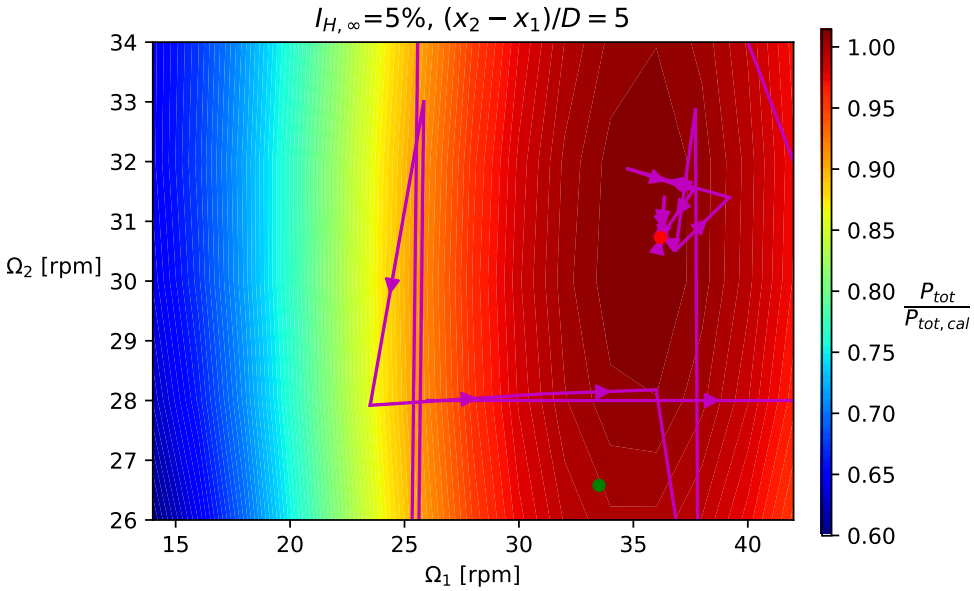

Figure C.3: Case 2 updated with optimized calibration.

The parametric study is slightly off the variable scaling value, because the assumption of $\theta_2 \approx -2.4$ and $\lambda_2 = 7.3$ might be slightly off the values predicted by method III-calibration.

C.2 4R-V29 optimization with high ambient TI

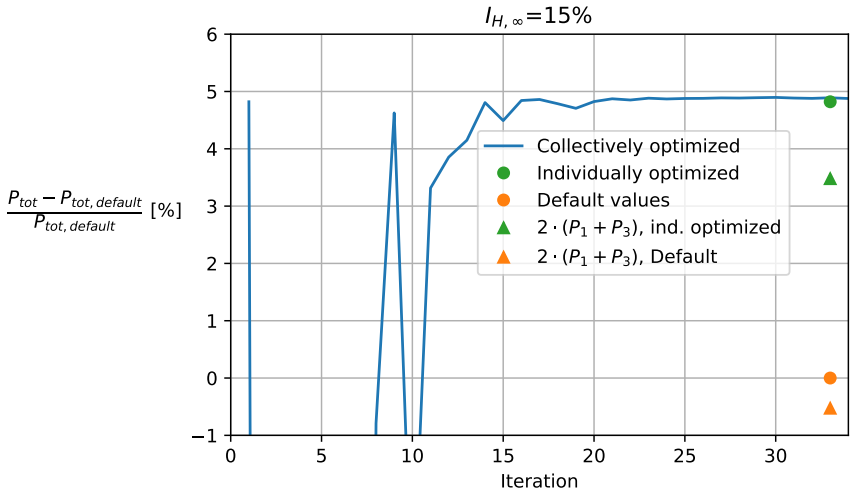

Figure C.4: Iteration process of the collective optimizer.

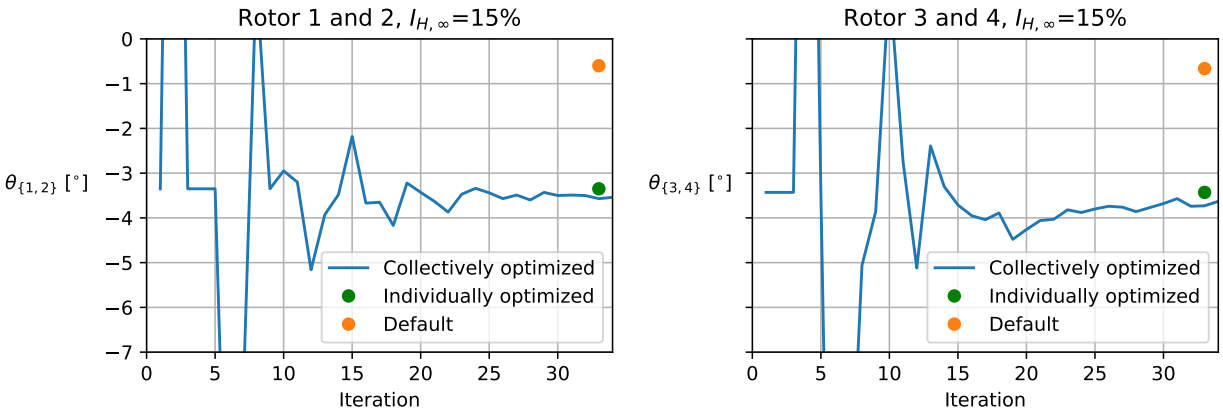

Figure C.5: Pitch vs. iteration in the collective optimizer.

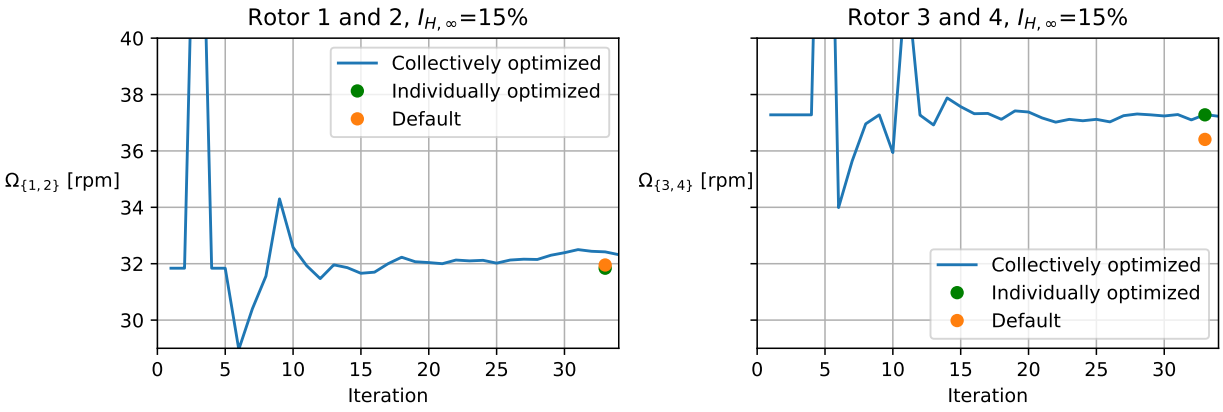

Figure C.6: Rotational speed vs. iteration in the collective optimizer.

Appendix D

PyEllipSys and Cluster FAQ

D.1 FAQ

Here is a list of problems and questions I have encountered in PyEllipSys/EllipSys3D during my thesis and their solutions:

- **What is the format of adinput.dat?**

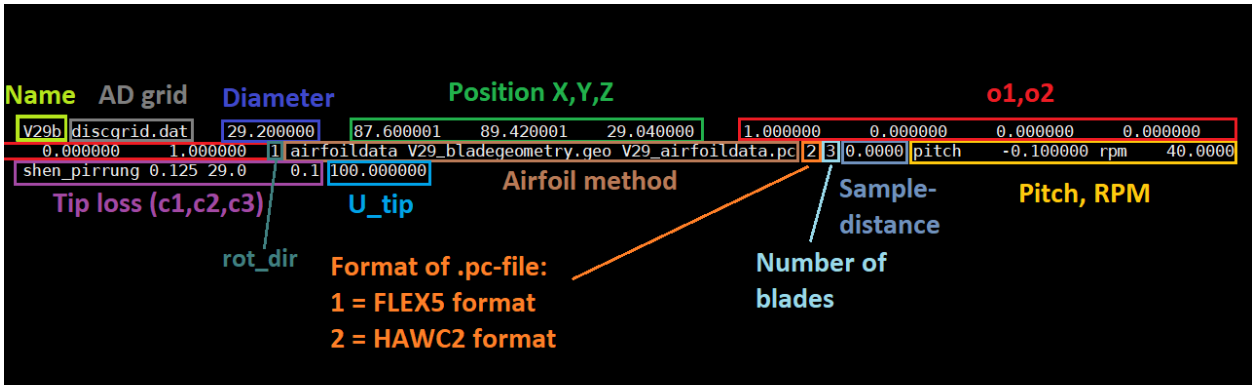

Figure D.1: adinput.dat structure for the airfoil method (aka. method III).

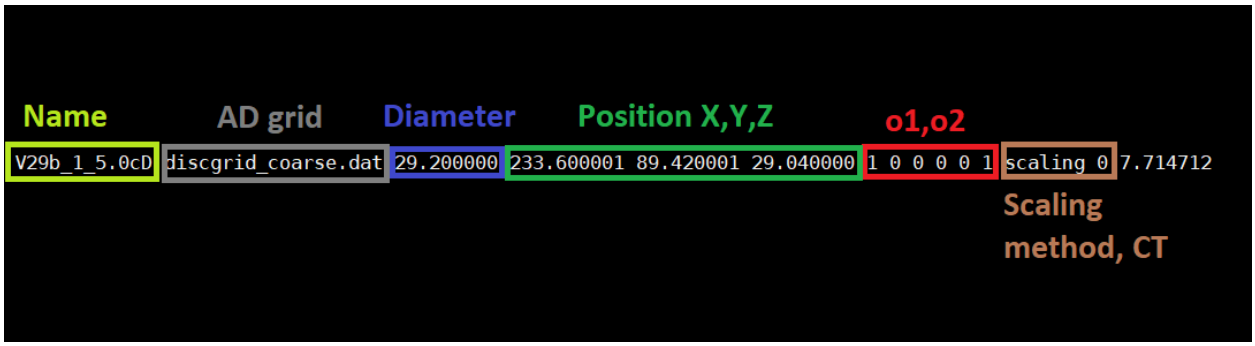

Figure D.2: adinput.dat structure for AD prescribed with scaled loading (aka. method 0). $C_T = 0$, because this disk is used as a "probe disk".

The distributions of $\hat{q}_N^{AD}(r)$ and $\hat{q}_T^{AD}(r)$ used in method 0 are supplied to PyEllipSys as a 4th and 5th column in `discgrid.dat`, but if $C_T = 0$ (as is the case in Figure D.2) or $U_{H,\infty} = 0$, then they can be omitted, because the force distribution will be 0 anyway. The disk in Figure D.2 has no rotational force distribution, but this can be added, by adding the keyword `rotation` to the end of the line.

- **What is rot_dir?**

  This is used to switch between a CW (rot_dir = 1) and CCW (rot_dir = −1) disk. This can be set in PyEllipSys via adinput.dat or with the `e3d.adcontrol.set_ad_rot_dir([disk number],[rot_dir])` method.

- **What is U_{tip} and "sample distance"?**

  U_{tip} is the velocity used to calculate the TSR and it can be controlled in PyEllipSys with set_adfreestream. The "sample distance" is the distance from the disk at which the velocities are sampled (I believe it is the normal distance, probably with o1 as the positive direction). These velocities are used in the AD methods to calculate the forces.

- **Can I use method I and II in PyEllipSys as well?**

  Method II can be used, which will have the keyword `variable_scaling`, where a file with $[U_\infty, C_T^*, C_P^*, \text{RPM}, \theta]$ needs to be supplied. I am not aware if method I can be used.

- **What is the format of ADres.dat?**

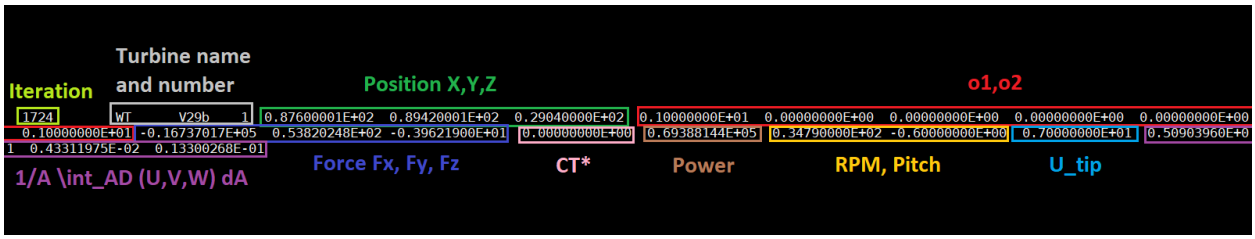

Figure D.3: ADres.dat structure.

Some small notes about C_T^* and U_{tip} in ADres.dat:

- For method 0 and I: $C_T^* = CT$.
- For method III: $C_T^* = 0$. The ADres.dat example in Figure D.3 is thus taken from a simulation with method III.
- For method III-calibration: C_T^* is obtained from the control-file and was used in the *old* version of PyEllipSys to calculate U_{tip}:

$$U_{tip} = \langle U \rangle_{AD} \cdot (1 + 0.25 C_T^*) \tag{D.1}$$

$$\langle U \rangle_{AD} = \frac{1}{A} \int_A U dA \tag{D.2}$$

In the *updated* version of PyEllipSys, U_{tip} is calculated as:

$$U_{tip} = \frac{\Omega^* R}{\lambda^*} \tag{D.3}$$

- **My scaling AD's used for probing velocity downstream are not working (PyEllipSys is either crashing with error 11 or all the probing disks are placed at the position of the last real AD)**

  - This problem occurs, if you in input.dat use `acdisc as_out 1 1 50`, since this only works for AD airfoils. So change this to `acdisc`.

  If all the scaling AD's are located at the same position as the last airfoil AD, it could also be because the parameters for scaling AD in input.dat have been seperated by tabs (should be seperated with space).

- **What is the difference between e3d.run() and e3d.step()?**

  - With **e3d.run()** PyEllipSys executes the simulation and finishes when the reslim specified in input.dat is reached. This is the simplest way of running PyEllipSys.
  - PyEllipSys simulates only 1 iteration with **e3d.step()**. A simulation often needs 1000's of iterations to converge and this method hence needs to be executed in a for or while loop. The advantage of using the *stepping method* is that you are in full control of the simulation, and for parametric studies (e.g. simulating the same turbine at 6 different yaw angles), a considerable amount of time can be saved using this method.

- **When I move my AD's, I get a "Polygon missing"-error?**

  This happens, when the AD is placed on the boundary between two cells, e.g. x/D=3 on a D/10 grid. The solution is to move the AD slightly, i.e. x/D=3.000001.

- **When using the step()-method discussed in the previous question, the program crashes when using e3d.adcontrol.set_ad_orientation(j,o1,o2)?**

  The set_ad_orientation-method requires that one step has already been taken. Solution: Run e3d.step(), before you set o1 and o2. *(This might seem a bit strange, since both set_ad_pitch and set_ad_rpm work fine without this trick.. But it's actually not: When calling set_ad_orientation, the intersectional grid has to be recomputed, which is not needed when rpm or pitch is changed.)*

- **My program stops at tipcorr == 2?**

  This is just before the mesh is loaded in, and the problem indeed has to due with the mesh. Solution: Go to the grid and look at how many blocks the grid consists of (see nblocks.dat). The number of processes used should be dividable in this. E.g. if there are nblocks=84, then you could for example use 42 processors (or 28, 21, 14, etc.), but not 43.

  This problem can also arise if your license have run out.

- **My program does not print out tipcorr == 2 nor AS area before the first iteration?**

  You have forgotten to write `acdisc` in the line after `actuatorshape [number]` in the input.dat-file.

- **The simulation stopped with "exit code 9"? (unsolved)** This is a memory problem. Has happenend to me with D/20 simulations. It has not been solved yet, but seems to have something to do with too many probe disks. It gets triggered by (a) Fine computational grid (i.e. D/20) (b) Too many probe disks (c) Too long simulation (e.g. parametric study with too many cases).

- **The program stops after grid level 2 with "signal 11"-code?**

  This error happened due to an error of stepping process and should e.g. not happen when `e3d.run()` is used instead. For my case, the bug was that the code was trying to step only at grid level 2, and never entered grid level 1.

- **RPM and power are both equal to 0 in ADres.dat?**

  This happened to me with the variable scaling airfoil method, when I accidentally wrote `rpmcontrol` instead of `rpm_control` in the adinput.dat-file.

- **The code proceeds to grid level 0, then -1, -2, etc. What is happening?**

  This can happen if the stepping method is used and the residuals reaches the reslim (set in input.dat). You should either increase reslim or figure why you are getting so low residuals.

- **My postprocessor got very slow after its license was renewed?**

  - Before renewal: qsub Bpost with 7700 points in 18 sec.
  - After renewal: qsub Bpost with 7700 points in 17 min 10 sec.

  The problem was caused by that the new postprocessor needed the pyelmod. The problem can be solved by modifying the Bpost script with two changes:

  1. Change `$mpirunn -np $NPROCS postprocessorMPI` to `mpirun -np $NPROCS postprocessorMPI`

2. Add `source pyelmod` before the above line.

- **How do I update EllipSys3D?**

  Just replace the EllipSys3DMPI.so-file with a new one.

- **How do I update PyEllipSys?**

  Replace the appropriate .py-file in the pyellipsys folder and then go one directory up to the folder, where setup.py is located. Enter "source pyelmod", to enter python mode. Then enter "pip install -e .", and then it should automatically install the updates and end the installation with a successful statement.

- **How do I check my version of EllipSys3D and PyEllipSys? (unsolved)**

  Python's version can be checked with `python --version` and VIM editor with `vi --version`, but unfortunately no equivalent exists for EllipSys3D and PyEllipSys.

- **What are the PBS variables in runbatch?**

  When a batch script is submitted with `qsub` , the first lines starting with #PBS are options to the resource manager (all other lines starting with # are comments) and the directory is changed to the home directory (i.e. /home/sXXXXX). A number of PBS (Portable Batch System) variables are also automatically initialized, which are shown in Table D.1.

Variable	Example
$PBS_O_WORKDIR	Absolute path to the directory from which qsub was executed.
$PBS_O_HOST	jess.dtu.dk, thul.fysik.dtu.dk, etc.
$PBS_JOBID	2094961.jess.dtu.dk (i.e. not only number, but also host!).
$PBS_JOBNAME	MRV29 (the name defined with #PBS -N option).
$PBS_NODEFILE	j-098 j-098 j-098 .. j-098 (#lines = #CPUS). Is copied to node_file.dat.
$PBS_JOBID	2094961.jess.dtu.dk (i.e. not only number, but also host!).

Table D.1: PBS variables initialized automatically.

- **What is the format of discgrid.dat?**

  The first line is [nr, nazi, columns]. The 3 columns are the x, y and z coordinates of the AD grid (i.e. the black vertices in Figure D.4). The velocities and forces are sampled in the center of the polygons created by these vertices (i.e. the blue dots in Figure D.4). The order of the points are: Starts at the smallest radius at 9 o'clock and moves CCW. Then it moves to the next-smallest radius at 9 o'clock and moves CCW, etc.

- **How can I get the distributions of AD normal and tangential forces/velocities?**

  - In input.dat use fx `acdisc as_out 1 2 50`, which prints out the AD distributions for every radial point and every 2 azimuthal point. It does this at every 50'th iteration and does it for all AD's defined in adinput.dat (only works for airfoil AD's). The output files are named grid.ASFN001, grid.ASFT001, etc.

- **What is the format of the grid.AS* files? How is the direction defined?**

  Each line represents an iteration output.

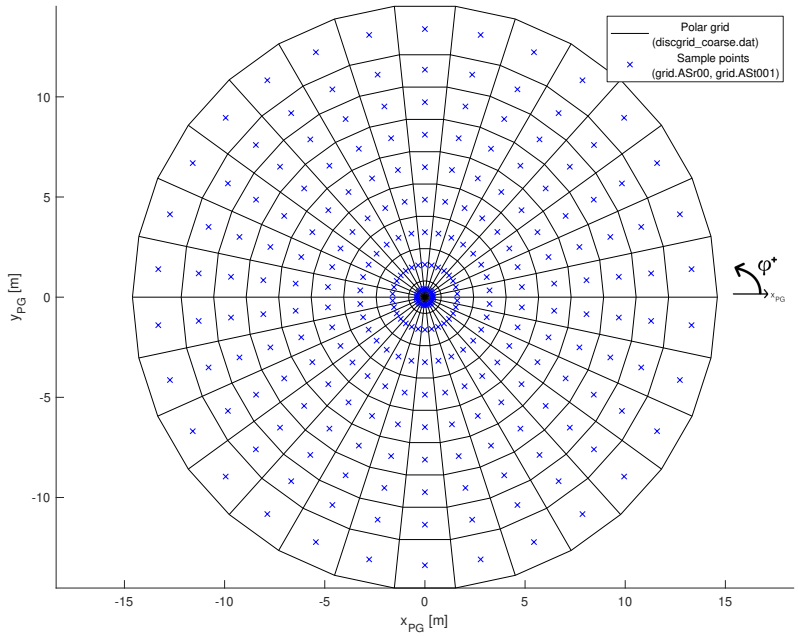

Figure D.4: Polar grid (black) with sample points (blue) seen from upstream.

As can be seen in Figure D.4, the sample points are located in the center of the cells.

grid.ASr00: Defines radial sample points. For some reason this is only produced once, even though more AD's are present.

j	r [m]
1	0.4056
2	1.6222
⋮	⋮
9	13.3833

Table D.2: Example of grid.ASr00.

grid.ASt*: Defines azimuthal sample points. The first half lacks a minus sign, so add it manually. The direction of φ is defined in Figure D.4 and $\varphi = 0$ at the positive y_{PG} axis.

i	$\varphi_{orig,i}$ [rad]	φ_i [rad]
1	3.0369	- 3.0369
2	2.8274	- 2.8274
⋮	⋮	⋮
8	$1.5708 \approx \pi/2$	$-1.5708 \approx -\pi/2$
⋮	⋮	⋮
15	0.1047	- 0.1047
16	0.1047	0.1047
⋮	⋮	⋮
29	2.8274	2.8274
30	3.0369	3.0369

Table D.3: Example of grid.ASt* and fix of all positive $\varphi_{orig,i}$ problem.

grid.FN*, grid.VN*: Defines normal force/area and normal velocity at each sample points. Positive direction in $-\hat{e}_{z_{PG}}$ direction, i.e. into the paper in Figure D.4. Starts at bottom of rotor, i.e. at $\varphi_8 \approx -\pi/2$.

iteration	$V_N(\varphi_8, r_1)$	$V_N(\varphi_8, r_2)$	...	$V_N(\varphi_8, r_9)$	$V_N(\varphi_9, r_1)$	$V_N(\varphi_9, r_2)$	...	$V_N(\varphi_7, r_9)$

Table D.4: Example of format of grid.VN*. Notice that it does NOT start at φ_1.

grid.FT*, grid.VT*: Defines the tangential force/area and velocity. Positive direction in $-\hat{e}_{\varphi}$ direction, i.e. clockwise in Figure D.4. The first value is located at (φ_8, r_1) and the structure is similar to Table D.4.

D.2 More help

There exists documentation on both PyEllipSys[23] and EllipSys3D[24], but they are both being developed at the moment.

[23] https://ellipsys.pages.windenergy.dtu.dk/pyellipsys/srcdocs.html
[24] EllipSys2D/3D User Manual (draft), Niels N. Sørensen, 2015

Appendix E

Errata

The following corrections have been made after the submission date, July 2, 2019:

- **Page v:** Symbol for rotor radius is R, not D.
- **Page v:** In the description of $U_{H,\infty}$ and $I_{H,\infty}$: "at height" $\rightarrow$ "height".

References

[1] J. Berg, J. Mann, M. Nielsen, and M. Kelly, *Introduction to Micro Meteorology for Wind Energy*. 2017, ISBN: 2005255546.

[2] J. Manwell, *Wind Energy Explained*. 2009, ISBN: 9780470015001.

[3] M. O. L. Hansen, *Aerodynamics of Wind Turbines*, 3rd ed. Routledge, 2015, ISBN: 9781844074389.

[4] Vindmølleindustrien. (2003). Drøm større, [Online]. Available: `http://dromstorre.dk/wp-content/wind/miller/windpower%20web/da/stat/units.htm` (visited on March 4, 2019).

[5] P. Jamieson, *Turbine Design Innovation in Wind*. 2011, ISBN: 9780470699812.

[6] J. F. Manwell, J. G. McGowan, S. Brena, and P. Verma, "A Comparative Study of a Three Rotor and a Single Rotor 5 MW Wind Turbine Based on Economic and Structural Considerations", *Wind Engineering*, vol. 38, no. 6, pp. 643–657, 2014, ISSN: 0309-524X. DOI: `10.1260/0309-524x.38.6.643`.

[7] P. Smulders, S. Orbons, and C. Moes, "Aerodynamic interaction between two wind rotors set next to each other in one plane", in *European Wind Energy Conference*, 1984.

[8] L. Kamp, *Learning in wind turbine development*. 2002, ISBN: 903933174X.

[9] D. Ransom, J. J. Moore, and M. Heronemus-Pate. (2010). Performance of Wind Turbines in a Closely Spaced Array - Renewable Energy World, [Online]. Available: `https://www.renewableenergyworld.com/articles/print/rewna/volume-2/issue-3/wind-power/performance-of-wind-turbines-in-a-closely-spaced-array.html` (visited on March 12, 2019).

[10] U. Göltenbott, "Aerodynamics of Multi-Rotor Wind Turbine Systems using Diffuser-Augmentation", PhD thesis, Kyushu University, 2017. DOI: `10.15017/1807035`.

[11] Y. Ohya, T. Karasudani, T. Nagai, and K. Watanabe, "Wind lens technology and its application to wind and water turbine and beyond", *Renewable Energy and Environmental Sustainability*, vol. 2, no. 2, 2017. DOI: `10.1051/rees/2016022`.

[12] Y. Ohya and K. Watanabe, "A New Approach Toward Power Output Enhancement Using Multirotor Systems With Shrouded Wind Turbines", *Journal of Energy Resources Technology*, vol. 141, no. 5, May 2019, ISSN: 0195-0738. DOI: `10.1115/1.4042235`.

[13] P. Chasapogiannis, J. M. Prospathopoulos, S. G. Voutsinas, and T. K. Chaviaropoulos, "Analysis of the aerodynamic performance of the multi-rotor concept", *Journal of Physics: Conference Series*, vol. 524, no. 1, 2014, ISSN: 17426596. DOI: `10.1088/1742-6596/524/1/012084`.

[14] N. S. Ghaisas, A. S. Ghate, and S. K. Lele, "Large-eddy simulation study of multi-rotor wind turbines", *Journal of Physics: Conference Series*, vol. 1037, no. 7, pp. 1–10, Jun. 2018, ISSN: 1742-6588. DOI: `10.1088/1742-6596/1037/7/072021`.

[15] P. van der Laan, S. J. Andersen, N. Ramos García, N. Angelou, G. R. Pirrung, S. Ott, M. Sjöholm, K. H. Sørensen, J. Xavier, V. Neto, M. Kelly, T. Krogh Mikkelsen, and G. C. Larsen, "Power curve and wake analyses of the Vestas multi-rotor demonstrator", *Wind Energ. Sci*, vol. 4, pp. 251–271, 2019. DOI: `10.5194/wes-4-251-2019`.

[16] P. van der Laan and M. Akbar, "Improved energy production of multi-rotor wind farms (postprint)", *Wake Conference 2019*, pp. 2–11, 2019.

[17] P. Kundu, *Fluid Mechanics*, 6th ed. Academic Press, 2016.

[18] J. D. Anderson, *Computational Fluid Dynamics*. McGraw Hill, 1995.

[19] J. D. Anderson, *Fundamentals of Aerodynamics*, 6th ed. McGraw Hill, 2017.

[20] N. N. Sørensen, "General purpose flow solver applied to flow over hills", PhD thesis, Technical University of Denmark, 1995.

[21] P. van der Laan, N. N. Sørensen, P.-E. Réthoré, J. Mann, M. C. Kelly, N. Troldborg, K. S. Hansen, and J. P. Murcia, "The k-ϵ-fp model applied to wind farms", *Wind Energy*, vol. 18, no. 12, pp. 2065–2084, December 2015, ISSN: 10954244. DOI: 10.1002/we.1804.

[22] P. van der Laan, "Efficient Turbulence Modeling for CFD Wake Simulations", PhD thesis, Technical University of Denmark, 2014.

[23] N. O. Jensen, "A Note on Wind Generator Interaction", *Riso-M-2411*, 1983.

[24] N. G. Nygaard, "Wakes in very large wind farms and the effect of neighbouring wind farms", *Journal of Physics: Conference Series*, vol. 524, no. 1, 2014, ISSN: 17426596. DOI: 10.1088/1742-6596/524/1/012162.

[25] A. Khamas, *Wind Farm Wake Modeling and Optimization Based on Multi Rotor Wind Turbines*. Aarhus University, 2018.

[26] P. van der Laan, N. N. Sørensen, P. E. Réthoré, J. Mann, M. C. Kelly, N. Troldborg, J. G. Schepers, and E. Machefaux, "An improved k-ϵ model applied to a wind turbine wake in atmospheric turbulence", *Wind Energy*, vol. 18, no. 5, pp. 889–907, May 2015, ISSN: 10991824. DOI: 10.1002/we.1736.

[27] P. van der Laan, N. N. Sørensen, P.-E. Réthoré, J. Mann, M. C. Kelly, and N. Troldborg, "The k-ϵ-fp model applied to double wind turbine wakes using different actuator disk force methods", *Wind Energy*, vol. 18, no. 12, pp. 2223–2240, December 2015, ISSN: 10954244. DOI: 10.1002/we.1816.

[28] P. J. Richards and R. P. Hoxey, "Appropriate boundary conditions for computational wind engineering models using the k-ϵ turbulence model", *Journal of Wind Engineering and Industrial Aerodynamics*, vol. 46-47, pp. 145–153, 1993, ISSN: 01676105. DOI: 10.1016/0167-6105(93)90124-7.

[29] P. van der Laan, M. C. Kelly, and N. N. Sørensen, "A new k-ϵ model consistent with Monin-Obukhov similarity theory", *Wind Energy*, vol. 20, no. 3, pp. 479–489, March 2017, ISSN: 10954244. DOI: 10.1002/we.2017.

[30] P.-E. Réthoré, P. van der Laan, N. Troldborg, F. Zahle, and N. N. Sørensen, "Verification and validation of an actuator disc model", *Wind Energy*, vol. 17, no. 6, pp. 919–937, Jun. 2014, ISSN: 10954244. DOI: 10.1002/we.1607.

[31] J. Michelsen, "Basic3D : A platform for development of multiblock PDE solvers", Technical University of Denmark, Lyngby, Tech. Rep., 1992.

[32] N. Troldborg, N. N. Sørensen, P.-E. Réthoré, and M. van der Laan, "A consistent method for finite volume discretization of body forces on collocated grids applied to flow through an actuator disk", *Computers & Fluids*, vol. 119, pp. 197–203, Sep. 2015, ISSN: 0045-7930. DOI: 10.1016/J.COMPFLUID.2015.06.028.

[33] P. van der Laan and S. J. Andersen, "The turbulence scales of a wind turbine wake: A revisit of extended k-epsilon models", *Journal of Physics: Conference Series*, vol. 1037, no. 7, 2018, ISSN: 17426596. DOI: 10.1088/1742-6596/1037/7/072001.

[34] T. Burton, D. Sharpe, N. Jenkings, and E. Bossanyi, *Wind Energy Handbook*. John Wiley & Sons, Ltd, 2001, ISBN: 0471489972.

[35] M. Bastankhah and F. Porté-Agel, "Experimental and theoretical study of wind turbine wakes in yawed conditions", *Journal of Fluid Mechanics*, vol. 806, no. 2016, pp. 506–541, 2016, ISSN: 0022-1120. DOI: 10.1017/jfm.2016.595.

[36] J. Schottler, F. Mühle, J. Bartl, J. Peinke, M. S. Adaramola, L. Sætran, and M. Hölling, "Comparative study on the wake deflection behind yawed wind turbine models", *Journal of Physics: Conference Series*, vol. 854, no. 1, 2017, ISSN: 17426596. DOI: 10.1088/1742-6596/854/1/012032.

[37] M. F. Howland, L. A. Martínez-Tossas, J. Meyers, J. Bossuyt, and C. Meneveau, "Wake structure in actuator disk models of wind turbines in yaw under uniform inflow conditions", *Journal of Renewable and Sustainable Energy*, vol. 8, no. 4, 2016. DOI: 10.1063/1.4955091.

[38] M. Abkar and F. Porté-Agel, "The effect of atmospheric stability on wind-turbine wakes: A large-eddy simulation study", *Journal of Physics: Conference Series*, vol. 524, no. 1, pp. 1–9, Jun. 2014, ISSN: 1742-6596. DOI: 10.1088/1742-6596/524/1/012138.

[39] M. Hartvig Hansen, L. C. Henriksen, C. Tibaldi, L. Bergami, D. Verelst, and G. Pirrung, "HAWCStab2 User Manual Wind 2017", pp. 1–32, 2017.

[40] J. N. Sørensen and W. Z. Shen, "Numerical Modeling of Wind Turbine Wakes", *Journal of Fluids Engineering*, vol. 124, no. 2, Jun. 2002, ISSN: 00982202. DOI: 10.1115/1.1471361.

[41] Vestas, *General Specification - Vestas V29-225kW 50 Hz Wind Turbine - ITEM no. 941521.R3*.

[42] A. Jiménez, A. Crespo, and E. Migoya, "Application of a LES technique to characterize the wake deflection of a wind turbine in yaw", *Wind Energy*, vol. 13, no. 6, pp. 559–572, 2009, ISSN: 10954244. DOI: 10.1002/we.380.

[43] N. Janssen, *Introduction to iSpin at WESA conference day 2019*, 2019.

[44] A. Vasel-Be-Hagh and C. L. Archer, "Wind farms with counter-rotating wind turbines", *Sustainable Energy Technologies and Assessments*, vol. 24, pp. 19–30, 2017. DOI: 10.1016/j.seta.2016.10.004.

[45] W. Yuan, A. Ozbay, W. Tian, and H. Hu, "An Experimental Investigation on the Effects of Turbine Rotation Directions on the Wake Interference of Wind Turbines", *51st AIAA Aerospace Sciences Meeting Including the New Horizons Forum and Aerospace Exposition 2013*, pp. 1–16, 2013.

[46] C. Bak, *Aerodynamic design of wind turbine rotors*. Woodhead Publishing Limited, 2010.

[47] T. Nishino and S. Draper, "Local blockage effect for wind turbines", *Journal of Physics: Conference Series*, Jun. 2015. DOI: 10.1088/1742-6596/625/1/012010.

[48] S. McTavish, S. Rodrigue, D. Feszty, and F. Nitzsche, "An investigation of in-field blockage effects in closely spaced lateral wind farm configurations", *Wind Energy*, vol. 18, no. 11, pp. 1989–2011, November 2015. DOI: 10.1002/we.1806.

[49] A. R. M. Forsting and N. Troldborg, "The effect of blockage on power production for laterally aligned wind turbines", *Journal of Physics: Conference Series*, vol. 625, Jun. 2015. DOI: 10.1088/1742-6596/625/1/012029.

[50] P.-E. Réthoré and N. N. Sørensen, "A discrete force allocation algorithm for modelling wind turbines in computational fluid dynamics", *Wind Energy*, vol. 15, no. 7, pp. 915–926, October 2012, ISSN: 10954244. DOI: 10.1002/we.525.

[51] N. N. Sørensen, A. Bechmann, J. Johansen, L. Myllerup, P. Botha, S. Vinther, and B. S. Nielsen, "Identification of severe wind conditions using a Reynolds Averaged Navier-Stokes solver", *Journal of Physics: Conference Series - Torque*, vol. 75, 2007. DOI: 10.1088/1742-6596/75/1/012053.